https://doi.org/10.15388/vu.thesis.61
https://orcid.org/0000-0002-4924-1345

VILNIUS UNIVERSITY
CENTER FOR PHYSICAL SCENCES AND TECHNOLOGY

Ieva
MIKALAUSKAITĖ

Tuning Optical Properties of Lanthanide Doped Upconverting Materials

DOCTORAL DISSERTATION

Natural sciences,
Chemistry N 003

VILNIUS 2020

This dissertation was written between 2015 and 2019 at Faculty of Chemistry and geosciences, Vilnius University. The research was supported by Research Council of Lithuania.
Academic supervisor – Prof. dr. Aldona Beganskienė (Vilnius University, Natural Sciences, Chemistry – N 003).

This doctoral dissertation will be defended in a public meeting of the Dissertation Defence Panel:
Chairman – Prof. habil. dr. Audrius Padarauskas (Vilnius University, Natural Sciences, Chemistry, N 003).
Members:
Prof. dr. Ingrida Ancutienė (Kaunas University of Technology, Natural Sciences, Chemistry, N 003);
Assoc. prof. dr. Virgaudas Kubilius (Vilnius University, Natural Sciences, Chemistry, N 003);
Dr. Vladimir Sivakov (Leibniz Institute of Photonic Technology, Natural Sciences, Chemistry, N 003);
Dr. Loreta Tamašauskaitė-Tamašiūnaitė (Center for Physical Sciences and Technology, Natural Sciences, Chemistry, N 003).

The dissertation shall be defended at a public meeting of the Dissertation Defence Panel at 2 p.m. on 25th September 2020 in Inorganic chemistry auditorium of the Faculty of Chemistry and Geosciences, Vilnius University.
Address: Naugarduko st. 24, LT-03225 Vilnius, Lithuania
Tel. 2193108; e-mail: info@chgf.vu.lt.
The text of this dissertation can be accessed at the libraries of Center for Physical Sciences and Technology and Vilnius University as well as on the website of Vilnius University: www.vu.lt/lt/naujienos/ivykiu-kalendorius

https://doi.org/10.15388/vu.thesis.61
https://orcid.org/0000-0002-4924-1345

VILNIAUS UNIVERSITETAS
FIZINIŲ IR TECHNOLOGIJOS MOKSLŲ CENTRAS

Ieva
MIKALAUSKAITĖ

Lantanoidais legiruotų apkonvertuojančių medžiagų optinių savybių tyrimas

DAKTARO DISERTACIJA

Gamtos mokslai,
Chemija N 003

VILNIUS 2020

Disertacija rengta 2015–2019 metais Vilniaus universitete, Chemijos ir geomokslų fakultete. Mokslinius tyrimus rėmė Lietuvos mokslo taryba.

Mokslinė vadovė – prof. dr. Aldona Beganskienė (Vilniaus universitetas, gamtos mokslai, chemija, N 003).

Gynimo taryba:
Pirmininkas – Prof. habil. dr. Audrius Padarauskas (Vilniaus universitetas, gamtos mokslai, chemija, N 003).
Nariai:
Prof. dr. Ingrida Ancutienė (Kauno technologijos universitetas, gamtos mokslai, chemija, N 003);
Doc. dr. Virgaudas Kubilius (Vilniaus universitetas, gamtos mokslai, chemija, N 003);
Dr. Vladimir Sivakov (Leibnico fotoninų technologijų institutas gamtos mokslai, chemija, N 003);
Dr. Loreta Tamašauskaitė-Tamašiūnaitė (Fizinių ir technologijos mokslų centras, gamtos mokslai, chemija, N 003)

Disertacija ginama viešame Gynimo tarybos posėdyje 2020 m. rugsėjo mėn. 25 d. 14 val. Vilniaus universiteto, Chemijos ir geomokslų fakulteto Neorganinės chemijos auditorijoje.
Adresas: Naugarduko g. 24, LT-03225, Vilnius, Lietuva
Tel. 2193108; el. paštas info@chgf.vu.lt .

Disertaciją galima peržiūrėti Fizinių ir technologijos mokslų centro, Vilniaus universiteto bibliotekose ir VU interneto svetainėje adresu: https://www.vu.lt/naujienos/ivykiu-kalendorius

CONTENTS

List of Abbreviations

CN – Coordination number
CR – Cross relaxation
CW – Continuous wave
DC – Downconversion
ED – Electric dipole
EMU – Energy migration upconversion
EQ – Electric quadrupole
ESA – Excited state absorption
ET – Energy transfer
ETU – Energy transfer upconversion
FE – Field emission
FIR – Fluorescence intensity ratio
FTIR – Fourier-transform infrared spectroscopy
GSA – Ground state absorption
HAADF – High angle annular dark field
ICP-OES – Inductively coupled plasma optical emission spectrometry
KTFA – Potassium trifluoroacetate
LiTFA – Lithium trifluoroacetate
LED – Light-emitting diode
MD – Magnetic dipole
MRI – Magnetic resonance imaging
NaTFA – Sodium trifluoroacetate
NIR – Near infrared region
OA – Oleic acid
ODE – 1-octadecene
OM – Oleylamine
PA – Photon avalanche
PAA – Polyacrylic acid
PEG – Polyethylene glycol
PEI – Polyethylenimine
PL – Photoluminescence
PVP – Polyvinylpyrrolidone
R/G – Red/Green ratio
RE – Rare earth
SEM – Scanning electron microscopy
TFA – Trifluoroacetic acid
TEM – Transmission electron microscopy
XRD – Powder X-ray diffraction
UC – Upconversion, upconverting
VIS – Visible

Introduction

An emerged amount of attention has been drawn to upconverting (UC) materials in recent years. Having a huge difference in comparison with the conventional luminescent materials, it is expected for the UC materials to significantly take part in various fields of application. The luminescence is achieved through a sequential absorption of two (or more) photons excited with lower energy near infrared (NIR) region. The unique electronic configuration of lanthanide ions (Ln^{3+}), having a relatively long-lived intermediate energy states, allows the UC process to occur in various types of materials [1].

Various approaches of designing UC materials have been employed in order to obtain effective luminescent probes. Colour emission output can be altered by carefully selecting concentration of activators and sensitizers doped into preferred host material. A strategy of doping ions of different size radii is expected to alter local site symmetry of host, whereas transition metal ions provide with an energy level structure to mediate non-radiative transitions. A surface decoration with additional inorganic shell is exploited in order to minimize non-radiative energy losses and expand application possibilities by combining different activator/sensitizer pairs in a single particle.

Deeper penetration into biological tissues as a result of lower absorption and reduced scattering of NIR [2] used for excitation of UC nanomaterials considered as contrast agents [3]. Due to high photostability, low toxicity and autofluorescence, UC materials could become a new generation of imaging agents [4, 5]. Among other benefits, the use of low power, continuous wave (CW) lasers ($1\text{-}10^3$ W/cm^2) to induce UC process must be highlighted [6]. However, some challenges in UC systems must be addressed. A limitation arising from absorption cross section, which is important for the excitation efficiency, has to be improved. The most commonly used sensitizer (Yb^{3+}) has large absorption in the range of 980 nm, while prolonged exposure to biological samples would result in overheating issues [7]. Thus, a shift in excitation wavelength to 800 nm (Nd^{3+} excitation) is an option in order to avoid overheating of the tissues and expand the application possibilities by generating a NIR-to-NIR imaging tool [8]. Due to their unique properties, UC materials are exploited in various fields of application including solar cells, security printing, thermal sensing and biomedicine [9]. Inserting Gd^{3+} ions into host material, a novel multimodal system of luminescence and magnetic resonance imaging

(MRI) [10] has been realized. However, in order to efficiently use UC materials in biological field as a tool of visualisation and therapy, additional steps to produce hydrophilic materials have to be performed.

The aim of current work was to synthesize and investigate optical properties of lanthanide doped (Yb^{3+}, Er^{3+}, Nd^{3+}) NaY/GdF_4 upconverting materials. Additional doping with alkali ions (Li^+ and K^+) was employed in order to study the impact of different size ionic radius to the phase formation and optical properties. Furthermore, doping with transition metal ions (Mn^{2+}, Cr^{3+}) was also applied in order to tune luminescence colour outcome of upconverting materials. Moreover, temperature sensing application possibilities were also investigated. The tasks for accomplishing the main goal were formulated as follows:

1. To synthesize alkali doped upconverting $NaGdF_4$ materials *via* thermal decomposition synthesis method and investigate the impact of Li^+ and K^+ ions on optical properties.
2. To synthesize transition metal doped upconverting NaY/GdF_4 materials *via* thermal decomposition synthesis method and investigate the impact of Mn^{2+} and Cr^{3+} ions on optical properties.
3. To investigate the impact of Yb^{3+} concentration to $Nd^{3+}\rightarrow Yb^{3+}$ energy transfer efficiency in $NaGdF_4$ system.
4. To investigate temperature dependent luminescence properties and evaluate temperature sensing properties.

Scientific novelty:

1. Doping alkali and transition metal ions resulted in a formation of different phase materials and tuning optical properties through altered red/green emission ratio.
2. Abnormal temperature dependent luminescence behaviour was observed in $NaGd_{0.995}Nd_{0.005}F_4$. An explanation of a mechanism involving neighbouring Nd^{3+} ions with temperature induced energy circling was adapted.
3. A positive impact on luminescence was observed when temperature is increased in $NaGd_{0.995-x}Yb_{0.4}Nd_{0.005}F_4$ sample. Prolonged Yb^{3+} emission lifetime values were recorded when temperature was above 300 K.
4. $NaGd_{0.78}Yb_{0.2}Er_{0.02}F_4$ and $NaGd_{0.475}Yb_{0.5}Er_{0.02}F_4$ were proposed as good candidates for temperature sensing application, since relative temperature sensitivity (S_r) values are close to 1% K^{-1}.

1. Lanthanide Luminescence in Upconverting Materials

The most distinctive feature of upconverting process is the involvement of two or more lower energy photons to obtain higher energy emission [11]. For this purpose, lanthanide ions with relatively long-lived (in micro- to millisecond range) intermediate levels are exploited. This occurs due to the unique 4f–4f forbidden intra-configurational transitions generating a sequential absorption of the energy [9]. Since inner 4f electrons are shielded by the outer levels of 5s and 5p electrons, the $[Xe]4f^N \rightarrow [Xe]4f^N$ transitions are chemically inert to different host materials.

Ln^{3+} energy states are characterised by Russel-Saunders notation ($^{2S+1}L_J$) where S, L and J are spin, orbital and total angular momentum [11, 12]. Chemical environment affects the spherical symmetry of electronic structure of Ln^{3+} ions that is split into Stark sub-levels [13]. The number of split sub-levels depend on site symmetry of the ion with possible values of $2J+1$ [14]. The f energy levels of lanthanide ions are affected by the combination of Coulomb, spin-orbit and crystal field interactions to a different extent (Table 1) [15].

Table 1. Energy interaction scale of lanthanide ions in crystals [15].

Interaction	Energy (cm^{-1})
Coulomb (electron repulsion)	10^4
Spin-orbit	10^3
Crystal field	10^2

Due to electrostatic interaction between 4f orbitals, ^{2S+1}L split in order of 10^4 cm^{-1}. Further split of 10^3 cm^{-1} is from spin-orbit interaction of $^{2S+1}L_J$ resulting in separation of J states. Finally, crystal field strength spreads the Stark split sub-levels in order of 10^2 cm^{-1}, resulting in a significant dependence on host material [11, 14].

Not all of the electronic transitions (e.g. sharp 4f-4f, wider 4f-5d and broad charge transfer) of lanthanide ions are allowed [16]. In case of forbidden 4f transitions, the requirement of Laporte selection rule (or parity rule) is not fulfilled. The states with the same parity cannot be connected by electronic dipole (ED) transitions [16]. However, the role of asymmetrical crystal field is to intermix the f states of Ln^{3+} ions with opposite parity thus increasing a probability of ED by mitigating the

Laporte's rule [11]. In this case, ED transitions become allowed (with low probability) and sometimes termed as induced or forced transitions [17]. Magnetic dipole (MD) and electric quadrupole (EQ) transitions that follow selection rules (listed in Table 2) are allowed within 4f shell.

Table 2. Selection rules for intra-configurational f-f transitions [13, 14, 16, 18].

Transition	Parity	ΔS	ΔL	ΔJ
ED	Opposite	0	≤6	≤6 (2, 4, 6 if J or J' = 0)
MD	Same	0	0	0; ±1
EQ	Same	0	0; ±1; ±2	0; ±1; ±2

However, MD transitions have weak intensity and are less affected by the crystal field [11]. Both ED and MD transitions are contributing to optical spectra, whereas EQ transition is significantly weaker and usually are not identified [13]. Some induced ED are sensitive to a change of Ln^{3+} environment because they follow some selection rules of EQ and are termed as hypersensitive transitions [13, 16, 19].

Each *J* multiplet is split under the influence of crystal field [20]. Therefore, the environment in which an ion is placed becomes important to a certain degree. The more asymmetric crystal lattice provide with the increased probability of f-f transitions, since the electronic coupling becomes enhanced [21]. An example of the impact on UC emission output between $NaYF_4$: Yb^{3+}, Er^{3+} hexagonal and cubic phase microcrystals was investigated [22] and an increase in both green and red emission was observed to be 4.4 times. Crystal field symmetry can also be reduced by introducing a different ionic size ion [23] e.g. Li^+. A successful tailoring of local crystal field was observed from the shifts of diffraction peaks and resulted in enhancement of UC emission [24]. Another approach of doping higher ionic radius (Gd^{3+}) in $NaYF_4$ facilitated a transition of symmetric cubic to less symmetrical, but more efficient hexagonal crystal phase [25].

2. Upconversion Mechanisms

A unique feature of absorption of lower energy photons through sequential multi-photon processes is known as upconversion. Inorganic host matrixes embedded with ladder-like lanthanide ions with metastable 4f energy levels are crucial components of generating higher energy photons. Since one UC system can be analyzed as a performance of multiple mechanisms, it becomes difficult to quantitatively evaluate the involved processes [12]. Several main mechanisms will be discussed in this Chapter. A schematic representation is depicted in Figure 2.1.

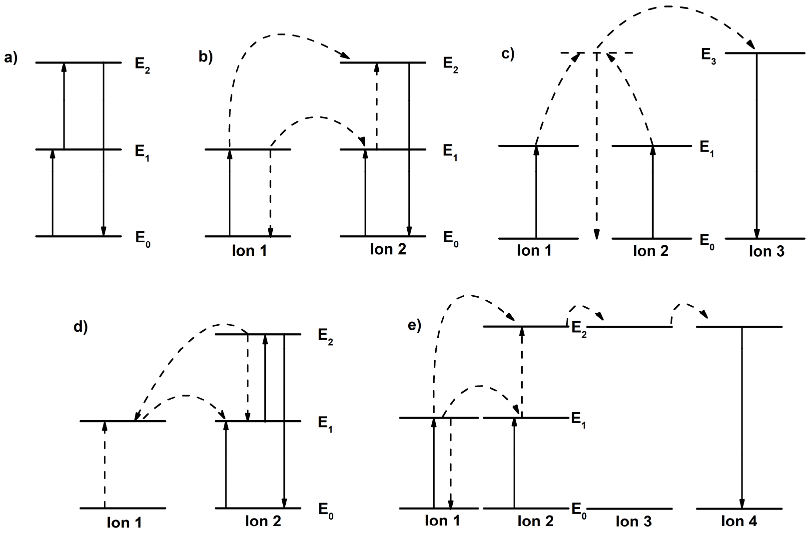

Figure 2.1. A schematic representation of UC mechanisms: a) ESA, b) ETU, c) CSU, d) PA, e) EMU [26, 27]. Upward and downward solid lines represent direct excitation and radiative emission processes respectively. Dashed arrows represent energy transfer (ET) processes.

2.1. Excited state absorption (ESA)

Excited state absorption (ESA) process typically occurs in a singly doped system, when the dopant concentration is low (<1%) [27, 28]. A successive absorption takes place due to previously mentioned ladder-like energy level arrangement abundant in lanthanide ions. When excitation energy is resonant with the transition from ground level (E_0, Fig. 2.1 a) to metastable energy level (E_1), a process called ground state absorption (GSA) takes place. Intermediate level E_1 intends to function as a reservoir while another photon promotes the ion from E_1 to a higher energy state E_2 [9]. A single ion absorbed photon energy results in an optical transition ($E_2 \rightarrow E_0$). The ESA occurs mainly in host materials with singly doped Nd^{3+}, Er^{3+}, Tm^{3+}, Ho^{3+} [29] ions (activators). Further increase in activator concentration could result in a significant increase of non-radiative cross-relaxation processes, thus overcoming the excited state absorption [27].

2.2. Energy transfer upconversion (ETU)

In the case of energy transfer upconversion (ETU), two neighbouring ions are involved in the process (Fig. 2.1 b). The ion with larger absorption cross section in the NIR region, e.g. Yb^{3+} with 1.2×10^{-20} cm^2 compared to Er^{3+} 1.7×10^{-21} cm^2 [30], is co-doped in a host matrix in order to operate as a sensitizer. Firstly, during the ground state absorption stage both Ion 1 (sensitizer) and Ion 2 (activator) are excited to their intermediate E_1 levels by sequential absorption of two photons [31]. The main difference from ESA is a non-radiative energy transfer (ET) from Ion 1 to Ion 2 exciting the latter to higher energy state E_2. Thus, the sensitizer ion relaxes to its initial ground state, while the activator receives enough energy to populate E_2.

Yb^{3+} ions are mainly used as sensitizers due to the $^2F_{7/2}\rightarrow{}^2F_{5/2}$ transition which resonates well with the lanthanide ions (Tm^{3+}, Ho^{3+}, Er^{3+}) typically used in upconversion [32] as activators. The concentration of dopant ions influences UC efficiency of ETU process, since it correlates with the average distance between Ion 1 and Ion 2 [33]. However, the concentration of Yb^{3+} is usually kept at 20-40% in order to avoid concentration quenching [28]. Distance of sensitizer and activator ion could be manipulated by varying the concentration of the latter resulting in emission lifetime tunability [34].

A simple measurement of luminescence decay under short pulse excitation could be used for the determination of the process occurring in UC system [35]. A single exponential decay curve is obtained where excited state absorption mechanism is present (Fig. 2.2). In the case where ETU takes place, two photon excitation of two separate ions result in a rise of a decay curve after a short pulse excitation, since energy transfer upconversion process is longer than the excitation pulse [31].

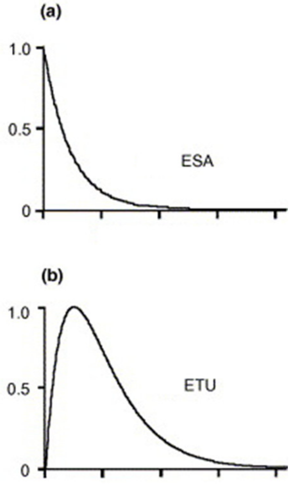

Figure 2.2. A schematic representation of time-evolution of the emission of UC mechanisms: ESA (a) and ETU (b) [31]

2.3. Cooperative sensitization upconversion (CSU)

Cooperative sensitization upconversion (CSU) is mainly occurring in bulk materials in which ion clusters can easily be formed [36]. Three ion centers are typically involved, two of them (Ion 1 and Ion 2) being of the same type (Fig. 2.1 c). The adjacent ions of the same origin are cooperatively activated to a virtual excited state followed by a simultaneous energy transfer to activator ion (Ion 3) [37]. However, relative efficiency of CSU in comparison with other UC mechanisms is lower (10^{-6}) by orders of magnitude than ESA (10^{-5}) and ETU (10^{-3}) which is considered the most efficient [29].

2.4. Photon avalanche (PA)

The process of photon avalanche (PA) occurs only in the systems, when several requirements are fulfilled. The looping process of PA (Fig. 2.1 d) is produced above certain threshold of excitation power [9]. Intermediate level (E_1) of Ion 2 is populated by a weak GSA, with immediately occurring further population to the upper level (E_2) with the energy transferred from Ion 1 [38]. With the transfer from Ion 1 to Ion 2, a looping of generating two Ion 2 at E_1 state occurs, which later generates four and eight Ion 2 at E_1 state, thus evoking avalanche [9]. As a result of continuous energy transfer, photon avalanche has a delayed response occurring from the numerous cycles of excited state absorption and cross-relaxation (CR) processes [27]. ESA is induced by efficient CR with the coinciding effective energy difference between energy levels involved [39]. Although, CR is known as a disadvantageous ion-ion interaction closely dependent on the dopant concentration [9], it plays one of the crucial roles in the PA mechanism.

2.5. Energy transfer-mediated upconversion (EMU)

Following the challenges and requirements for the application, more complex UC materials having brighter emission were produced [32]. Novel design of UC systems, require developing and discussing new pathways of energy transfer. Wang et al. [40] designed a core-shell structure with spatially separated lanthanide ions proposing energy migration-mediated pathway (EMU, Fig. 2.1 e).

Typically, four types of ions are involved in EMU system. Sensitizer (Ion 1) and accumulator (Ion 2) generate energy through a previously discussed GSA/ETU mechanism which is followed by the energy transfer to migration ions (Ion 3). The requirement for the accumulator and migrator is to have a long lifetime in order to accept, accumulate energy and bridge the energy transfer towards the activator (Ion 4) [11, 40]. Moreover, spatial separation of Ion 1 + Ion 2 and Ion 3 + Ion 4 reduces the possibility of cross-relaxation, trapping the energy on the activator in the shell where UC luminescence occurs [11]. A good example of energy transfer-mediated upconversion is discussed in literature, where in a $NaGdF_4$:Yb/Tm@$NaGdF_4$:X (X = Tb, Eu, Dy, Sm) core-shell system energy migrates through Gd^{3+} ions up through a distance of 5 nm [40]. Furthermore, another lanthanide ion (Yb^{3+}) has similar properties and is able to serve as a bridge in a core-shell concept of materials. For a successful energy transfer to take place, donor and acceptor should meet a resonance condition (good spectral overlap) and be arrayed within a short interionic distance [41]. It has been proven that Yb^{3+} ions were crucial components while transferring energy to activator ions in a Nd^{3+} sensitized $NaGdF_4$:Yb/Er@$NaGdF_4$ [42]. This new design of EMU mechanism enables lanthanide ions (Eu^{3+}, Tb^{3+}, Sm^{3+}) that could not be excited with 980 nm irradiation to be exploited in UC system [11].

3. Architecture of Upconverting Materials

Since the application of UC materials is very broad, a design of the system that will serve the purpose has to meet the expectations. The selection of host matrix, activator/sensitizer combination and doping concentration is important for the color tunability and efficiency of UC emission.

3.1. Host Material

Lanthanide ions are similar in their chemical, physical properties and ionic size. Therefore, inorganic compounds containing rare earth (RE) ions are considered an excellent option for the host material [43]. In addition, the lattices, containing cations similar to lanthanide in ionic size (Na^+, Ca^{2+}) inhibit crystal defects and lattice stress formation [33]. It is preferable for the host matrix to be chemically stable and optically transparent [9] as well as, have minimal amount of impurities, in order to reduce non-radiative relaxation pathways. Distance (R) between ions in host matrix is also an important factor, since the probability of energy transfer between sensitizer and activator ions is dependent on R^{-2} [29]. Highly controlled doping concentration tunes energy transfer of the Ln^{3+} ion depending on the occupied lattice position [41].

Table 3. Phonon energy of different host materials [3].

Host material	Highest phonon energy (cm^{-1})
Phosphate glass	1200
Silica glass	1100
Gd_2O_3	700
Y_2O_3	600
$NaYF_4$	370
LaF_3	350

Radiative emission related to host matrix properties is dependent on the phonon energy of different materials (Table 3). Higher phonon energy of a host material will result in a quenching through emerging non-radiative relaxation pathways. Application of certain halides (e.g. chlorides, bromides, iodides) and oxides is limited due to their hydroscopic properties or relatively high phonon vibration values (500 cm^{-1}), respectively [33]. Ions, with larger energy gap (ΔE), will not be susceptible to a phonon provided non-radiant energy transfer route if the energy gap is larger than the energy of six phonons [44]. This, in fact, is derived from characteristic energy gap law [45]:

$$A = A_0 e^{\frac{-\alpha}{\Delta E}} \qquad \text{(Eq. 1)}$$

where A is the multiphoton emission rate, A_0 and α are constants, dependent on host material, ΔE – energy gap between populated and the next higher energy level of Ln^{3+}. Therefore, fluoride compounds are considered as the most suitable host material, are chemically stable and have low phonon energy (~350 cm^{-1}) [43].

A possible route of tailoring local lanthanide ion environment in the crystal is additional doping of cations of different ionic radius, thus replacing initial cations or occupying interstitial sites [9] (see *Chapter 3.4 Engineering of Upconverting Materials*). Local crystal field has also an impact in outcome of UC luminescence. A less symmetric crystal field is more effective due to the increased probability of forbidden *f-f* transitions [3]. In fact, better intermixing and electronic coupling between 4*f* energy levels in hexagonal phase (β) NaYF$_4$:Yb/Er is about an order of magnitude higher UC emission efficiency than in cubic (α) phase sample [46].

3.2. Sensitizers

As previously discussed in *Chapter 2*, energy transfer upconversion is identified as the most efficient UC mechanism. The efficiency of ETU mechanism is mostly depend on large absorption cross-section of sensitizer as well as the match of energy levels of sensitizers and activators [27]. Yb^{3+} is considered as one of the best sensitizers due to the large absorption cross-section and simple energy level scheme that will take part in 980 nm excited UC [32]. The energy transition ($^2F_{7/2} \rightarrow {}^2F_{5/2}$) corresponds well (Fig. 3.1) with many activator Ln^{3+} ions (Er^{3+}, Tm^{3+}, Ho^{3+}) employed in various systems [3].

It is suggested that doping concentration of Yb^{3+} should be kept at 20-40% to avoid concentration quenching [28]. However, there are different approaches where the manipulation of Yb^{3+} concentration was exploited to a certain extent. Wang et al. co-doped NaYF$_4$ with Yb/Er and increased amount of Yb^{3+}, which led to an emission output modification [47]. A series of different Yb^{3+} concentration (25-60%) compounds were compared and the decrease of blue and green light emission was observed due to energy back-transfer from Er^{3+} to Yb^{3+}. The UC emission quenching effect, which appears due to back energy transfer, supposedly occurs from the energy migration towards surface quenching sites [9]. In order to efficiently increase Yb^{3+} content in an UC nanoparticle, a solution of spatial isolation will be introduced (*Chapter 3.4*). Another approach was proposed through design of certain crystal structure materials, where long distance energy migration in highly Yb^{3+} doped KYb_2F_7:Er was disfavored by clustering Yb^{3+} ions [48].

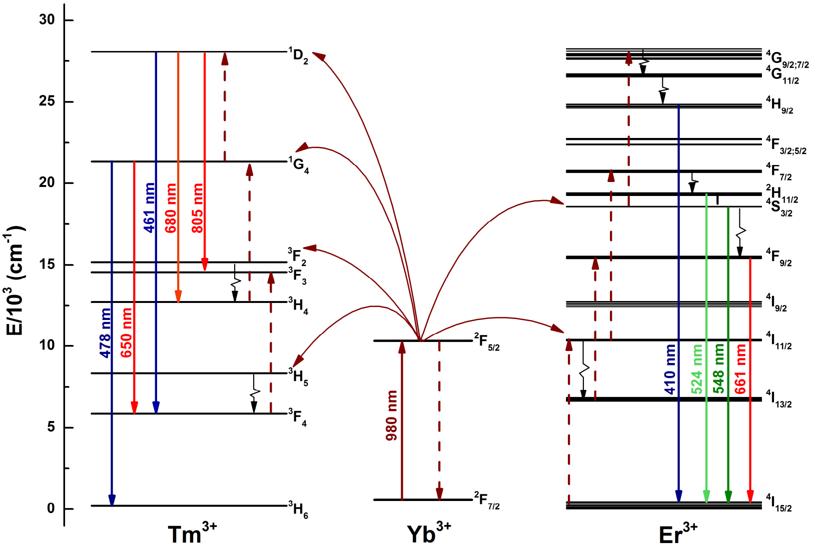

Figure 3.1. Energy level diagram of Er^{3+} and Tm^{3+} sensitized by Yb^{3+} with a possible UC scheme [27].

Slightly higher doping concentrations of Yb^{3+} were reported in the Tm^{3+} co-doped materials [49-51]. A more discrete Tm^{3+} energy level distribution enables ETU emission of Yb^{3+}-Tm^{3+} pair to occur from more than two photon involvement (Fig. 3.1) [27]. However, the main drawback of Yb^{3+} to be used as a sensitizer is the absorption in the range of water absorption, since it could be considered as damage to cells and tissue [35].

Another candidate to take part in UC system as a sensitizer was introduced recently. Nd^{3+} ions have large absorption cross-section at 808 nm (1.2×10^{-19} cm^2) and are expected to minimize excitation heating effect induced by laser [42]. During excitation process, energy is absorbed by the ground state $^4I_{9/2}$ of Nd^{3+} and transferred to higher energy level

$^4F_{3/2}$ (Fig. 3.2). The harvested photon is sequentially transferred to Yb^{3+} which takes part as the energy "migrator".

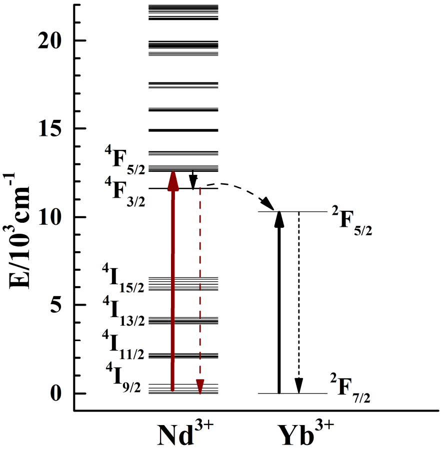

Figure 3.2. Nd^{3+}→Yb^{3+} energy transfer diagram under 808 nm laser excitation [52].

The process is followed by energy transfer of Yb^{3+} ions from $^2F_{5/2}$ level to activators (e.g. Er^{3+}) [53]. Additional step of energy transfer $^4F_{3/2}$ (Nd^{3+}) → $^2F_{5/2}$ (Yb^{3+}) occurs in Nd/Yb pair at 808 nm excitation. Non-radiative energy transfer Nd^{3+}→Yb^{3+} is reported to be efficient [54], thus additional pathway of excitation in a single type of triply doped material becomes an option. However, the concentration of Nd^{3+} doping is reported to be ≤1% with a possibility of direct quenching of UC emission with energy back-transfer routes from activators [32]. A solution was proposed to form a spatially separated "sandwich" type structure of $NaYF_4$:Yb/Er@$NaYF_4$/Yb@$NaNdF_4$/Yb to eliminate quenching by blocking Er^{3+}→Nd^{3+} energy transfer [55].

3.3. Activators

Trivalent lanthanide ions with long-lived excited states and a unique set of emission peaks are suitable for single doped UC systems. Typically Er^{3+}, Tm^{3+}, Ho^{3+} are used in ESA type of UC luminescence generation [43]. However, there are reports on other single doped lanthanide (III) ions being exploited [56, 57]. Since each step of the photon absorption requires the same photon energy, the efficiency of Er^{3+} emission is considered to be the highest [9, 32]. Energy difference (~10350 cm^{-1}) in Er^{3+} is similar between the $^4I_{11/2}$ and $^4I_{15/2}$ states, $^4I_{11/2}$ and $^4F_{7/2}$, $^4F_{9/2}$ and $^4I_{13/2}$ states, generating the emission resulting from 980 nm excitation [9]. Efforts to increase UC emission can simply be fulfilled with increasing dopant concentration in a host matrix [6]. On the other hand, non-radiative decay processes of cross-relaxation can be enhanced due to shortened ion-ion distance [9].

In order to improve UC emission efficiency, another approach of co-doped system is preferred. The combination of previously discussed ions, having broad absorption cross-section (sensitizers, e.g. Yb^{3+}) and low concentration (0.2-2%) of activators [32, 58] is paired to obtain an efficiently sensitized luminescent material. Yb^{3+}-Er^{3+} pair generates emission bands in red, green and blue regions (Fig. 3.1) corresponding to $^4F_{9/2}\rightarrow{}^4I_{15/2}$, $^2H_{11/2;}{}^4S_{3/2}\rightarrow{}^4I_{15/2}$ and $^2H_{9/2}\rightarrow{}^4I_{15/2}$ transitions, respectively. Typically, yellow colour is visible with 20% Yb^{3+}/2% Er^{3+} in cubic phase $NaYF_4$, while 20% Yb^{3+}/2% Tm^{3+} yields blue colour output [59].

Studies of doping higher activator concentrations were carried out with the outcome of enhanced UC luminescence when concentration of Tm^{3+} was increased [60]. By manipulating activator concentration, $NaYF_4$:Yb/Er or Tm compounds were synthesized, generating a broad range of colour output from VIS to NIR using the same excitation source [47]. Moreover, it is possible to tune the emission colour by doping several activator ions in one host material. Adding Ce^{3+} ions in $NaYF_4$: Yb, Ho resulted in introduced additional CR pathways, thus colour output was shifted from green to red [61]. White emission was observed when Y_2O_3 was co-doped with a combination of Yb^{3+}, Er^{3+}, Tm^{3+} [62]. Recently, attention was drawn to a shift towards second biological window (1000-1700 nm, NIR II) emission [63]. Due to reduced light scattering, deeper tissue penetration, emission of Tm^{3+}, Nd^{3+}, Yb^{3+}, Er^{3+} and Ho^{3+} located in the NIR II region is obtained through downconversion (DC) approach [64, 65]. Variation of activator concentration, pairing several different activator ions in one host material serve as a possible route to manipulate colour output depending on the desired application field.

3.4. Engineering of Upconverting Materials

As discussed earlier, an impact to the properties of UC is determined by a selection of host material, activator/sensitizer and their concentration. However, there are several possible emission modulation possibilities involving difficult designs of nanomaterials (core-shell approach) or doping alkali or transition metal ions.

3.4.1. Doping with Alkali and Transition Metal Ions

Since Ln^{3+} ions are sensitive to changes in local environment, reducing site symmetry for activators in host matrix is addressed in terms of UC luminescence modulation. Additional doping of ions with different ionic radius distorts the lattice sites by possibly altering the local field and modifying emission characteristics [66]. Alkali ions were suggested as a tool to modify the Ln^{3+} local site symmetry [67].

One of the most widely used UC host matrixes ($NaYF_4$) is considered as excellent for lanthanide ion doping either in cubic (α) or hexagonal (β) crystal phase [68]. As discussed in *Chapter 1. Lanthanide Luminescence in Upconverting Materials*, the more asymmetric hexagonal phase enhances the probability of f-f intermixing. Moreover, β-$NaYF_4$ in the space group $P6_3/m$ [22] has three types of cationic sites occupied by RE ion, both RE and sodium and sodium ion, with C_{3h} site symmetry for the first two and C_s for the last one, respectively [69]. Doping β-$NaYF_4$ with relatively larger K^+ ions instead of Na^+ could affect C_{3h} by lowering symmetry to C_s.

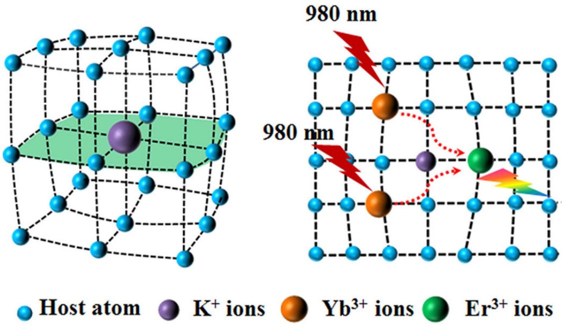

Figure 3.3. A scheme of β-$NaYF_4$ crystal lattice change after doping with K^+ ions [69].

Alkali ions (K^+ or Li^+) are chosen to replace Na^+ and change the size of unit cell, thus Yb–Er distance will also be altered [70]. Depending on the size of cation, a substitution with smaller ion, interstitial occupation or combination of both replacement possibilities take place, whereas an example of substitution with larger atom is shown in Fig. 3.3 [70]. Furthermore, reports of successful crystal field modification by doping smaller Li^+ ions instead of Na^+ showed an enhancement of UC luminescence either due to substitution of Na^+ or occupation of interstitial sites [71-73].

Another approach of doping transition metal ions into host matrix is also considered as a possibility to enhance UC luminescence [74]. Substitution of RE ion (Y^{3+} or Gd^{3+}) with Bi^{3+} [75] and Fe^{3+} [76] resulted in an enhanced UC emission, as well. Transition metals are also considered as dopants in UC system as a component to mediate energy transfer pathways of Ln^{3+} [27, 77]. Smaller size Mn^{2+} ions (r = 0.81 Å) were introduced instead of Y^{3+} (r = 0.89 Å) into $NaYF_4$ to increase red-to-green intensity ratio 200 times [78]. Furthermore, bright pure red emission was observed, when Mn^{2+} concentration reached 30%. Lifetimes of green ($^2H_{11/2}$; $^4S_{3/2} \rightarrow {}^4I_{15/2}$) and red ($^4F_{9/2} \rightarrow {}^4I_{15/2}$) emission bands of Er^{3+} decreased and increased, respectively, when Mn^{2+} concentration was increased [79]. It was assumed, that a non-radiative energy transfer pathway from $^2H_{11/2}$ and $^4S_{3/2}$ (Er^{3+}) to $^4T_1$ level of Mn^{2+} is essential for further back-energy transfer to $^4F_{9/2}$ (Er^{3+}) which results in an enhancement of the red emission [80]. Mn^{2+} ions were successfully used not only as a dopant in UC system, but also as a component of the host materials: $NaMnF_3$:Yb/Er [81], MnF_2:Yb/Er [82, 83], $KMnF_3$:Yb/Er [84]. Incorporation of Mn^{2+} ions affected Ho^{3+} and Tm^{3+} as well, shifting the emission color output to red region [84, 85]. Furthermore, UC luminescence enhancement was reported when Cr^{3+} was additionally doped in Yb^{3+}/Er^{3+} system [86]. A mechanism of energy transfer in Yb–Cr–Er system was proposed explaining the increase in red and green band emission [87].

3.4.2. Core/Shell Approach

UC nanomaterials have high surface-to-volume ratio, thus ligands ($-NH_2$ or –OH) with high-energy vibrational modes can quench luminescence by relaxation processes [88]. Moreover, surface defects from vibrational mode of 3350 cm^{-1} (OH^-) might suppress the green upconversion emission due to the matching energy gap between $^2H_{11/2}$, $^4S_{3/2}$ and $^4F_{9/2}$ states (3200 cm^{-1}) [27]. In order to protect activators and sensitizers from surface quenchers, a non-doped shell is usually coated around the core of nanoparticle [89]. A higher density of volume defects, that contribute to UC emission intensity decrease, is expected to appear in smaller core/shell particles [90].

A generally used surface coverage through a layer-by-layer coating process with a shell matching the core lattice (epitaxial shell) is produced to minimize non-radiative energy transfer processes [41]. Several different approaches are used to obtain a tunable shell: hot-injection and heat-up strategies (*see Chapter 3.5 Synthesis of Upconverting Materials*). The injection procedure to prepare $NaYF_4$:Yb/Er@$NaYF_4$ was developed from thermal decomposition synthesis of lanthanide trifluoroacetate precursors in a one-pot preparation strategy [91]. Coating of multiple shells with a well-controlled thickness and narrow size distribution ($\sigma<10\%$) was introduced by Zhao *et al.* [92]. The main difference of a heat-up procedure is that the synthesized core nanoparticles are extracted from reaction media and later used as nuclei for shell growth [93, 94]. Furthermore, concentration of shell precursor has to be low in order to avoid separate shell material formation instead of the anticipated epitaxial core/shell growth [94]. However, some groups have reported that core/shell nanoparticles obtained by heat-up procedure did not have uniform shell covering the core [93, 95].

Shell concept is used for passivation and for geometrical separation of dopant ions in order to avoid cross relaxation processes. Spatially separated ions interact by randomly hopping between donors and finally are trapped by the acceptors [32]. Furthermore, quenching effects originating from surface defects or solvent molecules are suppressed [27]. Suppression of non-radiative relaxations was evident from the enhancement of emission intensity and red/green (R/G) emission band ratio decrease. The effect was observed by coating a $NaYF_4$ shell for both crystal phase (cubic and hexagonal) nanoparticles [96]. Surface defect passivation due to CaF_2 coating increased emission intensity up to 15 times even when the concentration of sensitizer doped into $NaYF_4$ was 98% Yb^{3+} [97]. The UC emission depends on the thickness of a shell until a certain value is reached [66, 98, 99].

A role of shell in order to enhance the luminescence intensity was tackled by suggesting the active-core/active-shell concept and coating a low phonon energy $NaGdF_4$:Er^{3+} (2%), Yb^{3+} (20%) nanoparticles with a $NaGdF_4$:Yb^{3+} (20%) shell [100]. A combination of Nd^{3+}/Yb^{3+} sensitized UC system was designed through core/shell/shell structure [101]. This “sandwich” structure of $NaYF_4$:Yb, Er@$NaYF_4$:Yb@$NaNdF_4$:Yb prevented from energy back transfer to Nd^{3+} ions with the precise control of thickness of inter layer. An approach of elevating Nd^{3+} concentration was suggested through doping low 2% concentration in the core and 20% on the shell which results in 7 times higher UC emission comparing to an inert shell coated material [101]. High Nd^{3+} content in the shell was designed to exploit $Nd^{3+} \rightarrow Yb^{3+} \rightarrow Er^{3+}$ transfer process with UC luminescence being observed with a 740 nm LED excitation source [102]. Dye sensitized UC nanomaterials have recently been investigated in order to broaden absorption spectra [103]. NIR excitation range was broadened to over 150 nm for dye sensitized $NaYbF_4$:Tm^{3+}@$NaYF_4$:Nd^{3+} and had 25 times higher luminescence intensity comparing to $NaYF_4$:Yb^{3+}, Tm^{3+}@$NaYF_4$ under 980 nm excitation [104].

3.5. Synthesis of Upconverting Materials

Since properties of UC materials depend on their composition, crystalline phase, shape and size, it is important to develop a facile strategy to obtain high quality, controllable materials suitable for desired applications in diverse fields [105]. A variety of methods are used for UC materials synthesis, such as co-precipitation [46, 47, 106-110], hydrothermal synthesis [25, 47, 111-116], sol-gel process [117-119], microwave [120, 121] and combustion [122] synthesis. However, the most widely used synthesis is based on thermal decomposition method in high-boiling temperature organic solvents [9].

The general description of a thermal decomposition process is described as organometallic precursor decomposition in a mixture of high boiling point organic solvent and surfactant [123]. The synthesis can be divided into stages according to the concept of "burst-nucleation" developed by LaMer [33, 124]. Precursor concentration is increased above the limit of nucleation in time due to the existing extremely high barrier for a spontaneous nucleation to appear [123]. Overcoming the nucleation barrier in the second stage, stable nuclei accumulate, gradually decreasing the monomer concentration and starting the formation of crystals [33]. Further stage of nanoparticle growth provides with a uniform final product [125].

The non-coordinating solvent (ODE) provides sufficient energy for the nucleation and crystal formation stage at high temperature, while the coordination solvent (OA or OM) prevents from nanoparticle agglomeration and enhances the dispersibility of the particles [126]. Usually a RE trifluoroacetate solution in OA/ODE is injected to another OA/ODE mixture under inert atmosphere at elevated temperature (>300 °C) where the decomposition of $RE(CF_3COO)_3$ occurs. The hot-injection procedure is adapted from Zhang *et al.* [127] monodisperse LaF_3 formation from trifluoroacetate precursors at 280 °C for 1 h under inert atmosphere. The approach was later developed as a common route for NaY/GdF_4 synthesis [59, 88]. It was confirmed that the shape, crystalline phase can be tuned through Na/RE ratio control, solvent composition, reaction temperature and time variation [128, 129]. A narrow size distribution $NaYF_4$:Yb^{3+}/Er^{3+} (Tm^{3+}) nanoparticles with average 28 nm diameter were synthesized by Capobianco group [130]. A simple phase control is achieved through the use of larger ionic size lanthanide ions when Y^{3+} (r = 1.159 Å) were replaced by Gd^{3+} (r = 1.193 Å) [131] to obtain more efficient hexagonal (β) phase $NaYF_4$ [25]. Various UC materials were successfully synthesized, including $BaGdF_5$ [132], KY_3F_{10} [133], $BaLuF_5$ [134] and $LiYF_4$ [50], confirming the versatility of thermal decomposition procedure.

Although, thermal decomposition has advantages in terms of controllable size and high quality pure crystal phase, usually toxic side products (fluorinated and oxyfluorinated carbon species) are generated, as well as additional preparation step of thermodegradable precursors is required [129, 135, 136]. However, the use of trifluoroacetate precursors is designated only for fluoride-based compound synthesis and is not suitable to produce oxide, sulfide, phosphate or vanadate based materials [105].

A different approach (heat-up) was developed by mixing of RE salts in a solution of OA/ODE with further addition of NH_4F and NaOH and heating up the reaction vessel to 300 °C [137, 138]. Ultra-small (<10 nm) $\beta-$NaGdF$_4$ nanoparticles were obtained by modifying the conditions of synthesis [139]. Sphere, nanoplate and elliptic shape nanoparticles were synthesized by changing the amount of OA in the precursor solution [140]. Different groups have adopted heat-up method for $NaREF_4$ [141], $NaGdF_4$ [142, 143], LaF_3 [144], Na_3ZrF_7 [145], $KMnF_3$ [146] and $LiYF_4$ [147] synthesis.

3.6. Biocompatibility and Thermal Sensing

3.6.1. Surface Modification

The main disadvantage of widely used methods of synthesis is the presence of coordinating hydrophobic ligands (e.g. OA) attached to the surface of the obtained products [148]. Therefore, the procedures of surface modification were developed in order to broaden the application possibilities in the field of biomedical imaging. The biocompatibility of UC nanoparticles has already been proven by several groups with cell viability investigations [149], both *in vivo* [150, 151] and *ex vivo* [152] measurements.

Different strategies were addressed in order to improve hydrophilic properties of UC materials including ligand exchange, oxidation, attraction, surface silanization or layer-by-layer assembly [43]. A general ligand exchange method was developed by simply choosing a molecule with strong coordinating functional group (e.g. PAA) and mixing with hydrophobic nanoparticles at elevated temperature [153]. A successful exchange of ligands was reported for PAA [154-156], PVP [157], PEI [158], PEG–phosphate molecules [159]. Oxidation method involving the carbon-

carbon double bond oxidation by Lemieux-von Rudloff is not employed very often, since the procedure requires relatively long reaction time and has comparatively low yield [160]. A different approach of capping with a secondary ligand on the original hydrophobic surface component has been used widely [161]. It involves the adsorption of amphiphilic polymer through the hydrophobic van der Waals interaction [43]. With the addition of amphiphilic block copolymers, a further possibility to use the surface functionalized materials is established [162]. Coating $NaYF_4$:Yb/Er with octylamine and isopropylamine modified PAA provide with nanoparticles decorated with carboxyl groups [91] which could later be applied in coupling $–NH_2$ groups via carbodiimide chemistry [163]. Layer-by-layer assembly involves sequential adsorption of opposite charge linear polyions. It is a method that produces a precisely controlled thickness hydrophilic layer. A successful modification of $NaYF_4$:Yb/Er with positively charged poly(allylamine hydrochloride) and negatively charged poly(sodium 4–styrenesulfonate) provide with amino-rich outer shell [43, 164, 165]. Various functional groups (–COOH, $–NH_2$ or maleimide) are introduced on the surface of nanoparticles to be covalently conjugated to biomolecules involving folic acid, peptides, proteins or DNA. Bioconjugation is required for the nanoparticles to be applied as theranostic agents in tumor targeting, multimodal imaging or photodynamic therapy [9].

3.6.2. Temperature Sensing

UC materials have attracted attention due to their possibility to be applied in a variety of different fields, such as bioimaging (VIS, NIR, MRI) [5, 159, 166-168], drug delivery [169], photodynamic therapy [170], theranostic [9], security printing [171], solar cells [172-174], biosensing [175] etc. Another possible field of application of lanthanide luminescence due to their unique energy level distribution is nanothermometry [176]. The main approaches for temperature determination are the shift of a given transition, integrated intensity of a single transition or a pair and decay profiles from lifetime measurements [177]. Thermally coupled energy levels (TCL) used for temperature sensing are spaced near each other and follows a Boltzmann distribution populating these levels under influence of temperature [52, 178]. The distance between TCLs has to be between 200 and 2000 cm^{-1} in order to have the best sensitivity [179]. Furthermore, the radiative transition from upper level should dominate its non-radiative transition [180]. Apart from the usually used temperature responsive intensity ratio of $^2H_{11/2}$ and $^4S_{3/2}$ levels of Er^{3+} [179, 181, 182], other lanthanide ions have been considered for temperature sensing (Nd^{3+} [183], Ho^{3+} [184], Tm^{3+} [185]). Intensities form two closely spaced energy levels are proportional to the population of these energy levels following Boltzmann distribution [186, 187]:

$$FIR = \frac{I_2}{I_1} = Ce^{(-\Delta E/k_B T)} \qquad \text{(Eq. 2)}$$

where I_2 and I_1 are the fluorescence intensities of upper and lower energy levels, respectively; C is a constant, ΔE – effective energy difference between these two thermally coupled energy levels, k_B – Boltzmann constant (8.617342×10^{-5} eV/K) [188], T – absolute temperature. In order to evaluate and compare different nanothermometers, a relative thermal sensitivity (S_r) is determined:

$$S_r = \frac{E}{k_B T^2} \qquad \text{(Eq. 3)}$$

More responsive temperature change can be detected when the energy gap between two thermally coupled levels increases [182, 186]. Typical values of S_r are limited to approximately 1.0% K^{-1} [189]. NIR-to-NIR nanothermometers of Ho^{3+}-Nd^{3+} and Er^{3+}-Nd^{3+} systems were investigated displaying S_r value of 1.1 K^{-1} [190].

Since pathological cells display higher temperature due to increased metabolic activity [181], it is relevant to measure temperature after photothermal treatments at the tumor site [191, 192]. Thermally induced cell death was observed when external heating of $NaYF_4$:Yb^{3+}, Er^{3+} was applied [192]. UC nanoparticles were proposed to be used in a system performing a controlled hyperthermia [193].

4. Experimental Part

4.1. Materials

Starting materials used in sample preparation: gadolinium (III) oxide Gd_2O_3 (99.99% Treibacher Industrie AG), ytterbium (III) oxide Yb_2O_3 (99.99% Sigma Aldrich), erbium (III) oxide Er_2O_3 (99.99 % Sigma Aldrich), neodymium (III) oxide Nd_2O_3 (99.99 % Tailorlux), yttrium (III) oxide Y_2O_3 (99.99% Treibacher Industrie AG), trifluoracetic acid CF_3COOH (99.9% Carl Roth), sodium trifluoroacetate CF_3CO_2Na (98.0% Alfa Aesar), lithium trifluoroacetate CF_3CO_2Li (97.0% Alfa Aesar), potassium trifluoroacetate CF_3CO_2K (98.0% Alfa Aesar), oleic acid $C_{18}H_{34}O_2$ (90.0% Alfa Aesar), 1-octadecene $CH_3(CH_2)_{15}CH=CH_2$ (90.0% Alfa Aesar), hexane C_6H_{14} (99.0% Honeywell), acetone $(CH_3)_2CO$ (pure p.a. Eurochemicals), manganese (II) carbonate $MnCO_3$ (99.9% Alfa Aesar), chromium (III) chloride hexahydrate $CrCl_3 \cdot 6H_2O$ (≥98.0% Sigma Aldrich), sodium hydroxide NaOH (99% Eurochemicals), ammonium fluoride NH_4F (≥98.0% Alfa Aesar), hydrochloric acid HCl (pure p.a. Eurochemicals), ethanol C_2H_5OH, toluene C_7H_8 (99.9% Eurochemicals).

4.2. Synthesis

4.2.1. Synthesis of $Na_{1-x}Li_xGd_{0.78}Yb_{0.2}Er_{0.02}F_4$ and $Na_{1-x}K_xGd_{0.78}Yb_{0.2}Er_{0.02}F_4$

$Na_{1-x}Li_xGd_{0.78}Yb_{0.2}Er_{0.02}F_4$ particles were prepared via thermal decomposition of metal trifluoroacetates in a mixture of organic solvents (Fig. 4.1) at elevated temperature [59]. All the samples were prepared with 20% Yb and 2% Er doping concentration since it is reported to be optimal in $NaYF_4$ upconverting materials [194]. Rare earth trifluoroacetates were prepared by dissolving corresponding RE_2O_3 (1.25 mmol) in trifluoroacetic acid (TFA, 50%) at 80 °C. After the mixture became clear, residual solution was evaporated under vacuum. 2.5 mmol of NaTFA and LiTFA (or KTFA) were added together with 7.5 mL of each oleic acid and 1-octadecene. The solution (Sol A) was stirred and heated at 150 °C under N_2 atmosphere to remove oxygen and water. Another solution (Sol B) was prepared by adding 12.5 mL of each oleic acid and 1-octadecene and stirred at elevated temperature under N_2 flow. After the Sol A became transparent, the mixture was slowly injected to Sol B at 330 °C. The solution was heated and stirred for 1 hour. Later, it was left to cool down at room temperature; nanoparticles were precipitated and washed three times with hexane/acetone (1:4) mixture by centrifugation (30 min, 7000 rpm) and dried at room temperature. A series of $Na_{1-x}Li_xGd_{0.78}Yb_{0.2}Er_{0.02}F_4$ was synthesized with different Li^+ concentration (x = 0, 0.1, 0.2, 0.3, 0.4, 0.5, 0.6, 0.7, 0.8, 0.9, 1.0) and another series of $Na_{1-x}K_xGd_{0.78}Yb_{0.2}Er_{0.02}F_4$ with different K^+ concentration (x = 0, 0.1, 0.2, 0.3, 0.4, 0.5, 0.6, 0.7, 0.8, 0.9, 1.0).

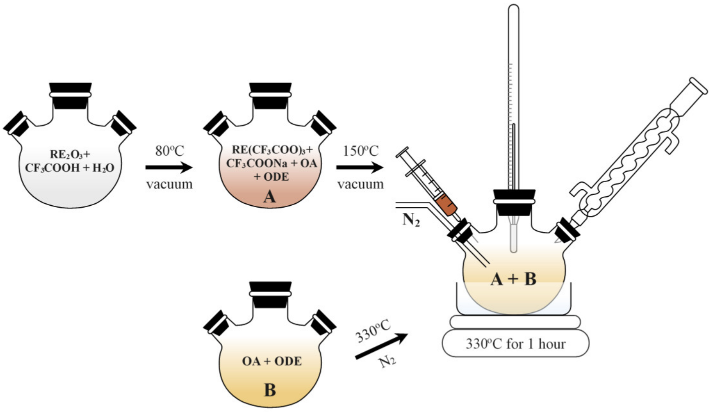

Figure 4.1. Scheme of thermal decomposition synthesis of UC materials.

4.2.2. Synthesis of $NaY_{0.78-x}Mn_xYb_{0.2}Er_{0.02}F_4$

$NaY_{0.78-x}Mn_xYb_{0.2}Er_{0.02}F_4$ particles were prepared via thermal decomposition of trifluoroacetates in mixture of organic solvents (Fig. 4.1) at elevated temperature. Rare earth trifluoroacetates were prepared by dissolving corresponding RE_2O_3 (1.25 mmol) and $MnCO_3$ in trifluoroacetic acid (TFA, 50%) at 80 °C separately. After both mixtures became clear, residual solution was evaporated under vacuum. 2.5 mmol of NaTFA were added together with 7.5 mL of each oleic acid and 1-octadecene. The procedure has already been described in *Section 4.2.1*. A series of $NaY_{0.78-x}Mn_xYb_{0.2}Er_{0.02}F_4$ were synthesized with different Mn^{2+} concentration (x = 0, 0.05, 0.1, 0.15, 0.2, 0.5, 0.78).

4.2.3. Synthesis of $NaGd_{0.78-x}Cr_xYb_{0.2}Er_{0.02}F_4$ and $NaGd_{0.78-x}Mn_xYb_{0.2}Er_{0.02}F_4$

$NaGd_{0.78-x}Cr_xYb_{0.2}Er_{0.02}F_4$ and $NaGd_{0.78-x}Mn_xYb_{0.2}Er_{0.02}F_4$ particles were prepared via thermal decomposition heat-up method [195] (Fig. 4.2). RE_2O_3 were dissolved in hydrochloric acid and water to obtain $RECl_3$. After the mixture became clear, residual solution was evaporated under vacuum. $RECl_3$ were washed three times with water and dried. $RECl_3$ and $CrCl_3 \cdot 6H_2O$ were dissolved in methanol and added to 12 mL oleic acid and 30 mL of 1-octadecene and stirred for 1 h. In case of $NaGd_{0.78-x}Mn_xYb_{0.2}Er_{0.02}F_4$, additional step of preparation of $MnCl_2$ was carried out using $MnCO_3$ as a starting material. The mixture was heated up to 120 °C under N_2 atmosphere and maintained until solution became clear. When the solution became clear, the heating was stopped. Another solution of 5 mmol sodium hydroxide together with 8 mmol ammonium fluoride in methanol was injected. The mixture was stirred for 0.5 h at room temperature, following an increase to 120 °C in order to evaporate methanol. Afterwards, the temperature was raised to 300 °C and the solution was stirred for 1 h. Nanoparticles were precipitated by adding hexane:acetone (1:4) mixture and centrifuged at 8000 rpm (30 min) repeating the procedure twice. In order to remove by-product (sodium chloride), additional washing step, involving mixture of ethanol:acetone (1:1) is necessary, followed by centrifugation and washing with hexane:acetone (1:4) and drying at room temperature. A series of $NaGd_{0.78-x}Cr_xYb_{0.2}Er_{0.02}F_4$ were synthesized with different Cr^{3+} concentration (x = 0, 0.05, 0.15, 0.2, 0.5) and another series of $NaGd_{0.78-x}Mn_xYb_{0.2}Er_{0.02}F_4$ with different Mn^{2+} concentration (x = 0, 0.05, 0.1, 0.15, 0.2, 0.25, 0.5).

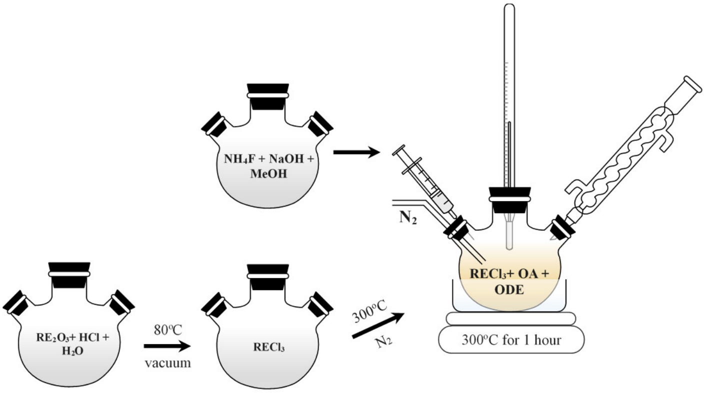

Figure 4.2. Scheme of thermal decomposition synthesis of UC materials

4.2.4. Synthesis of $NaGd_{0.995-x}Yb_xNd_{0.005}F_4$ and $NaGd_{0.975-x}Yb_xEr_{0.02}Nd_{0.005}F_4$

A series of $NaGd_{0.995-x}Yb_xNd_{0.005}F_4$ and $NaGd_{0.975-x}Yb_xEr_{0.02}Nd_{0.005}F_4$ particles were prepared by previously (*Section 4.2.1*) described method with different Yb^{3+} concentration: $x = 0, 0.005, 0.01, 0.05, 0.1, 0.15, 0.2, 0.3, 0.4, 0.5, 0.6, 0.8, 0.995$ and $x = 0, 0.03, 0.15, 0.2, 0.5$ (when additionally doping with Er^{3+}).

4.3. Characterisation

4.3.1. Powder X-ray Diffraction

X-ray diffraction (XRD) data of obtained compounds were collected with Rigaku MiniFlex diffractometer in the range $10° \leq 2\theta \leq 90°$, using Ni-filtered Cu K_α radiation. Step width and scanning speed were 0.02° and 5°/min, respectively.

XRD data of obtained compounds used for determination of lattice parameters were collected with Bruker D8 Advance using Cu K_α radiation in the range $10° \leq 2\theta \leq 90°$, with Bragg-Brentano focusing geometry and LynxEYE detector. Step width and integration time were 0.001° and 0.3 s, respectively. Lattice parameters were calculated with TOPAS program using Le Bail method (calculation error ±0.0002).

4.3.2. Elemental Composition Analysis

Samples were digested by using microwave reaction system Anton Paar Multiwave 3000 (XF100 rotor with PTFE liners) in nitric acid (HNO_3, Rotipuran® Supra 69%, Carl Roth). The obtained solutions were analysed by inductively coupled plasma optical emission spectrometry (ICP-OES) with Perkin Elmer Optima 7000 DV.

4.3.3. Scanning Electron Microscopy

Scanning electron microscopy (SEM) images of obtained compounds were taken by FE-SEM Hitachi SU-70 scanning electron microscope.

Samples for analysis were prepared by coating 0.5% dispersions of nanoparticles in toluene on silica plate.

4.3.4. Transmission Electron Microscopy

Transmission electron microscopy (TEM) images of obtained compounds were taken by Tecnai G2 F20 X-TWIN. Schottky type field emission electron source was used with high angle annular dark field (HAADF) detector and a 11 MPix ORIUS SC1000B (Gatan) CCD camera. Samples for analysis were prepared by coating 0.5% dispersions of nanoparticles in toluene on copper grid.

4.3.5. Fourier-transform Infrared Spectroscopy

Fourier-transform infrared (FTIR) spectroscopy data was collected with Bruker Alfa ATR spectrometer in the range from 4000 to 400 cm^{-1}, 24 scans with spectral resolution of 4 cm^{-1}.

4.3.6. Luminescence Properties

Upconversion (UC) and downconversion (DC) luminescence spectra in the VIS and NIR ranges were measured with Edinburgh Instruments FLS980 spectrometer equipped with double grating Czerny-Turner emission monochromator and Hamamatsu R928P photomultiplier. Powder samples were measured as dispersions in toluene (8.8 mg/2 mL) carrying out measurements under continuous stirring. For excitation at 980 nm and 808 nm (for UC and DC), CW lasers were used. Bandwidth and step size were set to 0.5 nm, integration time was 0.4 s.

4.3.7. Lifetime Measurements

UC luminescence decay measurements were performed with Edinburgh Instruments FLS980 spectrometer, using a pulsed laser for excitation at 980 nm. Frequency of laser was set to 100 Hz, while emission was monitored at 407, 539 and 653 nm wavelengths. For DC decay measurements, a pulsed 808 nm laser (frequency 50 Hz) was used for excitation, monitoring the emission at 864 nm. The collected data were fitted with decay equation:

$$I(t) = B + A_1 e^{(-t/\tau_1)} + A_2 e^{(-t/\tau_2)} \qquad \text{(Eq. 4)}$$

where $I(t)$ is intensity of luminescence at a certain time t; A_1, A_2, B correspond to pre-exponential constants and background, respectively; τ_1, τ_2 are emission lifetime values. Average decay values ($\bar{\tau}$) were calculated using the following equation:

$$\bar{\tau} = \frac{A_1 \times \tau_1^2 + A_2 \times \tau_2^2}{A_1 \times \tau_1 + A_2 \times \tau_2} \qquad \text{(Eq. 5)}$$

where A_1, A_2 are constants and τ_1, τ_2 are emission lifetime values.

4.3.8. Temperature Dependent Luminescence Properties

Temperature dependent luminescence measurements were performed with Edinburgh Instruments FLS980 spectrometer employed with a cryostat MicrostatN from Oxford Instruments. Sample holder was cooled with liquid nitrogen. Temperature stabilization interval was set to 90 s with temperature tolerance interval ±5 K. Measurements were performed at 77 K and in the 100 – 500 K range with a continuous increase step of 50 K.

Effective energy difference (ΔE) was calculated using the equation from *Section 3.6.2* (Eq. 2). Relative sensitivity (S_r) was calculated using the equation from *Section 3.6.2* (Eq. 3).

5. $NaGd_{0.78}Yb_{0.2}Er_{0.02}F_4$ doped with Li^+ and K^+ ions

As it has been discussed in *Section 3.4.1*, additional doping of different size alkali ions in $NaYF_4$ affects Yb–Er distance and will tune the optical properties. Thus, thermal decomposition synthesis of $NaGd_{0.78}Yb_{0.2}Er_{0.02}F_4$ was performed, doping Li^+ and K^+ ions instead of Na^+. Structural analysis, as well as investigation of optical properties will be discussed.

5.1. Structural Analysis

The XRD data of synthesized $Na_{1-x}Li_xGd_{0.78}Yb_{0.2}Er_{0.02}F_4$ with Li^+ concentration x = 0.1, 0.3, 0.5, 1.0 and $NaGd_{0.78}Yb_{0.2}Er_{0.02}F_4$ are presented in Figure 5.1. Pure hexagonal phase compounds are obtained and correspond well with PDF#(ICDD) 00-027-0699 when Li^+ concentration is small (up to x = 0.3).

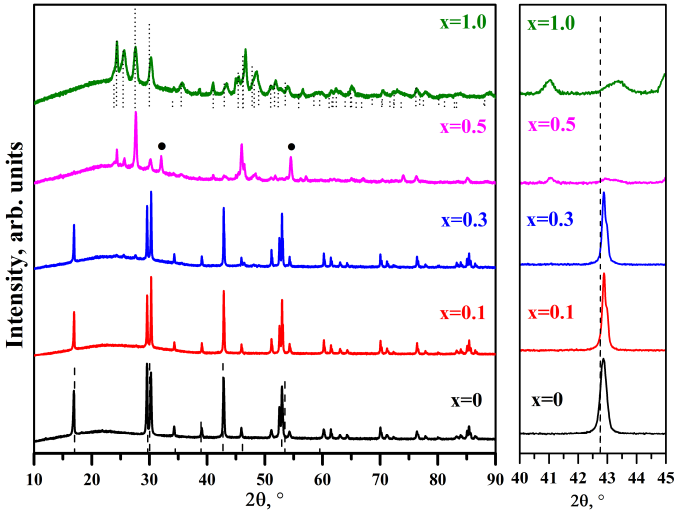

Figure 5.1. Powder XRD patterns of $Na_{1-x}Li_xGd_{0.78}Yb_{0.2}Er_{0.02}F_4$ samples (x = 0, 0.1, 0.3, 0.5, 1.0) and reference patterns of $NaGdF_4$ (PDF#(ICDD) 00-027-0699, dashed line) and GdF_3 (PDF#(ICDD) 00-049-1804). Cubic phase peaks are marked with ●.

As it can be seen from Fig. 5.1, an increase of Li^+ concentration to x = 0.5 leads to formation of mixture of both cubic phase $NaGdF_4$ (PDF#(ICDD) 00-27-0697) and GdF_3 (PDF#(ICDD) 00-049-1804) compounds. Cations in hexagonal phase can occupy two types of cationic sites with different coordination number (CN = 6 or 9), therefore an interval of ionic radius is presented. A successful incorporation of Li^+ ions (r = 0.90 – 1.06 Å) with smaller radius instead of larger Na^+ ions (r = 1.16 – 1.38 Å) was confirmed by a shift towards higher *2θ* angles (Fig. 5.1). When concentration of Li^+ ions reaches x = 0.8, GdF_3 compounds were formed.

The XRD data of synthesized $Na_{1-x}K_xGd_{0.78}Yb_{0.2}Er_{0.02}F_4$ with K^+ concentration (x = 0.1, 0.4, 0.5, 0.7, 1.0) and $NaGd_{0.78}Yb_{0.2}Er_{0.02}F_4$ are presented in Figure 5.2. Pure hexagonal phase compounds are obtained and correspond well with PDF#(ICDD) 00-027-0699 until K^+ concentration reaches 50%. Moreover, impurities in Fig. 5.2 marked as ● correspond well with cubic phase $NaGdF_4$ (PDF#(ICDD) 00-27-0697).

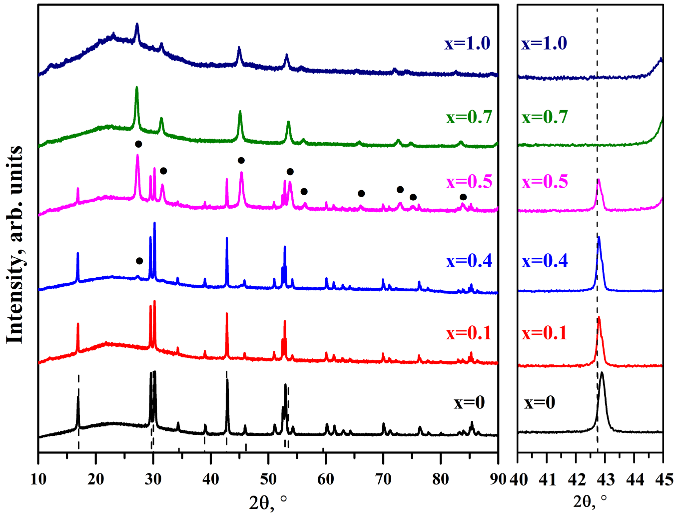

Figure 5.2. Powder XRD patterns of $Na_{1-x}K_xGd_{0.78}Yb_{0.2}Er_{0.02}F_4$ samples (x = 0, 0.1, 0.4, 0.5, 0.7, 1.0) and reference pattern of $NaGdF_4$ (PDF#(ICDD) 00-027-0699, dashed line). Cubic phase peaks are marked with ●.

A successful incorporation of larger K^+ ions (1.52 – 1.69 Å) into $NaGd_{0.78}Yb_{0.2}Er_{0.02}F_4$ was confirmed by an increase of unit cell parameters presented in Table 5.1. However, the results of a_h and c_h, when both hexagonal and cubic phases are present in a single compound, decreased. When concentration of K^+ ions reaches x = 0.7, cubic phase $NaGdF_4$ doped with K^+ was formed. As for the cubic phase (a_c) cell parameter, a constant increase was seen for K^+ ion concentrations of pure cubic phase compounds.

Table 5.1. Calculated unit cell parameters (a_h, c_h – hexagonal, a_c – cubic phase) of $Na_{1-x}K_xGd_{0.78}Yb_{0.2}Er_{0.02}F_4$ nanoparticles.

x (K^+)	a_h, Å	c_h, Å	a_c, Å
0	6.0288	3.5716	
0.1	6.0362	3.5771	
0.2	6.0355	3.5761	
0.3	6.0357	3.5762	
0.4	6.0345	3.5738	5.6405
0.5	6.0376	3.5781	5.652
0.6	6.0383	3.5798	5.6483
0.7			5.6703
0.8			5.6918
0.9			5.7125
1.0			5.7266

Thermal decomposition synthesis produces $NaGdF_4$ capped with hydrophobic oleic acid. It is reported [196] that oleic acid molecules are adsorbed on the surface through COO^- group. The adsorption was confirmed by FTIR spectroscopy (Fig. 5.3) from the decreased C=O vibration at 1707 cm^{-1}.

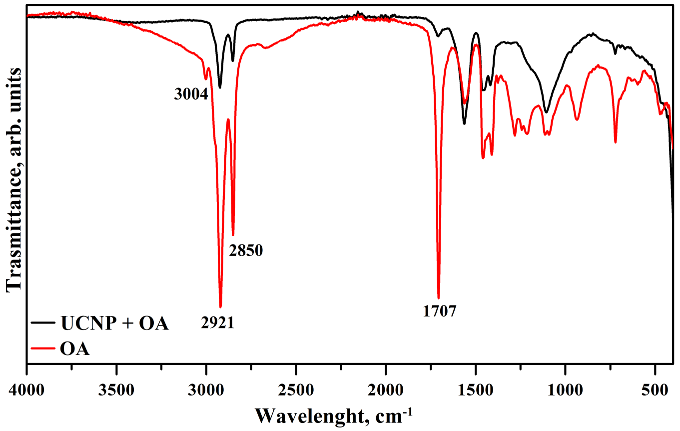

Figure 5.3. FTIR spectra of pure OA (red line) and oleic acid capped $NaGd_{0.78}Yb_{0.2}Er_{0.02}F_4$.

It is worth to mention, that all the samples were analyzed with FTIR spectroscopy and no distinctive difference was observed. Thus, the spectra will not be presented in further Sections.

5.2. Luminescent properties

Upconverting properties of $Na_{1-x}Li_xGd_{0.78}Yb_{0.2}Er_{0.02}F_4$ were investigated in 350 – 750 nm region under 980 nm excitation. All the observed emission lines were attributed to Er^{3+} ion transitions (Fig. 5.4): $^4G_{11/2}\rightarrow{}^4I_{15/2}$ (ca. 380 nm), $^2H_{9/2}\rightarrow{}^4I_{15/2}$ (ca. 407 nm), $^4F_{7/2}\rightarrow{}^4I_{15/2}$ (very weak, ca. 502 nm), $^2H_{11/2}\rightarrow{}^4I_{15/2}$ (515 – 535 nm), $^4S_{3/2}\rightarrow{}^4I_{15/2}$ (535 – 565 nm), $^4F_{9/2}\rightarrow{}^4I_{15/2}$ (635 – 680 nm), $^2H_{9/2}\rightarrow{}^4I_{11/2}$ (ca. 695 nm). Since Yb^{3+} ions are typically ascribed to take part as the sensitizer under current conditions [32], a mechanism of processes leading to luminescence could be adapted from *Chapter 3.2* Fig. 3.1. For better interpretation of the results, emission spectra were normalized to intensity at 539 nm.

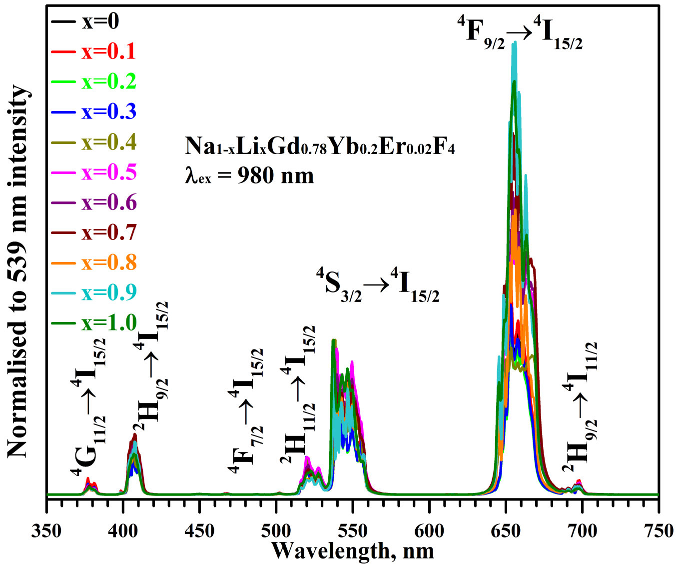

Figure 5.4. Upconversion emission spectra of $Na_{1-x}Li_xGd_{0.78}Yb_{0.2}Er_{0.02}F_4$ nanoparticles with different Li^+ concentration (λ_{ex} = 980 nm).

When Li^+ concentration is low, the intensity of both green ($^2H_{11/2}$, $^4S_{3/2}\rightarrow{}^4I_{15/2}$) and red ($^4F_{9/2}\rightarrow{}^4I_{15/2}$) emission lines is similar. With the increase of Li^+ amount in $Na_{1-x}Li_xGd_{0.78}Yb_{0.2}Er_{0.02}F_4$, a rise of $^4F_{9/2}\rightarrow{}^4I_{15/2}$ energy transfer is observed. This corresponds to subsequent red/green (R/G) ratio dependency graph in Figure 5.6.

Luminescence measurements of $Na_{1-x}K_xGd_{0.78}Yb_{0.2}Er_{0.02}F_4$ compounds are presented in Figure 5.5. Investigation of luminescent properties of larger ionic radii doped into $NaGdF_4$ led to similar tendency Er^{3+} emission lines as observed in the case of Li^+ doping (Fig. 5.4). For better interpretation of the results, emission spectra were normalized to intensity at 539 nm.

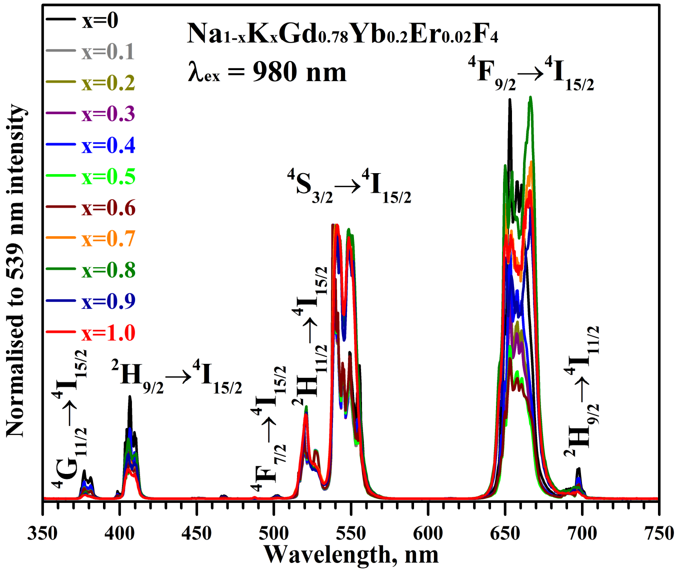

Figure 5.5. Upconversion emission spectra of $Na_{1-x}K_xGd_{0.78}Yb_{0.2}Er_{0.02}F_4$ nanoparticles with different K^+ concentration (λ_{ex} = 980 nm).

When K^+ concentration increases, the intensity of blue emission ($^4G_{11/2}\rightarrow{}^4I_{15/2}$, $^2H_{9/2}\rightarrow{}^4I_{15/2}$) decreased. The same tendency is seen for red emission originating from $^4F_{9/2}\rightarrow{}^4I_{15/2}$ and $^2H_{9/2}\rightarrow{}^4I_{11/2}$ transitions up to $x = 0.6$ K^+. The increase in red range emission could be related to cubic phase $Na_{1-x}K_xGd_{0.78}Yb_{0.2}Er_{0.02}F_4$ formation from $x = 0.7$ to $x = 1.0$ concentration. Thus, changes in unit cell parameters affect Yb Er distance.

As it can be seen from upconversion emission spectra (Fig. 5.4, 5.5), ratio between Er^{3+} red ($^4F_{9/2}\rightarrow{}^4I_{15/2}$ (635 − 680 nm)) and green ($^2H_{11/2}$, $^4S_{3/2}\rightarrow{}^4I_{15/2}$ (515 – 565 nm)) transitions varies with a change of doped Li^+ or K^+ concentration. A tendency of increased R/G ratio with regard to a phase of obtained compounds is represented in Figure 5.6.

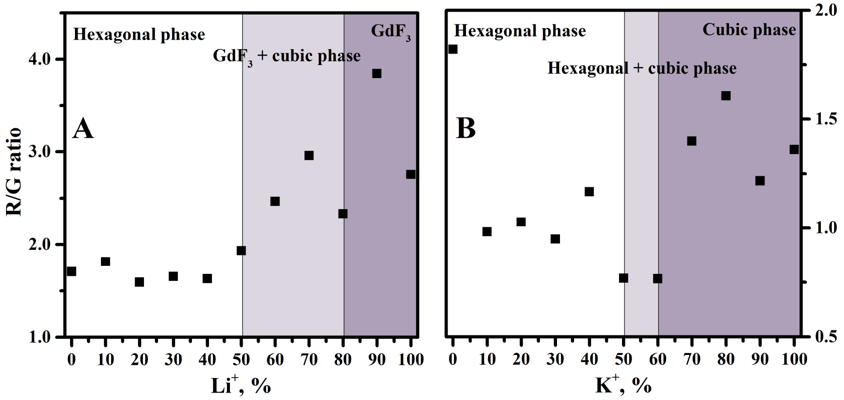

Figure 5.6. R/G ($^4F_{9/2}\rightarrow{}^4I_{15/2}$ (635 – 680 nm)), ($^2H_{11/2}$, $^4S_{3/2}\rightarrow{}^4I_{15/2}$ (515 – 565 nm)) ratio dependency on Li^+ (A) and K^+ (B) concentration.

It is evident that a double R/G ratio increase (Fig. 5.6 A) depends on the concentration of Li^+ ions when comparing to $x = 0$. However, there is a slight drop at $x = 0.8$, when single GdF_3 phase is obtained. Furthermore, when concentration of K^+ ions introduced to the $NaGd_{0.78}Yb_{0.2}Er_{0.02}F_4$ system is $x = 0.1$, a drop in R/G ratio from 1.7 to 1.0 is seen (Fig. 5.6 B). An increase in R/G ratio is observed when single cubic phase is obtained.

Decay measurements of $Na_{1-x}Li_xGd_{0.78}Yb_{0.2}Er_{0.02}F_4$ were performed under 980 nm laser excitation. Decay curves were monitored at $^2H_{9/2}\rightarrow{}^4I_{15/2}$, $^2H_{11/2}$,$^4S_{3/2}\rightarrow{}^4I_{15/2}$ and $^4F_{9/2}\rightarrow{}^4I_{15/2}$ energy transfers assigned to Er^{3+} ions. The average lifetime values were calculated (Eq. 5) by fitting the experimental results by an equation (Eq. 4) and are represented in Fig. 5.7. Due to the impurities from XRD data and formation of different crystal phase during synthesis, a tendency of lifetime values could not be introduced. Although results do not correlate between amount of doped Li^+ ions into $Na_{1-x}Li_xGd_{0.78}Yb_{0.2}Er_{0.02}F_4$, an increase of average lifetimes is seen when $x = 0.6$. Moreover, a tendency of faster decrease in lifetime values of $^2H_{9/2}\rightarrow{}^4I_{15/2}$ (407 nm), $^2H_{11/2}$,$^4S_{3/2}\rightarrow{}^4I_{15/2}$ (539 nm) energy transfers is observed comparing to $^4F_{9/2}\rightarrow{}^4I_{15/2}$ (653 nm) which corresponds well with results represented in Fig. 5.6 A.

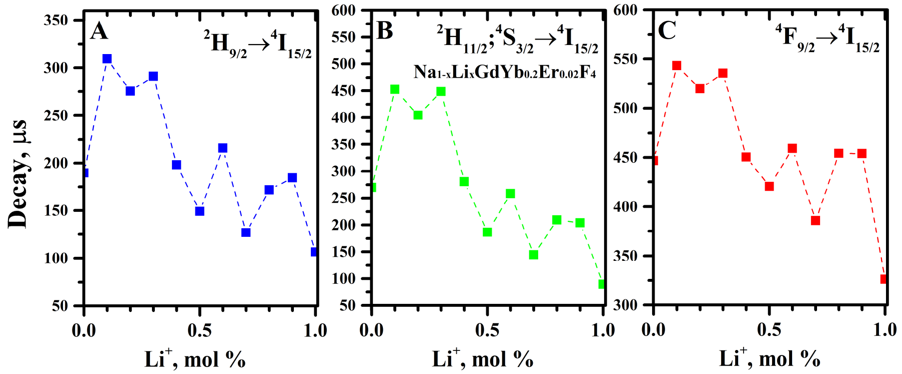

Figure 5.7. Average lifetime value dependency on Li$^+$ concentration in $Na_{1-x}Li_xGd_{0.78}Yb_{0.2}Er_{0.02}F_4$ samples (λ_{ex} = 980 nm). Emission monitored at $^2H_{9/2}\rightarrow{}^4I_{15/2}$ (A), $^2H_{11/2},{}^4S_{3/2}\rightarrow{}^4I_{15/2}$ (B) and $^4F_{9/2}\rightarrow{}^4I_{15/2}$ (C) energy transfers.

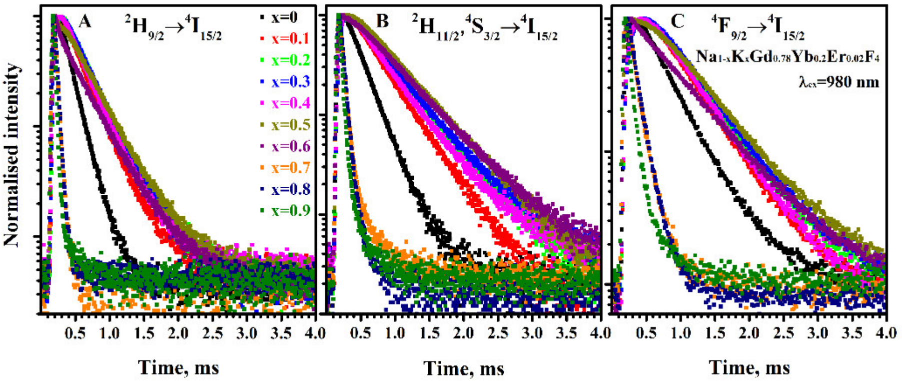

Figure 5.8. Decay curves of $Na_{1-x}K_xGd_{0.78}Yb_{0.2}Er_{0.02}F_4$ samples (λ_{ex} = 980 nm). Emission monitored at $^2H_{9/2}\rightarrow{}^4I_{15/2}$ (A), $^2H_{11/2},{}^4S_{3/2}\rightarrow{}^4I_{15/2}$ (B) and $^4F_{9/2}\rightarrow{}^4I_{15/2}$ (C) energy transfers.

Decay measurements of $Na_{1-x}K_xGd_{0.78}Yb_{0.2}Er_{0.02}F_4$ were performed under 980 nm laser excitation (Fig. 5.8). Decay curves were monitored $^2H_{9/2}\rightarrow{}^4I_{15/2}$, $^2H_{11/2},{}^4S_{3/2}\rightarrow{}^4I_{15/2}$ and $^4F_{9/2}\rightarrow{}^4I_{15/2}$ energy transfers assigned to Er^{3+} ions. As it can be seen from decay curves monitored at different Er^{3+} energy transfers, there is a decrease in steepness with K^+ concentration increase.

The average lifetime values were calculated (Eq. 5) by fitting the experimental results by an equation (Eq. 4). Furthermore, prolonged average lifetime values of Er^{3+} energy transfers were observed when K^+ concentration was increased to $x = 0.6$ (Fig. 5.9). Comparing these results with XRD measurements (Fig. 5.2), a tendency of shorter emission lifetime values is observed with the samples where hexagonal phase is not detected.

However, single hexagonal $NaGdF_4$ phase sample with highest amount of K^+ ions (x = 0.4) had a small drop (~10%) in average lifetime values, comparing to x = 0.3. A decrease in all average lifetime values was seen when single cubic $NaGdF_4$ phase was formed (x = 0.7, 0.8, 0.9).

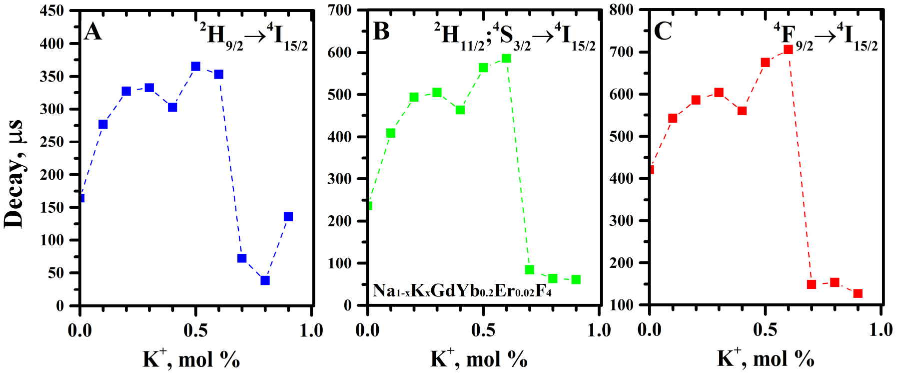

Figure 5.9. Average lifetime value dependency on K^+ concentration in $Na_{1-x}K_xGd_{0.78}Yb_{0.2}Er_{0.02}F_4$ samples (λ_{ex} = 980 nm). Emission monitored at $^2H_{9/2}\rightarrow{}^4I_{15/2}$ (A), $^2H_{11/2},{}^4S_{3/2}\rightarrow{}^4I_{15/2}$ (B) and $^4F_{9/2}\rightarrow{}^4I_{15/2}$ (C) energy transfers.

The mechanisms of upconversion processes are very complex, especially when several different phase compounds are formed during a synthesis process. However, a shift of R/G ratio of emission intensities is achieved when Li^+ or K^+ ions are doped into $NaGd_{0.78}Yb_{0.2}Er_{0.02}F_4$.

6. $NaY_{0.78}Yb_{0.2}Er_{0.02}F_4$ doped with Mn^{2+}

Additional doping of transition metal ions in $NaYF_4$ was discussed in *Section 3.4.1*. In order to affect energy transfer pathways and tune the optical properties, Mn^{2+} ions were inserted into $NaY_{0.78}Yb_{0.2}Er_{0.02}F_4$ matrix. Thus, thermal decomposition synthesis of $NaY_{0.78}Yb_{0.2}Er_{0.02}F_4$ was performed, doping Mn^{2+} instead of Y^{3+}. Structural analysis, as well as investigation of optical properties will be discussed.

6.1. Structural Analysis

The XRD data of synthesized $NaY_{0.78-x}Mn_xYb_{0.2}Er_{0.02}F_4$ with Mn^{2+} concentration x = 0, 0.05, 0.1, 0.2, 0.5, 0.78 are presented in Figure 6.1. Since a more distinctive red emission is observed in cubic phase, the latter was the object of investigation of manipulation in colour outcome. Cubic phase compounds are obtained in all doping concentrations and correspond well with PDF#(ICDD) 00-077-2042. However, as it can be seen from Fig. 6.1, an increase of Mn^{2+} concentration to x = 0.78 leads to a formation of $NaMnF_3$ phase (PDF#(ICDD) 00-018-1224) impurities at 21.04, 26.75, 30.97, 39.55, 50.75 *2θ* angles (Fig 6.1 marked with ♦). A successful incorporation of Mn^{2+} ions (CN = 6, 0.81 Å) with smaller radius instead of larger Y^{3+} ions (CN = 6, 0.89 Å) was confirmed by a shift towards higher *2θ* angles (Fig. 6.1 B).

The actual concentration of ions in synthesized $NaY_{0.78-x}Mn_xYb_{0.2}Er_{0.02}F_4$ compounds was determined carrying out ICP-OES analysis. The obtained results are represented in Table 6.1. Ratio of actual concentration of Y^{3+}, Mn^{2+}, Yb^{3+} and Er^{3+} ions correlate well with the initial amounts added during the synthesis, which confirms successful doping.

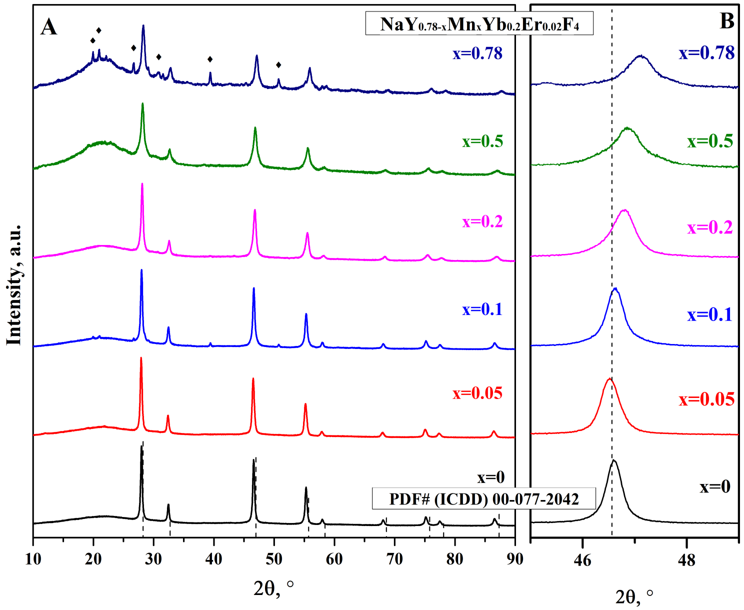

Figure 6.1. Powder XRD patterns of $NaY_{0.78-x}Mn_xYb_{0.2}Er_{0.02}F_4$ powders (x=0, 0.05, 0.1, 0.2, 0.5, 0.78) and reference pattern of $NaGdF_4$ (PDF#(ICDD) 00-077-2042, dashed line). $NaMnF_3$ phase peaks are marked with ◆ (PDF#(ICDD) 00-018-1224).

Table 6.1. Ratio of Y, Mn, Yb, Er elements, measured with ICP-OES.

Expected ratio Y:Mn:Yb:Er	Y, mol%	Mn, mol%	Yb, mol%	Er, mol%
0.78:0:0.2:0.02	0.78	-	0.2	0.02
0.73:0.05:0.2:0.02	0.75	0.04	0.2	0.02
0.68:0.1:0.2:0.02	0.69	0.08	0.2	0.02
0.63:0.15:0.2:0.02	0.67	0.10	0.2	0.02
0.58:0.2:0.2:0.02	0.59	0.19	0.2	0.02
0.28:0.5:0.2:0.02	0.28	0.51	0.19	0.02
0:0.78:0.2:0.02	-	0.77	0.2	0.01

The morphology of $NaY_{0.78-x}Mn_xYb_{0.2}Er_{0.02}F_4$ compounds was investigated by SEM analysis. From the images represented in Fig 6.2, a spherical shape ~50 nm nanoparticles are seen with increasing Mn^{2+} concentration (Fig 6.2 (a), (b)). Moreover, when Mn^{2+} concentration increases to x = 0.5 (Fig 6.2 (d)), the size of particles has visually decreased, which was also confirmed from the average particle size calculations (~27 nm) with ImageJ. Furthermore, two distinct size particles can be seen in Fig 6.2 (d) image.

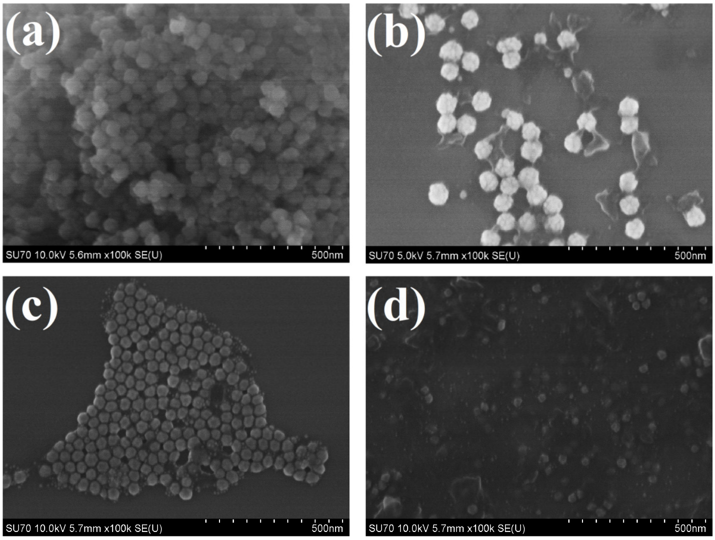

Figure 6.2. SEM images of $NaY_{0.78-x}Mn_xYb_{0.2}Er_{0.02}F_4$: (a) x = 0.0, (b) x = 0.05, (c) x = 0.1, (d) x = 0.5.

6.2. Luminescent properties

Upconverting properties of $NaY_{0.78-x}Mn_xYb_{0.2}Er_{0.02}F_4$ were investigated in 350 – 750 nm region under 980 nm excitation. All the observed emission lines were attributed to Er^{3+} ion transitions (Fig. 4.3): $^4G_{11/2}\rightarrow^4I_{15/2}$ (ca. 380 nm), $^2H_{9/2}\rightarrow^4I_{15/2}$ (ca. 407 nm), $^2H_{11/2}\rightarrow^4I_{15/2}$ (515 – 535 nm), $^4S_{3/2}\rightarrow^4I_{15/2}$ (535 – 565 nm), $^4F_{9/2}\rightarrow^4I_{15/2}$ (635 – 680 nm), $^2H_{9/2}\rightarrow^4I_{11/2}$ (ca. 695 nm). Since Yb^{3+} ions are typically ascribed to take part as the sensitizer under current conditions [32], a mechanism of processes leading to luminescence could be adapted from *Chapter 3.2* Fig. 3.1. For better interpretation of the results, emission spectra were normalized to intensity at 669 nm.

Approach of embedding transition metal ions in order to shift emission colour output has already been discussed in *Section 3.4.1*. Mn^{2+} ions doped in $NaYF_4$ matrix provide additional intermediate energy levels that take part in processes resulting in upconversion luminescence [78]. As it can be seen from luminescence spectra (Fig. 6.3) a decrease in green emission region

($^2H_{11/2}$,$^4S_{3/2}$→$^4I_{15/2}$) is evident comparing to fixed red region ($^4F_{9/2}$→$^4I_{15/2}$) when Mn^{2+} concentration increases.

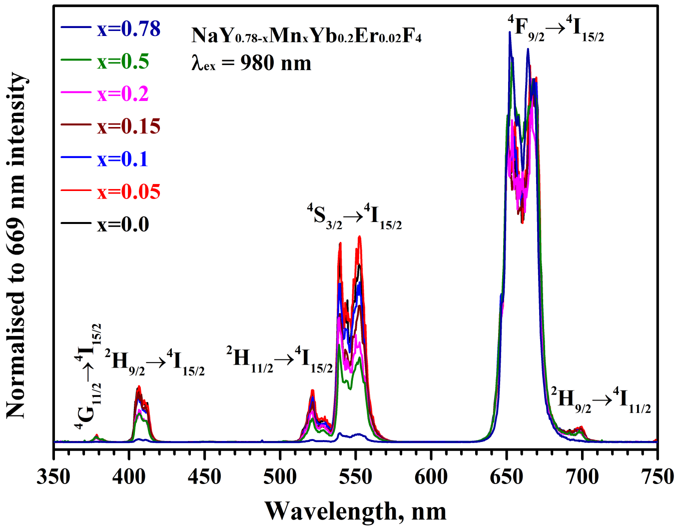

Figure 6.3. Upconversion emission spectra of $NaY_{0.78-x}Mn_xYb_{0.2}Er_{0.02}F_4$ nanoparticles with different Mn^{2+} concentration (λ_{ex} = 980 nm).

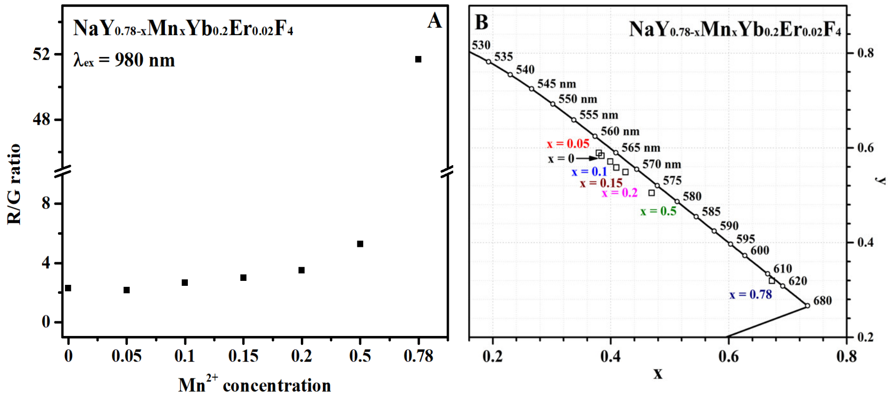

Figure 6.4. Ratio between red ($^4F_{9/2}$→$^4I_{15/2}$) and green ($^2H_{11/2}$, $^4S_{3/2}$→$^4I_{15/2}$) transitions (A); CIE 1931 chromaticity diagram of $NaY_{0.78-x}Mn_xYb_{0.2}Er_{0.02}F_4$ (B).

Moreover, the change of ratio (Fig. 6.4 A) between red ($^4F_{9/2}$→$^4I_{15/2}$ (625 – 708 nm)) and green ($^2H_{11/2}$, $^4S_{3/2}$→$^4I_{15/2}$ (509 – 574 nm)) transitions becomes more obvious when concentration reaches x = 0.5 and x = 0.78 when Y^{3+} are completely replaced. A non-radiative energy transfer pathway from $^2H_{11/2}$ and $^4S_{3/2}$ (Er^{3+}) to $^4T_1$ level of Mn^{2+} provides with further back-energy transfer to $^4F_{9/2}$ (Er^{3+}) which results in an enhancement of the red emission. Therefore, the upconversion luminescence outcome of $NaY_{0.78-x}Mn_xYb_{0.2}Er_{0.02}F_4$ is affected by Mn^{2+} doping (Fig. 6.4 B) and shifts to red region yielding almost pure red colour emission.

Decay measurements of $NaY_{0.78-x}Mn_xYb_{0.2}Er_{0.02}F_4$ samples were recorded under 980 nm laser excitation. Decay curves (Fig. 6.5) were monitored at $^2H_{9/2}\rightarrow{}^4I_{15/2}$, $^2H_{11/2}$,$^4S_{3/2}\rightarrow{}^4I_{15/2}$ and $^4F_{9/2}\rightarrow{}^4I_{15/2}$ energy transfers assigned to Er^{3+} ions. Obtained UC decay curves were fitted with a bi-exponential decay function (Eq. 4). Average lifetime values were calculated (Eq. 5) and represented in Fig. 6.6.

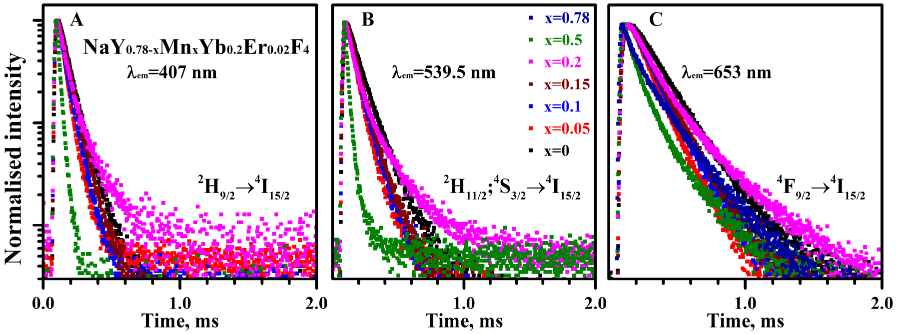

Figure 6.5. Decay curves of $NaY_{0.78-x}Mn_xYb_{0.2}Er_{0.02}F_4$ samples (λ_{ex} = 980 nm). Emission monitored at $^2H_{9/2}\rightarrow{}^4I_{15/2}$ (A), $^2H_{11/2}$,$^4S_{3/2}\rightarrow{}^4I_{15/2}$ (B) and $^4F_{9/2}\rightarrow{}^4I_{15/2}$ (C) energy transfers.

As it can be seen from (Fig. 6.5), the decay curves monitored at different Er^{3+} energy transfers become steeper when Mn^{2+} concentration is increased to x = 0.05. Furthermore, a drop of average lifetime values for $NaY_{0.73}Mn_{0.05}Yb_{0.2}Er_{0.02}F_4$ sample is seen from Fig. 6.6. However, a gradual increase in average lifetime values was observed for all the samples and reached highest value when Mn^{2+} concentration was increased up to x = 0.2. Further addition of higher concentration Mn^{2+} ions (x = 0.5) have reduced the average lifetime values for all the investigated emission lines. Following these observations, an optimal Mn^{2+} concentration for relatively longer emission of blue, green and red energy transfers in $NaY_{0.78-x}Mn_xYb_{0.2}Er_{0.02}F_4$ system is x = 0.2.

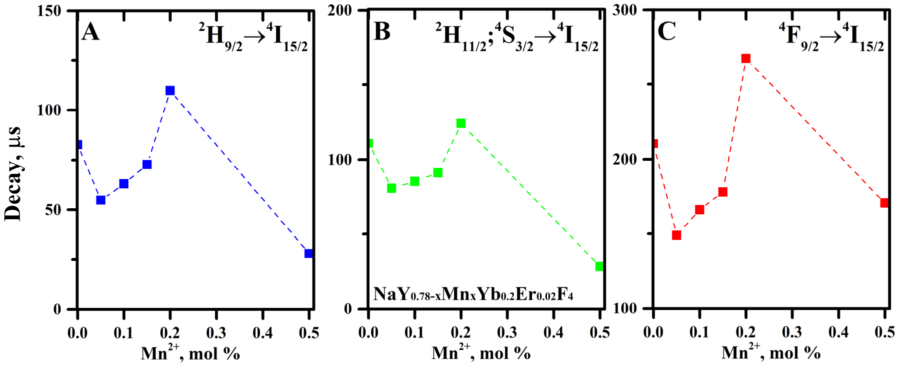

Figure 6.6. Average lifetime value dependency on Mn^{2+} concentration in $NaY_{0.78-x}Mn_xYb_{0.2}Er_{0.02}F_4$ samples (λ_{ex} = 980 nm). Emission monitored at $^2H_{9/2}\rightarrow{}^4I_{15/2}$ (A), $^2H_{11/2},{}^4S_{3/2}\rightarrow{}^4I_{15/2}$ (B) and $^4F_{9/2}\rightarrow{}^4I_{15/2}$ (C) energy transfers.

A simple approach of incorporating transition metal ions (Mn^{2+}) affects luminescent properties of $NaY_{0.78}Yb_{0.2}Er_{0.02}F_4$ by suppressing green emission with additional depletion pathways. Thus, doping $NaY_{0.78-x}Mn_xYb_{0.2}Er_{0.02}F_4$ with certain amount of Mn^{2+} ions, provide with a possibility to tune emission colour outcome towards red spectral range.

7. $NaGd_{0.78}Yb_{0.2}Er_{0.02}F_4$ doped with Mn^{2+}

Additional doping of transition metal ions in $NaYF_4$ was discussed in *Section 3.4.1*. In order to affect energy transfer pathways and tune the optical properties, Mn^{2+} ions were inserted into $NaGd_{0.78}Yb_{0.2}Er_{0.02}F_4$ matrix. Thus, thermal decomposition synthesis of $NaGd_{0.78}Yb_{0.2}Er_{0.02}F_4$ was performed, doping Mn^{2+} instead of Gd^{3+}. Structural analysis, as well as investigation of optical properties will be discussed.

7.1. Structural Analysis

The XRD data of synthesized $NaGd_{0.78-x}Mn_xYb_{0.2}Er_{0.02}F_4$ with Mn^{2+} concentration x = 0.05, 0.1, 0.15, 0.2, 0.25, 0.5 and $NaGd_{0.78}Yb_{0.2}Er_{0.02}F_4$ are presented in Figure 7.1. Pure hexagonal phase compounds are obtained and correspond well with PDF#(ICDD) 00-027-0699 (space group $P6_3/m$). A successful incorporation of Mn^{2+} ions with smaller radius (CN = 6, 0.81 Å) instead of larger Gd^{3+} ions (CN = 9, r = 1.107 Å) was confirmed by a shift of (201) peak towards higher *2θ* angles (Fig. 7.1 B).

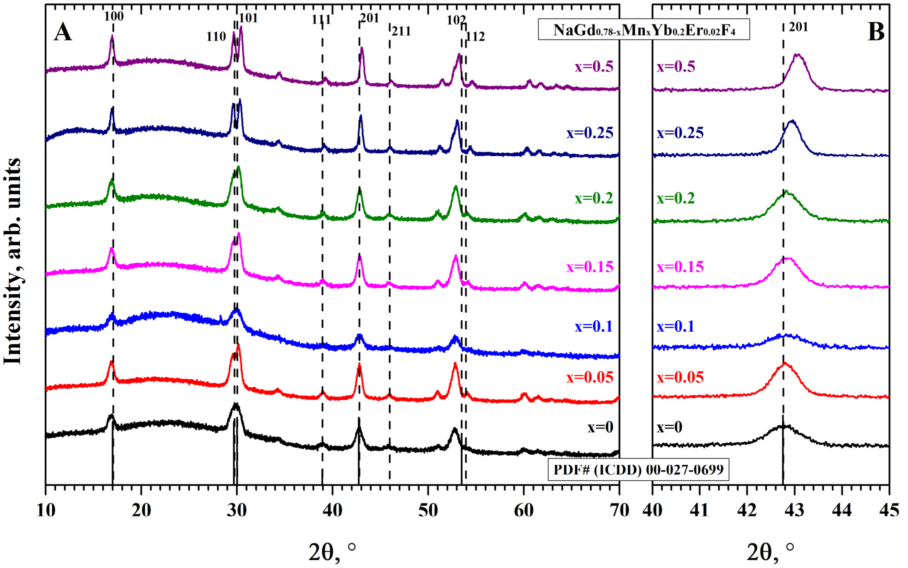

Figure 7.1. Powder XRD patterns of $NaGd_{0.78-x}Mn_xYb_{0.2}Er_{0.02}F_4$ powders (x=0, 0.05, 0.1, 0.15, 0.2, 0.25, 0.5) and reference pattern of $NaGdF_4$ (PDF#(ICDD) 00-027-0699, dashed line).

7.2. Luminescent properties

Upconverting properties of $NaGd_{0.78-x}Mn_xYb_{0.2}Er_{0.02}F_4$ were investigated in 350 – 750 nm region under 980 nm excitation. All the observed emission lines were attributed to Er^{3+} ion transitions (Fig. 7.2): $^4G_{11/2}\rightarrow{}^4I_{15/2}$ (ca. 380 nm), $^2H_{9/2}\rightarrow{}^4I_{15/2}$ (ca. 407 nm), $^2H_{11/2}\rightarrow{}^4I_{15/2}$ (515 – 535 nm), $^4S_{3/2}\rightarrow{}^4I_{15/2}$ (535 – 565 nm), $^4F_{9/2}\rightarrow{}^4I_{15/2}$ (635 – 680 nm), $^2H_{9/2}\rightarrow{}^4I_{11/2}$ (ca. 695 nm). Since Yb^{3+} ions are typically ascribed to take part as the sensitizer under current conditions [32], a mechanism of processes leading to luminescence could be adapted from *Chapter 3.2*. For better interpretation of the results, emission spectra were normalized to intensity at 539 nm. $^4F_{9/2}\rightarrow{}^4I_{15/2}$ (630 – 685 nm) and $^2H_{11/2}$, $^4S_{3/2}\rightarrow{}^4I_{15/2}$ (515 – 570 nm) emission lines were integrated and red to green ratio (R/G) was calculated (inset of Fig. 7.2).

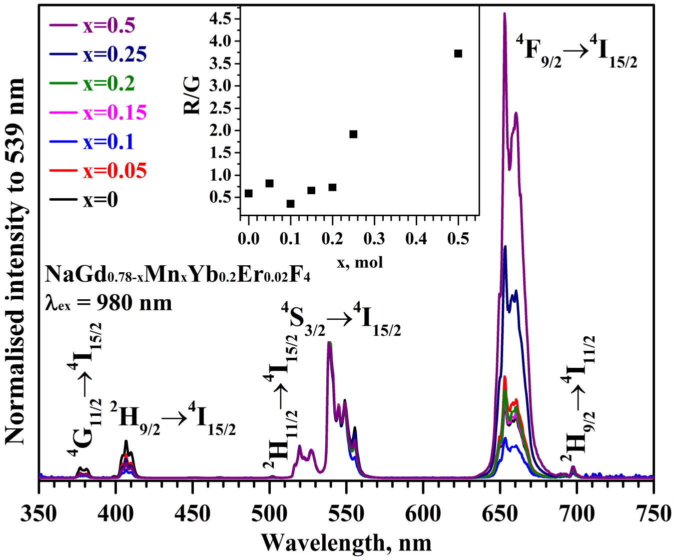

Figure 7.2. Upconversion emission spectra of $NaGd_{0.78-x}Mn_xYb_{0.2}Er_{0.02}F_4$ nanoparticles with different Mn^{2+} concentration (λ_{ex} = 980 nm). Inset: ratio of red (R) (630 – 685 nm) and green (G) (515 – 570 nm) integrated emission intensity.

Approach of embedding transition metal ions in order to shift emission colour output has already been discussed in *Section 3.4.1*. Mn^{2+} ions doped in $NaYF_4$ matrix provide additional intermediate energy levels that take part in processes resulting in upconversion luminescence [78]. An impact of

Mn^{2+} doping on luminescence properties of $NaGdF_4$ host material is investigated.

As it can be seen from luminescence spectra (Fig. 7.2) a decrease in green emission region ($^2H_{11/2},^4S_{3/2}\rightarrow^4I_{15/2}$) is evident comparing to red region ($^4F_{9/2}\rightarrow^4I_{15/2}$) when Mn^{2+} concentration increases. Moreover, the change of ratio (Fig. 7.2 inset) between red ($^4F_{9/2}\rightarrow^4I_{15/2}$ (625 – 708 nm)) and green ($^2H_{11/2}$, $^4S_{3/2}\rightarrow^4I_{15/2}$ (509 – 574 nm)) transitions reaches values of 1.9 and 3.7 when Mn^{2+} concentration is $x = 0.25$ and $x = 0.5$, respectively. The modification of standard energy migration pathways by interacting with additional energy states of Mn^{2+} were discussed in literature [197]. A non-radiative energy transfer pathway from $^2H_{11/2}$ and $^4S_{3/2}$ (Er^{3+}) to $^4T_1$ level of Mn^{2+} provides with further back-energy transfer to $^4F_{9/2}$ (Er^{3+}). An enhancement of the red emission increased by 6.4 times (Fig. 7.2 inset) when $x = 0.5$. Therefore, the upconversion luminescence outcome of $NaY_{0.78-x}Mn_xYb_{0.2}Er_{0.02}F_4$ is affected by Mn^{2+} doping (Fig. 7.2) and shifts to red region.

Decay measurements of $NaGd_{0.78-x}Mn_xYb_{0.2}Er_{0.02}F_4$ samples were recorded under 980 nm laser excitation. Decay curves (Fig. 7.3) were monitored at $^2H_{9/2}\rightarrow^4I_{15/2}$, $^2H_{11/2},^4S_{3/2}\rightarrow^4I_{15/2}$ and $^4F_{9/2}\rightarrow^4I_{15/2}$ energy transfers assigned to Er^{3+} ions. Obtained UC decay curves were fitted with a bi-exponential decay function (Eq. 4). Average lifetime values were calculated (Eq. 5) and represented in Fig. 7.4.

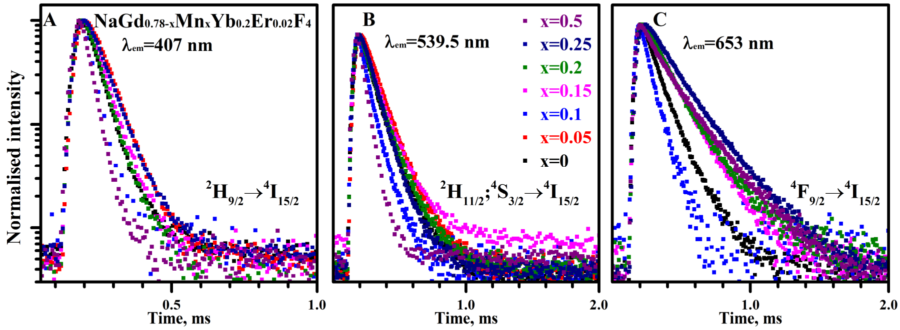

Figure 7.3. Decay curves of $NaGd_{0.78-x}Mn_xYb_{0.2}Er_{0.02}F_4$ samples (λ_{ex} = 980 nm). Emission monitored at $^2H_{9/2}\rightarrow^4I_{15/2}$ (A), $^2H_{11/2},^4S_{3/2}\rightarrow^4I_{15/2}$ (B) and $^4F_{9/2}\rightarrow^4I_{15/2}$ (C) energy transfers.

As it can be seen from (Fig. 7.3), the decay curves monitored at different Er^{3+} energy transfers become steeper for the Mn^{2+} concentration $x = 0.1$. Furthermore, a drop of average lifetime values for $NaY_{0.68}Mn_{0.1}Yb_{0.2}Er_{0.02}F_4$ sample is seen from Fig. 7.4. However, further increase in average lifetime values was observed for samples with increased Mn^{2+} concentration up to x = 0.25. Addition higher concentration Mn^{2+} ions (x = 0.5) has reduced the average lifetime values for blue and green emission lines, while red transition ($^4F_{9/2}\rightarrow{}^4I_{15/2}$) has not been greatly affected comparing to x = 0.25.

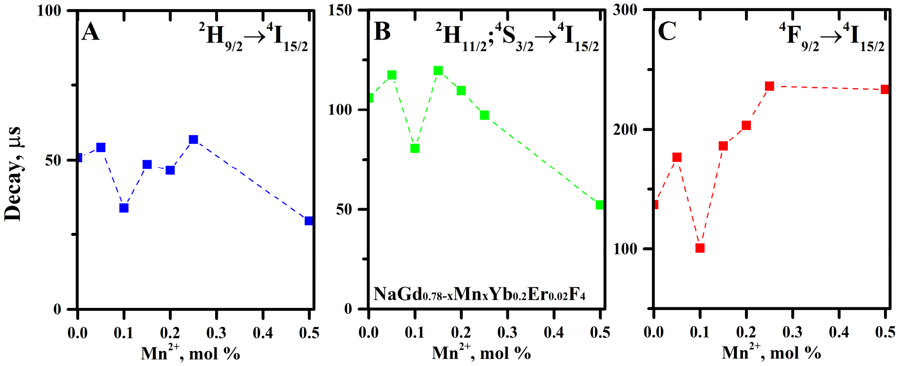

Figure 7.4. Average lifetime value dependency on Mn^{2+} concentration in $NaGd_{0.78-x}Mn_xYb_{0.2}Er_{0.02}F_4$ samples (λ_{ex} = 980 nm). Emission monitored at $^2H_{9/2}\rightarrow{}^4I_{15/2}$ (A), $^2H_{11/2},{}^4S_{3/2}\rightarrow{}^4I_{15/2}$ (B) and $^4F_{9/2}\rightarrow{}^4I_{15/2}$ (C) energy transfers.

Following these observations, an optimal Mn^{2+} concentration for relatively longer emission of blue, green and red energy transfers in $NaGd_{0.78-x}Mn_xYb_{0.2}Er_{0.02}F_4$ system is x = 0.25. A simple approach of incorporating transition metal ions (Mn^{2+}) affects luminescent properties of $NaGd_{0.78}Yb_{0.2}Er_{0.02}F_4$ by suppressing green emission with additional depletion pathways. Thus, doping $NaGd_{0.78-x}Mn_xYb_{0.2}Er_{0.02}F_4$ with certain amount of Mn^{2+} ions, provide with a possibility to tune emission colour outcome towards red spectral range.

8. $NaGd_{0.78}Yb_{0.2}Er_{0.02}F_4$ doped with Cr^{3+}

Additional doping of transition metal ions was discussed in *Section 3.4.1*. In order to affect energy transfer pathways and tune the optical properties, Cr^{3+} ions were inserted into $NaGd_{0.78}Yb_{0.2}Er_{0.02}F_4$ matrix. Thus, thermal decomposition synthesis of $NaGd_{0.78}Yb_{0.2}Er_{0.02}F_4$ was performed, doping Cr^{3+} instead of Gd^{3+}. Structural analysis, as well as investigation of optical properties and temperature dependent luminescence will be discussed.

8.1. Structural Analysis

The XRD data of synthesized $NaGd_{0.78-x}Cr_xYb_{0.2}Er_{0.02}F_4$ with Cr^{3+} concentration x = 0.05, 0.15, 0.2, 0.5 and $NaGd_{0.78}Yb_{0.2}Er_{0.02}F_4$ are presented in Figure 8.1. Pure hexagonal phase compounds are obtained and correspond well with PDF#(ICDD) 00-027-0699 (space group $P6_3/m$) regardless broad Cr^{3+} concentration range. A successful incorporation of Cr^{3+} ions (CN = 6, r = 0.62 Å) with smaller radius instead of larger Gd^{3+} ions (CN = 9, r = 1.107 Å) [131, 198] was confirmed by a shift of (201) peak towards higher *2θ* angles (Fig. 8.1 B).

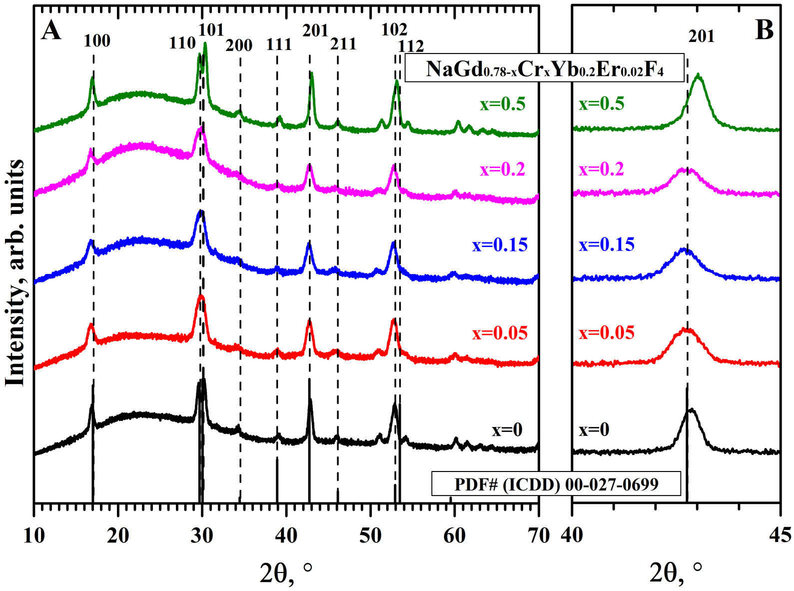

Figure 8.1. Powder XRD patterns of $NaGd_{0.78-x}Cr_xYb_{0.2}Er_{0.02}F_4$ powders (x= 0.05, 0.15, 0.2, 0.5) and reference pattern of $NaGdF_4$ (PDF#(ICDD) 00-027-0699, dashed line).

The actual concentration of ions in the synthesized $NaGd_{0.78-x}Cr_xYb_{0.2}Er_{0.02}F_4$ compounds was determined by carrying out ICP-OES analysis. The obtained results are represented in Table 8.1. Ratio of actual concentration of Gd^{3+}, Cr^{3+}, Yb^{3+} and Er^{3+} ions differs from the initial amounts added during synthesis. The measured amount of Gd^{3+} in all the investigated compounds was estimated to be higher than the initial experimental amount, whereas in case of Cr^{3+} ions – the estimated amount is lower than the expected. Similar results were mentioned in literature [199], however in both cases, the discrepancies of estimated concentration need a thorough investigation.

Table 8.1. Ratio of Gd, Cr, Yb, Er elements, measured with ICP-OES.

Expected ratio Gd:Cr:Yb:Er	Gd, mol%	Cr, mol%	Yb, mol%	Er, mol%
0.78:0:0.2:0.02	0.81	-	0.17	0.02
0.73:0.05:0.2:0.02	0.84	0.03	0.11	0.02
0.63:0.15:0.2:0.02	0.79	0.07	0.12	0.02
0.58:0.2:0.2:0.02	0.72	0.13	0.13	0.02
0.28:0.5:0.2:0.02	0.39	0.31	0.27	0.03

The morphology of $NaGd_{0.78-x}Cr_xYb_{0.2}Er_{0.02}F_4$ compounds was investigated by TEM analysis. A spherical shape of nanoparticles can be seen from the images of $x = 0$, 0.05, 0.15, 0.2 and 0.5 Cr^{3+} represented in Fig 8.2. The shape of nanoparticles was not impacted by Cr^{3+} concentration increase. Atomic planes in Fig. 8.2 B image suggest high crystallinity of $NaGd_{0.78}Yb_{0.2}Er_{0.02}F_4$. From average particle size calculation (Table 8.2), it is evident, that the size of particles is relatively similar and ranges from 11.4 ±2.4 nm ($x = 0$) to 10.6 ±1.2 nm ($x = 0.2$). Further Cr^{3+} concentration increase to $x = 0.5$ led to both small and large nanoparticle formation (Fig. 8.2 f) with calculated two average size of 10.0 and 16.9 nm (Table 8.2). Since average particle size was about 10 nm for the samples with up to $x = 0.2$ concentration of Cr^{3+}, the appearance of two distinct particle size values is concentration related. Moreover, no additional phase was indicated from XRD measurements (Fig. 8.1), thus different size nanoparticles have the same hexagonal crystal structure.

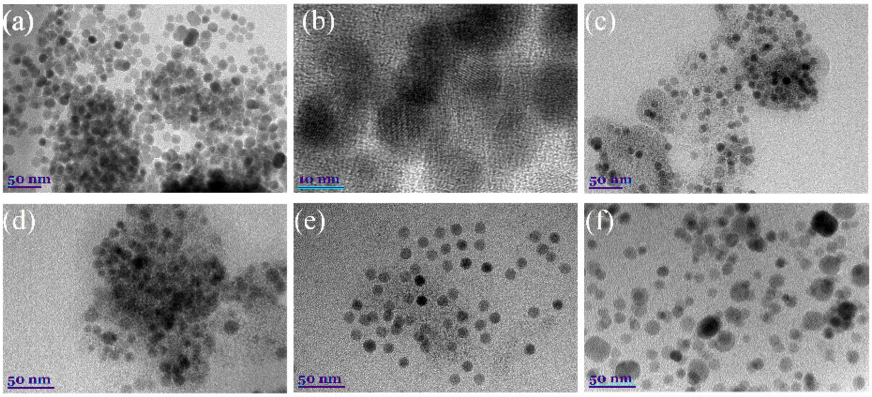

Figure 8.2. Bright-field TEM images of $NaGd_{0.78-x}Cr_xYb_{0.2}Er_{0.02}F_4$ nanoparticles: (a) and (b) $x = 0.0$, (c) $x = 0.05$, (d) $x = 0.15$, (e) $x = 0.2$, (f) $x = 0.5$.

Table 8.2. Average diameter of $NaGd_{0.78-x}Cr_xYb_{0.2}Er_{0.02}F_4$ as a function of Cr^{3+} concentration.

x	d, nm
0	11.4±2.4
0.05	10.4±1.6
0.15	9.0±2.5
0.2	10.6±1.2
0.5	10.0±2.3 and 16.9±6.0

8.2. Luminescence properties

Upconverting properties of $NaGd_{0.78-x}Cr_xYb_{0.2}Er_{0.02}F_4$ were investigated in 350 – 750 nm region under 980 nm excitation. All the observed emission lines were attributed to Er^{3+} ion transitions (Fig. 8.3): $^4G_{11/2}\rightarrow{}^4I_{15/2}$ (ca. 380 nm), $^2H_{9/2}\rightarrow{}^4I_{15/2}$ (ca. 407 nm), $^4F_{7/2}\rightarrow{}^4I_{15/2}$ (very weak, ca. 502 nm), $^2H_{11/2}\rightarrow{}^4I_{15/2}$ (515 – 535 nm), $^4S_{3/2}\rightarrow{}^4I_{15/2}$ (535 – 565 nm), $^4F_{9/2}\rightarrow{}^4I_{15/2}$ (635 – 680 nm), $^2H_{9/2}\rightarrow{}^4I_{11/2}$ (ca. 695 nm). For better interpretation of the results, emission spectra were normalized to intensity at 539 nm. $^4F_{9/2}\rightarrow{}^4I_{15/2}$ (635 – 680 nm) and $^2H_{11/2}$, $^4S_{3/2}\rightarrow{}^4I_{15/2}$ (515 – 565 nm) emission lines were integrated and red to green ratio (R/G) was calculated (Fig. 8.3 inset).

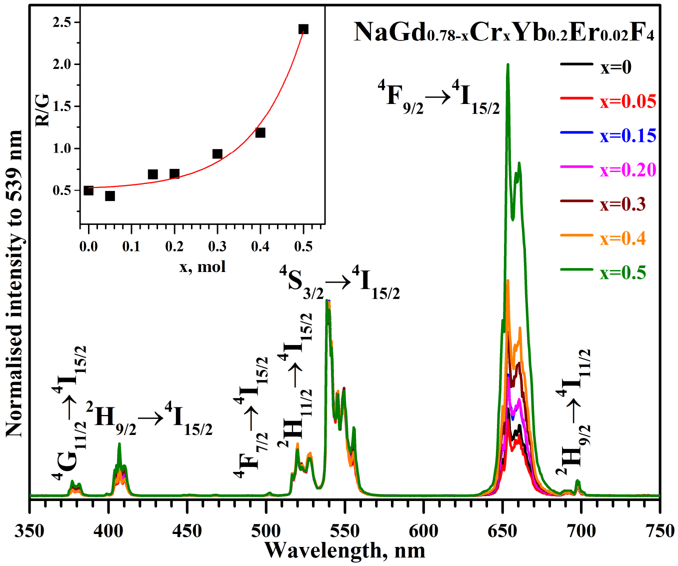

Figure 8.3. Upconversion emission spectra of $NaGd_{0.78-x}Cr_xYb_{0.2}Er_{0.02}F_4$ nanoparticles with different Cr^{3+} concentration (λ_{ex} = 980 nm). Inset: ratio of red (R) (635 – 680 nm) and green (G) (515 – 565 nm) integrated emission intensity. A red line was drawn to guide an eye.

A five time increase in R/G ratio was observed in both Fig. 8.3 and Fig. 8.3 inset when Cr^{3+} concentration was increased. The UC luminescence investigation data suggests that emission colour output can be manipulated by varying Cr^{3+} amount. The modification of standard energy migration pathways by interacting with additional energy states of Cr^{3+} were discussed in literature [197]. A successful interaction in Yb–Er–Cr system was expressed by the relatively increased red emission comparing to green in addition to no distinctive occurrence of Cr^{3+} emission in Fig. 8.3. A mechanism (Fig. 8.4) of Cr^{3+} induced emission shift has been proposed [200] suggesting that $^2T_2$ is populated transferring energy from Yb^{3+} ($^2F_{7/2}$). Enhanced red emission is a result of relaxation from $^4T_2$ to $^4A_2$ by subsequently transferring the relaxation energy to $^4F_{9/2}$ level of Er^{3+} ions.

Decay measurements of $NaGd_{0.78-x}Cr_xYb_{0.2}Er_{0.02}F_4$ samples were recorded under 980 nm laser excitation. Decay curves (Fig. 8.5) were monitored at $^2H_{9/2}\rightarrow{}^4I_{15/2}$, $^2H_{11/2}$,$^4S_{3/2}\rightarrow{}^4I_{15/2}$ and $^4F_{9/2}\rightarrow{}^4I_{15/2}$ energy transfers assigned to Er^{3+} ions. Obtained UC decay curves were fitted with a bi-exponential decay function (Eq. 4). Average lifetime values were calculated (Eq. 5) and represented in Table 8.3.

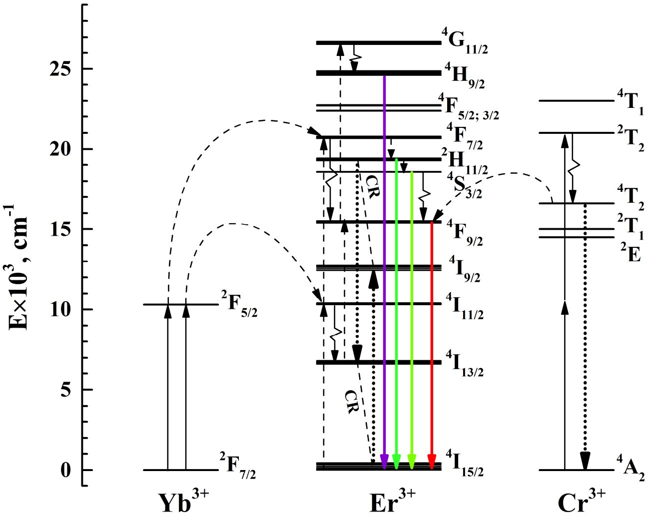

Figure 8.4. Energy level diagram with a possible transfer processes in Yb–Er–Cr system under 980 nm laser excitation. Solid coloured lines occur from energy transfer upconversion (ETU) processes.

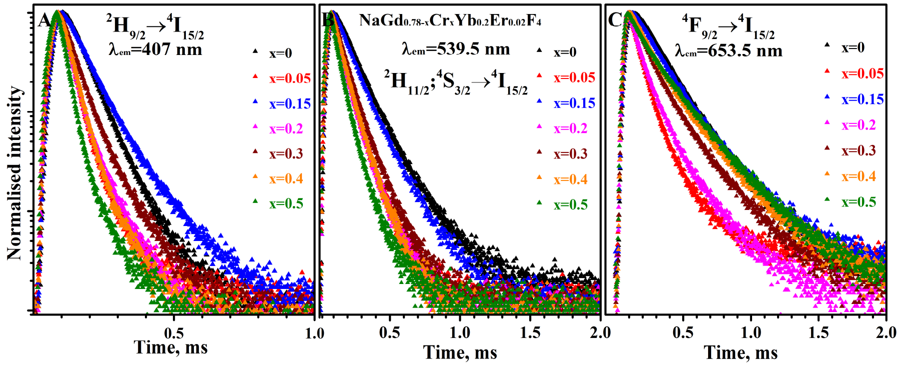

Figure 8.5. Decay curves of $NaGd_{0.78-x}Cr_xYb_{0.2}Er_{0.02}F_4$ samples (λ_{ex} = 980 nm). Emission monitored at $^2H_{9/2}\rightarrow{}^4I_{15/2}$ (A), $^2H_{11/2},{}^4S_{3/2}\rightarrow{}^4I_{15/2}$ (B) and $^4F_{9/2}\rightarrow{}^4I_{15/2}$ (C) energy transfers.

Two distinctive decay components τ_1 and τ_2 can be attributed to the faster decay values of Er^{3+} ions near the surface (τ_1) and in the core of the nanoparticle (τ_2), respectively. A more disordered Er^{3+} local environment and defects located near the surface result in a more probable nonradiative relaxation of the excited state [201, 202]. Thus, the fluorescence lifetime decrease, i.e. becomes faster (Table 8.3).

A decrease of lifetime values recorded for all investigated emission wavelengths was observed for $NaGd_{0.73}Cr_{0.05}Yb_{0.2}Er_{0.02}F_4$. However, further increase of Cr^{3+} concentration to x = 0.15 resulted in slightly higher lifetime values. The addition of higher concentration of Cr^{3+} ions (x = 0.2, 0.5) has reduced the average lifetime values ($\bar{\tau}$) of green (${}^4S_{3/2}$;${}^2H_{11/2}\rightarrow{}^4I_{15/2}$) and blue (${}^2H_{9/2}\rightarrow{}^4I_{15/2}$) transitions. Since the decrease of average lifetimes was observed with increasing Cr^{3+} concentration, a possible depletion pattern involving various non-radiative decay processes should be taken into consideration. Despite the fact that initial (Cr^{3+} free) nanoparticles had the highest $\bar{\tau}$, further doping of Cr^{3+} up to x = 0.15 showed an increase in blue and red emission lifetimes. In the case of ${}^4F_{9/2}\rightarrow{}^4I_{15/2}$ energy transfer, an increase of $\bar{\tau}$ could occur from a ${}^4T_2\rightarrow{}^4A_2$ transition followed by a subsequent transfer to ${}^4F_{9/2}$ level of Er^{3+} ions.

Table 8.3. Average lifetime values (µs) of $NaGd_{0.78-x}Cr_xYb_{0.2}Er_{0.02}F_4$ nanoparticles excited with 980 nm laser radiation (emission monitored at 407, 539.5 and 653.5 nm).

x	**${}^2H_{9/2}\rightarrow{}^4I_{15/2}$ (λ_{em} = 407 nm)**		**${}^4S_{3/2}$;${}^2H_{11/2}\rightarrow{}^4I_{15/2}$ (λ_{em} = 539.5 nm)**		**${}^4F_{9/2}\rightarrow{}^4I_{15/2}$ (λ_{em} = 653.5 nm)**	
0	59.88 (91.68%)	$\bar{\tau}$=67.98	120.00 (77.15%)	$\bar{\tau}$=147.17	176.54 (82.30%)	$\bar{\tau}$=205.62
	157.25 (8.32%)		238.91 (22.85%)		340.87 (17.70%)	
0.05	32.63 (82.44%)	$\bar{\tau}$=45.70	64.39 (71.27%)	$\bar{\tau}$=100.67	74.19 (73.94%)	$\bar{\tau}$=109.72
	107.12 (17.56%)		141.60 (28.73%)		210.52 (26.06%)	
0.1	30.56 (87.86%)	$\bar{\tau}$=41.26	62.35 (70.65%)	$\bar{\tau}$=83.96	77.47 (73.81%)	$\bar{\tau}$=112.20
	118.68 (12.14%)		135.97 (29.35%)		210.06 (26.19%)	
0.15	68.40 (79.56%)	$\bar{\tau}$=84.88	114.11 (80.17%)	$\bar{\tau}$=137.11	154.72 (58.67%)	$\bar{\tau}$=217.15
	149.03 (20.44%)		230.12 (19.83%)		305.78 (41.33%)	
0.2	33.35 (73.43%)	$\bar{\tau}$=48.57	65.07 (71.36%)	$\bar{\tau}$=87.86	82.81 (63.20%)	$\bar{\tau}$=136.20
	90.60 (26.57%)		144.62 (28.64%)		227.87 (36.80%)	
0.5	25.44 (83.58%)	$\bar{\tau}$=37.16	53.20 (75.33%)	$\bar{\tau}$=72.51	115.20 (26.94%)	$\bar{\tau}$=231.64
	96.83 (16.42%)		131.48 (24.67%)		274.56 (73.06%)	

Green emission from thermally coupled Er^{3+} states (${}^4S_{3/2}$ and ${}^2H_{11/2}$) is used in developing temperature sensing materials [182, 193]. The population of certain energy levels is proportional to relative integrated emission intensities of ${}^2H_{11/2}\rightarrow{}^4I_{15/2}$ and ${}^4S_{3/2}\rightarrow{}^4I_{15/2}$ energy transfers following the Boltzmann distribution (Eq. 2) [203].

Temperature dependent upconversion emission spectra of $NaGd_{0.63}Cr_{0.15}Yb_{0.2}Er_{0.02}F_4$ sample were recorded in the range of 77 − 500 K (Fig. 8.6). The intensity of UC emission spectra was normalized at 539.5 nm for better interpretation of results. As it can be seen from Fig. 8.6, virtually no emission of ${}^2H_{11/2}\rightarrow{}^4I_{15/2}$ transition was observed in green region at low temperatures (77 and 100 K). Starting from 150 K, a weak emission originates and comparing to the $^4S_{3/2}\rightarrow{}^4I_{15/2}$ transition is gradually increasing with further temperature increase. Data show that $^4S_{3/2}$ level is firstly populated, due to the relaxation from $^4F_{7/2}$ or higher energy levels. It is evident that $^2H_{11/2}$ level is thermally populated at elevated temperature. These results correlate with previous observations in the literature [204].

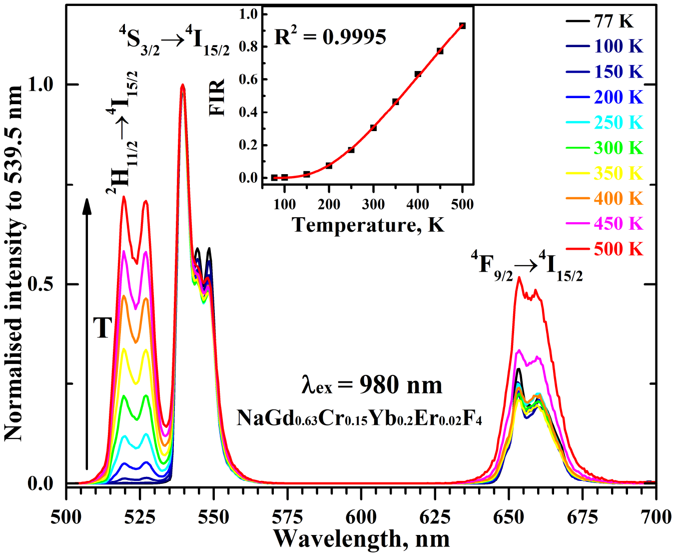

Figure 8.6. Upconversion emission spectra of $NaGd_{0.63}Cr_{0.15}Yb_{0.2}Er_{0.02}F_4$ recorded at various temperatures under 980 nm excitation. Inset shows Boltzmann equation fit of FIR data.

For the calculation of FIR (Eq. 2) value, the recorded emission intensities were integrated in the ranges 507 – 534 nm ($^2H_{11/2}\rightarrow{}^4I_{15/2}$ transition) and 534 – 560 nm ($^4S_{3/2}\rightarrow{}^4I_{15/2}$ transition). Virtually perfect Boltzmann fit was obtained with $R^2 = 0.9995$ and is shown in Fig. 8.6 inset. Furthermore, the effective energy difference (ΔE) between $^2H_{11/2}$ and $^4S_{3/2}$ of Er^{3+} ions was calculated to be 690 ±6 cm^{-1} and 576 ±8 cm^{-1} for $NaGd_{0.78-x}Cr_xYb_{0.2}Er_{0.02}F_4$ samples with $x = 0$ and $x = 0.15$, respectively.

Relative sensitivity (S_r) for $NaGd_{0.78-x}Cr_xYb_{0.2}Er_{0.02}F_4$ system has to be determined in order to evaluate the possibility for UC nanoparticles to be used in temperature sensing. According to (Eq. 3) equation, S_r parameter indicates that temperature change is responsive to the magnitude of energy gap between thermally coupled levels [182, 203]. Thus, the increase of effective energy distance in various systems implies a more suitable material used for thermal sensing.

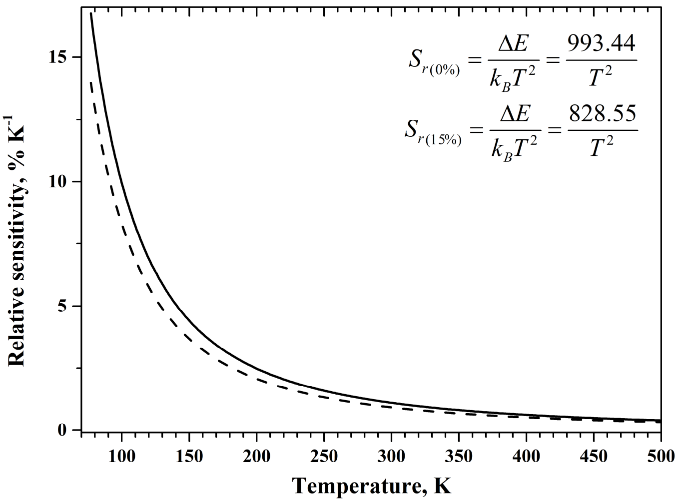

Figure 8.7. Relative (S_r) sensitivity curves of $NaGd_{0.78}Yb_{0.2}Er_{0.02}F_4$ (solid line) and $NaGd_{0.63}Cr_{0.15}Yb_{0.2}Er_{0.02}F_4$ (dashed line).

The calculated S_r curves of $NaGd_{0.78}Yb_{0.2}Er_{0.02}F_4$ and $NaGd_{0.63}Cr_{0.15}Yb_{0.2}Er_{0.02}F_4$ in the 77 – 500 K temperature range are presented in Fig. 8.7. S_r values at 298 K were larger for the sample without additional Cr^{3+} ions ($S_r = 1.12\%\ K^{-1}$) comparing to $NaGd_{0.63}Cr_{0.15}Yb_{0.2}Er_{0.02}F_4$ ($S_r = 0.93\%\ K^{-1}$). Different materials with S_r values reported in the literature are summarized in Table 8.4.

Table 8.4. Relative temperature sensitivity of different materials.

Matrix	T, K	S_r, % K^{-1}	Reference
$NaYF_4$:20% Yb, 2% Er	300	1.20	[205]
$NaYF_4$:Yb, Gd, Er, Nd	288	1.37	[206]
K_2GdF_5:18% Yb, 2% Er	307	1.1	[207]
$NaBiF_4$:Er/Yb	303	1.24	[208]
$NaGd_{0.78}Yb_{0.2}Er_{0.02}F_4$	298	1.12	this work
$NaGd_{0.63}Cr_{0.15}Yb_{0.2}Er_{0.02}F_4$	298	0.93	this work

The values of $NaGd_{0.78}Yb_{0.2}Er_{0.02}F_4$ and $NaGd_{0.63}Cr_{0.15}Yb_{0.2}Er_{0.02}F_4$ are very close to the examples, mentioned in the literature. Thus, our synthesized compounds could also be successfully used as luminescent temperature sensors.

9. $NaGd_{0.995}Nd_{0.005}F_4$ doped with Yb^{3+}

The importance of expanding imaging possibilities for UC systems in order to avoid tissue overheating is addressed in *Chapter 3.2*. Doping of Nd^{3+} ions in $NaGd_{0.995-x}Yb_xF_4$ host will provide a platform of multiple excitations. An evaluation of $Nd^{3+}\rightarrow Yb^{3+}$ energy transfer will be presented, as well as temperature dependent luminescence and thermal sensing ability will be discussed.

9.1. Structural Analysis

The XRD data of synthesized $NaGd_{0.995-x}Nd_{0.005}Yb_xF_4$ with Yb^{3+} concentration $x = 0.01$, 0.05, 0.2, 0.5, 0.6 and $NaGd_{0.995}Nd_{0.05}F_4$ are presented in Figure 9.1.

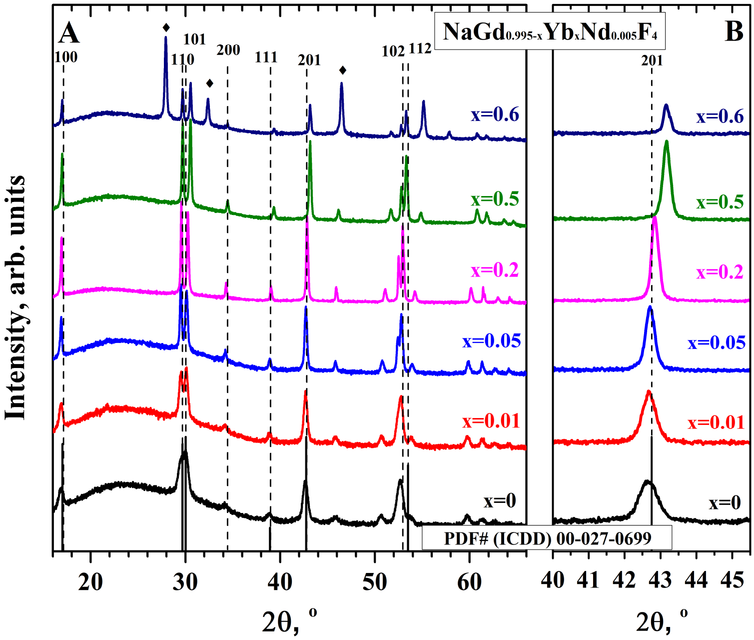

Figure 9.1. Powder XRD patterns of $NaGd_{0.995-x}Yb_xNd_{0.005}F_4$ powders ($x = 0$, 0.01, 0.05, 0.2, 0.5, 0.6%) and reference pattern (dashed line) of $NaGdF_4$ (PDF#(ICDD) 00-027-0699). Cubic phase peaks are marked with .

Pure hexagonal (β) phase compounds are obtained and correspond well with PDF#(ICDD) 00-027-0699 (space group $P6_3/m$) when Yb^{3+} concentration is up to $x = 0.5$. Further doping with Yb^{3+} ($x = 0.6$) led to an additional cubic (α) phase formation and the single cubic phase compound is obtained when x = 0.995. Hexagonal phase formation is favoured with lanthanides of larger ionic radii [25], since $\alpha \rightarrow \beta$ phase transition barrier is lowered [209]. Furthermore, with the decrease of amount of Gd^{3+}, a mixture of both cubic and hexagonal phase $NaGd_{0.995-x}Nd_{0.05}Yb_xF_4$ occurs due to more probable $\beta \rightarrow \alpha$ phase transition. A successful incorporation of Yb^{3+} ions with smaller radius (CN = 9, r = 1.042 Å) instead of larger Gd^{3+} ions (CN = 9, r = 1.107 Å) [131] was confirmed by a shift of (201) peak towards higher 2θ angles (Fig. 9.1 B).

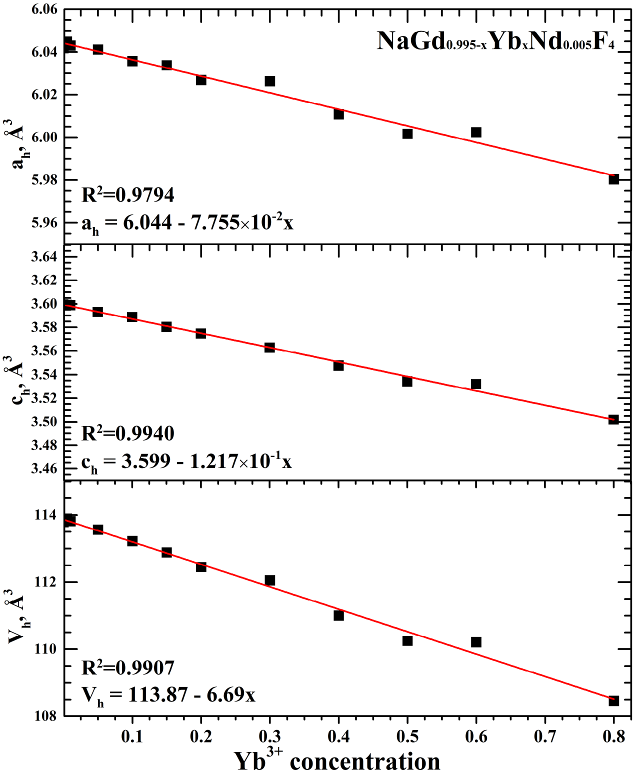

Figure 9.2. Unit cell parameters of $NaGd_{0.995-x}Yb_xNd_{0.005}F_4$ nanoparticles obtained from Le Bail fit.

Unit cell parameters were affected by the Yb^{3+} concentration increase (Fig. 9.2). Unit cell volume (V_h) shrinkage was a result of the tendency to decrease in the size of both hexagonal unit cell parameters (a_h and c_h). The calculated values of a_h, c_h and a_c are tabulated in Table 9.1.

Table 9.1. Calculated unit cell parameters (a_h, c_h – hexagonal, a_c – cubic phase) of $NaGd_{0.995-x}Yb_xNd_{0.005}F_4$ nanoparticles.

x (Yb^{3+})	**a_h, Å**	**c_h, Å**	**a_c, Å**
0	6.0418	3.5995	-
0.005	6.0448	3.5991	-
0.01	6.043	3.5988	-
0.05	6.0411	3.5931	-
0.1	6.0357	3.5887	-
0.15	6.0337	3.5804	-
0.2	6.0268	3.5747	-
0.3	6.0263	3.5627	-
0.4	6.0108	3.5476	-
0.5	6.0016	3.5343	-
0.6	6.0024	3.532	5.5197
0.8	5.9803	3.5018	5.4941
0.995	-	-	5.4707

Table 9.2. $NaGd_{0.995-x}Yb_xNd_{0.005}F_4$ composition determined by ICP-OES.

Expected ratio Gd:Nd:Yb	**Gd, mol%**	**Nd, mol%**	**Yb, mol%**
0.995:0.005:0	0.9944	0.0056	0
0.99:0.005:0.005	0.9895	0.005	0.0055
0.985:0.005:0.01	0.9847	0.005	0.0103
0.945:0.005:0.05	0.9456	0.0047	0.0496
0.895:0.005:0.1	0.8958	0.005	0.0992
0.845:0.005:0.15	0.8463	0.0065	0.1473
0.795:0.005:0.2	0.797	0.0064	0.1966
0.595:0.005:0.4	0.5822	0.0048	0.413
0.495:0.005:0.5	0.4753	0.0051	0.5197
0.395:0.005:0.6	0.3825	0.0037	0.6138
0.195:0.005:0.8	0.1882	0.0044	0.8074
0:0.005:0.995	0.0013	0.0034	0.9952

The actual concentration of ions in synthesized $NaGd_{0.995-x}Yb_xNd_{0.005}F_4$ compounds was determined by carrying out ICP-OES analysis. The ratio of Gd^{3+}, Nd^{3+}, Yb^{3+} are represented in Table 9.2. The obtained results fit very well with the initial values concluding a successful synthesis of the intended compounds.

The morphology of $NaGd_{0.995-x}Yb_xNd_{0.005}F_4$ compounds was investigated by taking TEM images. A spherical shape of nanoparticles can be seen from the images of x = 0.01, 0.6 and 0.995 Yb^{3+} represented in Fig 9.3. The shape of nanoparticles was not impacted by the increase of Yb^{3+} concentration. For $NaGd_{0.995-x}Yb_xNd_{0.005}F_4$ (x = 0.01, 0.6 and 0.995) compounds the average calculated particle sizes were 22.2, 48.1, and 57.2 nm, respectively. High crystallinity of synthesized $NaGd_{0.985}Yb_{0.01}Nd_{0.005}F_4$ is seen from the atomic planes visible in Fig. 9.3 a. From previous XRD results, two crystalline phase (α and β) nanoparticles were obtained at x = 0.6 and x = 0.995 Yb^{3+}. However, there was no evident difference of shape or size between particles represented in Fig. 9.3 b and Fig. 9.3 c. Furthermore, the quality of synthesized nanoparticles was not sufficient for imaging due to the agglomeration.

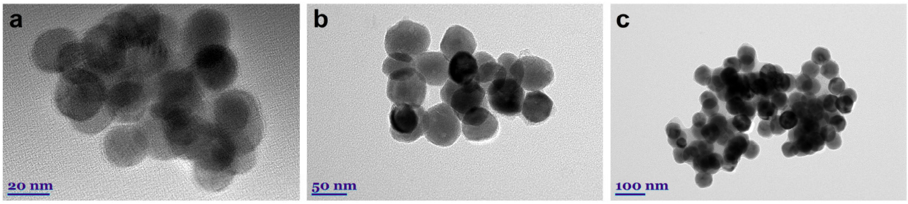

Figure 9.3. Bright-field TEM images of $NaGd_{0.995-x}Yb_xNd_{0.005}F_4$ nanoparticles: a – x = 0.01, b – x = 0.6, c – x = 0.995 Yb^{3+}.

9.2. Luminescence properties

Luminescence properties of $NaGd_{0.995-x}Yb_xNd_{0.005}F_4$ were investigated in 850 – 1150 nm region under 808 nm excitation. The observed downconversion (DC) emission lines were attributed to Nd^{3+} and Yb^{3+} ion transitions (Fig. 9.4): Nd^{3+}:$^4F_{3/2}\rightarrow^4I_{9/2}$ (850 – 920 nm), Nd^{3+}:$^4F_{3/2}\rightarrow^4I_{11/2}$ (1030 – 1070 nm) and Yb^{3+}:$^2F_{5/2}\rightarrow^2F_{7/2}$ (ca. 976 nm). For better interpretation of the results, emission spectra were normalized to intensity at 976 nm.

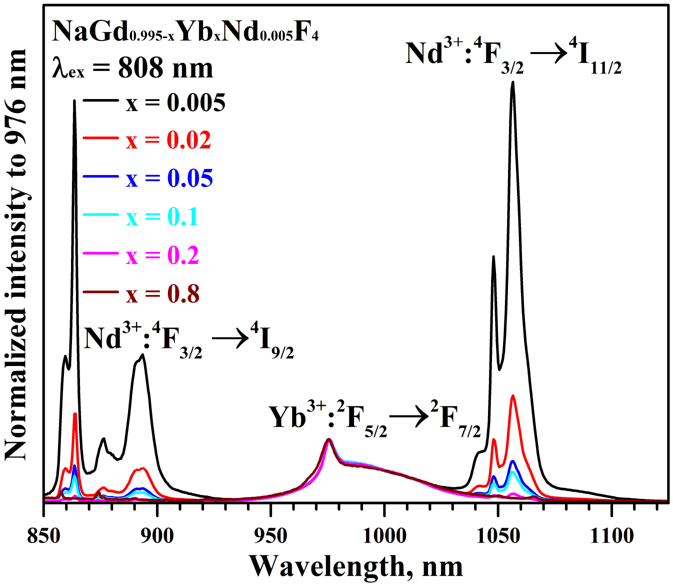

Figure 9.4. Emission spectra of $NaGd_{0.995-x}Yb_xNd_{0.005}F_4$ nanoparticles under 808 nm laser excitation.

At low Yb^{3+} concentration, emission from $^4F_{3/2}\rightarrow{}^4I_{9/2}$ and $^4F_{3/2}\rightarrow{}^4I_{11/2}$ attributed to Nd^{3+} is very intense. However, when the amount of Yb^{3+} increases, Nd^{3+} emission decreases gradually due to originating $Nd^{3+}\rightarrow Yb^{3+}$ energy transfer. The increase of Yb^{3+} ion concentration leads to a statistical distribution of ions in $NaGd_{0.995-x}Yb_xNd_{0.005}F_4$ matrix. Therefore, Yb^{3+} and Nd^{3+} ions get closer facilitating the possibility for $Nd^{3+}\rightarrow Yb^{3+}$ energy transfer to occur. As a result, emission of Nd^{3+} starts to decrease [210]. A mechanism of processes leading to luminescence is adapted from *Chapter 3.2,* Fig. 3.2 [211]. In comparison with Yb^{3+} ions (a typical UC sensitizer), an order of magnitude larger absorption cross-section of Nd^{3+} [32] is a considerable approach to broaden the application possibilities. However, since energy is being pumped through Nd^{3+} as a “bridge”, the efficiency of energy transfer from Nd^{3+} to Yb^{3+} ions needs to be investigated further.

Decay measurements of $NaGd_{0.995-x}Yb_xNd_{0.005}F_4$ samples were recorded under 808 nm laser excitation. Decay curves (Fig. 9.5) were monitored at $^4F_{3/2}\rightarrow{}^4I_{9/2}$ and $^2F_{5/2}\rightarrow{}^2F_{7/2}$ energy transfers assigned to Nd^{3+} and Yb^{3+} ions, respectively. Obtained DC decay curves were fitted with a bi-exponential decay function (Eq. 4). Average lifetime values were calculated (Eq. 5) and represented in Table 9.3.

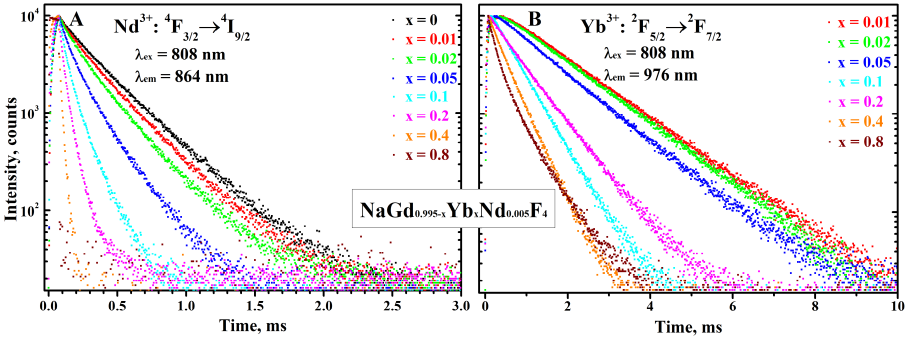

Figure 9.5. Decay curves of $NaGd_{0.995-x}Yb_xNd_{0.005}F_4$ samples (λ_{ex} = 808 nm). Emission monitored at $^4F_{3/2}\rightarrow{}^4I_{9/2}$ (A) and $^2F_{5/2}\rightarrow{}^2F_{7/2}$ (B) energy transfers of Nd^{3+} and Yb^{3+} respectively.

Table 9.3. $Nd^{3+}\rightarrow Yb^{3+}$ energy transfer efficiencies and average lifetime values (μs) of $NaGd_{0.995-x}Yb_xNd_{0.005}F_4$ samples excited with 808 nm laser radiation (emission monitored at 864 nm and 976 nm).

X, mol %(Yb^{3+})	**$\bar{\tau}$ (μs), $^4F_{3/2}\rightarrow{}^4I_{9/2}$ (λ_{em} = 864 nm)**	**$\bar{\tau}$ (μs), $^2F_{5/2}\rightarrow{}^2F_{7/2}$ (λ_{em} = 976 nm)**	**η, % ($Nd^{3+}\rightarrow Yb^{3+}$)**
0	306	-	-
0.005	306	1538	0
0.01	280	1459	8.5
0.02	239	1421	21.9
0.05	174	1256	43.1
0.1	95	589	68.8
0.15	63	425	79.3
0.2	56	781	81.6
0.4	24	441	92.3
0.5	5	423	98.5
0.6	3	524	99.0
0.8	1	471	99.7
0.995	1	110	99.6

With the increase of Yb^{3+} concentration, decay curves of both energy transfers ($^4F_{3/2}\rightarrow{}^4I_{9/2}$ and $^2F_{5/2}\rightarrow{}^2F_{7/2}$) become steeper. This corresponds with the calculated average lifetime values of $^4F_{3/2}\rightarrow{}^4I_{9/2}$ transfer (Table 9.3) which continuously decrease from 306 μs (x = 0) to 5 μs (x = 0.5) due to the increased probability of energy transfer to Yb^{3+}. A decrease in luminescence lifetime values is observed for $^2F_{5/2}\rightarrow{}^2F_{7/2}$ (Yb^{3+}) possibly due to energy back transfer to Nd^{3+}, migration among neighbouring Yb^{3+} ions or impurities occurring in $NaGd_{0.995-x}Yb_xNd_{0.005}F_4$ crystal lattice [54]. Moreover, energy transfer efficiency (η, Table 9.3) in $Nd^{3+}\rightarrow Yb^{3+}$ system [212] was calculated using following equation:

$$\eta = 1 - \frac{\tau_{Nd-Yb}}{\tau_{Nd}} \qquad \text{(Eq. 6)}$$

where, $\tau_{Nd\text{-}Yb}$ and τ_{Nd} are average lifetime values of $^4F_{3/2}\rightarrow{}^4I_{9/2}$ transition (Nd^{3+}) for samples with and without Yb^{3+} ions, respectively. The results in Table 9.3 imply the growth of energy transfer efficiency with the increase of Yb^{3+} concentration. $Nd^{3+}\rightarrow Yb^{3+}$ energy transfer efficiency of 98.5% is obtained when Yb^{3+} concentration reaches $x = 0.5$. Further increase of Yb^{3+} concentration did not result in a significant energy transfer efficiency value growth. Moreover, the $NaGd_{0.995-x}Yb_xNd_{0.005}F_4$ samples with values higher than $x = 0.5$ contained both cubic and hexagonal crystal phase, thus energy transfer processes become more complex.

Temperature dependent DC emission spectra of $NaGd_{0.995}Nd_{0.005}F_4$ sample were recorded in the range of 77 – 500 K (Fig. 9.6). The temperature dependent emission was integrated and is presented on the inset of Fig. 9.6. It is worth to mention, that the integrated emission increases up to 350 K, followed by a decrease at higher temperatures (400 – 500 K). This phenomenon could be explained as an occurrence of thermal population of higher excited state energy levels [213].

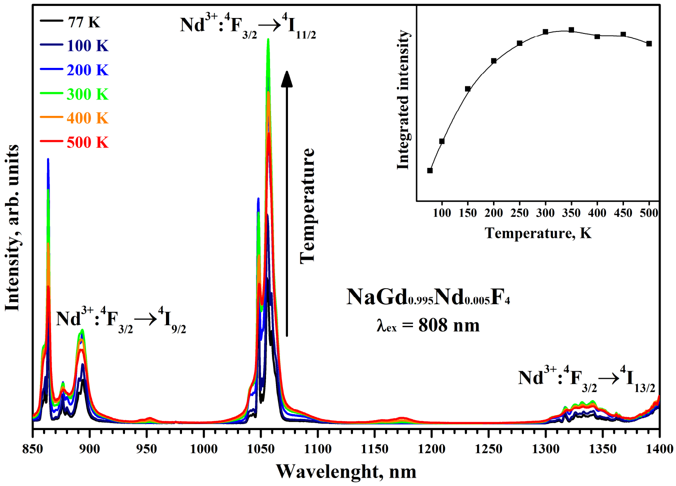

Figure 9.6. Downconversion (DC) emission spectra of $NaGd_{0.995}Nd_{0.005}F_4$ recorded at various temperatures under 808 nm excitation. Integrated emission intensity at certain temperature is shown on the inset.

Furthermore, temperature dependent emission measurements were carried out with samples of various Yb^{3+} concentrations and are represented in Fig. 9.7 (x = 0.01, 0.15, 0.2, 0.4). Luminescence from emission band $^2F_{5/2}\rightarrow{}^2F_{7/2}$ which was assigned to Yb^{3+} appears even at low concentration (x = 0.01) sample. Further increase of Yb^{3+} concentration resulted in more evident growth of $^2F_{5/2}\rightarrow{}^2F_{7/2}$ emission. However, a decrease of all Nd^{3+} energy transfer ($^4F_{3/2}\rightarrow{}^4I_{9/2}$, $^4F_{3/2}\rightarrow{}^4I_{11/2}$ and $^4F_{3/2}\rightarrow{}^4I_{13/2}$) intensities was also observed at higher Yb^{3+} concentrations. Evidently, energy absorbed by Nd^{3+} ions is later transferred to Yb^{3+}, increasing the intensity of $^2F_{5/2}\rightarrow{}^2F_{7/2}$ emission. Nd^{3+} emission decreases gradually until it is no longer visible in at x = 0.4 (Fig. 9.7 D). Nd^{3+} emission increase can only be seen at low temperatures until it starts to decrease at 200 K for all concentrations that have been investigated in Fig. 9.7.

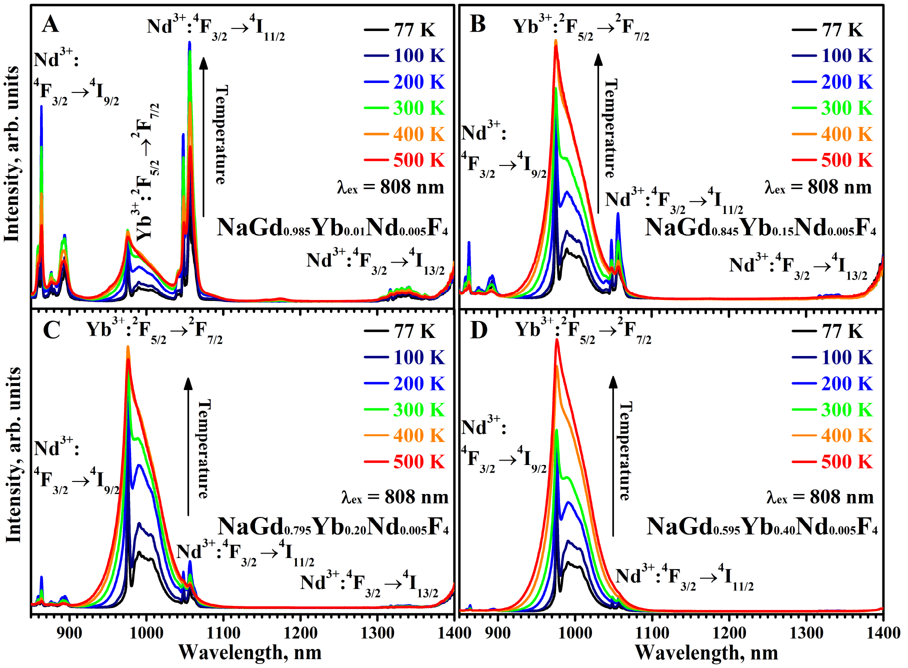

Figure 9.7. Emission spectra of $NaGd_{0.995-x}Yb_xNd_{0.005}F_4$ nanoparticles (A – x = 0.01, B – x = 0.15, C – x = 0.2, D – x = 0.4) recorded at various temperatures (77 - 500 K) under 808 nm excitation.

Temperature dependent DC luminescence decay curves of $NaGd_{0.995}Nd_{0.005}F_4$ (Nd^{3+}:$^4F_{3/2}\rightarrow{}^4I_{9/2}$) were recorded and are represented in Figure 9.8. The data shows that all decay curves are overlapping in measured temperature range (77 – 500 K). It indicates, that lifetime values of the investigated sample are very close in the given temperature range. Obtained decay curves were fitted with a decay function (Eq. 4). Average lifetime values were calculated (Eq. 5) and are represented in Table 9.4. The values were close to each other (around 400 μs) with a slight tendency of increasing values up to 450 K.

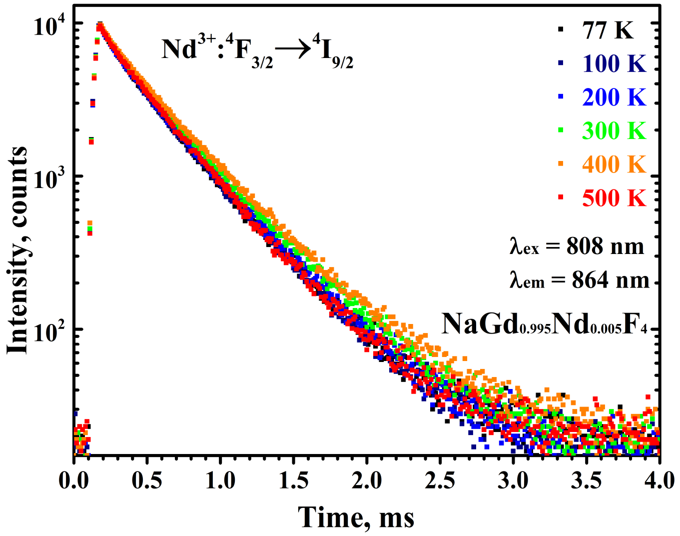

Figure 9.8. Decay curves of $NaGd_{0.995}Nd_{0.005}F_4$ sample (λ_{ex} = 808 nm) recorded at various temperatures.

Table 9.4. Average lifetime values (μs) of $Nd^{3+}\rightarrow Yb^{3+}$ energy transfer in $NaGd_{0.995}Nd_{0.005}F_4$ sample excited with 808 nm laser radiation (emission monitored at 864 nm).

T, K	$\bar{\tau}$, $^4F_{3/2}\rightarrow{}^4I_{9/2}$ (λ_{em} = 864 nm)
77	371.75
100	374.72
150	380.40
200	385.53
250	395.83
300	401.31
350	411.18
400	419.64
450	425.14
500	367.09

The phenomenon was observed and discussed in literature [214] as a result of energy circling between neighbouring Nd^{3+} ions caused by temperature increase. Temperature induced energy transfer between Nd^{3+} ions is suggested to occur as a result of increased population of the $^4I_{11/2}$ state. Proportionally to the elevation of the temperature, the population of $^4I_{11/2}$ is increased due to emission occurring from $^4F_{3/2}$ energy level together with a cross relaxation of $^4F_{3/2}$ - $^4I_{9/2}$ energy levels of separate Nd^{3+} ions [214].

Temperature dependent decay measurements of $NaGd_{0.995-x}Yb_xNd_{0.005}F_4$ samples (x = 0.1 and 0.4) were recorded under 808 nm laser excitation. Decay curves (Fig. 9.9 and Fig. 9.10) were monitored at $^4F_{3/2}\rightarrow{}^4I_{9/2}$ and $^2F_{5/2}\rightarrow{}^2F_{7/2}$ energy transfers assigned to Nd^{3+} and Yb^{3+} ions, respectively. Obtained DC decay curves were fitted with a bi-exponential decay function (Eq. 4). Average lifetime values were calculated (Eq. 5) and represented in Table 9.5.

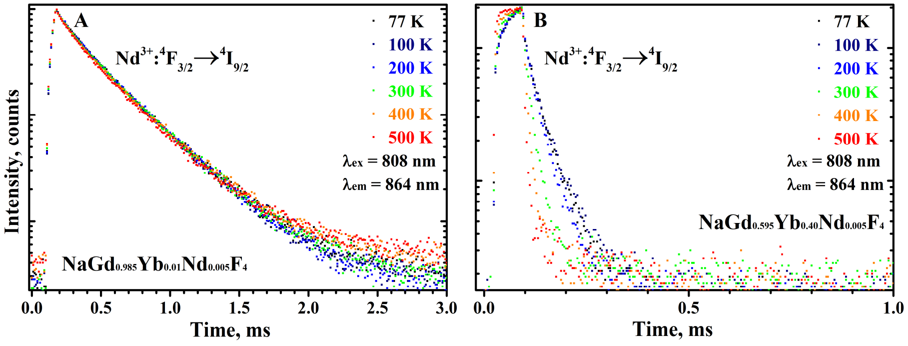

Figure 9.9. Decay curves of $NaGd_{0.995-x}Yb_xNd_{0.005}F_4$ samples (λ_{ex} = 808 nm) recorded at various temperatures (λ_{em} = 864 nm): A) x = 0.01, B) x = 0.4.

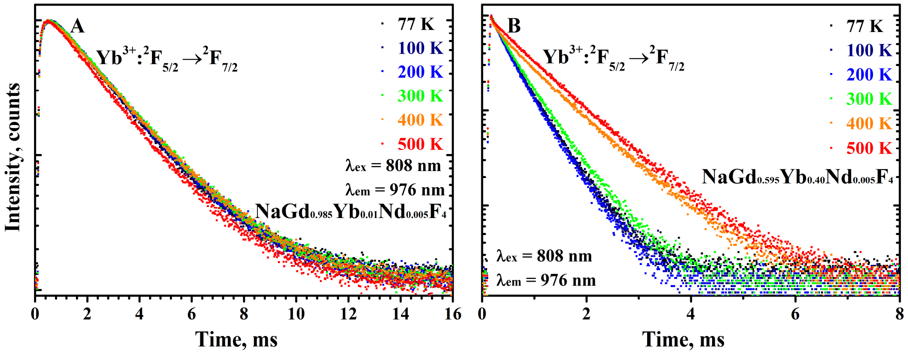

Figure 9.10. Decay curves of $NaGd_{0.995-x}Yb_xNd_{0.005}F_4$ samples (λ_{ex} = 808 nm) recorded at various temperatures (λ_{em} = 976 nm): A) x = 0.01, B) x = 0.4.

Table 9.5. Nd^{3+}→Yb^{3+} energy transfer efficiencies and average lifetime values (μs) of $NaGd_{0.995-x}Yb_xNd_{0.005}F_4$ samples excited with 808 nm laser radiation (emission monitored at 864 nm and 976 nm).

	$NaGd_{0.985}Yb_{0.01}Nd_{0.005}F_4$			$NaGd_{0.595}Yb_{0.40}Nd_{0.005}F_4$		
T, K	**$\bar{\tau}$, μs** **$^4F_{3/2}$→$^4I_{9/2}$**	**$\bar{\tau}$, μs** **$^2F_{5/2}$→$^2F_{7/2}$**	**η, %**	**$\bar{\tau}$, μs** **$^4F_{3/2}$→$^4I_{9/2}$**	**$\bar{\tau}$, μs** **$^2F_{5/2}$→$^2F_{7/2}$**	**η, %**
77	327.7	1823.0	11.9	44.8	458.1	87.9
100	324.0	1835.6	13.5	47.7	456.2	87.3
150	330.9	1858.9	13.0	42.4	452.1	88.9
200	323.9	1879.2	16.0	36.8	441.6	90.5
250	331.2	1902.8	16.3	28.2	446.0	92.9
300	328.0	1908.0	18.3	28.0	508.3	93.0
350	329.2	1921.5	19.9	23.8	679.4	94.2
400	327.7	1921.9	21.9	15.8	827.6	96.2
450	333.2	1885.3	21.6	14.7	870.0	96.5
500	335.8	1759.8	8.5	11.1	874.3	97.0

Decay curves of Nd^{3+} ($^4F_{3/2}$→$^4I_{9/2}$) when concentration of Yb^{3+} is low ($x = 0.1$, Fig. 9.9 A), were virtually the same with average lifetime values of 320 − 340 μs (Table 9.5). Moreover, the same tendency of steady decay curves for Yb^{3+} energy transfer ($^2F_{5/2}$→$^2F_{7/2}$, Fig. 9.10 A) was observed when the temperature is increased. However, different behaviour of PL decay curves appears when Yb^{3+} concentration is $x = 0.4$. A tendency of steeper decay curves for Nd^{3+} transition ($^4F_{3/2}$→$^4I_{9/2}$) related to the temperature increase is seen from Fig. 9.9 B. However, the decay curves of Yb^{3+} ($^2F_{5/2}$→$^2F_{7/2}$) transition (Fig. 9.10 B) had prolonged average lifetime values starting at 350 K. Thus, thermally induced population of $^4I_{11/2}$ (Nd^{3+}) is achieved through energy circling and cross relaxation processes. Moreover, it contributes to Yb^{3+} emission enhancement which can be seen from the increased energy transfer efficiency (η) values represented in Table 9.5.

In order to investigate this interesting thermal quenching behavior in Nd Yb system, $NaGd_{0.995-x}Yb_xNd_{0.005}F_4$ was additionally doped with Er^{3+} ions. $NaGd_{0.475}Yb_{0.5}Er_{0.02}Nd_{0.005}F_4$ emission in NIR region (850–1200 nm) under 808 nm excitation was compared to $NaGd_{0.495}Yb_{0.5}Nd_{0.005}F_4$ (Fig. 9.11).

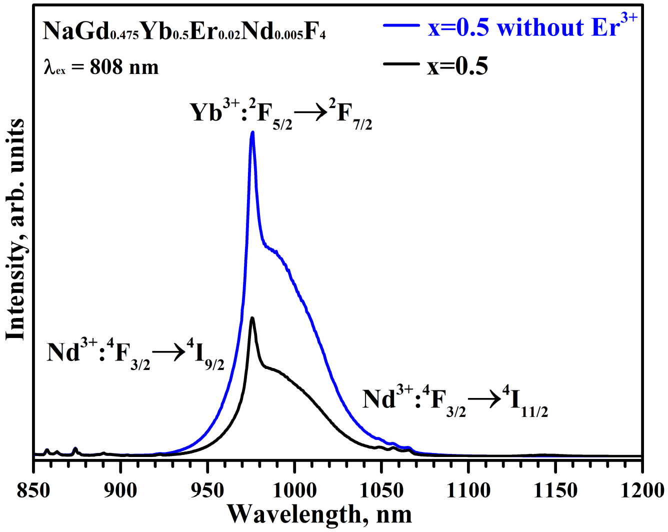

Figure 9.11. Emission spectra of $NaGd_{0.475}Yb_{0.5}Er_{0.02}Nd_{0.005}F_4$ and $NaGd_{0.495}Yb_{0.5}Nd_{0.005}F_4$ nanoparticles under 808 nm laser excitation.

The observed emission lines were attributed to Nd^{3+} and Yb^{3+} ion transitions (Fig. 9.11): Nd^{3+}:$^4F_{3/2}\rightarrow{}^4I_{9/2}$ (ca. 860 nm), Nd^{3+}:$^4F_{3/2}\rightarrow{}^4I_{11/2}$ (1030 – 1070 nm) and Yb^{3+}:$^2F_{5/2}\rightarrow{}^2F_{7/2}$ (ca. 976 nm). Additional energy transfer pathway occurring due to the doping with Er^{3+} ions is evident from the decreased intensity of Yb^{3+} ($^2F_{5/2}\rightarrow{}^2F_{7/2}$) emission band.

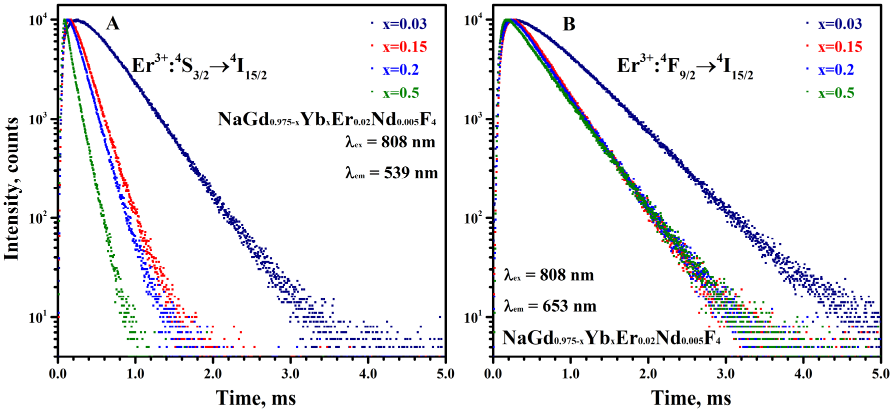

Figure 9.12. Decay curves of $NaGd_{0.975-x}Yb_xEr_{0.02}Nd_{0.005}F_4$ samples (x = 0.03, 0.15, 0.2, 0.5) (λ_{ex} = 808 nm). Emission monitored at $^4S_{3/2}\rightarrow{}^4I_{15/2}$ (A) and $^2F_{9/2}\rightarrow{}^2I_{15/2}$ (B).

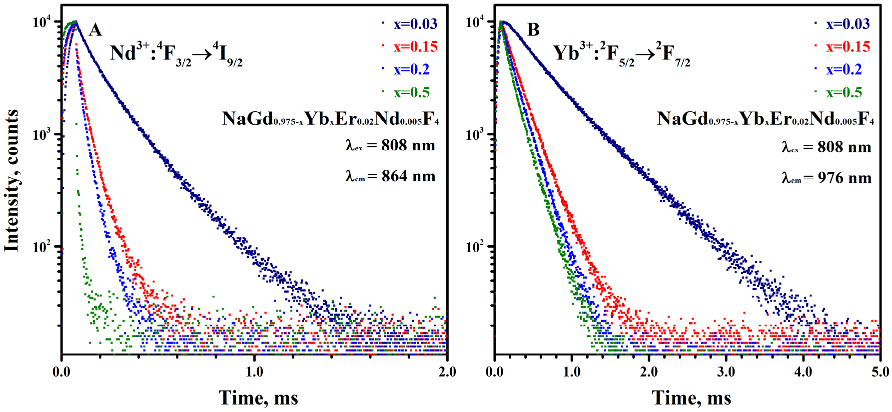

Figure 9.13. Decay curves of $NaGd_{0.975-x}Yb_xEr_{0.02}Nd_{0.005}F_4$ samples (x = 0.03, 0.15, 0.2, 0.5) (λ_{ex} = 808 nm). Emission monitored at $^4F_{3/2}$→$^4I_{9/2}$ (A) and $^2F_{5/2}$→$^2F_{5/2}$ (B).

Decay measurements of $NaGd_{0.975-x}Yb_xEr_{0.02}Nd_{0.005}F_4$ samples (x = 0.03, 0.15, 0.2, 0.5) were recorded under 808 nm laser excitation. Decay curves (Fig. 9.12 and Fig. 9.13) were monitored at $^4S_{3/2}$→$^4I_{15/2}$ and $^2F_{9/2}$→$^2I_{15/2}$ energy transfers assigned to Er^{3+}, $^4F_{3/2}$→$^4I_{9/2}$ to Nd^{3+} and $^2F_{5/2}$→$^2F_{5/2}$ to Yb^{3+} ions, respectively. As it can be seen from Fig. 9.12, an increase in Yb^{3+} concentration led to an occurrence of steeper decay curves for $^4S_{3/2}$→$^4I_{15/2}$ transfer (Fig. 9.12 A). However, a different behaviour of $^2F_{9/2}$→$^2I_{15/2}$ transition (Fig. 9.12 B) suggests that red emission band (ca. 653 nm) will be less affected by the increase of Yb^{3+} concentration. Thus, a ratio of green/red Er^{3+} emission is influenced with additional energy relaxation pathways at the expense of suppressed green emission.

Decay curves of Nd^{3+} ions (Fig. 9.13 A) become steeper with the increase of Yb^{3+} concentration, indicating a successful Nd^{3+}→Yb^{3+} energy transfer, as it was observed in the samples without Er^{3+} (Fig. 9.5). The steeper Yb^{3+} decay curves (Fig. 9.13 B) could be a result of an increased amount of Yb^{3+} ions located at the surface of nanoparticles. Quenching of $^2F_{5/2}$→$^2F_{5/2}$ transition through non-radiative relaxations could be caused by the increased number of surface defects [215].

Green emission from thermally coupled Er^{3+} states ($^4S_{3/2}$ and $^2H_{11/2}$) is used in developing temperature sensing materials [181, 182]. The population of certain energy levels is proportional to relative integrated emission intensities of $^2H_{11/2}$→$^4I_{15/2}$ and $^4S_{3/2}$→$^4I_{15/2}$ transitions following the Boltzmann distribution (Eq. 2) [187, 203]. Temperature dependent UC emission spectra of $NaGd_{0.475}Yb_{0.5}Er_{0.02}Nd_{0.005}F_4$ sample were recorded in the range of 77 – 500 K (Fig. 9.14). The intensity of UC emission spectra was normalized at 539 nm for better interpretation of results. As it can be seen from Fig. 9.14, virtually no emission of $^2H_{11/2}\rightarrow^4I_{15/2}$ transition was observed in green region at low temperatures (77 and 100 K). A weak emission originates at 200 K and, comparing to the $^4S_{3/2}\rightarrow^4I_{15/2}$ transition, is gradually increasing with further temperature increase. Data show that $^4S_{3/2}$ level is firstly populated, due to the relaxation from $^4F_{7/2}$ or higher energy levels. It is evident that $^2H_{11/2}$ level is thermally populated at elevated temperature. These results correlate with previous observations in the literature [204].

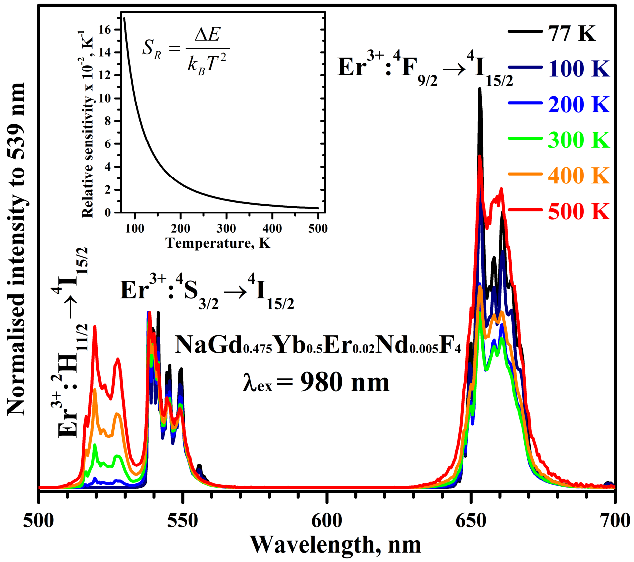

Figure 9.14. Upconversion emission spectra of $NaGd_{0.475}Yb_{0.5}Er_{0.02}Nd_{0.005}F_4$ recorded at various temperatures under 980 nm excitation. Inset shows relative temperature sensitivity (S_r) values in 77 – 500 K temperature range.

For the calculation of FIR (Eq. 2) value, the recorded emission intensity integrated in the ranges of 507 − 533 nm ($^2H_{11/2}\rightarrow^4I_{15/2}$ transition) and 533 − 575 nm ($^4S_{3/2}\rightarrow^4I_{15/2}$ transition) was used. Virtually perfect Boltzmann fit was obtained with $R^2 = 0.9988$. Furthermore, the effective energy difference (ΔE) between $^2H_{11/2}$ and $^4S_{3/2}$ of Er^{3+} ions was calculated to be 699 ±16 cm^{-1} and is in good agreement with the theoretical value (700-800 cm^{-1}) [205].

Relative sensitivity (S_r) for $NaGd_{0.475}Yb_{0.5}Er_{0.02}Nd_{0.005}F_4$ system has to be determined in order to evaluate the possibility for UC nanoparticles to be used in temperature sensing. According to (Eq. 3) equation, S_r parameter indicates that temperature change is responsive to the magnitude of energy gap between thermally coupled levels [182, 203]. The calculated S_r curve of $NaGd_{0.475}Yb_{0.5}Er_{0.02}Nd_{0.005}F_4$ in the 77 – 500 K temperature range are presented in Fig. 9.14 inset. S_r value at 300 K was 1.11% K^{-1} and suggests a possibility for application as a temperature sensor.

10. Conclusions

1. Successful doping of alkali ions (Li^+, K^+) into $Na_{1-x}Gd_{0.78}Yb_{0.2}Er_{0.02}F_4$ was performed and single hexagonal phase materials were obtained at $x = 0.4$. Further concentration increase led to a multiple phase formation of α-$NaGdF_4$ or GdF_3.
2. The upconverting properties of $Na_{1-x}Gd_{0.78}Yb_{0.2}Er_{0.02}F_4$ materials were affected by Li^+ and K^+ doping with a change in red/green (R/G) intensity ratio. Increasing amount of Li^+ led to a R/G ratio increase in the range of $x = 0.1$ to $x = 0.7$ by suppressing green Er^{3+} emission. K^+ concentration increase was followed by the decrease in R/G ratio from 1.7 to 1.0. However, higher concentration of K^+ ions ($x = 0.8$) led to an increase of R/G to 1.6.
3. Doping of Mn^{2+} (synthesized via hot injection or "heat up" methods) or Cr^{3+} ions led to a pure phase formation of cubic $NaYF_4$ and hexagonal $NaGdF_4$ particles up to $x = 0.5$.
4. The influence of transition metal doping was evaluated by the shift of ratio in green and red regions of emission spectra. Energy transfer pathways were influenced by the Mn^{2+} doping to obtain pure red emission in $NaY_{0.78-x}Yb_{0.2}Er_{0.02}F_4$ when $x = 0.78$. For the $NaGdF_4$ compounds, a shift towards red emission was observed in six- and five-times increased values of R/G ratio for Mn^{2+} and Cr^{3+} ions, respectively.
5. Doping of Yb^{3+} ions into $NaGd_{0.995-x}Nd_{0.005}F_4$ led to a pure hexagonal phase formation until $x = 0.5$. A successful incorporation was confirmed by the decrease of unit cell parameters and ICP-OES measurements.
6. Intense Nd^{3+} emission arising from 808 nm laser excitation decreased with the increased amount of Yb^{3+} ions in $NaGd_{0.995-x}Yb_xNd_{0.005}F_4$. Energy transfer $Nd^{3+} \rightarrow Yb^{3+}$ efficiency was evaluated from decay measurements and the highest value was ~99% when Yb^{3+} concentration reached $x = 0.6$.
7. Abnormal temperature dependent luminescence behaviour was observed in $NaGd_{0.995}Nd_{0.005}F_4$ where increased integrated emission values were recorded. A mechanism involving neighbouring Nd^{3+} ions with temperature induced energy circling resulted in an increased emission.
8. Temperature dependent decay curves were not affected by the temperature increase until $x = 0.4$ Yb^{3+} concentration. Prolonged Yb^{3+} emission lifetime values were recorded when temperature was

above 300 K. Moreover, higher energy transfer efficiency values (~97%) were observed suggesting a positive impact on luminescence at elevated temperatures.

9. Fluorescence intensity ratio was investigated and effective energy difference (ΔE) for thermally coupled levels of Er^{3+} was calculated from temperature dependent luminescence measurements. The ΔE value for $NaGd_{0.78}Yb_{0.2}Er_{0.02}F_4$ and $NaGd_{0.475}Yb_{0.5}Er_{0.02}F_4$ samples was found to be 690 ± 6 cm^{-1} and 699 ± 16 cm^{-1}, respectively, and is in good agreement with the theoretical value.
10. Relative temperature sensitivity measurements suggested that these upconverting materials have a broader range of application. In fact, with S_r values close to 1% K^{-1}, $NaGd_{0.78}Yb_{0.2}Er_{0.02}F_4$ and $NaGd_{0.475}Yb_{0.5}Er_{0.02}F_4$ are good candidates to be successfully used as temperature sensors.

REFERENCES

[1] F. Wang, D. Banerjee, Y.S. Liu, X.Y. Chen, X.G. Liu, Upconversion nanoparticles in biological labeling, imaging, and therapy, Analyst., **135** (2010) 1839-1854.

[2] G.Y. Chen, H. Agren, T.Y. Ohulchanskyy, P.N. Prasad, Light upconverting core-shell nanostructures: nanophotonic control for emerging applications, Chem. Soc. Rev., **44** (2015) 1680-1713.

[3] A. Gulzar, J.T. Xu, P.P. Yang, F. He, L.G. Xu, Upconversion processes: versatile biological applications and biosafety, Nanoscale, **9** (2017) 12248-12282.

[4] S.W. Wu, G. Han, D.J. Milliron, S. Aloni, V. Altoe, D.V. Talapin, B.E. Cohen, P.J. Schuck, Non-blinking and photostable upconverted luminescence from single lanthanide-doped nanocrystals, P. Natl. Acad. Sci. USA, **106** (2009) 10917-10921.

[5] D.K. Chatteriee, A.J. Rufalhah, Y. Zhang, Upconversion fluorescence imaging of cells and small animals using lanthanide doped nanocrystals, Biomaterials, **29** (2008) 937-943.

[6] M.V. DaCosta, S. Doughan, Y. Han, U.J. Krull, Lanthanide upconversion nanoparticles and applications in bioassays and bioimaging: A review, Anal. Chim. Acta, **832** (2014) 1-33.

[7] X.J. Xie, N.Y. Gao, R.R. Deng, Q. Sun, Q.H. Xu, X.G. Liu, Mechanistic Investigation of Photon Upconversion in Nd^{3+}-Sensitized Core-Shell Nanoparticles, J. Am. Chem. Soc., **135** (2013) 12608-12611.

[8] S.Q. He, J. Song, J.L. Qu, Z. Cheng, Crucial breakthrough of second near-infrared biological window fluorophores: design and synthesis toward multimodal imaging and theranostics, Chem. Soc. Rev., **47** (2018) 4258-4278.

[9] G.Y. Chen, H.L. Qju, P.N. Prasad, X.Y. Chen, Upconversion Nanoparticles: Design, Nanochemistry, and Applications in Theranostics, Chem. Rev., **114** (2014) 5161-5214.

[10] J. Zhou, Y. Sun, X.X. Du, L.Q. Xiong, H. Hu, F.Y. Li, Dual-modality in vivo imaging using rare-earth nanocrystals with near-infrared to near-infrared (NIR-to-NIR) upconversion luminescence and magnetic resonance properties, Biomaterials, **31** (2010) 3287-3295.

[11] A. Nadort, J.B. Zhao, E.M. Goldys, Lanthanide upconversion luminescence at the nanoscale: fundamentals and optical properties, Nanoscale, **8** (2016) 13099-13130.

[12] G.K. Liu, Advances in the theoretical understanding of photon upconversion in rare-earth activated nanophosphors, Chem. Soc. Rev., **44** (2015) 1635-1652.

[13] S.V. Eliseeva, J.C.G. Bunzli, Lanthanide luminescence for functional materials and bio-sciences, Chem. Soc. Rev., **39** (2010) 189-227.

[14] B.M. Walsh, Judd-Ofelt theory: principles and practices, in, Springer Netherlands, Dordrecht, 2006, pp. 403-433.

[15] G. Liu, B. Jacquier, Spectroscopic Properties of Rare Earths in Optical Materials, Springer, Berlin, Heidelberg, 2005.
[16] J.C.G. Bünzli, S.V. Eliseeva, Basics of Lanthanide Photophysics, Springer, Berlin, Heidelberg, 2010.
[17] J.C.G. Bunzli, Lanthanide Luminescence for Biomedical Analyses and Imaging, Chem. Rev., **110** (2010) 2729-2755.
[18] A. Katelnikovas, Synthesis and Characterization of Luminescent Materials for Solid State Light Sources, Vilnius University, Vilnius, 2012, p. 119.
[19] M. Hatanaka, S. Yabushita, Mechanisms of f-f hypersensitive transition intensities of lanthanide trihalide molecules: a spin-orbit configuration interaction study, Theor. Chem. Acc., **133** (2014) 12615-12625.
[20] P.S. Peijzel, A. Meijerink, R.T. Wegh, M.F. Reid, G.W. Burdick, A complete 4(f^n) energy level diagram for all trivalent lanthanide ions, J. Solid. State. Chem., **178** (2005) 448-453.
[21] F. Wang, X.G. Liu, Recent advances in the chemistry of lanthanide-doped upconversion nanocrystals, Chem. Soc. Rev., **38** (2009) 976-989.
[22] K.W. Kramer, D. Biner, G. Frei, H.U. Gudel, M.P. Hehlen, S.R. Luthi, Hexagonal sodium yttrium fluoride based green and blue emitting upconversion phosphors, Chem. Mater., **16** (2004) 1244-1251.
[23] Q.M. Huang, J.C. Yu, E. Ma, K.M. Lin, Synthesis and Characterization of Highly Efficient Near-Infrared Upconversion $Sc^{3+}/Er^{3+}/Yb^{3+}$ Tridoped $NaYF_4$, J. Phys. Chem. C, **114** (2010) 4719-4724.
[24] G.Y. Chen, H.C. Liu, H.J. Liang, G. Somesfalean, Z.G. Zhang, Upconversion emission enhancement in Yb^{3+}/Er^{3+}-codoped Y_2O_3 nanocrystals by tridoping with Li^+ ions, J. Phys. Chem. C, **112** (2008) 12030-12036.
[25] F. Wang, Y. Han, C.S. Lim, Y.H. Lu, J. Wang, J. Xu, H.Y. Chen, C. Zhang, M.H. Hong, X.G. Liu, Simultaneous phase and size control of upconversion nanocrystals through lanthanide doping, Nature, **463** (2010) 1061-1065.
[26] F.F. Jia, G.L. Li, B. Yang, B. Yu, Y.Q. Shen, H.L. Cong, Investigation of rare earth upconversion fluorescent nanoparticles in biomedical field, Nanotechnol. Rev., **8** (2019) 1-17.
[27] H. Dong, L.D. Sun, C.H. Yan, Energy transfer in lanthanide upconversion studies for extended optical applications, Chem. Soc. Rev., **44** (2015) 1608-1634.
[28] C.L. Chen, C.G. Li, Z. Shi, Current Advances in Lanthanide-Doped Upconversion Nanostructures for Detection and Bioapplication, Adv. Sci., **3** (2016) 1600029.
[29] F. Auzel, Upconversion and anti-stokes processes with f and d ions in solids, Chem. Rev., **104** (2004) 139-173.
[30] C. Strohhofer, A. Polman, Absorption and emission spectroscopy in Er^{3+}-Yb^{3+} doped aluminum oxide waveguides, Opt. Mater., **21** (2003) 705-712.

[31] J.F. Suyver, A. Aebischer, D. Biner, P. Gerner, J. Grimm, S. Heer, K.W. Kramer, C. Reinhard, H.U. Gudel, Novel materials doped with trivalent lanthanides and transition metal ions showing near-infrared to visible photon upconversion, Opt. Mater., **27** (2005) 1111-1130.

[32] L.P. Tu, X.M. Liu, F. Wu, H. Zhang, Excitation energy migration dynamics in upconversion nanomaterials, Chem. Soc. Rev., **44** (2015) 1331-1345.

[33] F. Zhang, Photon upconversion nanomaterials, 1 ed., Springer-Verlag Berlin Heidelberg.

[34] Y.Q. Lu, J.B. Zhao, R. Zhang, Y.J. Liu, D.M. Liu, E.M. Goldys, X.S. Yang, P. Xi, A. Sunna, J. Lu, Y. Shi, R.C. Leif, Y.J. Huo, J. Shen, J.A. Piper, J.P. Robinson, D.Y. Jin, Tunable lifetime multiplexing using luminescent nanocrystals, Nat. Photonics, **8** (2014) 33-37.

[35] X.M. Li, F. Zhang, D.Y. Zhao, Highly efficient lanthanide upconverting nanomaterials: Progresses and challenges, Nano Today, **8** (2013) 643-676.

[36] R.S. Liu, Phosphors, Up Conversion Nano Particles, Quantum Dots and Their Applications, Springer Verlag, Singapore, 2016.

[37] W. Strek, P. Deren, A. Bednarkiewicz, Cooperative processes in $KYb(WO_4)_2$ crystal doped with Eu^{3+} and Tb^{3+} ions, J. Lumin., **87-89** (2000) 999-1001.

[38] S. Sivakumar, F.C.J.M. van Veggel, P.S. May, Near-infrared (NIR) to red and green up-conversion emission from silica sol-gel thin films made with $La_{0.45}Yb_{0.50}Er_{0.05}F_3$ nanoparticles, hetero-looping-enhanced energy transfer (Hetero-LEET): A new up-conversion process, J. Am. Chem. Soc., **129** (2007) 620-625.

[39] M.F. Joubert, S. Guy, B. Jacquier, Model of the Photon-Avalanche Effect, Phys. Rev. B, **48** (1993) 10031-10037.

[40] F. Wang, R.R. Deng, J. Wang, Q.X. Wang, Y. Han, H.M. Zhu, X.Y. Chen, X.G. Liu, Tuning upconversion through energy migration in core-shell nanoparticles, Nat. Mater., **10** (2011) 968-973.

[41] X. Chen, D.F. Peng, Q. Ju, F. Wang, Photon upconversion in core-shell nanoparticles, Chem. Soc. Rev., **44** (2015) 1318-1330.

[42] Y.F. Wang, G.Y. Liu, L.D. Sun, J.W. Xiao, J.C. Zhou, C.H. Yan, Nd^{3+}-Sensitized Upconversion Nanophosphors: Efficient In Vivo Bioimaging Probes with Minimized Heating Effect, ACS Nano, **7** (2013) 7200-7206.

[43] F. Wang, X.G. Liu, Recent advances in the chemistry of lanthanide-doped upconversion nanocrystals, Chem. Soc. Rev., **38** (2009) 976-989.

[44] D. Vennerberg, Z.Q. Lin, Upconversion Nanocrystals: Synthesis, Properties, Assembly and Applications, Sci. Adv. Mater., **3** (2011) 26-40.

[45] L.E. Bausa, J. Garcia Sole, D. Jaque, An Introduction to The Optical Spectroscopy of Inorganic Solids, John Wiley & Sons, Ltd 2005.

[46] S. Heer, K. Kompe, H.U. Gudel, M. Haase, Highly efficient multicolour upconversion emission in transparent colloids of lanthanide-doped $NaYF_4$ nanocrystals, Adv. Mater., **16** (2004) 2102-2105.

[47] F. Wang, X.G. Liu, Upconversion multicolor fine-tuning: Visible to near-infrared emission from lanthanide-doped $NaYF_4$ nanoparticles, J. Am. Chem. Soc., **130** (2008) 5642-5643.

[48] J. Wang, R.R. Deng, M.A. MacDonald, B.L. Chen, J.K. Yuan, F. Wang, D.Z. Chi, T.S.A. Hor, P. Zhang, G.K. Liu, Y. Han, X. Liu, Enhancing multiphoton upconversion through energy clustering at sublattice level, Nat. Mater., **13** (2014) 157-162.

[49] A.X. Yin, Y.W. Zhang, L.D. Sun, C.H. Yan, Colloidal synthesis and blue based multicolor upconversion emissions of size and composition controlled monodisperse hexagonal $NaYF_4$:Yb,Tm nanocrystals, Nanoscale, **2** (2010) 953-959.

[50] V. Mahalingam, F. Vetrone, R. Naccache, A. Speghini, J.A. Capobianco, Colloidal Tm^{3+}/Yb^{3+}-Doped $LiYF_4$ Nanocrystals: Multiple Luminescence Spanning the UV to NIR Regions via Low-Energy Excitation, Adv. Mater., **21** (2009) 4025-4028.

[51] H. Crosswhite. W.T. Carnall, H.M. Crosswhite, Energy Level Structure and Transition Probabilities in the Spectra of the Trivalent Lanthanides in LaF_3, in, Argonne National Laboratory Report, Lemont, IL, USA, 1977.

[52] I. Mikalauskaite, G. Pleckaityte, L. Sinusaite, V. Plausinaitiene, A. Katelnikovas, A. Beganskiene, Temperature induced emission enhancement and investigation of Nd^{3+}→Yb^{3+} energy transfer efficiency in $NaGdF_4$:Nd^{3+}, Yb^{3+}, Er^{3+} upconverting nanoparticles, J. Lumin., **223** (2020) 117237.

[53] S.T. Dibaba, X.Q. Ge, W. Ren, L.N. Sun, Recent progress of energy transfer and luminescence intensity boosting mechanism in Nd^{3+}-sensitized upconversion nanoparticles, J. Rare Earth., **37** (2019) 791-805.

[54] X.B. Dong, F.T. You, H.S. Peng, S.H. Huang, Ultraviolet to near-infrared energy transfer in $NaYF_4$:Nd^{3+},Yb^{3+} crystals, J. Rare Earth., **34** (2016) 863-867.

[55] Y.T. Zhong, G. Tian, Z.J. Gu, Y.J. Yang, L. Gu, Y.L. Zhao, Y. Ma, J.N. Yao, Elimination of Photon Quenching by a Transition Layer to Fabricate a Quenching-Shield Sandwich Structure for 800 nm Excited Upconversion Luminescence of Nd^{3+} Sensitized Nanoparticles, Adv. Mater., **26** (2014) 2831-2837.

[56] S.W. Hao, W. Shao, H.L. Qiu, Y.F. Shang, R.W. Fan, X.Y. Guo, L.L. Zhao, G.Y. Chen, C.H. Yang, Tuning the size and upconversion emission of $NaYF_4$:Yb^{3+}/Pr^{3+} nanoparticles through Yb^{3+} doping, RSC. Adv., **4** (2014) 56302-56306.

[57] J.R. Silva, L.A. Bueno, A.S. Gouveia-Neto, Multicolor frequency upconversion luminescence in Eu^{3+}/Tb^{3+}/Yb^{3+} -codoped fluorogermanate glass excited at 980 nm, J. Lumin., **154** (2014) 531-534.

[58] W. Wang, M.M. Wu, G.K. Liu, Analysis of upconversion fluorescence dynamics in $NaYF_4$ codoped with Er^{3+} and Yb^{3+}, Spectrosc. Lett., **40** (2007) 259-269.

[59] J.C. Boyer, F. Vetrone, L.A. Cuccia, J.A. Capobianco, Synthesis of colloidal upconverting $NaYF_4$ nanocrystals doped with Er^{3+}, Yb^{3+} and Tm^{3+},

Yb^{3+} via thermal decomposition of lanthanide trifluoroacetate precursors, J. Am. Chem. Soc., **128** (2006) 7444-7445.

[60] J.B. Zhao, D.Y. Jin, E.P. Schartner, Y.Q. Lu, Y.J. Liu, A.V. Zvyagin, L.X. Zhang, J.M. Dawes, P. Xi, J.A. Piper, E.M. Goldys, T.M. Monro, Single-nanocrystal sensitivity achieved by enhanced upconversion luminescence, Nat. Nanotechnol., **8** (2013) 729-734.

[61] G.Y. Chen, H.C. Liu, G. Somesfalean, H.J. Liang, Z.G. Zhang, Upconversion emission tuning from green to red in Yb^{3+}/Ho^{3+}-codoped $NaYF_4$ nanocrystals by tridoping with Ce^{3+} ions, Nanotechnology, **20** (2009).

[62] G.Y. Chen, Y. Liu, Y.G. Zhang, G. Somesfalean, Z.G. Zhang, Q. Sun, F.P. Wang, Bright white upconversion luminescence in rare-earth-ion-doped Y_2O_3 nanocrystals, Appl. Phys. Lett., **91** (2007).

[63] U. Resch-Genger, H.H. Gorris, Perspectives and challenges of photon-upconversion nanoparticles - Part I: routes to brighter particles and quantitative spectroscopic studies, Anal. Bioanal. Chem., **409** (2017) 5855-5874.

[64] E. Hemmer, P. Acosta-Mora, J. Mendez-Ramos, S. Fischer, Optical nanoprobes for biomedical applications: shining a light on upconverting and near-infrared emitting nanoparticles for imaging, thermal sensing, and photodynamic therapy, J. Mater. Chem. B, **5** (2017) 4365-4392.

[65] Y.T. Zhong, H.J. Dai, A mini-review on rare-earth down-conversion nanoparticles for NIR-II imaging of biological systems, Nano Res., (2020).

[66] G. Tessitore, G.A. Mandl, M.G. Brik, W. Park, J.A. Capobianco, Recent insights into upconverting nanoparticles: spectroscopy, modeling, and routes to improved luminescence, Nanoscale, **11** (2019) 12015-12029.

[67] N. Dhananjaya, H. Nagabhushana, B.M. Nagabhushana, B. Rudraswamy, C. Shivakumara, R.P.S. Chakradhar, Effect of Li^{+}-ion on enhancement of photoluminescence in $Gd_2O_3:Eu^{3+}$ nanophosphors prepared by combustion technique, J. Alloy. Compd., **509** (2011) 2368-2374.

[68] D.T. Tu, Y.S. Liu, H.M. Zhu, R.F. Li, L.Q. Liu, X.Y. Chen, Breakdown of Crystallographic Site Symmetry in Lanthanide-Doped $NaYF_4$ Crystals, Angew. Chem. Int. Edit., **52** (2013) 1128-1133.

[69] M.Y. Ding, D.Q. Chen, S.L. Yin, Z.G. Ji, J.S. Zhong, Y.R. Ni, C.H. Lu, Z.Z. Xu, Simultaneous morphology manipulation and upconversion luminescence enhancement of beta-$NaYF_4:Yb^{3+}/Er^{3+}$ microcrystals by simply tuning the KF dosage, Sci. Rep., **5** (2015) 12745.

[70] Q.Q. Dou, Y. Zhang, Tuning of the Structure and Emission Spectra of Upconversion Nanocrystals by Alkali Ion Doping, Langmuir, **27** (2011) 13236-13241.

[71] Q. Cheng, J.H. Sui, W. Cai, Enhanced upconversion emission in Yb^{3+} and Er^{3+} codoped $NaGdF_4$ nanocrystals by introducing Li^{+} ions, Nanoscale, **4** (2012) 779-784.

[72] C.Z. Zhao, X.G. Kong, X.M. Liu, L.P. Tu, F. Wu, Y.L. Zhang, K. Liu, Q.H. Zeng, H. Zhang, Li^{+} ion doping: an approach for improving the

crystallinity and upconversion emissions of $NaYF_4$:Yb^{3+}, Tm^{3+} nanoparticles, Nanoscale, **5** (2013) 8084-8089.

[73] G.Y. Chen, H.C. Liu, G. Somesfalean, Y.Q. Sheng, H.J. Liang, Z.G. Zhang, Q. Sun, F.P. Wang, Enhancement of the upconversion radiation in Y_2O_3:Er^{3+} nanocrystals by codoping with Li^+ ions, Appl. Phys. Lett., **92** (2008) 113114.

[74] S.Y. Han, R.R. Deng, X.J. Xie, X.G. Liu, Enhancing Luminescence in Lanthanide-Doped Upconversion Nanoparticles, Angew. Chem. Int. Edit., **53** (2014) 11702-11715.

[75] N. Niu, F. He, S.L. Gai, C.X. Li, X. Zhang, S.H. Huang, P.P. Yang, Rapid microwave reflux process for the synthesis of pure hexagonal $NaYF_4$:Yb^{3+},Ln^{3+},Bi^{3+} (Ln^{3+} = Er^{3+}, Tm^{3+}, Ho^{3+}) and its enhanced UC luminescence, J. Mater. Chem., **22** (2012) 21613-21623.

[76] P. Ramasamy, P. Chandra, S.W. Rhee, J. Kim, Enhanced upconversion luminescence in $NaGdF_4$:Yb,Er nanocrystals by Fe^{3+} doping and their application in bioimaging, Nanoscale, **5** (2013) 8711-8717.

[77] J. Wang, F. Wang, C. Wang, Z. Liu, X.G. Liu, Single-Band Upconversion Emission in Lanthanide-Doped $KMnF_3$ Nanocrystals, Angew. Chem. Int. Edit., **50** (2011) 10369-10372.

[78] G. Tian, Z.J. Gu, L.J. Zhou, W.Y. Yin, X.X. Liu, L. Yan, S. Jin, W.L. Ren, G.M. Xing, S.J. Li, Y.L. Zhao, Mn^{2+} Dopant-Controlled Synthesis of $NaYF_4$:Yb/Er Upconversion Nanoparticles for in vivo Imaging and Drug Delivery, Adv. Mater., **24** (2012) 1226-1231.

[79] Z.Y. Huang, H.P. Gao, Y.L. Mao, Understanding the effect of Mn^{2+} on Yb^{3+}/Er^{3+} upconversion and obtaining a maximum upconversion fluorescence enhancement in inert-core/active-shell/inert-shell structures, RSC. Adv., **6** (2016) 83321-83327.

[80] M.H. Yuan, R. Wang, C.F. Zhang, Z.N. Yang, X. Yang, K. Han, J.F. Ye, H.Y. Wang, X.J. Xu, Revisiting the Enhanced Red Upconversion Emission from a Single -$NaYF_4$:Yb/Er Microcrystal By Doping with Mn^{2+} Ions, Nanoscale Res. Lett., **14** (2019) 103.

[81] Y. Zhang, J.D. Lin, V. Vijayaragavan, K.K. Bhakoo, T.T.Y. Tan, Tuning sub-10 nm single-phase $NaMnF_3$ nanocrystals as ultrasensitive hosts for pure intense fluorescence and excellent T_1 magnetic resonance imaging, Chem. Commun., **48** (2012) 10322-10324.

[82] Z.H. Bai, H. Lin, J. Johnson, S.C.R. Gui, K. Imakita, R. Montazami, M. Fujii, N. Hashemi, The single-band red upconversion luminescence from morphology and size controllable Er^{3+}/Yb^{3+} doped MnF_2 nanostructures, J. Mater. Chem. C, **2** (2014) 1736-1741.

[83] M.Y. Xie, X.N. Peng, X.F. Fu, J.J. Zhang, G.L. Lia, X.F. Yu, Synthesis of Yb^{3+}/Er^{3+} co-doped MnF_2 nanocrystals with bright red up-converted fluorescence, Scripta Mater., **60** (2009) 190-193.

[84] J. Wang, F. Wang, C. Wang, Z. Liu, X.G. Liu, Single-Band Upconversion Emission in Lanthanide-Doped $KMnF_3$ Nanocrystals, Angew. Chem. Int. Edit., **50** (2011) 10369-10372.

[85] Y. Zhang, J.D. Lin, V. Vijayaragavan, K.K. Bhakoo, T.T.Y. Tan, Tuning sub-10 nm single-phase $NaMnF_3$ nanocrystals as ultrasensitive hosts for pure intense fluorescence and excellent T_1 magnetic resonance imaging, Chem. Commun., **48** (2012) 10322-10324.

[86] C.Y. Wang, X.H. Cheng, Influence of Cr^{3+} ions doping on growth and upconversion luminescence properties of beta-$NaYF_4$:Yb^{3+}/Er^{3+} microcrystals, J. Alloy. Compd., **649** (2015) 196-203.

[87] B.T. Huy, Z. Gerelkhuu, J.W. Chung, V.D. Dao, G. Ajithkumar, Y.I. Lee, Enhanced light harvesting with chromium in $NaLu_{0.70-x}Gd_{0.10}F_4$: $Yb_{0.18}Er_{0.02}Cr_x$ ($0 \leq x \leq 0.25$) upconversion system, Mater. Sci. Eng. B-Adv., **223** (2017) 91-97.

[88] M. Haase, H. Schafer, Upconverting Nanoparticles, Angew. Chem. Int. Edit., **50** (2011) 5808-5829.

[89] T.Y. Sun, R.H. Ma, X.S. Qiao, X.P. Fan, F. Wang, Shielding Upconversion by Surface Coating: A Study of the Emission Enhancement Factor, Chemphyschem, **17** (2016) 766-770.

[90] F. Wang, J.A. Wang, X.G. Liu, Direct Evidence of a Surface Quenching Effect on Size-Dependent Luminescence of Upconversion Nanoparticles, Angew. Chem. Int. Edit., **49** (2010) 7456-7460.

[91] G.S. Yi, G.M. Chow, Water-soluble $NaYF_4$:Yb,Er(Tm)/$NaYF_4$/polymer core/shell/shell nanoparticles with significant enhancement of upconversion fluorescence, Chem. Mater., **19** (2007) 341-343.

[92] X.M. Li, D.K. Shen, J.P. Yang, C. Yao, R.C. Che, F. Zhang, D.Y. Zhao, Successive Layer-by-Layer Strategy for Multi-Shell Epitaxial Growth: Shell Thickness and Doping Position Dependence in Upconverting Optical Properties, Chem. Mater., **25** (2013) 106-112.

[93] F. Zhang, R.C. Che, X.M. Li, C. Yao, J.P. Yang, D.K. Shen, P. Hu, W. Li, D.Y. Zhao, Direct Imaging the Upconversion Nanocrystal Core/Shell Structure at the Subnanometer Level: Shell Thickness Dependence in Upconverting Optical Properties, Nano Lett., **12** (2012) 2852-2858.

[94] Y. Fan, L. Liu, F. Zhang, Exploiting lanthanide-doped upconversion nanoparticles with core/shell structures, Nano Today, **25** (2019) 68-84.

[95] K.A. Abel, J.C. Boyer, C.M. Andrei, F.C.J.M. van Veggel, Analysis of the Shell Thickness Distribution on $NaYF_4$/$NaGdF_4$ Core/Shell Nanocrystals by EELS and EDS, J. Phys. Chem Lett., **2** (2011) 185-189.

[96] H.X. Mai, Y.W. Zhang, L.D. Sun, C.H. Yan, Highly efficient multicolor up-conversion emissions and their mechanisms of monodisperse $NaYF_4$:Yb, Er core and core/shell-structured nanocrystals, J. Phys. Chem. C, **111** (2007) 13721-13729.

[97] B. Shen, S.M. Cheng, Y.Y. Gu, D.R. Ni, Y.L. Gao, Q.Q. Su, W. Feng, F.Y. Li, Revisiting the optimized doping ratio in core/shell nanostructured upconversion particles, Nanoscale, **9** (2017) 1964-1971.

[98] Y.F. Wang, L.D. Sun, J.W. Xiao, W. Feng, J.C. Zhou, J. Shen, C.H. Yan, Rare-Earth Nanoparticles with Enhanced Upconversion Emission and Suppressed Rare-Earth-Ion Leakage, Chem-Eur J, **18** (2012) 5558-5564.

[99] H. Li, X. Wang, D.X. Huang, G.Y. Chen, Recent advances of lanthanide-doped upconversion nanoparticles for biological applications, Nanotechnology, **31** (2020) 072001.

[100] F. Vetrone, R. Naccache, V. Mahalingam, C.G. Morgan, J.A. Capobianco, The Active-Core/Active-Shell Approach: A Strategy to Enhance the Upconversion Luminescence in Lanthanide-Doped Nanoparticles, Adv. Funct. Mater., **19** (2009) 2924-2929.

[101] Y.T. Zhong, G. Tian, Z.J. Gu, Y.J. Yang, L. Gu, Y.L. Zhao, Y. Ma, J.N. Yao, Elimination of Photon Quenching by a Transition Layer to Fabricate a Quenching-Shield Sandwich Structure for 800 nm Excited Upconversion Luminescence of Nd^{3+} Sensitized Nanoparticles, Adv. Mater., **26** (2014) 2831-2837.

[102] Y.T. Zhong, I. Rostami, Z.H. Wang, H.J. Dai, Z.Y. Hu, Energy Migration Engineering of Bright Rare-Earth Upconversion Nanoparticles for Excitation by Light-Emitting Diodes, Adv. Mater., **27** (2015) 6418-6422.

[103] S.H. Wen, J.J. Zhou, K.Z. Zheng, A. Bednarkiewicz, X.G. Liu, D.Y. Jin, Advances in highly doped upconversion nanoparticles, Nat. Commun., **9** (2018).

[104] G.Y. Chen, J. Damasco, H.L. Qiu, W. Shao, T.Y. Ohulchanskyy, R.R. Valiev, X. Wu, G. Han, Y. Wang, C.H. Yang, H. Agren, P.N. Prasad, Energy-Cascaded Upconversion in an Organic Dye-Sensitized Core/Shell Fluoride Nanocrystal, Nano Lett., **15** (2015) 7400-7407.

[105] S.L. Gai, C.X. Li, P.P. Yang, J. Lin, Recent Progress in Rare Earth Micro/Nanocrystals: Soft Chemical Synthesis, Luminescent Properties, and Biomedical Applications, Chem. Rev., **114** (2014) 2343-2389.

[106] J.W. Stouwdam, F.C.J.M. van Veggel, Near-infrared emission of redispersible Er^{3+}, Nd^{3+}, and Ho^{3+} doped LaF_3 nanoparticles, Nano Lett., **2** (2002) 733-737.

[107] J.H. Zeng, J. Su, Z.H. Li, R.X. Yan, Y.D. Li, Synthesis and upconversion luminescence of hexagonal-phase $NaYF_4$:Yb, Er^{3+}, phosphors of controlled size and morphology, Adv. Mater., **17** (2005) 2119-2123.

[108] Z.Q. Li, Y. Zhang, Monodisperse silica-coated polyvinylpyrrolidone/$NaYF_4$ nanocrystals with multicolor upconversion fluorescence emission, Angew. Chem. Int. Edit., **45** (2006) 7732-7735.

[109] S. Heer, O. Lehmann, M. Haase, H.U. Gudel, Blue, green, and red upconversion emission from lanthanide-doped $LuPO_4$ and $YbPO_4$ nanocrystals in a transparent colloidal solution, Angew. Chem. Int. Edit., **42** (2003) 3179-3182.

[110] G.S. Yi, H.C. Lu, S.Y. Zhao, G. Yue, W.J. Yang, D.P. Chen, L.H. Guo, Synthesis, characterization, and biological application of size-controlled nanocrystalline $NaYF_4$:Yb,Er infrared-to-visible up-conversion phosphors, Nano Lett., **4** (2004) 2191-2196.

[111] G.F. Wang, Q. Peng, Y.D. Li, Upconversion Luminescence of Monodisperse CaF_2:Yb^{3+}/Er^{3+} Nanocrystals, J. Am. Chem. Soc., **131** (2009) 14200-14201.

[112] F. Zhang, D.Y. Zhao, Synthesis of Uniform Rare Earth Fluoride ($NaMF_4$) Nanotubes by In Situ Ion Exchange from Their Hydroxide [$M(OH)_3$] Parents, ACS Nano, **3** (2009) 159-164.

[113] F. Zhang, J. Li, J. Shan, L. Xu, D.Y. Zhao, Shape, Size, and Phase-Controlled Rare-Earth Fluoride Nanocrystals with Optical Up-Conversion Properties, Chem-Eur J, **15** (2009) 11010-11019.

[114] L.Y. Wang, Y.D. Li, Controlled synthesis and luminescence of lanthanide doped $NaYF_4$ nanocrystals, Chem. Mater., **19** (2007) 727-734.

[115] L.Y. Wang, Y.D. Li, $Na(Y_{1.5}Na_{0.5})F_6$ single-crystal nanorods as multicolor luminescent materials, Nano Lett., **6** (2006) 1645-1649.

[116] F. Zhang, Y. Wan, T. Yu, F.Q. Zhang, Y.F. Shi, S.H. Xie, Y.G. Li, L. Xu, B. Tu, D.Y. Zhao, Uniform nanostructured arrays of sodium rare-earth fluorides for highly efficient multicolor upconversion luminescence, Angew. Chem. Int. Edit., **46** (2007) 7976-7979.

[117] K.S. Yang, F. Zheng, R.N. Wu, H.S. Li, X.Y. Zhang, Upconversion luminescent properties of YVO_4:Yb^{3+} , Er^{3+} nano-powder by sol-gel method, J. Rare Earth., **24** (2006) 162-166.

[118] A.L. Pellegrino, M.R. Catalano, P. Cortelletti, G. Lucchini, A. Speghini, G. Malandrino, Novel sol-gel fabrication of Yb^{3+}/Tm^{3+} co-doped -$NaYF_4$ thin films and investigation of their upconversion properties, Photoch. Photobio. Sci., **17** (2018) 1239-1246.

[119] X. Gao, N.L. Wang, T. Shi, S. Wang, M.H. Zhang, W. Zhang, J.L. Zhong, H.Z. Tong, X.Y. Zhang, Sol-gel synthesis of beta-$NaYF_4$:Yb^{3+}/Nd^{3+}/Tm^{3+}/Mn^{2+} nanophosphors and color-tunable upconversion luminescence, J. Fluorine. Chem., **188** (2016) 23-27.

[120] K.L. Reddy, N. Prabhakar, R. Arppe, J.M. Rosenholm, V. Krishnan, Microwave-assisted one-step synthesis of acetate-capped $NaYF_4$:Yb/Er upconversion nanocrystals and their application in bioimaging, J. Mater. Sci., **52** (2017) 5738-5750.

[121] N. Panov, R. Marin, E. Hemmer, Microwave-Assisted Solvothermal Synthesis of Upconverting and Downshifting Rare-Earth-Doped $LiYF_4$ Microparticles, Inorg. Chem., **57** (2018) 14920-14929.

[122] X. Qin, T. Yokomori, Y.G. Ju, Flame synthesis and characterization of rare-earth (Er^{3+}, Ho^{3+}, and Tm^{3+}) doped upconversion nanophosphors, Appl. Phys. Lett., **90** (2007) 073104.

[123] X.M. Li, F. Zhang, D.Y. Zhao, Lab on upconversion nanoparticles: optical properties and applications engineering via designed nanostructure, Chem. Soc. Rev., **44** (2015) 1346-1378.

[124] V.K. Lamer, R., H. Dinegar, Theory, Production and Mechanism of Formation of Monodispersed Hydrosol, J. Am. Chem. Soc., **72** (1950) 4847-4854.

[125] C.B. Murray, C.R. Kagan, M.G. Bawendi, Synthesis and characterization of monodisperse nanocrystals and close-packed nanocrystal assemblies, Annu. Rev. Mater. Sci., **30** (2000) 545-610.

[126] B. Qiao, S. Zhao, Y. Zheng, Synthesis and Preparation of Upconverting Phosphor Particles, Springer, Singapore, 2019.

[127] Y.W. Zhang, X. Sun, R. Si, L.P. You, C.H. Yan, Single-crystalline and monodisperse LaF_3 triangular nanoplates from a single-source precursor, J. Am. Chem. Soc., **127** (2005) 3260-3261.

[128] H.X. Mai, Y.W. Zhang, R. Si, Z.G. Yan, L.D. Sun, L.P. You, C.H. Yan, High-quality sodium rare-earth fluoride nanocrystals: Controlled synthesis and optical properties, J. Am. Chem. Soc., **128** (2006) 6426-6436.

[129] H.J. Chang, J. Xie, B.Z. Zhao, B.T. Liu, S.L. Xu, N. Ren, X.J. Xie, L. Huang, W. Huang, Rare Earth Ion-Doped Upconversion Nanocrystals: Synthesis and Surface Modification, Nanomaterials, **5** (2015) 1-25.

[130] J.C. Boyer, L.A. Cuccia, J.A. Capobianco, Synthesis of colloidal upconverting $NaYF_4$:Er^{3+}/Yb^{3+} and Tm^{3+}/Yb^{3+} monodisperse nanocrystals, Nano Lett., **7** (2007) 847-852.

[131] R.D. Shannon, Revised Effective Ionic Radii and Systematic Studies of Interatomic Distances in Halides and Chalcogenides, Acta Crystallogr. A, **A32** (1976) 751-767.

[132] D.M. Yang, C.X. Li, G.G. Li, M.M. Shang, X.J. Kang, J. Lin, Colloidal synthesis and remarkable enhancement of the upconversion luminescence of $BaGdF_5$:Yb^{3+}/Er^{3+} nanoparticles by active-shell modification, J. Mater. Chem., **21** (2011) 5923-5927.

[133] V. Mahalingam, F. Vetrone, R. Naccache, A. Speghini, J.A. Capobianco, Structural and optical investigation of colloidal Ln^{3+}/Yb^{3+} co-doped KY_3F_{10} nanocrystals, J. Mater. Chem., **19** (2009) 3149-3152.

[134] S. Sarkar, B. Meesaragandla, C. Hazra, V. Mahalingam, Sub-5 nm Ln^{3+}-doped $BaLuF_5$ Nanocrystals: A Platform to Realize Upconversion via Interparticle Energy Transfer (IPET), Adv. Mater., **25** (2013) 856-860.

[135] C.L. Yan, H.G. Zhao, D.F. Perepichka, F. Rosei, Lanthanide Ion Doped Upconverting Nanoparticles: Synthesis, Structure and Properties, Small, **12** (2016) 3888-3907.

[136] H.S. Mader, P. Kele, S.M. Saleh, O.S. Wolfbeis, Upconverting luminescent nanoparticles for use in bioconjugation and bioimaging, Curr. Opin. Chem. Biol., **14** (2010) 582-596.

[137] Z.Q. Li, Y. Zhang, An efficient and user-friendly method for the synthesis of hexagonal-phase $NaYF_4$: Yb, Er/Tm nanocrystals with controllable shape and upconversion fluorescence, Nanotechnology, **19** (2008) 345606.

[138] H.S. Qian, Y. Zhang, Synthesis of Hexagonal-Phase Core-Shell $NaYF_4$ Nanocrystals with Tunable Upconversion Fluorescence, Langmuir, **24** (2008) 12123-12125.

[139] N.J.J. Johnson, W. Oakden, G.J. Stanisz, R.S. Prosser, F.C.J.M. van Veggel, Size-Tunable, Ultrasmall $NaGdF_4$ Nanoparticles: Insights into Their T_1 MRI Contrast Enhancement, Chem. Mater., **23** (2011) 3714-3722.

[140] Z.Q. Li, Y. Zhang, S. Jiang, Multicolor Core/Shell-Structured Upconversion Fluorescent Nanoparticles, Adv. Mater., **20** (2008) 4765-4769.

[141] S.L. Gai, G.X. Yang, X.B. Li, C.X. Li, Y.L. Dai, F. He, P.P. Yang, Facile synthesis and up-conversion properties of monodisperse rare earth fluoride nanocrystals, Dalton T, **41** (2012) 11716-11724.

[142] G.Y. Chen, T.Y. Ohulchanskyy, S. Liu, W.C. Law, F. Wu, M.T. Swihart, H. Agren, P.N. Prasad, Core/Shell $NaGdF_4:Nd^{3+}/NaGdF_4$ Nanocrystals with Efficient Near-Infrared to Near-Infrared Downconversion Photoluminescence for Bioimaging Applications, ACS Nano, **6** (2012) 2969-2977.

[143] F. Wang, R.R. Deng, X.G. Liu, Preparation of core-shell $NaGdF_4$ nanoparticles doped with luminescent lanthanide ions to be used as upconversion-based probes, Nat. Protoc., **9** (2014) 1634-1644.

[144] S. Gayathri, O.S.N. Ghosh, P. Sudhakara, A.K. Viswanath, Chitosan conjugation: A facile approach to enhance the cell viability of LaF_3:Yb,Er upconverting nanotransducers in human breast cancer cells, Carbohyd. Polym., **121** (2015) 302-308.

[145] J. Song, G.S. Wang, S. Ye, Y.L. Tian, M.Z. Xiong, D. Wang, H.B. Niu, J.L. Qu, Lanthanide-doped Na_3ZrF_7 upconversion nanoparticles synthesized by a facile method, J. Alloy. Compd., **658** (2016) 914-919.

[146] Z.Y. Huang, M.J. Yi, H.P. Gao, Z.L. Zhang, Y.L. Mao, Enhancing single red band upconversion luminescence of $KMnF_3:Yb^{3+}/Er^{3+}$ nanocrystals by Mg^{2+} doping, J. Alloy. Compd., **694** (2017) 241-245.

[147] A.R. Hong, S.Y. Kim, S.H. Cho, K. Lee, H.S. Jang, Facile synthesis of multicolor tunable ultrasmall $LiYF_4$:Yb,Tm,Er/$LiGdF_4$ core/shell upconversion nanophosphors with sub-10 nm size, Dyes Pigments, **139** (2017) 831-838.

[148] M. Wang, G. Abbineni, A. Clevenger, C.B. Mao, S.K. Xu, Upconversion nanoparticles: synthesis, surface modification and biological applications, Nanomed-Nanotechnol, **7** (2011) 710-729.

[149] J.C. Zhou, Z.L. Yang, W. Dong, R.J. Tang, L.D. Sun, C.H. Yan, Bioimaging and toxicity assessments of near-infrared upconversion luminescent $NaYF_4$:Yb,Tm nanocrystals, Biomaterials, **32** (2011) 9059-9067.

[150] J. Chen, C.R. Guo, M. Wang, L. Huang, L.P. Wang, C.C. Mi, J. Li, X.X. Fang, C.B. Mao, S.K. Xu, Controllable synthesis of $NaYF_4$:Yb,Er upconversion nanophosphors and their application to in vivo imaging of Caenorhabditis elegans, J. Mater. Chem., **21** (2011) 2632-2638.

[151] Y.X. Ao, K.H. Zeng, B. Yu, Y. Miao, W. Hung, Z.Z. Yu, Y.H. Xue, T.T.Y. Tan, T. Xu, M. Zhen, X.L. Yang, Y. Zhang, S.B. Gao, An Upconversion Nanoparticle Enables Near Infrared-Optogenetic Manipulation of the Caenorhabditis elegans Motor Circuit, ACS Nano, **13** (2019) 3373-3386.

[152] A. Lay, O.H. Sheppard, C. Siefe, C.A. McLellan, R.D. Mehlenbacher, S. Fischer, M.B. Goodman, J.A. Dionne, Optically Robust and Biocompatible Mechanosensitive Upconverting Nanoparticles, ACS Central Sci., **5** (2019) 1211-1222.

[153] T.R. Zhang, J.P. Ge, Y.X. Hu, Y.D. Yin, A general approach for transferring hydrophobic nanocrystals into water, Nano Lett., **7** (2007) 3203-3207.

[154] G.Y. Chen, J. Shen, T.Y. Ohulchanskyy, N.J. Patel, A. Kutikov, Z.P. Li, J. Song, R.K. Pandey, H. Agren, P.N. Prasad, G. Han, (alpha-$NaYbF_4:Tm^{3+}$)/CaF_2 Core/Shell Nanoparticles with Efficient Near-Infrared to Near-Infrared Upconversion for High-Contrast Deep Tissue Bioimaging, ACS Nano, **6** (2012) 8280-8287.

[155] L.Q. Xiong, T.S. Yang, Y. Yang, C.J. Xu, F.Y. Li, Long-term in vivo biodistribution imaging and toxicity of polyacrylic acid-coated upconversion nanophosphors, Biomaterials, **31** (2010) 7078-7085.

[156] Q. Liu, J.J. Peng, L.N. Sun, F.Y. Li, High-Efficiency Upconversion Luminescent Sensing and Bioimaging of Hg(II) by Chromophoric Ruthenium Complex-Assembled Nanophosphors, ACS Nano, **5** (2011) 8040-8048.

[157] Z.Y. Hou, Y.X. Zhang, K.R. Deng, Y.Y. Chen, X.J. Li, X.R. Deng, Z.Y. Cheng, H.Z. Lian, C.X. Li, J. Lin, UV-Emitting Upconversion-Based TiO_2 Photosensitizing Nanoplatform: Near-Infrared Light Mediated in Vivo Photodynamic Therapy via Mitochondria-Involved Apoptosis Pathway, ACS Nano, **9** (2015) 2584-2599.

[158] Y. Xiao, L.Y. Zeng, T. Xia, Z.G. Wu, Z.H. Liu, Construction of an Upconversion Nanoprobe with Few-Atom Silver Nanoclusters as the Energy Acceptor, Angew. Chem. Int. Edit., **54** (2015) 5323-5327.

[159] J.C. Boyer, M.P. Manseau, J.I. Murray, F.C.J.M. van Veggel, Surface Modification of Upconverting $NaYF_4$ Nanoparticles with PEG-Phosphate Ligands for NIR (800 nm) Biolabeling within the Biological Window, Langmuir, **26** (2010) 1157-1164.

[160] H. Hu, M.X. Yu, F.Y. Li, Z.G. Chen, X. Gao, L.Q. Xiong, C.H. Huang, Facile Epoxidation Strategy for Producing Amphiphilic Up-Converting Rare-Earth Nanophosphors as Biological Labels, Chem. Mater., **20** (2008) 7003-7009.

[161] A. Gnach, A. Bednarkiewicz, Lanthanide-doped up-converting nanoparticles: Merits and challenges, Nano Today, **7** (2012) 532-563.

[162] Z.N. Wu, C.R. Guo, S. Liang, H. Zhang, L.P. Wang, H.C. Sun, B. Yang, A pluronic F127 coating strategy to produce stable up-conversion $NaYF_4$:Yb,Er (Tm) nanoparticles in culture media for bioimaging, J. Mater. Chem., **22** (2012) 18596-18602.

[163] A. Bagheri, Z. Sadrearhami, N.N.M. Adnan, C. Boyer, M. Lim, Surface functionalization of upconversion nanoparticles using visible light-mediated polymerization, Polymer, **151** (2018) 6-14.

[164] H. Zhang, Y.J. Li, I.A. Ivanov, Y.Q. Qu, Y. Huang, X.F. Duan, Plasmonic Modulation of the Upconversion Fluorescence in $NaYF_4$:Yb/Tm Hexaplate Nanocrystals Using Gold Nanoparticles or Nanoshells, Angew. Chem. Int. Edit., **49** (2010) 2865-2868.

[165] L.Y. Wang, R.X. Yan, Z.Y. Hao, L. Wang, J.H. Zeng, J. Bao, X. Wang, Q. Peng, Y.D. Li, Fluorescence resonant energy transfer biosensor based on upconversion-luminescent nanoparticles, Angew. Chem. Int. Edit., **44** (2005) 6054-6057.

[166] S. Jiang, Y. Zhang, K.M. Lim, E.K.W. Sim, L. Ye, NIR-to-visible upconversion nanoparticles for fluorescent labeling and targeted delivery of siRNA, Nanotechnology, **20** (2009) 155101.

[167] H. Hu, L.Q. Xiong, J. Zhou, F.Y. Li, T.Y. Cao, C.H. Huang, Multimodal-Luminescence Core-Shell Nanocomposites for Targeted Imaging of Tumor Cells, Chem-Eur J, **15** (2009) 3577-3584.

[168] E. Hemmer, N. Venkatachalam, H. Hyodo, A. Hattori, Y. Ebina, H. Kishimoto, K. Soga, Upconverting and NIR emitting rare earth based nanostructures for NIR-bioimaging, Nanoscale, **5** (2013) 11339-11361.

[169] Y. Zhang, Z.Z. Yu, J.Q. Li, Y.X. Ao, J.W. Xue, Z.P. Zeng, X.L. Yang, T.T.Y. Tan, Ultrasmall-Superbright Neodymium-Upconversion Nanoparticles via Energy Migration Manipulation and Lattice Modification: 808 nm-Activated Drug Release, ACS Nano, **11** (2017) 2846-2857.

[170] Y.C. Tsai, P. Vijayaraghavan, W.H. Chiang, H.H. Chen, T.I. Liu, M.Y. Shen, A. Omoto, M. Kamimura, K. Soga, H.C. Chiu, Targeted Delivery of Functionalized Upconversion Nanoparticles for Externally Triggered Photothermal/Photodynamic Therapies of Brain Glioblastoma, Theranostics, **8** (2018) 1435-1448.

[171] J.M. Meruga, W.M. Cross, P.S. May, Q. Luu, G.A. Crawford, J.J. Kellar, Security printing of covert quick response codes using upconverting nanoparticle inks, Nanotechnology, **23** (2012) 395201.

[172] S.W. Hao, Y.F. Shang, D.Y. Li, H. Agren, C.H. Yang, G.Y. Chen, Enhancing dye-sensitized solar cell efficiency through broadband near-infrared upconverting nanoparticles, Nanoscale, **9** (2017) 6711-6715.

[173] Y.F. Shang, S.W. Hao, C.H. Yang, G.Y. Chen, Enhancing Solar Cell Efficiency Using Photon Upconversion Materials, Nanomaterials, **5** (2015) 1782-1809.

[174] D.Y. Li, H. Agren, G.Y. Chen, Near infrared harvesting dye-sensitized solar cells enabled by rare-earth upconversion materials, Dalton T, **47** (2018) 8526-8537.

[175] P. Vilela, A. El-Sagheer, T.M. Millar, T. Brown, O.L. Muskens, A.G. Kanaras, Graphene Oxide-Upconversion Nanoparticle Based Optical Sensors for Targeted Detection of mRNA Biomarkers Present in Alzheimer's Disease and Prostate Cancer, ACS Sens., **2** (2017) 52-56.

[176] D. Jaque, F. Vetrone, Luminescence nanothermometry, Nanoscale, **4** (2012) 4301-4326.

[177] C.D.S. Brites, A. Millán, L.D. Carlos, Handbook on the Physics and Chemistry of Rare Earths, Elsevier, 2016.

[178] Y. Cheng, Y. Gao, H. Lin, F. Huang, Y.S. Wang, Strategy design for ratiometric luminescence thermometry: circumventing the limitation of thermally coupled levels, J. Mater. Chem. C, **6** (2018) 7462-7478.

[179] K. Pavani, J.S. Kumar, K. Srikanth, M.J. Soares, E. Pereira, A.J. Neves, M.P.F. Graca, Highly efficient upconversion of Er^{3+} in Yb^{3+} codoped non-cytotoxic strontium lanthanum aluminate phosphor for low temperature sensors, Sci Rep, **7** (2017) 17646.

[180] X.F. Wang, Q. Liu, Y.Y. Bu, C.S. Liu, T. Liu, X.H. Yan, Optical temperature sensing of rare-earth ion doped phosphors, RSC. Adv., **5** (2015) 86219-86236.

[181] K. Nigoghossian, S. Ouellet, J. Plain, Y. Messaddeq, D. Boudreau, S.J.L. Ribeiro, Upconversion nanoparticle-decorated gold nanoshells for near-infrared induced heating and thermometry, J. Mater. Chem. B, **5** (2017) 7109-7117.

[182] F.F. Chi, F.F. Hu, X.T. Wei, Y.H. Chen, M. Yin, Synthesis and thermometric properties of Yb^{3+}-Er^{3+} co-doped K_2GdF_5 up-conversion phosphors, J. Rare Earth., **35** (2017) 436-440.

[183] P. Huang, W. Zheng, D.T. Tu, X.Y. Shang, M.R. Zhang, R.F. Li, J. Xu, Y. Liu, X.Y. Chen, Unraveling the Electronic Structures of Neodymium in $LiLuF_4$ Nanocrystals for Ratiometric Temperature Sensing, Adv Sci, **6** (2019) 1802282.

[184] W. Xu, H. Zhao, Y.X. Li, L.J. Zheng, Z.G. Zhang, W.W. Cao, Optical temperature sensing through the upconversion luminescence from Ho^{3+}/Yb^{3+} codoped $CaWO_4$, Sensor. Actuat. B-Chem., **188** (2013) 1096-1100.

[185] B.S. Cao, J.L. Wu, Z.Q. Feng, B. Dong, Investigation of near-infrared-to-ultraviolet upconversion luminescence of Tm^{3+} doped $NaYF_4$ phosphors by Yb^{3+} codoping, Mater. Chem. Phys., **142** (2013) 333-338.

[186] S.A. Wade, S.F. Collins, G.W. Baxter, Fluorescence intensity ratio technique for optical fiber point temperature sensing, J. Appl. Phys., **94** (2003) 4743-4756.

[187] W. Xu, Q.T. Song, L.J. Zheng, Z.G. Zhang, W.W. Cao, Optical temperature sensing based on the near-infrared emissions from Nd^{3+}/Yb^{3+} codoped $CaWO_4$, Opt. Lett., **39** (2014) 4635-4638.

[188] CRC Handbook of Chemistry and Physics, 90th ed. (CD-ROM Version 2010); CRC Press/Taylor and Francis: Boca Raton, FL.

[189] C.D.S. Brites, E.D. Martinez, R.R. Urbano, C. Rettori, L.D. Carlos, Self-Calibrated Double Luminescent Thermometers Through Upconverting Nanoparticles, Front. Chem., **7** (2019) 267.

[190] A. Skripka, A. Benayas, R. Marin, P. Canton, E. Hemmer, F. Vetrone, Double rare-earth nanothermometer in aqueous media: opening the third optical transparency window to temperature sensing, Nanoscale, **9** (2017) 3079-3085.

[191] B. del Rosal, D. Jaque, Upconversion nanoparticles for in vivo applications: limitations and future perspectives, Methods Appl Fluores, **7** (2019) 022001.

[192] F. Vetrone, R. Naccache, A. Zamarron, A.J. de la Fuente, F. Sanz-Rodriguez, L.M. Maestro, E.M. Rodriguez, D. Jaque, J.G. Sole, J.A. Capobianco, Temperature Sensing Using Fluorescent Nanothermometers, ACS Nano, **4** (2010) 3254-3258.

[193] K. Nigoghossian, S. Ouellet, J. Plain, Y. Messaddeq, D. Boudreau, S.J.L. Ribeiro, Upconversion nanoparticle-decorated gold nanoshells for near-infrared induced heating and thermometry, J Mater Chem B, **5** (2017) 7109-7117.

[194] D.J. Gargas, E.M. Chan, A.D. Ostrowski, S. Aloni, M.V.P. Altoe, E.S. Barnard, B. Sanii, J.J. Urban, D.J. Milliron, B.E. Cohen, P.J. Schuck, Engineering bright sub-10-nm upconverting nanocrystals for single-molecule imaging, Nat. Nanotechnol., **9** (2014) 300-305.

[195] F. Chen, W.B. Bu, S.J. Zhang, X.H. Liu, J.N. Liu, H.Y. Xing, Q.F. Xiao, L.P. Zhou, W.J. Peng, L.Z. Wang, J.L. Shi, Positive and Negative Lattice Shielding Effects Co-existing in Gd (III) Ion Doped Bifunctional Upconversion Nanoprobes, Adv. Funct. Mater., **21** (2011) 4285-4294.

[196] N. Bogdan, F. Vetrone, G.A. Ozin, J.A. Capobianco, Synthesis of Ligand-Free Colloidally Stable Water Dispersible Brightly Luminescent Lanthanide-Doped Upconverting Nanoparticles, Nano Lett, **11** (2011) 835-840.

[197] S. Heer, K. Petermann, H.U. Gudel, Upconversion excitation of Cr^{3+} emission in $YAlO_3$ codoped with Cr^{3+} and Yb^{3+}, J. Lumin., **102** (2003) 144-150.

[198] A. Herrmann, M. Tylkowski, C. Bocker, C. Russel, Cubic and Hexagonal $NaGdF_4$ Crystals Precipitated from an Aluminosilicate Glass: Preparation and Luminescence Properties, Chem. Mater., **25** (2013) 2878-2884.

[199] Z. Gerelkhuu, B.T. Huy, J.W. Chung, T.L. Phan, E. Conte, Y.I. Lee, Influence of Cr^{3+} on upconversion luminescent and magnetic properties of $NaLu_{0.86-x}Gd_{0.12}F_4{:}Cr_x^{3+}/Er_{0.02}^{3+}$ ($0 \leq x \leq 0.24$) material, J. Lumin., **187** (2017) 40-45.

[200] B.T. Huy, Z. Gerelkhuu, J.W. Chung, V.D. Dao, G. Ajithkumar, Y.I. Lee, Enhanced light harvesting with chromium in $NaLu_{0.70-x}Gd_{0.10}F_4$: $Yb_{0.18}Er_{0.02}Cr_x$ ($0 \leq x \leq 0.25$) upconversion system, Mater. Sci. Eng. B-Adv., **223** (2017) 91-97.

[201] G.Y. Chen, T.Y. Ohulchanskyy, W.C. Law, H. Agren, P.N. Prasad, Monodisperse $NaYbF_4$: $Tm^{3+}/NaGdF_4$ core/shell nanocrystals with near-infrared to near-infrared upconversion photoluminescence and magnetic resonance properties, Nanoscale, **3** (2011) 2003-2008.

[202] W. Yu, W. Xu, H.W. Song, S. Zhang, Temperature-dependent upconversion luminescence and dynamics of $NaYF_4{:}Yb^{3+}/Er^{3+}$ nanocrystals:

influence of particle size and crystalline phase, Dalton T, **43** (2014) 6139-6147.

[203] S.A. Wade, S.F. Collins, G.W. Baxter, Fluorescence intensity ratio technique for optical fiber point temperature sensing, J. Appl. Phys., **94** (2003) 4743-4756.

[204] A. Bayart, F. Szczepanski, J.F. Blach, J. Rousseau, A. Katelnikovas, S. Saitzek, Upconversion luminescence properties and thermal quenching mechanisms in the layered perovskite $La_{1.9}Er_{0.1}Ti_2O_7$ towards an application as optical temperature sensor, J. Alloy. Compd., **744** (2018) 516-527.

[205] S.S. Zhou, K.M. Deng, X.T. Wei, G.C. Jiang, C.K. Duan, Y.H. Chen, M. Yin, Upconversion luminescence of $NaYF_4$: Yb^{3+}, Er^{3+} for temperature sensing, Opt. Commun., **291** (2013) 138-142.

[206] D.T. Klier, M.U. Kumke, Upconversion $NaYF_4$:Yb:Er nanoparticles co-doped with Gd^{3+} and Nd^{3+} for thermometry on the nanoscale, RSC. Adv., **5** (2015) 67149-67156.

[207] F.F. Chi, F.F. Hu, X.T. Wei, Y.H. Chen, M. Yin, Synthesis and thermometric properties of Yb^{3+}-Er^{3+} co-doped K_2GdF_5 up-conversion phosphors, J. Rare Earth., **35** (2017) 436-440.

[208] P. Du, L.H. Luo, X.Y. Huang, J.S. Yu, Ultrafast synthesis of bifunctional Er^{3+}/Yb^{3+}-codoped $NaBiF_4$ upconverting nanoparticles for nanothermometer and optical heater, J. Colloid. Interf. Sci., **514** (2018) 172-181.

[209] J.A. Damasco, G.Y. Chen, W. Shao, H. Agren, H.Y. Huang, W.T. Song, J.F. Lovell, P.N. Prasad, Size-Tunable and Monodisperse Tm^{3+}/Gd^{3+}-Doped Hexagonal $NaYbF_4$ Nanoparticles with Engineered Efficient Near Infrared-to-Near Infrared Upconversion for In Vivo Imaging, ACS Appl. Mater. Inter., **6** (2014) 13884-13893.

[210] L.J. Tian, Z. Xu, S.L. Zhao, Y. Cui, Z.Q. Liang, J.J. Zhang, X.R. Xu, The Upconversion Luminescence of $Er^{3+}/Yb^{3+}/Nd^{3+}$ Triply-Doped β-$NaYF_4$ Nanocrystals under 808-nm Excitation, Materials, **7** (2014) 7289-7303.

[211] D.T. Klier, M.U. Kumke, Upconversion $NaYF_4$:Yb:Er nanoparticles co-doped with Gd^{3+} and Nd^{3+} for thermometry on the nanoscale, RSC. Adv., **5** (2015) 67149-67156.

[212] A. Lupei, V. Lupei, A. Ikesue, C. Gheorghe, S. Hau, Nd→Yb energy transfer in (Nd, Yb):Y_2O_3 transparent ceramics, Opt. Mater., **32** (2010) 1333-1336.

[213] D. Wawrzynczyk, A. Bednarkiewicz, M. Nyk, W. Strek, M. Samoc, Neodymium (III) doped fluoride nanoparticles as non-contact optical temperature sensors, Nanoscale, **4** (2012) 6959-6961.

[214] L. Marciniak, A. Bednarkiewicz, K. Elzbieciak, NIR-NIR photon avalanche based luminescent thermometry with Nd^{3+} doped nanoparticles, J. Mater. Chem. C, **6** (2018) 7568-7575.

[215] M.Y. Hossan, A. Hor, Q. Luu, S.J. Smith, P.S. May, M.T. Berry, Explaining the Nanoscale Effect in the Upconversion Dynamics of beta-

$NaYF_4$:Yb^{3+}, Er^{3+} Core and Core-Shell Nanocrystals, J. Phys. Chem. C, **121** (2017) 16592-16606.

SUMMARY

DISERTACIJOS SANTRAUKA

Ieva
MIKALAUSKAITĖ

Lantanoidais legiruotų apkonvertuojančių medžiagų optinių savybių tyrimas

DAKTARO DISERTACIJA

Gamtos mokslai,
Chemija N 003

VILNIUS 2020

1. ĮVADAS

Pastaraisiais metais pastebimas padidėjęs dėmesys apkonvertuojančioms medžiagoms. Tikimasi, jog šie junginiai, bus pritaikyti įvairiose srityse dėl unikalių savybių. Liuminescencijos proceso išskirtinumas – nuoseklus dviejų (ar daugiau) fotonų sužadinimas mažesnės energijos artimosios infraraudonosios (*abbrev. NIR*) spektro dalies spinduliuote. Lantanoidų (Ln^{3+}) elektronų konfigūracija bei energetinių lygmenų, kurių sužadintos būsenos gyvavimo laikas yra kelių milisekundžių trukmės, leidžia įvykti apkonversijos procesui skirtinguose junginiuose.

Pasitelkiami įvairūs medžiagų kūrimo metodai siekiant gauti efektyvias apkonvertuojančias medžiagas. Parenkant aktyvatorių ir sensibilizatorių koncentracijas įterpiant į tam tikrą matricą, koordinuojama emituojamos spalvos pozicija spektro dalyje. Liuminescencinės savybės gali būti modifikuojamos įvedant į matricą skirtingų dydžių joninių spindulių jonus, taip pakeičiant kristalinės gardelės parametrus. Pereinamųjų elementų energijos lygmenų išsidėstymas leidžia vykti papildomiems nespinduliniams šuoliams, kurie pakeičia spindulinių šuolių energijos srautus, t.y. keičiamos optinės savybės. Literatūroje aprašomi paviršiuje sudaromo neorganinio apvalkalo metodai, sumažinantys nespindulinius šuolius, atsiradusius dėl nanodalelių paviršiuje esančių defektų. Taip pat šis apvalkalas sukuria galimybę vienoje sistemoje apjungti kelias skirtingas aktyvatorių ir sensibilizatorių poras kartu praplečiant ir pritaikymo galimybes.

Apkonvertuojančios medžiagos turi pranašumą prieš kitas optinio vaizdinimo priemones dėl mažesnės žadinimo šaltinio absorbcijos, išsklaidymo bei gilesnės skvarbos į audinius. Didžiausi pranašumai – fotostabilumas, medžiagos nėra toksiškos, nepasižymi autofluorescencija bei gali būti žadinamos nuolatinės veiklos lazerine spinduliuote ($1\text{-}10^3$ W/cm^2). Tačiau vienas didžiausių trūkumų yra žadinimo šaltinio (980 nm) sukeliama terminė pažaida, dėl toje srityje esančios vandens molekulių sugerties. Dėl šios priežasties pastaruoju metu bandomi nauji žadinimo šaltiniai, kurie veikia bangos ilgiuose, nesukeliančiuose pašalinio poveikio biologinėse terpėse. Tam tinkami Nd^{3+} jonai, kurių žadinimo sritis (apie 800 nm) yra palanki naudojimui terpėse, kurių sudėtyje yra vandens. Dėl unikalių savybių apkonvertuojančios medžiagos yra naudojamos saulės baterijose, dokumentų apsaugoje, biomedicinoje kaip vaizdinimo priemonės ar temperatūros jutikliai. Pagrindinėje matricoje esant Gd^{3+} jonams, gali būti panaudojama magnetinio rezonanso vaizdinime.

Šio darbo tikslas – susintetinti ir ištirti lantanoidais (Yb^{3+}, Er^{3+}, Nd^{3+}) legiruotų NaY/GdF_4 apkonvertuojančių medžiagų optines savybes.

Papildomas skirtingo joninio spindulio elementų įterpimas gali turėti įtakos besiformuojančių medžiagų kristalinei struktūrai ir optinėms savybėms. Tikslui pasiekti buvo iškelti šie uždaviniai:

1. Atlikti šarminiais metalais (Li^+, K^+) pakeistų $NaGdF_4$ junginių sintezę terminio skaidymo metodu bei ištirti gautų junginių optines savybes.
2. Atlikti pereinamaisiais metalais (Mn^{2+}, Cr^{3+}) pakeistų NaY/GdF_4 junginių sintezę terminio skaidymo metodu bei ištirti gautų junginių optines savybes.
3. Ištirti Yb^{3+} koncentracijos įtaką $Nd^{3+}\rightarrow Yb^{3+}$ energijos pernašos efektyvumui $NaGdF_4$ sistemoje.
4. Ištirti temperatūros pokyčio įtaką liuminescencinėms savybėms.

2. EKSPERIMENTINĖ DALIS

2.1. Reagentai

Medžiagos, naudojamos sintezėje ir bandinių paruošime: gadolinio (III) oksidas Gd_2O_3 (99,99 % Treibacher Industrie AG), iterbio (III) oksidas Yb_2O_3 (99,99 % Sigma Aldrich), erbio (III) oksidas Er_2O_3 (99,99 % Sigma Aldrich), neodimio (III) oksidas Nd_2O_3 (99,99 % Tailorlux), itrio (III) oksidas Y_2O_3 (99,99 % Treibacher Industrie AG), trifluoracto rūgštis CF_3COOH (99,9 % Carl Roth), natrio trifluoracetatas CF_3CO_2Na (98,0 % Alfa Aesar), ličio trifluoracetatas CF_3CO_2Li (97,0 % Alfa Aesar), kalio trifluoracetatas CF_3CO_2K (98,0 % Alfa Aesar), oleino rūgštis $C_{18}H_{34}O_2$ (90,0 % Alfa Aesar), 1-oktadecenas $CH_3(CH_2)_{15}CH{=}CH_2$ (90,0 % Alfa Aesar), heksanas C_6H_{14} (99,0 % Honeywell), acetonas $(CH_3)_2CO$ (analitinio grynumo, Eurochemicals), mangano (II) karbonatas $MnCO_3$ (99,9 % Alfa Aesar), chromo (III) chlorido heksahidratas $CrCl_3{\cdot}6H_2O$ ($\geq$98,0 % Sigma Aldrich), natrio hidroksidas NaOH (99 % Eurochemicals), amonio fluoridas NH_4F ($\geq$98,0 % Alfa Aesar), druskos rūgštis HCl (analitinio grynumo Eurochemicals), etanolis C_2H_5OH, toluenas C_7H_8 (99,9 % Eurochemicals).

2.2. Sintezės metodai

2.2.1. $Na_{1-x}Li_xGd_{0,78}Yb_{0,2}Er_{0,02}F_4$ arba $Na_{1-x}K_xGd_{0,78}Yb_{0,2}Er_{0,02}F_4$ sintezė

$Na_{1-x}Li_xGd_{0,78}Yb_{0,2}Er_{0,02}F_4$ dalelės buvo sintetinamos terminio skaidymo būdu aukštos virimo temperatūros organinių tirpiklių mišinyje. Retųjų žemių trifluoracetatai gaunami ištirpinus atitinkamus retųjų žemių oksidus RE_2O_3 (1,25 mmol) trifluoracto rūgšties ir vandens mišinyje esant 80 °C temperatūrai. Mišiniui tapus skaidriu, tirpalas buvo išgarintas. 2,5 mmol natrio trifruoracetato ir ličio trifluoracetato (arba kalio trifluoracetato) maišomi kartu su po 7,5 mL oleino rūgšties bei 1-oktadeceno. Mišinys (A) buvo maišomas kaitinant 150 °C temperatūroje N_2 atmosferoje tam, kad pasišalintų deguonis ir vanduo. Kitas mišinys (B) susidedantis iš 12,5 mL oleino rūgšties ir 12,5 mL 1-oktadeceno ir maišomas kaitinant N_2 atmosferoje. Mišiniui A tapus skaidriu, 330 °C temperatūroje lėtai sulašinamas mišinys B. Gautas tirpalas maišant kaitinamas 1 val. Paliekamas atvėsti kambario temperatūroje, medžiaga išsodinama ir plaunama tris kartus heksano/acetono (1:4) mišiniu centrifuguojant (30 min, 7000 rpm) ir džiovinama kambario temperatūroje. $Na_{1-x}Li_xGd_{0,78}Yb_{0,2}Er_{0,02}F_4$ bei

$Na_{1-x}K_xGd_{0,78}Yb_{0,2}Er_{0,02}F_4$ sintezės buvo atliekamos įterpiant skirtingos koncentracijos Li^+ bei K^+ jonus (x = 0; 0,1; 0,2; 0,3; 0,4; 0,5; 0,6; 0,7; 0,8; 0,9; 1,0).

2.2.2. $NaY_{0,78-x}Mn_xYb_{0,2}Er_{0,02}F_4$ sintezė

$NaY_{0,78-x}Mn_xYb_{0,2}Er_{0,02}F_4$ dalelės buvo sintetinamos terminio skaidymo būdu aukštos virimo temperatūros organinių tirpiklių mišinyje. Retųjų žemių trifluoracetatai gaunami ištirpinus atitinkamus retųjų žemių oksidus RE_2O_3 (1,25 mmol) ir mangano (II) karbonatą trifluoracto rūgšties ir vandens mišinyje esant 80 °C temperatūroje. Mišiniui tapus skaidriu, tirpalas buvo išgarintas. 2,5 mmol natrio trifruoracetato maišoma kartu su po 7,5 mL oleino rūgšties bei 1-oktadeceno. Tolimesni etapai aprašyti 2.2.1 skyriuje. $NaY_{0,78-x}Mn_xYb_{0,2}Er_{0,02}F_4$ sintezės buvo atliekamos įterpiant skirtingus kiekius Mn^{2+} (x = 0; 0,05; 0,1; 0,15; 0,2; 0,5; 0,78).

2.2.3. $NaGd_{0,78-x}Mn_xYb_{0,2}Er_{0,02}F_4$ arba $NaGd_{0,78-x}Cr_xYb_{0,2}Er_{0,02}F_4$ sintezė

$NaGd_{0,78-x}Mn_xYb_{0,2}Er_{0,02}F_4$ ir $NaGd_{0,78-x}Cr_xYb_{0,2}Er_{0,02}F_4$ dalelės buvo sintetinamos terminio skaidymo būdu kaitinant reagentus iki reikiamos temperatūros. Retųjų žemių metalų oksidai ištirpinami druskos rūgštyje, gaunami retųjų žemių metalų chloridai. Mišiniui tapus skaidriu, tirpalas buvo išgarintas, retųjų žemių chloridai buvo tris kartus plaunami vandeniu ir išdžiovinti vakuume. Retųjų žemių chloridai ir chromo chloridas heksahidratas ištirpinami metanolyje ir supilami į 12 mL oleino rūgšties ir 30 mL 1-oktadeceno mišinį ir maišomi 1 val. Mišinys kaitinamas 120 °C temperatūroje N_2 atmosferoje kol tampa skaidrus. Kaitinimas nutraukiamas ir leidžiama tirpalui atvėsti iki kambario temperatūros. Ištirpinama 5 mmol natrio šarmo ir 8 mmol amonio fluorido metanolyje bei kambario temperatūroje supilama į paruoštą tirpalą. Mišinys maišomas 0,5 val., vėliau padidinama temperatūra iki 120 °C ir išgarinamas metanolis. Mišinio temperatūra keliama iki 300 °C ir maišant kaitinama 1 val.

Nanodalelės išsodinamos ir plaunamos tris kartus pridedant heksano/acetono (1:4) mišinį, centrifuguojant 30 min 8000 rpm. Papildomas plovimas etanolio/acetono (1:1) mišiniu reikalingas natrio chlorido pašalinimui. Gaunami milteliai džiovinami kambario temperatūroje. Atliekant $NaGd_{0,78-x}Mn_xYb_{0,2}Er_{0,02}F_4$ sintezę, reikalingas papildomas pradinių medžiagų gavimo etapas, ištirpinant $MnCO_3$ druskos rūgštyje siekiant gauti mangano (II) chloridą.

$NaGd_{0,78-x}Mn_xYb_{0,2}Er_{0,02}F_4$ arba $NaGd_{0,78-x}Cr_xYb_{0,2}Er_{0,02}F_4$ sintezės buvo atliekamos įterpiant skirtingos koncentracijos Mn^{2+} (x = 0; 0,05; 0,1; 0,15; 0,2; 0,25; 0,5) ar Cr^{3+} (0; 0,05; 0,15; 0,2; 0,5) jonus.

2.2.4. $NaGd_{0,995-x}Yb_xNd_{0,005}F_4$ ir $NaGd_{0,975-x}Yb_xEr_{0.02}Nd_{0,005}F_4$ sintezė

$NaGd_{0,995-x}Yb_xNd_{0,005}F_4$ ir $NaGd_{0,975-x}Yb_xEr_{0.02}Nd_{0,005}F_4$ sintezės buvo atliekamos įterpiant skirtingos koncentracijos Yb^{3+} jonus: x = 0; 0,005; 0,01; 0,05; 0,1; 0,15; 0,2; 0,3; 0,4; 0,5; 0,6; 0,8; 0,995 ir 0; 0,03; 0,15; 0,2; 0,5 (kai papildomai įterpiami Er^{3+} jonai). Sintezių metodikos aprašytos 2.2.1 skyriuje.

2.3. Tyrimų metodikos

2.3.1. Rentgeno spindulių difrakcinė analizė

Susintetintų junginių rentgeno spindulių difrakcinė analizė atlikta Rigaku MiniFlex difraktometru $10° \leq 2\theta \leq 90°$ ruože, naudojant Cu Kα spinduliuotę be Ni filtrą, plyšio plotis 0,02°, skenavimo greitis 5°/min. Gardelės parametrų nustatymui rentgeno spindulių difrakcinė analizė atlikta Bruker D8 Advance difraktometru naudojant Cu Kα spinduliuotę $10° \leq 2\theta \leq 90°$ ruože su Bragg-Brentano geometrija ir LynxEYE detektoriumi. Plyšio plotis 0,001°, integravimo laikas 0,3 s. Gardelės parametrai skaičiuojami programa TOPAS naudojant Le Bail metodą (skaičiavimo paklaida ±0,0002).

2.3.2. Elementinė analizė

Junginiai mineralizuojami naudojant mikrobangę Anton Paar Multiwave 3000 sistemą (XF100 rotorius tefloniniai indeliai) koncentruotoje azoto rūgštyje. Gauti tirpalai buvo analizuojami induktyviai susietos plazmos optinės emisijos spektrometrijos (ICP-OES) metodu Perkin Elmer Optima 7000 DV spektrometru.

2.3.3. Skenuojanti elektroninė mikroskopija

Junginių skenuojančios elektroninės mikroskopijos vaizdai gauti FE-SEM Hitachi SU-70 skenuojančiu elektroniniu mikroskopu. Mėginiai paruošiami padengiant 0,5 % nanodalelių dispersijas toluene ant silicio padėklo.

2.3.4. Peršviečiamoji elektroninė mikroskopija

Junginių peršviečiamosios elektroninės mikroskopijos vaizdai gauti Tecnai G2 F20 X-TWIN mikroskopu. Šotki tipo lauko emisijos elektronų šaltinis su HAADF detektoriumi ir 11MPix ORIUS SC1000B (Gatan) CCD kamera. Mėginiai paruošiami padengiant 0,5 % nanodalelių dispersijas toluene ant varinio tinklelio.

2.3.5. Furjė transformacijos infraraudonųjų spindulių spektroskopija

Furjė transformacijos infraraudonųjų spindulių spektroskopijos tyrimai atliekami Bruker Alfa ATR spektrometru, 4000 – 400 cm^{-1} ruože atliekant 24 skenavimus.

2.3.6. Liuminescencinės savybės

Apkonversijos liuminescencijos spektrai NIR ir VIS ruožuose registruojami Edinburgh Instruments FLS980 spektrometru su Czerny-Turner emisijos monochromatoriumi ir Hamamatsu R928P fotodaugintuvu. Junginiai buvo tiriami paruošiant 8,8 ml/2 mL dispersijas toluene pastoviai maišant. Žadinimo šaltiniai – 980 nm ir 808 nm nuolatinės veiklos lazeriai. Plyšio plotis ir žingsnis – 0,5 nm, integravimo laikas – 0,4 s.

2.3.7. Liuminescencijos gyvavimo trukmių matavimai

Apkonversijos liuminescencijos gyvavimo trukmių matavimai atliekami Edinburgh Instruments FLS980 spektrometru žadinimui naudojant 980 nm lazerio impulsą. Lazerio dažnis – 100 Hz, emisija tiriama 407, 539 ir 653 nmm bangos ilgiuose. Žadinant 808 nm lazerio (dažnis 50 Hz) impulsu, emisija tiriama 864 nm bangos ilgyje. Duomenys buvo naudojami skaičiuojant gyvavimo trukmes pagal formulę:

$$I(t) = B + A_1 e^{(-t/\tau_1)} + A_2 e^{(-t/\tau_2)} \quad (1)$$

kur *I(t)* liuminescencijos intensyvumas tam tikru laiku *t*; A_1, A_2, *B* – konstantos; τ_1 τ_2 – emisijos gyvavimo trukmės. Vidutinės gyvavimo trukmės skaičiuojamos pagal formulę:

$$\bar{\tau} = \frac{A_1 \times \tau_1^2 + A_2 \times \tau_2^2}{A_1 \times \tau_1 + A_2 \times \tau_2} \quad (2)$$

kur A_1, A_2 yra konstantos, τ_1 τ_2 – emisijos gyvavimo trukmės.

2.3.8. Nuo temperatūros priklausančios liuminescencijos matavimai

Nuo temperatūros priklausančios apkonversijos liuminescencijos spektrai registruojami Edinburgh Instruments FLS980 spektrometru su kriostatu MicrostatN. Mėginio laikiklis šaldomas skystu azotu. Temperatūros stabilizavimo laikas – 90 s, tolerancijos intervalas – ±5 K. matavimai atliekami 77 K temperatūroje ir 100 – 500 K intervale didinant temperatūrą kas 50 K.

Skirtumas tarp termiškai susietų energetinių lygmenų (ΔE) skaičiuojamas pagal formulę:

$$FIR = \frac{I_2}{I_1} = Ce^{(-\Delta E/k_B T)} \quad (3)$$

kur I_2 ir I_1 yra aukštesniojo ir žemesniojo lygmens liuminescencijos intensyvumai, *C* – konstanta, ΔE – skirtumas tarp termiškai susietų lygmenų, k_B – Boltzmano konstanta ($8{,}617342 \times 10^{-5}$ eV/K), T – absoliuti temperatūra.

Santykinis šiluminis jautrumas (S_r) skaičiuojamas pagal formulę:

$$S_r = \frac{E}{k_B T^2} \quad (4)$$

3. REZULTATAI IR JŲ APTARIMAS

Disertacijos santraukoje pateikiami pagrindiniai rezultatai, kurie detaliau analizuojami disertacijoje. Nagrinėjama į apkonvertuojančias medžiagas įterpiamų jonų įtaka liuminescencinėms savybėms tiriant 2.3 skyriuje paminėtomis tyrimų metodikomis terminio skaidymo būdu susintetintas medžiagas. Apžvelgiama į skirtingų joninių spindulių dydžių Li^+, K^+, Mn^{2+}, Cr^{3+} jonų įtaką NaY/GdF_4 apkonvertuojančų medžiagų savybėms bei Yb^{3+} koncentracijos įtaką $Nd^{3+} \rightarrow Yb^{3+}$ energijos pernašos efektyvumui.

3.1. $Na_{1-x}Li_xGd_{0,78}Yb_{0,2}Er_{0,02}F_4$ ir $Na_{1-x}K_xGd_{0,78}Yb_{0,2}Er_{0,02}F_4$ analizė

Susintetintų ir išgrynintų $Na_{1-x}Li_xGd_{0.78}Yb_{0.2}Er_{0.02}F_4$ junginių rentgeno spindulių difraktogramose (3.1 pav. A) matoma, jog vienfaziai heksagoninės struktūros junginiai susiformavo esant nedidelei Li^+ koncentracijai (iki $x = 0,3$). Didinant mažesnio joninio spindulio ličio jonų kiekį (lyginant su Na^+) nuo $x = 0,5$ stebimas kubinės $NaGdF_4$ ir GdF_3 fazių susidarymas.

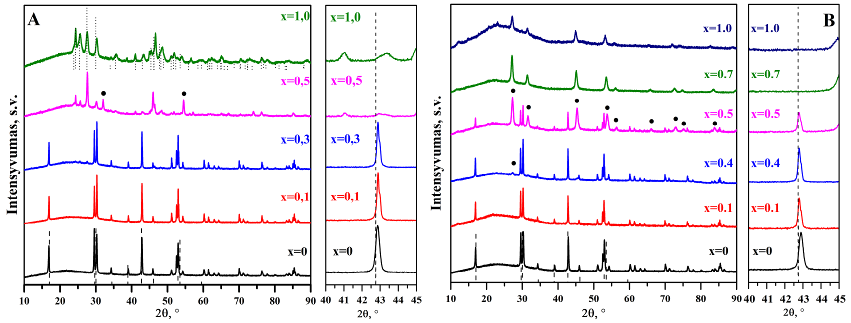

3.1 pav. A) $Na_{1-x}Li_xGd_{0.78}Yb_{0.2}Er_{0.02}F_4$ junginių ($x = 0$; 0,1; 0,3; 0,5; 1,0) ir B) $Na_{1-x}K_xGd_{0.78}Yb_{0.2}Er_{0.02}F_4$ junginių ($x = 0$; 0,1; 0,4; 0,5; 0,7; 1,0) rentgeno spindulių difraktogramos. $NaGdF_4$ standartas (PDF#(ICDD) 00-027-0699, punktyrinė linija) ir GdF_3 (PDF#(ICDD) 00-049-1804). Kubinės fazės priemaišos pažymėtos ●.

Ištyrus susintetintus $Na_{1-x}K_xGd_{0.78}Yb_{0.2}Er_{0.02}F_4$ junginius rentgeno spindulių difrakcine analize, 3.1 pav. B matome, jog gauti junginiai yra heksagoninės struktūros, tačiau kubinės fazės $NaGdF_4$ smailė yra stebima ties $x = 0,4$ koncentracija. Didinant kalio jonų kiekį gaunamas kubinės ir heksagoninės struktūros mišinys iki x = 0,7, kai susiformuoja vienfazis kubinės struktūros junginys. Sėkmingas didesnio joninio spindulio (lyginant su Na^+) K^+ įterpimas matomas iš disertacijoje pateiktų gardelės parametrų skaičiavimo duomenų. Stebimas a_h ir c_h parametrų didėjimas didinant įterpiamų K^+ jonų koncentraciją. Susiformavus vienfaziam kubinės $NaGdF_4$ struktūros junginiui (x = 0,7) matomas a_c parametro didėjimas.

Terminio skaidymo sintezės metu gaunami $NaGdF_4$ junginiai, nepriklausomai nuo įterpiamų jonų, yra su organiniu oleino rūgšties apvalkalu. Oleino rūgšties molekulės adsorbuojasi ant paviršiaus sudarydamos ryšius su lantanoidais per COO^- grupę. Adsorbcija patvirtinta atlikus FTIR spektroskopijos matavimus (3.2 pav.).

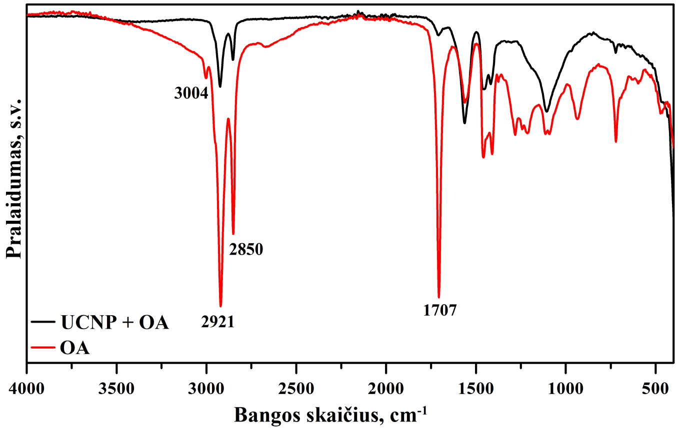

3.2 pav. FTIR spektrai: oleino rūgšties (raudona linija), $NaGd_{0.78}Yb_{0.2}Er_{0.02}F_4$ su oleino rūgšties apvalkalu (juoda linija).

Iš 3.2 pav. pateiktų FTIR spektrų matomas sumažėjęs santykinis C=O grupės intensyvumas ties 1707 cm^{-1} $NaGd_{0.78}Yb_{0.2}Er_{0.02}F_4$ junginyje su oleino rūgšties apvalkalu.

$Na_{1-x}Li_xGd_{0.78}Yb_{0.2}Er_{0.02}F_4$ ir $Na_{1-x}K_xGd_{0.78}Yb_{0.2}Er_{0.02}F_4$ junginių apkonvertuojančios savybės tiriamos žadinant 980 nm nuolatinės veiklos lazeriu. Visos 3.3 pav. identifikuotos emisijos juostos priskiriamos Er^{3+} jonams būdingai emisijai: $^4G_{11/2}\rightarrow{}^4I_{15/2}$ (380 nm), $^2H_{9/2}\rightarrow{}^4I_{15/2}$ (407 nm), $^4F_{7/2}\rightarrow{}^4I_{15/2}$ (silpnas, 502 nm), $^2H_{11/2}\rightarrow{}^4I_{15/2}$ (515 – 535 nm), $^4S_{3/2}\rightarrow{}^4I_{15/2}$ (535 – 565 nm), $^4F_{9/2}\rightarrow{}^4I_{15/2}$ (635 – 680 nm), $^2H_{9/2}\rightarrow{}^4I_{11/2}$ (695 nm). Geresnei rezultatų interpretacijai, emisijos juostos normuojamos pagal 539 nm emisijos intensyvumą.

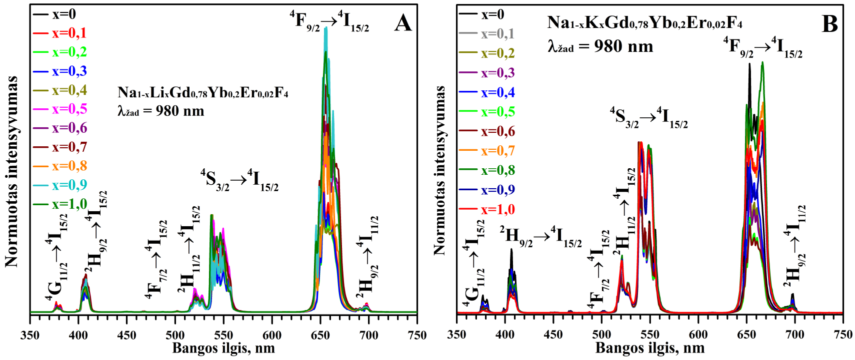

3.3 pav. Apkonversijos emisijos spektrai esant skirtingiems įterpiamų Li^+ ir K^+ jonų kiekiams: A) $Na_{1-x}Li_xGd_{0,78}Yb_{0,2}Er_{0,02}F_4$, B) $Na_{1-x}K_xGd_{0,78}Yb_{0,2}Er_{0,02}F_4$. Žadinimo bangos ilgis $\lambda_{žad}$ = 980 nm.

Keičiant Li^+ ir K^+ jonų kiekį $NaGd_{0,78}Yb_{0,2}Er_{0,02}F_4$ junginiuose, stebimas emisijos juostų intensyvumų pokytis. Lyginant raudonosios ($^4F_{9/2}\rightarrow{}^4I_{15/2}$) bei žaliosios ($^2H_{11/2}$, $^4S_{3/2}\rightarrow{}^4I_{15/2}$) emisijos juostų santykį pastebimas nežymus padidėjimas, kol junginiai buvo heksagoninės struktūros (3.4 pav.). Esant dviejų fazių mišiniui ir Li^+ jonų koncentracijai $x = 0,9$ – stebimas 2 kartus padidėjęs R/Ž santykis, lyginant su $x = 0$. Tačiau Li^+ koncentracijai esant $x = 0,8$, susiformuoja GdF_3 junginys ir matomas R/Ž santykio sumažėjimas. K^+ jonų įterpimas sumažino R/Ž santykį nuo 1,7 iki 1,0. Didinant K^+ koncentraciją stebimas R/Ž juostų santykio padidėjimas beveik iki pradinės 1,7 vertės.

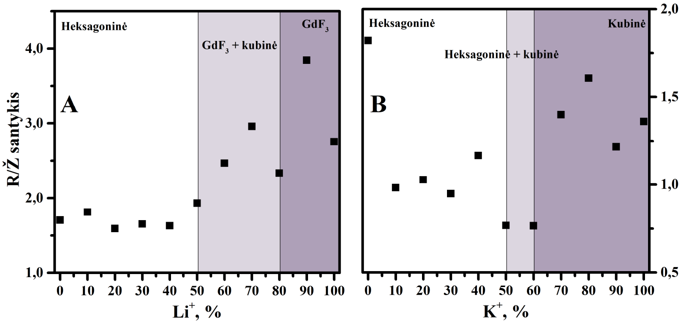

3.4 pav. R/Ž ($^4F_{9/2}\rightarrow{}^4I_{15/2}$ (635 – 680 nm)) ($^2H_{11/2}$, $^4S_{3/2}\rightarrow{}^4I_{15/2}$ (515 – 565 nm)) emisijos juostų santykio priklausomybė nuo Li^+ (A) ir K^+ (B) koncentracijos.

Liuminescencijos gyvavimo trukmės matavimai atliekami žadinant 980 nm lazerio impulsu $Na_{1-x}Li_xGd_{0,78}Yb_{0,2}Er_{0,02}F_4$ bei $Na_{1-x}K_xGd_{0,78}Yb_{0,2}Er_{0,02}F_4$ junginius ir registruojant emisiją 407 nm, 539 nm ir 635 nm bangos ilgiuose. Iš eksperimentinių duomenų paskaičiuotos gyvavimo trukmės (1 formulė). Vidutinės gyvavimo trukmės junginiams su įterptais Li$^+$ jonais paskaičiuotos naudojantis (2) formule ir pavaizduotos grafiškai 3.5 paveiksle.

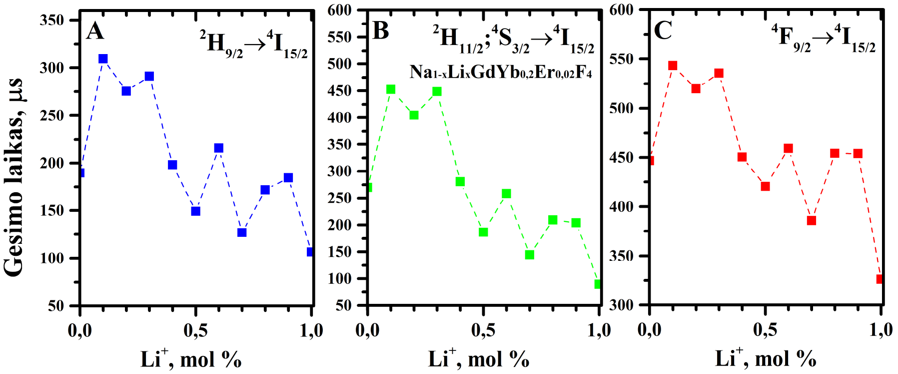

3.5 pav. Na$_{1-x}$Li$_x$Gd$_{0,78}$Yb$_{0,2}$Er$_{0,02}$F$_4$ vidutinių gyvavimo trukmių priklausomybė nuo Li$^+$ koncentracijos: A) $^2H_{9/2}\rightarrow{}^4I_{15/2}$, B) $^2H_{11/2};{}^4S_{3/2}\rightarrow{}^4I_{15/2}$, C) $^4F_{9/2}\rightarrow{}^4I_{15/2}$.

Vidutinių gyvavimo trukmių mažėjimo tendencija stebima nepriklausomai nuo susidariusių junginių kristalinės fazės. Vidutinių gyvavimo trukmių padidėjimas stebimas kai ličio jonų koncentracija $x = 0,6$. Iš 3.5 paveiksle pateiktų duomenų matoma, jog $^2H_{9/2}\rightarrow{}^4I_{15/2}$ bei $^2H_{11/2};{}^4S_{3/2}\rightarrow{}^4I_{15/2}$ energijos pernašos emisijos gesimo trukmių mažėjimas yra spartesnis, lyginant su $^4F_{9/2}\rightarrow{}^4I_{15/2}$.

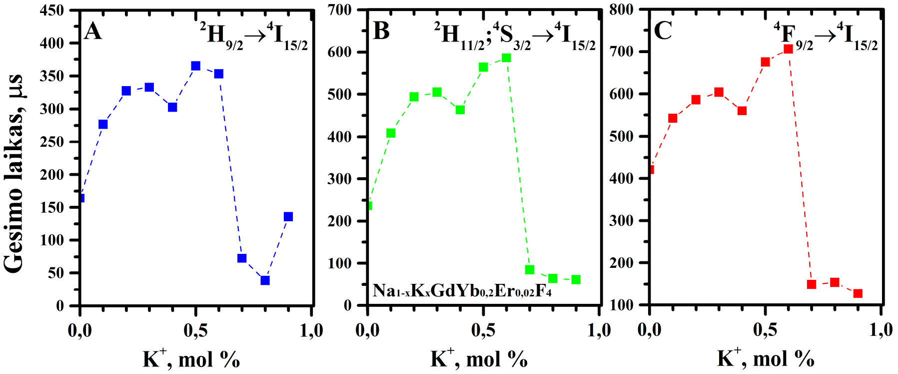

3.6 pav. Na$_{1-x}$K$_x$Gd$_{0,78}$Yb$_{0,2}$Er$_{0,02}$F$_4$ vidutinių gyvavimo trukmių priklausomybė nuo K$^+$ koncentracijos: A) $^2H_{9/2}\rightarrow{}^4I_{15/2}$, B) $^2H_{11/2};{}^4S_{3/2}\rightarrow{}^4I_{15/2}$, C) $^4F_{9/2}\rightarrow{}^4I_{15/2}$.

Iš 3.6 paveiksle pateiktų duomenų matoma, jog vidutinių gyvavimo trukmių didėjimo tendencija stebima esant nedidelėms K^+ jonų koncentracijoms (iki $x = 0,6$). Vidutinių gyvavimo trukmių sumažėjimas stebimas nuo $x = 0,7$, kai iš XRD duomenų matoma, jog nebesusiformuoja heksagoninė fazė.

Apkonversijos procesų mechanizmai yra sudėtingi, ypač kai sintezės metu susiformuoja kelių skirtingų fazių junginiai. Tačiau įterpti ličio ir kalio jonai keičia R/Ž juostų santykį $NaGd_{0,78}Yb_{0,2}Er_{0,02}F_4$ junginiuose.

3.2. $NaY_{0,78-x}Mn_xYb_{0,2}Er_{0,02}F_4$ analizė

Susintetintų ir išgrynintų $NaY_{0,78-x}Mn_xYb_{0,2}Er_{0,02}F_4$ junginių rentgeno spindulių difraktogramose (3.7 pav. A) matoma, jog vienfaziai kubinės struktūros junginiai susiformavo Mn^{2+} koncentracijai esant $x = 0$; 0,05; 0,1; 0,2; 0,5. Tačiau mangano (II) koncentracijai esant $x = 0,78$, matomas papildomos $NaMnF_3$ fazės (PDF#(ICDD) 00-018-1224) susidarymas. Sėkmingas mažesnio spindulio Mn^{2+} jonų (KS = 6, r = 0,81 Å) įterpimas vietoje didesnių Y^{3+} jonų (KS = 6, r = 0,89 Å) matomas 3.7 pav. B iš 2θ laipsnių poslinkio.

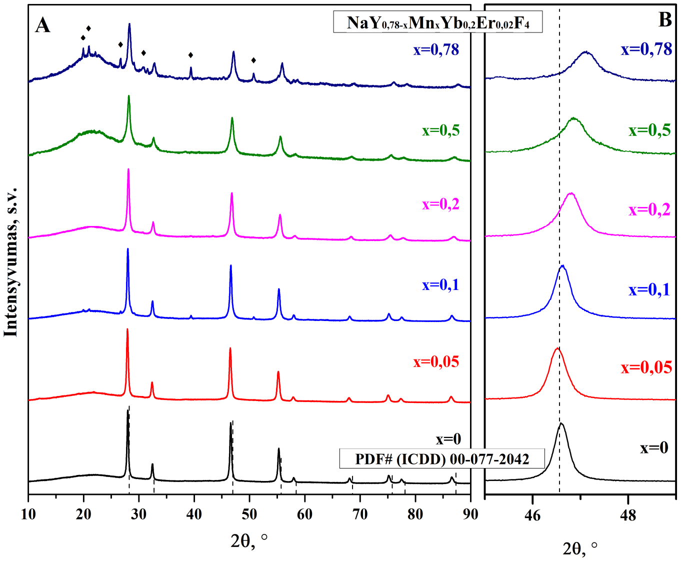

3.7 pav. $NaY_{0,78-x}Mn_xYb_{0,2}Er_{0,02}F_4$ junginių (x = 0; 0,05; 0,1; 0,2; 0,5; 0,78) rentgeno spindulių difraktogramos. $NaGdF_4$ standartas (PDF#(ICDD) 00-077-2042) žymimas punktyrine linija. $NaMnF_3$ (PDF#(ICDD) 00-018-1224) priemaišos pažymėtos ♦.

$NaY_{0,78-x}Mn_xYb_{0,2}Er_{0,02}F_4$ junginių koncentracija nustatyta induktyviai susietos plazmos optinės emisijos spektrometrijos (ICP-OES) metodu. Gauti rezultatai pateikiami disertacijoje, kur matoma, jog tiriamų Y^{3+}, Mn^{2+}, Yb^{3+} ir Er^{3+} jonų koncentracija susintetintuose junginiuose koreliuoja su teoriniais skaičiavimais. Gautų $NaY_{0,78-x}Mn_xYb_{0,2}Er_{0,02}F_4$ junginių morfologija tiriama SEM analize. Iš vaizdų, pateiktų 3.8 paveiksle matoma, jog susiformuoja sferinės formos ~50 nm nanodalelės. Mn^{2+} koncentracijai padidėjus iki x = 0,5 (3.8 pav. d), vidutinis dalelių dydis sumažėja iki 27 nm.

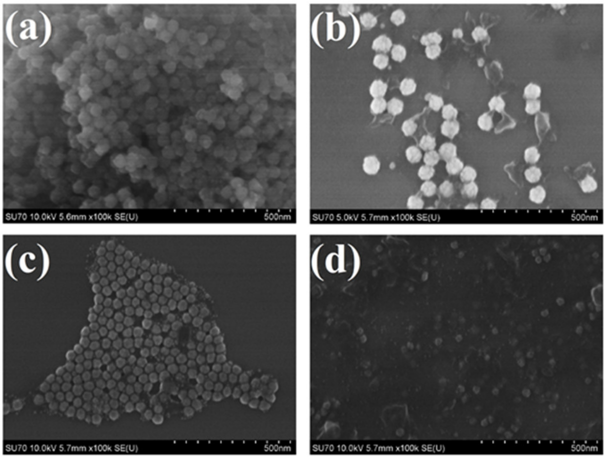

3.8 pav. $NaY_{0,78-x}Mn_xYb_{0,2}Er_{0,02}F_4$ junginių SEM vaizdai:
(a) x = 0, (b) x = 0,05, (c) x = 0,1, (d) x = 0,5.

$NaY_{0,78-x}Mn_xYb_{0,2}Er_{0,02}F_4$ junginių apkonvertuojančios savybės tiriamos žadinant 980 nm nuolatinės veiklos lazeriu. Visos 3.9 pav. identifikuotos emisijos juostos priskiriamos Er^{3+} jonams būdingai emisijai: $^4G_{11/2}\rightarrow{}^4I_{15/2}$ (380 nm), $^2H_{9/2}\rightarrow{}^4I_{15/2}$ (407 nm), $^2H_{11/2}\rightarrow{}^4I_{15/2}$ (515 – 535 nm), $^4S_{3/2}\rightarrow{}^4I_{15/2}$ (535 – 565 nm), $^4F_{9/2}\rightarrow{}^4I_{15/2}$ (635 – 680 nm), $^2H_{9/2}\rightarrow{}^4I_{11/2}$ (695 nm). Geresnei rezultatų interpretacijai, emisijos juostos normuojamos pagal 669 nm emisijos intensyvumą. Mn^{2+} jonų įterpimas į $NaYF_4$ matricą suteikia papildomų energijos lygmenų, galinčių dalyvauti energijos pernašos procesuose ir keisti apkonversijos liuminescencijos savybes.

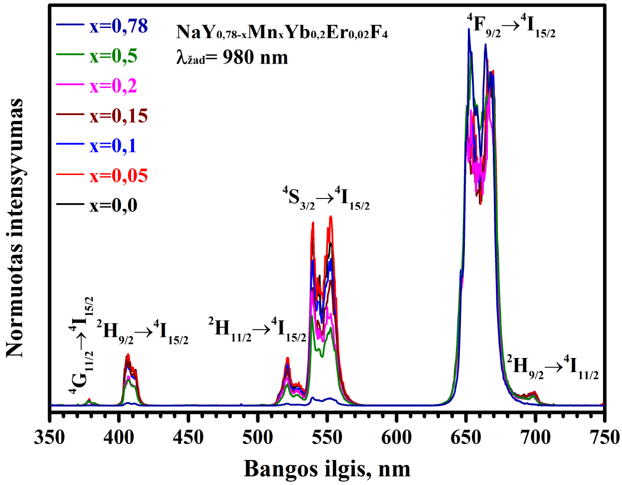

3.9 pav. $NaY_{0,78\text{-}x}Mn_xYb_{0,2}Er_{0,02}F_4$ apkonversijos emisijos spektrai esant skirtingam įterpiamų Mn^{2+} jonų kiekiui. Žadinimo bangos ilgis $\lambda_{žad} = 980$ nm.

Iš 3.9 paveiksle esančių spektrų matomas žaliosios emisijos juostos ($^2H_{11/2}$;$^4S_{3/2}$→$^4I_{15/2}$) intensyvumo sumažėjimas didėjant Mn^{2+} koncentracijai. Taip pat R/Ž emisijos juostų ($^4F_{9/2}$→$^4I_{15/2}$ (625 – 708 nm)), ($^2H_{11/2}$, $^4S_{3/2}$→$^4I_{15/2}$ (509 – 574 nm)) santykio pokytis matomas, kai $x = 0,5$ ir $x = 0,78$ (3.10 pav.). Nespindulinė energijos pernaša tarp $^2H_{11/2}$ bei $^4S_{3/2}$ (Er^{3+}) ir $^4T_1$ (Mn^{2+}) lygmenų ir sekanti tolimesnė energijos perdava atgal į $^4F_{9/2}$ (Er^{3+}), padidina raudonosios srities emisijos intensyvumą. Dėl šios priežasties $NaY_{0,78\text{-}x}Mn_xYb_{0,2}Er_{0,02}F_4$ junginių emisijos spalva CIE 1931 koordinačių plokštumoje iš geltonos tampa beveik grynos raudonos spalvos.

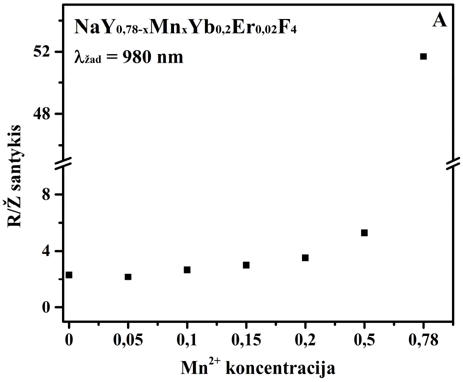

3.10 pav. $NaY_{0,78\text{-}x}Mn_xYb_{0,2}Er_{0,02}F_4$ R/Ž emisijos juostų ($^4F_{9/2}$→$^4I_{15/2}$/$^2H_{11/2}$, $^4S_{3/2}$→$^4I_{15/2}$) santykio priklausomybė nuo Mn^{2+} koncentracijos.

Liuminescencijos gyvavimo trukmės matavimai atliekami žadinant 980 nm lazerio impulsu $NaY_{0,78-x}Mn_xYb_{0,2}Er_{0,02}F_4$ junginius ir registruojant emisiją 407 nm, 539 nm ir 635 nm bangos ilgiuose. Iš eksperimentinių duomenų paskaičiuotos gyvavimo trukmės (1 formulė). Vidutinės gyvavimo trukmės junginiams su įterptais Mn^{2+} jonais paskaičiuotos naudojantis (2) formule ir pavaizduotos grafiškai 3.11 paveiksle.

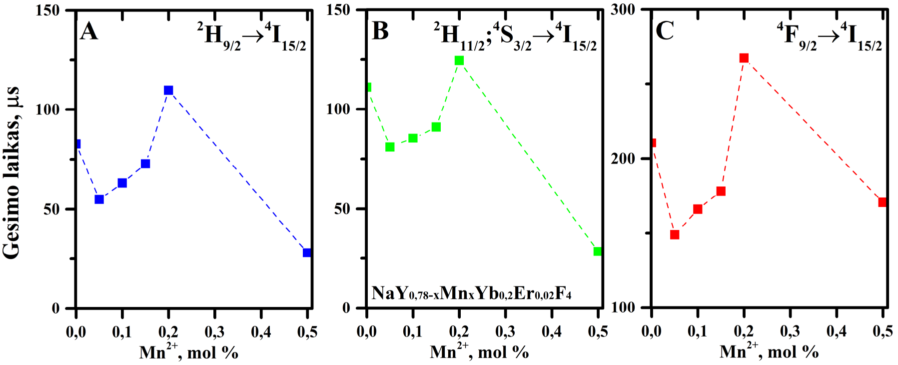

3.11 pav. $NaY_{0,78-x}Mn_xYb_{0,2}Er_{0,02}F_4$ vidutinių gyvavimo trukmių priklausomybė nuo Mn^{2+} koncentracijos: A) $^2H_{9/2}\rightarrow{}^4I_{15/2}$, B) $^2H_{11/2};{}^4S_{3/2}\rightarrow{}^4I_{15/2}$, C) $^4F_{9/2}\rightarrow{}^4I_{15/2}$.

Iš 3.11 paveiksle pateiktų duomenų matoma, jog vidutinių gyvavimo trukmių sumažėjimas stebimas esant Mn^{2+} jonų koncentracijai $x = 0,05$. Tačiau didinant Mn^{2+} koncentraciją matomas vidutinių gyvavimo trukmių padidėjimas iki $x = 0,2$. Tolimesnis Mn^{2+} jonų koncentracijos didinimas iki $x = 0,5$ vidutinių gyvavimo trukmių vertes sumažino. Remiantis šiais duomenimis, optimali Mn^{2+} jonų koncentracija prailginanti gyvavimo trukmes $NaY_{0,78-x}Mn_xYb_{0,2}Er_{0,02}F_4$ junginiuose stebėtuose emisijos bangos ilgiuose yra $x = 0,2$.

3.3. $NaGd_{0,78-x}Mn_xYb_{0,2}Er_{0,02}F_4$ analizė

Susintetintų ir išgrynintų $NaGd_{0,78-x}Mn_xYb_{0,2}Er_{0,02}F_4$ junginių rentgeno spindulių difraktogramose (3.12 pav. A) matoma, jog vienfaziai heksagoninės (P63/m) struktūros junginiai susiformavo Mn^{2+} koncentracijai esant $x = 0$; 0,05; 0,1; 0,15; 0,2; 0,25; 0,5. Sėkmingas mažesnio spindulio Mn^{2+} jonų (KS = 6, r = 0,81 Å) įterpimas vietoje didesnių Gd^{3+} jonų (KS = 9, r = 1,107 Å) matomas iš (201) smailės poslinkio (3.12 pav. B).

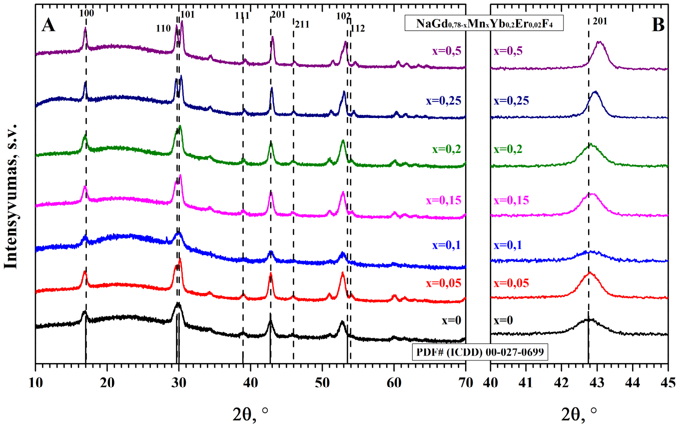

3.12 pav. $NaGd_{0,78-x}Mn_xYb_{0,2}Er_{0,02}F_4$ junginių (x = 0; 0,05; 0,1; 0,15; 0,2; 0,25; 0,5) rentgeno spindulių difraktogramos. $NaGdF_4$ standartas (PDF#(ICDD) 00-027-0699) žymimas punktyrine linija.

$NaGd_{0,78-x}Mn_xYb_{0,2}Er_{0,02}F_4$ junginių apkonvertuojančios savybės tiriamos žadinant 980 nm nuolatinės veiklos lazeriu. Visos 3.13 pav. identifikuotos emisijos juostos priskiriamos Er^{3+} jonams būdingai emisijai. Geresnei rezultatų interpretacijai, emisijos juostos normuojamos pagal 539 nm emisijos intensyvumą. Mn^{2+} jonų įterpimas į $NaGdF_4$ matricą suteikia papildomų energijos lygmenų, galinčių dalyvauti energijos pernašos procesuose ir keisti apkonversijos liuminescencijos savybes.

Iš 3.13 paveiksle esančių spektrų matomas žaliosios emisijos juostos ($^2H_{11/2}$;$^4S_{3/2}$→$^4I_{15/2}$) intensyvumo sumažėjimas didėjant Mn^{2+} koncentracijai. Taip pat R/Ž emisijos juostų ($^4F_{9/2}$→$^4I_{15/2}$ (625 – 708 nm)), ($^2H_{11/2}$, $^4S_{3/2}$→$^4I_{15/2}$ (509 – 574 nm)) santykio vertės yra 1,9 ir 3,7, kai x = 0,25 ir x = 0,5 (3.13 pav.). Nespindulinė energijos pernaša tarp $^2H_{11/2}$ bei $^4S_{3/2}$ (Er^{3+}) ir $^4T_1$ (Mn^{2+}) lygmenų ir sekanti tolimesnė energijos perdava atgal į $^4F_{9/2}$ (Er^{3+}), padidina raudonosios srities emisijos intensyvumą. Kai Mn^{2+} koncentracija yra x = 0,5, R/Ž santykis padidėja 6,4 karto lyginant su $NaGd_{0,78}Yb_{0,2}Er_{0,02}F_4$ junginio emisija. Apkonversijos liuminescencinės savybės yra paveiktos įterpiamų Mn^{2+} jonų koncentracija bei stebimas emisijos poslinkis į raudonąją regimojo spektro dalį.

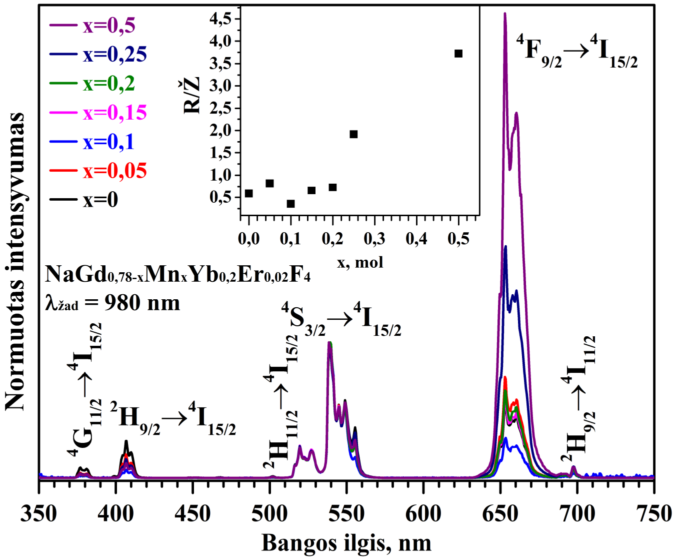

3.13 pav. $NaGd_{0,78-x}Mn_xYb_{0,2}Er_{0,02}F_4$ apkonversijos emisijos spektrai esant skirtingam įterpiamų Mn^{2+} jonų kiekiui. Žadinimo bangos ilgis $\lambda_{žad}$ = 980 nm.

Liuminescencijos gyvavimo trukmės matavimai atliekami žadinant 980 nm lazerio impulsu $NaGd_{0,78-x}Mn_xYb_{0,2}Er_{0,02}F_4$ junginius ir registruojant emisiją 407 nm, 539 nm ir 635 nm bangos ilgiuose. Iš eksperimentinių duomenų paskaičiuotos gyvavimo trukmės (1 formulė). Vidutinės gyvavimo trukmės junginiams su įterptais Mn^{2+} jonais paskaičiuotos naudojantis (2) formule ir pavaizduotos grafiškai 3.14 paveiksle.

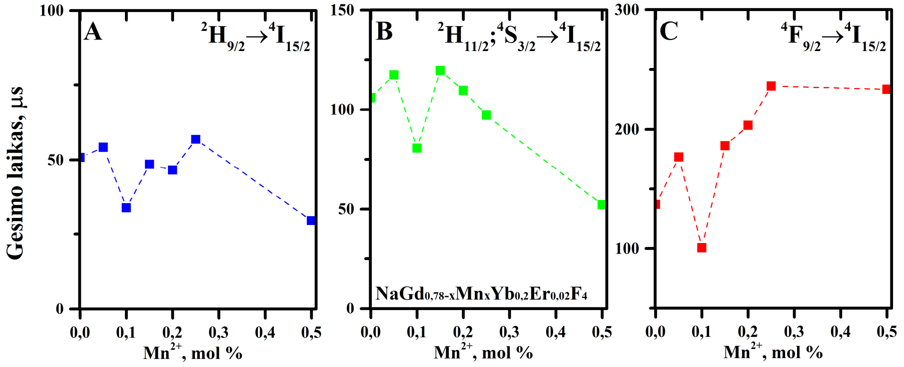

3.14 pav. $NaGd_{0,78-x}Mn_xYb_{0,2}Er_{0,02}F_4$ vidutinių gyvavimo trukmių priklausomybė nuo Mn^{2+} koncentracijos: A) $^2H_{9/2}\rightarrow{}^4I_{15/2}$, B) $^2H_{11/2};{}^4S_{3/2}\rightarrow{}^4I_{15/2}$, C) $^4F_{9/2}\rightarrow{}^4I_{15/2}$.

Iš 3.14 paveiksle pateiktų duomenų matoma, jog vidutinių gyvavimo trukmių sumažėjimas stebimas esant $\mathrm{Mn^{2+}}$ jonų koncentracijai x = 0,1. Tačiau didinant $\mathrm{Mn^{2+}}$ koncentraciją matomas mėlynosios (3.14 pav. A) bei raudonosios (3.14 pav. C) sričių vidutinių gyvavimo trukmių padidėjimas iki x = 0,25. Tolimesnis $\mathrm{Mn^{2+}}$ jonų koncentracijos didinimas iki x = 0,5 vidutinių gyvavimo trukmių vertes sumažino. Tačiau raudonosios srities (3.14 pav. C) gesimo trukmės išliko panašios, lyginant su x = 0,25 ir yra ~233 µs. Remiantis šiais duomenimis, optimali $\mathrm{Mn^{2+}}$ jonų koncentracija prailginanti gyvavimo trukmes $\mathrm{NaGd_{0,78-x}Mn_xYb_{0,2}Er_{0,02}F_4}$ junginiuose stebėtuose emisijos bangos ilgiuose yra x = 0,25. Papildomi energijos pernašos keliai, kurie atsiranda įterpus $\mathrm{Mn^{2+}}$ jonų yra naudingi norint pakeisti emisijos juostų santykį.

3.4. $\mathrm{NaGd_{0,78-x}Cr_xYb_{0,2}Er_{0,02}F_4}$ analizė

Susintetintų ir išgrynintų $\mathrm{NaGd_{0,78-x}Cr_xYb_{0,2}Er_{0,02}F_4}$ junginių rentgeno spindulių difraktogramose (3.15 pav. A) matoma, jog vienfaziai heksagoninės (P63/m) struktūros junginiai susiformavo $\mathrm{Cr^{3+}}$ koncentracijai esant x = 0; 0,05; 0,15; 0,2; 0,5. Sėkmingas mažesnio spindulio $\mathrm{Mn^{2+}}$ jonų (KS = 6, r = 0,62 Å) įterpimas vietoje didesnių $\mathrm{Gd^{3+}}$ jonų (KS = 9, r = 1,107 Å) matomas iš (201) smailės poslinkio (3.15 pav. B).

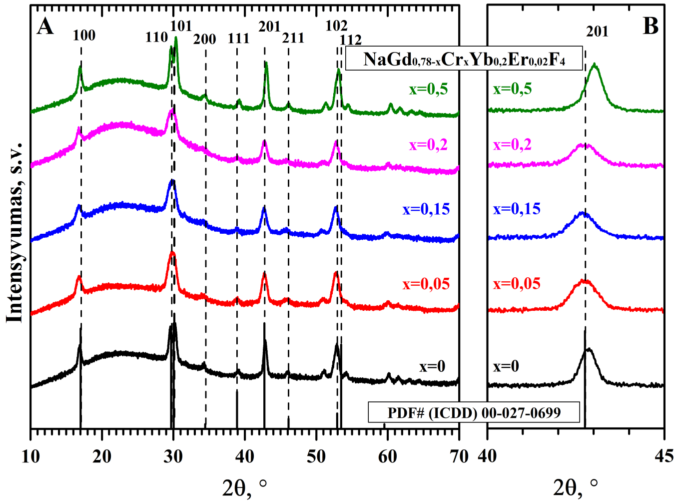

3.15 pav. $\mathrm{NaGd_{0,78-x}Cr_xYb_{0,2}Er_{0,02}F_4}$ junginių (x = 0; 0,05; 0,15; 0,2; 0,5) rentgeno spindulių difraktogramos. $\mathrm{NaGdF_4}$ standartas (PDF#(ICDD) 00-027-0699) žymimas punktyrine linija.

$NaGd_{0,78-x}Cr_xYb_{0,2}Er_{0,02}F_4$ junginių koncentracija nustatyta induktyviai susietos plazmos optinės emisijos spektrometrijos (ICP-OES) metodu. Gauti rezultatai pateikiami disertacijoje, kur matoma, jog tiriamų Gd^{3+}, Cr^{2+}, Yb^{3+} ir Er^{3+} jonų koncentracija skiriasi nuo teorinių verčių. Gd^{3+} jonų kiekis susintetintuose junginiuose yra didesnis, nei teorinių skaičiavimų rezultatai, o Cr^{3+} – mažesnis. Panašūs rezultatai taip pat aptariami ir literatūros šaltiniuose.

Gautų $NaGd_{0,78-x}Cr_xYb_{0,2}Er_{0,02}F_4$ junginių morfologija tiriama TEM analize. Iš vaizdų, pateiktų 3.16 paveiksle matoma, jog visose Cr^{3+} koncentracijose susiformuoja sferinės formos nanodalelės. $NaGd_{0,78-x}Cr_xYb_{0,2}Er_{0,02}F_4$ junginiai pasižymi aukštu kristališkumu, matomu iš 3.16 pav. b) esančių plokštumų.

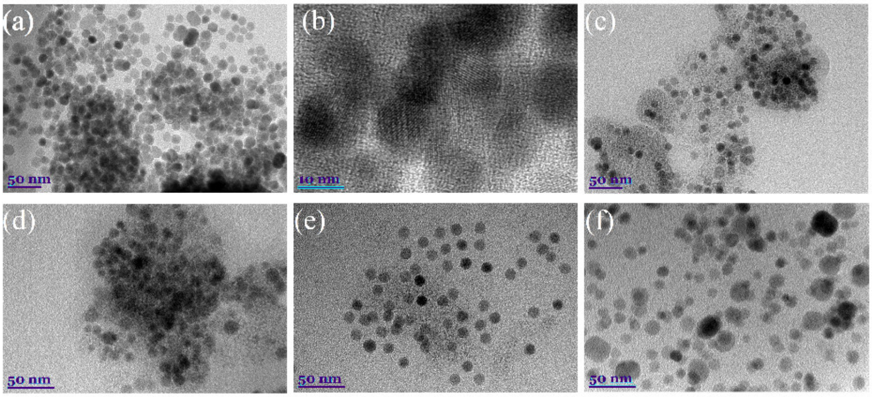

3.16 pav. $NaGd_{0,78-x}Cr_xYb_{0,2}Er_{0,02}F_4$ nanodalelių TEM vaizdai: (a) ir (b) x = 0, (c) x = 0,05, (d) x = 0,15, (e) x = 0,2, (f) x = 0,5.

3.1 lentelė. $NaGd_{0.78-x}Cr_xYb_{0.2}Er_{0.02}F_4$ vidutiniai dalelių dydžiai, esant skirtingai Cr^{3+} koncentracijai.

x	d, nm
0	11,4±2,4
0,05	10,4±1,6
0,15	9,0±2,5
0,2	10,6±1,2
0,5	10,0±2,3 ir 16,9±6,0

Paskaičiuoti vidutiniai dalelių dydžiai (3.1 lentelė) yra panašūs visuose susintetintuose $NaGd_{0,78-x}Cr_xYb_{0,2}Er_{0,02}F_4$ su skirtingomis Cr^{3+} jonų koncentracijomis. Tačiau, esant didesnei Cr^{3+} koncentracijai (x = 0,5), matomos susidariusios dviejų skirtingų vidutinių dydžių dalelės: 10,0 nm ir

16,9 nm. Iš rentgeno difrakcinės analizės duomenų nebuvo pastebėtas pašalinės fazės susidarymas, tad šios skirtingų dydžių nanodalelės yra heksagoninės struktūros.

$NaGd_{0,78-x}Cr_xYb_{0,2}Er_{0,02}F_4$ junginių apkonvertuojančios savybės tiriamos žadinant 980 nm nuolatinės veiklos lazeriu. Visos 3.17 pav. identifikuotos emisijos juostos priskiriamos Er^{3+} jonams būdingai emisijai. Geresnei rezultatų interpretacijai, emisijos juostos normuojamos pagal 539 nm emisijos intensyvumą. Cr^{3+} jonų įterpimas į $NaGdF_4$ matricą suteikia papildomų energijos lygmenų, galinčių dalyvauti energijos pernašos procesuose ir keisti apkonversijos liuminescencijos savybes.

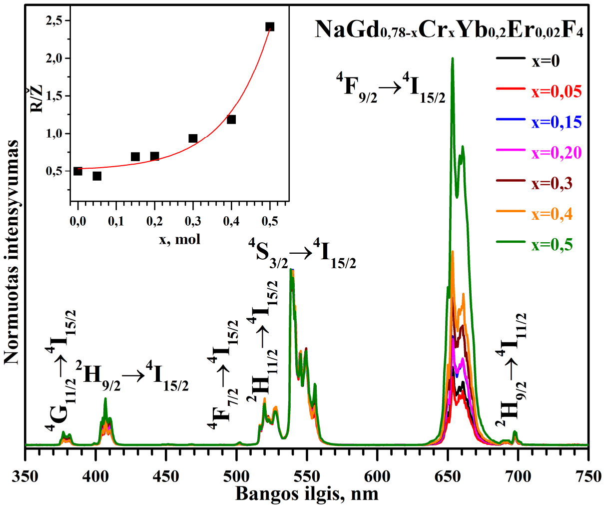

3.17 pav. $NaGd_{0,78-x}Cr_xYb_{0,2}Er_{0,02}F_4$ apkonversijos emisijos spektrai esant skirtingam įterpiamų Cr^{3+} jonų kiekiui. Žadinimo bangos ilgis $\lambda_{\text{žad}} = 980$ nm.

Iš 3.17 paveiksle esančių spektrų matomas žaliosios emisijos juostos ($^2H_{11/2}$;$^4S_{3/2} \rightarrow {}^4I_{15/2}$) intensyvumo sumažėjimas didėjant Cr^{3+} koncentracijai. Taip pat, didėjant Cr^{3+} jonų koncentracijai, didėja ir R/Ž emisijos juostų ($^4F_{9/2} \rightarrow {}^4I_{15/2}$ (625 – 708 nm)), ($^2H_{11/2}$, $^4S_{3/2} \rightarrow {}^4I_{15/2}$ (509 – 574 nm)) santykio vertės. Nespindulinės energijos pernašos Yb–Er–Cr sistemoje mechanizmas pateikiamas 3.18 paveiksle. Pagal šią schemą, Cr^{3+} jonų lygmuo $^2T_2$ užpildomas energijos pernašos būdu iš $^2F_{7/2}$ (Yb^{3+}) lygmens. Raudonosios emisijos intensyvumo padidėjimas stebimas dėl tarp $^4T_2$ ir $^4A_2$ vykstančios relaksacijos, kurios metu gauta energija yra perduodama Er^{3+} jonų $^4F_{9/2}$ lygmeniui.

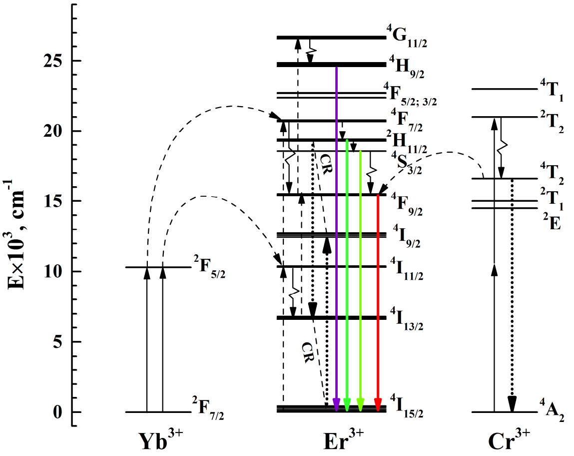

3.18 pav. Yb^{3+}, Er^{3+}, Cr^{3+} apkonversijos mechanizmo schema (žadinimo bangos ilgis $\lambda_{žad}$ = 980 nm).

Liuminescencijos gyvavimo trukmės matavimai atliekami žadinant 980 nm lazerio impulsu $NaGd_{0,78-x}Cr_xYb_{0,2}Er_{0,02}F_4$ junginius ir registruojant emisiją 407 nm, 539 nm ir 635 nm bangos ilgiuose. Iš eksperimentinių duomenų paskaičiuotos gyvavimo trukmės (1 formulė). Vidutinės gyvavimo trukmės junginiams su įterptais Cr^{3+} jonais paskaičiuotos naudojantis (2) formule ir pavaizduotos grafiškai 3.19 paveiksle. Disertacijoje aprašomos dvi komponentės (τ_1, τ_2), priskiriamos trumpesniems gyvavimo laikams, kurių atsiradimas susijęs dėl Er^{3+} jonais esančių arčiau nanodalelių paviršiaus (τ_1) ir dalelės viduje (τ_2). Defektai esantys arti nanodalelių paviršiaus gali būti nespindulinės relaksacijos priežastis.

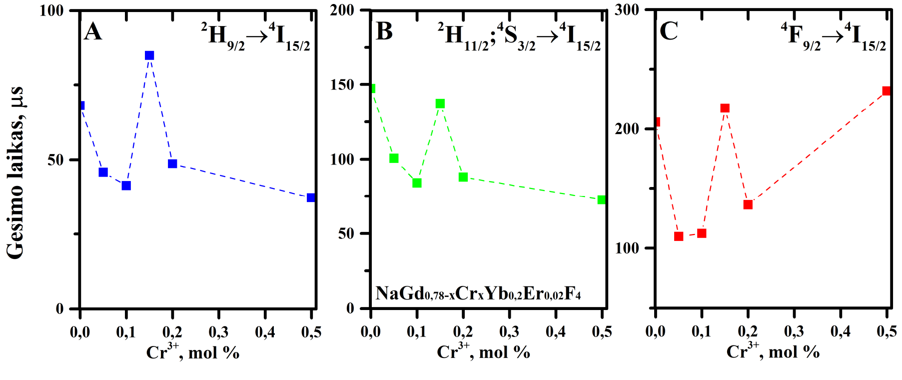

3.19 pav. $NaGd_{0,78-x}Cr_xYb_{0,2}Er_{0,02}F_4$ vidutinių gyvavimo trukmių priklausomybė nuo Cr^{3+} koncentracijos: A) $^2H_{9/2}\rightarrow{}^4I_{15/2}$, B) $^2H_{11/2};{}^4S_{3/2}\rightarrow{}^4I_{15/2}$, C) $^4F_{9/2}\rightarrow{}^4I_{15/2}$.

Iš 3.19 paveiksle pateiktų duomenų matoma, jog vidutinių gyvavimo trukmių sumažėjimas stebimas Cr^{3+} jonų koncentracijai didėjant iki x = 0,1. Tačiau, didinant Cr^{3+} koncentraciją, matomas vidutinių gyvavimo trukmių padidėjimas, kai x = 0,15. Tolimesnis Cr^{3+} jonų koncentracijos didinimas iki x = 0,5 vidutinių gyvavimo trukmių vertes sumažino mėlynoje ($^2H_{9/2}\rightarrow{}^4I_{15/2}$) ir žaliojoje ($^4S_{3/2}$;$^2H_{11/2}\rightarrow{}^4I_{15/2}$) srityje. Tačiau Cr^{3+} koncentracijai esant x = 0,5, raudonosios srities vidutinė gyvavimo trukmė yra didžiausia (231 µs). Raudonosios srities gyvavimo trukmės pailgėjimas, esant didesnei Cr^{3+} koncentracijai, galintis atsirasti dėl $^4T_2\rightarrow{}^4A_2$ šuolio bei energijos perdavos $^4F_{9/2}$ (Er^{3+}) lygmeniui. Apkonversijos liuminescencinės savybės yra paveiktos įterpiamų Cr^{3+} jonų koncentracija bei stebimas emisijos poslinkis į raudonąją regimojo spektro dalį.

Kadangi žinoma, jog Er^{3+} jonai turi termiškai susietus energijos lygmenis, buvo atlikti $NaGd_{0,63}Cr_{0,15}Yb_{0,2}Er_{0,02}F_4$ junginio liuminescencijos matavimai (3.20 pav.) esant skirtingai temperatūrai (77 – 500 K). Geresnei rezultatų interpretacijai, emisijos juostos normuojamos pagal 539 nm emisijos intensyvumą. 3.20 pav. matoma, jog mažas $^2H_{11/2}\rightarrow{}^4I_{15/2}$ energijos pernašos intensyvumas palaipsniui didėja nuo 150 K temperatūros. $^4S_{3/2}$ lygmuo yra užpildomas dėl relaksacijos procesų iš $^4F_{7/2}$ ar aukštesnių lygmenų, o $^2H_{11/2}$ užpildomas tik aukštesnėje temperatūroje.

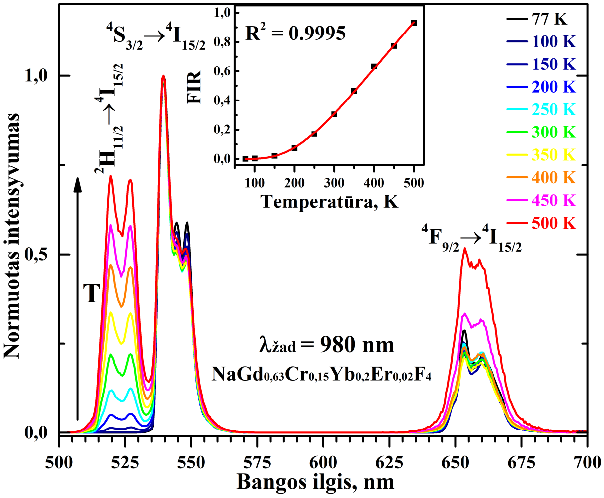

3.20 pav. $NaGd_{0,63}Cr_{0,15}Yb_{0,2}Er_{0,02}F_4$ emisijos spektrai esant skirtingai temperatūrai ($\lambda_{žad}$ = 980 nm).

Integruojant emisijos juostų intensyvumą galima paskaičiuoti atstumą (*ΔE*) tarp $^2H_{11/2}$ ir $^4S_{3/2}$ lygmenų (3 formulė). Gautos $NaGd_{0,63}Cr_{0,15}Yb_{0,2}Er_{0,02}F_4$ junginio *ΔE* (576±8 cm^{-1}) bei

$NaGd_{0,78}Yb_{0,2}Er_{0,02}F_4$ (690 ±6 cm^{-1}) vertės atitinka literatūroje pateikiamas teorines vertes. Taip pat paskaičiuotas (4 formulė) šiluminio jautrumo parametras (S_r), kuris leidžia tarpusavyje palyginti skirtingus temperatūros jutiklius. Šis parametras susijęs su termiškai susietų energijos lygmenų skirtumu. $NaGd_{0,78}Yb_{0,2}Er_{0,02}F_4$ ir $NaGd_{0,63}Cr_{0,15}Yb_{0,2}Er_{0,02}F_4$ paskaičiuoti šiluminio jautrumo parametrai atitinkamai yra $S_r = 1.12\%\ K^{-1}$ ir $S_r = 0.93\%\ K^{-1}$ ir parodo, jog šie junginiai gali būti panaudojami kaip temperatūros jutikliai.

3.5. $NaGd_{0,995-x}Yb_xNd_{0,005}Er_{0,02}F_4$ ir $NaGd_{0,975-x}Yb_xEr_{0,02}Nd_{0,005}F_4$ analizė

Susintetintų ir išgrynintų $NaGd_{0,995-x}Nd_{0,005}Yb_xF_4$ junginių rentgeno spindulių difraktogramose (3.21 pav. a) matoma, jog vienfaziai heksagoninės (P63/m) struktūros junginiai susiformavo Yb^{3+} koncentraciją didinant iki x = 0,5. Didinant Yb^{3+} koncentraciją pastebimas kubinės (α) fazės susidarymas (x = 0,6), o Yb^{3+} koncentracijai esant x = 0,995 susidaro vienfazis kubinės struktūros junginys.

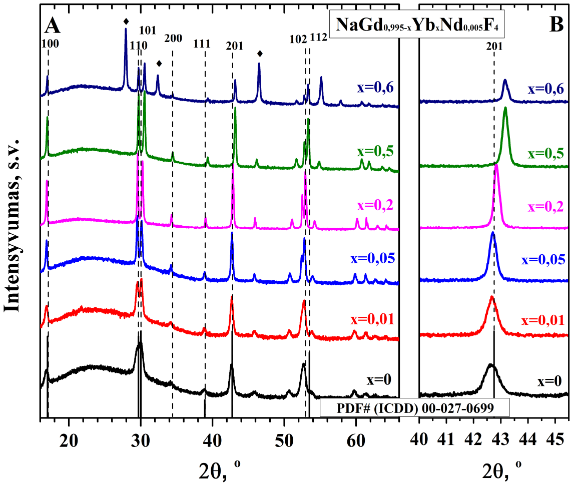

3.21 pav. $NaGd_{0,995-x}Nd_{0,005}Yb_xF_4$ junginių (x = 0; 0,01; 0,05; 0,2; 0,5; 0,6) rentgeno spindulių difraktogramos. $NaGdF_4$ standartas (PDF#(ICDD) 00-027-0699) žymimas punktyrine linija. Kubinės fazės smailės pažymėtos .

Šis heksagoninės ir kubinės fazių susidarymas susijęs su matricoje esančių lantanoidų joninio spindulio dydžiu. $\beta \rightarrow \alpha$ fazių susidarymo tendenciją galima paaiškinti mažesnio joninio spindulio

(KS = 9, r = 1,042 Å) įterpiamų Yb^{3+} jonų koncentracijos didėjimu vietoje didesnio joninio spindulio Gd^{3+} jonų (KS = 9, r = 1,107 Å). Šis pokytis lemia kubinės fazės susidarymą. Sėkmingas mažesnio spindulio Yb^{3+} jonų įterpimas vietoje didesnių Gd^{3+} jonų matomas iš (201) smailės poslinkio (3.21 pav. B). Yb^{3+} jonų įterpimą patvirtina disertacijoje pateikti gardelės parametrų skaičiavimo duomenys. Stebimas a_h ir c_h parametrų mažėjimas didinant įterpiamų Yb^{3+} jonų koncentraciją.

$NaGd_{0,995-x}Nd_{0,005}Yb_xF_4$ junginių koncentracija nustatyta induktyviai susietos plazmos optinės emisijos spektrometrijos (ICP-OES) metodu. Gauti rezultatai pateikiami disertacijoje, kur matoma, jog tiriamų Gd^{3+}, Nd^{3+}, Yb^{3+} jonų koncentracija susintetintuose junginiuose koreliuoja su teoriniais skaičiavimais.

Gautų $NaGd_{0,995-x}Nd_{0,005}Yb_xF_4$ junginių morfologija buvo tiriama TEM analize. Iš vaizdų, pateiktų 3.22 paveiksle matoma, jog susiformuoja sferinės formos nanodalelės. $NaGd_{0,995-x}Nd_{0,005}Yb_xF_4$ junginių forma nepriklauso nuo įterpiamų Yb^{3+} jonų koncentracijos. Paskaičiuotas 3.22 pav. (a, b, c) pateiktuose junginiuose vidutinis dalelių dydis atitinkamai 22,2, 48,1 ir 57,2 nm. Rentgeno difrakcinės analizės duomenimis, kai Yb^{3+} koncentracija yra x = 0,6 – susidaro dviejų fazių nanodalelės, tačiau 3.22 pav. b skirtingos formos ar dydžio dalelių atskirti negalime.

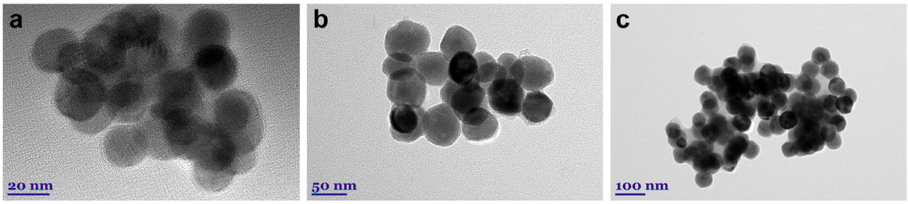

3.22 pav. $NaGd_{0,995-x}Nd_{0,005}Yb_xF_4$ nanodalelių TEM vaizdai:
a – x = 0,01, b – x = 0,6, c – x = 0,995 Yb^{3+}.

Liuminescencinės $NaGd_{0.995-x}Yb_xNd_{0.005}F_4$ savybės tiriamos žadinant 808 nm nuolatinės veiklos lazeriu. 3.23 pav. identifikuotos emisijos juostos priskiriamos Nd^{3+} bei Yb^{3+} jonams būdingai emisijai: Nd^{3+}:$^4F_{3/2}\rightarrow{}^4I_{9/2}$ (850 – 920 nm), Nd^{3+}:$^4F_{3/2}\rightarrow{}^4I_{11/2}$ (1030 – 1070 nm) ir Yb^{3+}:$^2F_{5/2}\rightarrow{}^2F_{7/2}$ (976 nm). Geresnei rezultatų interpretacijai, emisijos juostos normuojamos pagal 976 nm emisijos intensyvumą. Esant mažoms Yb^{3+} jonų koncentracijoms, Nd^{3+} jonams priskiriama emisija ($^4F_{3/2}\rightarrow{}^4I_{9/2}$ ir $^4F_{3/2}\rightarrow{}^4I_{11/2}$ šuoliai) yra intensyvi. Tačiau didinant įterpiamų Yb^{3+} jonų kiekį, Nd^{3+} emisijos intensyvumas mažėja dėl atsiradusios $Nd^{3+}\rightarrow Yb^{3+}$ energijos pernašos.

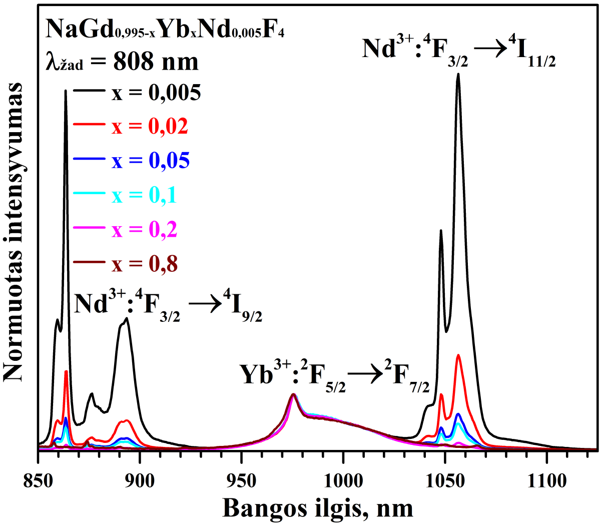

3.23 pav. $NaGd_{0,995-x}Yb_xNd_{0,005}F_4$ emisijos spektrai esant skirtingam įterpiamų Yb^{3+} jonų kiekiui. Žadinimo bangos ilgis $\lambda_{žad}$ = 808 nm.

Į $NaGd_{0,995-x}Yb_xNd_{0,005}F_4$ matricą įterpus Nd^{3+} jonų, pastarieji gali būti sužadinti 808 nm lazerine spinduliuote, kuri yra tinkamesnė naudoti biologinėse terpėse. Žadinant junginį, kuriame yra ir Nd^{3+}, ir Yb^{3+} jonų vyksta energijos pernašos procesas, kurio schema pavaizduota 3.24 paveiksle. Energija yra sugeriama $^4I_{9/2}$ (Nd^{3+}) energijos lygmens ir sužadinama į $^4F_{3/2}$. Šis fotonas perduoda energiją Yb^{3+} $^2F_{5/2}$ lygmeniui ir suteikiant energiją aktyvatoriaus jonams (pvz. Er^{3+}) regima apkonversijos emisija. Atsiradusio papildomo $^4F_{3/2}$ (Nd^{3+}) → $^2F_{5/2}$ (Yb^{3+}) energijos pernašos etapo efektyvumą svarbu įvertinti dėl tolimesnių perdavos procesų.

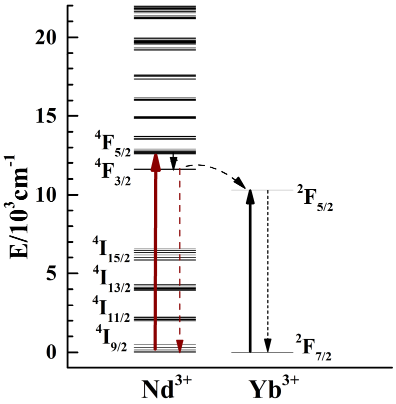

3.24 pav. Nd^{3+}→Yb^{3+} energijos pernašos proceso schema. Žadinimo bangos ilgis $\lambda_{žad}$ = 808 nm.

Liuminescencijos gyvavimo trukmės matavimai atliekami žadinant 808 nm lazerio impulsu $NaGd_{0,995-x}Yb_xNd_{0,005}F_4$ junginius ir registruojant emisiją 864 nm, ir 976 nm bangos ilgiuose. Iš eksperimentinių duomenų paskaičiuotos gyvavimo trukmės (1 formulė). Vidutinės gyvavimo trukmės junginiams su įterptais Yb^{3+} jonais paskaičiuotos naudojantis (2) formule ir pateikiamos 3.2 lentelėje.

3.2 lentelė. $NaGd_{0,995-x}Yb_xNd_{0,005}F_4$ junginių vidutinės gyvavimo trukmės (µs) ir Nd^{3+}→Yb^{3+} energijos pernašos efektyvumas ($\lambda_{žad}$ = 808 nm, λ_{em} = 864 nm ir 976 nm).

X, mol %(Yb^{3+})	**$\bar{\tau}$ (µs), $^4F_{3/2}\rightarrow{}^4I_{9/2}$ (λ_{em} = 864 nm)**	**$\bar{\tau}$ (µs), $^2F_{5/2}\rightarrow{}^2F_{7/2}$ (λ_{em} = 976 nm)**	**η, % ($Nd^{3+}\rightarrow Yb^{3+}$)**
0	306	-	-
0,005	306	1538	0
0,01	280	1459	8,5
0,02	239	1421	21,9
0,05	174	1256	43,1
0,1	95	589	68,8
0,15	63	425	79,3
0,2	56	781	81,6
0,4	24	441	92,3
0,5	5	423	98,5
0,6	3	524	99,0
0,8	1	471	99,7
0,995	1	110	99,6

Didinant Yb^{3+} jonų koncentraciją, stebimas $^4F_{3/2}\rightarrow{}^4I_{9/2}$ energijos šuolio vidutinės gyvavimo trukmės mažėjimas nuo 306 µs (x = 0) iki 5 µs (x = 0,5) dėl padidėjusios Nd^{3+}→Yb^{3+} energijos pernašos tikimybės. Taip pat stebimas $^2F_{5/2}\rightarrow{}^2F_{7/2}$ pernašos gyvavimo trukmių sumažėjimas dėl galimos energijos migracijos tarp kaimyninių Yb^{3+} jonų, atsiradusių defektų ar atgalinės energijos perdavos Nd^{3+} jonams. Nd^{3+}→Yb^{3+} energijos pernašos efektyvumas paskaičiuojamas pagal formulę:

$$\eta = 1 - \frac{\tau_{Nd-Yb}}{\tau_{Nd}} \qquad (5)$$

kur τ_{Nd-Yb} ir τ_{Nd} yra vidutinės gyvavimo trukmės $^4F_{3/2}\rightarrow{}^4I_{9/2}$ šuolio (Nd^{3+}) mėginyje, kuriame yra Yb^{3+} jonų (τ_{Nd-Yb}) ir, kuriame nėra (τ_{Nd}). 3.2 lentelėje pateikti skaičiavimo duomenys, iš kurių galime daryti išvadą, jog energijos pernašos efektyvumas didėjo įterpiant daugiau Yb^{3+} jonų. Didžiausias energijos pernašos Nd^{3+}→Yb^{3+} efektyvumas 98,5% yra, kai Yb^{3+} koncentracija $x = 0,5$. Tolimesnis Yb^{3+} koncentracijos didinimas neturėjo didelės įtakos pernašos efektyvumui.

Atlikti NaGd$_{0,995}$Nd$_{0,005}$F$_4$ liuminescencijos matavimai (3.25 pav.) esant skirtingai temperatūrai (77 – 500 K). Integruota emisija esant skirtingai temperatūrai pateikiama 3.25 pav. įtarpe. Neįprastas temperatūrinės liuminescencijos intensyvumo didėjimas matomas iki 350 K. Šis reiškinys atsiranda dėl terminio aukštesnių lygmenų užpildymo.

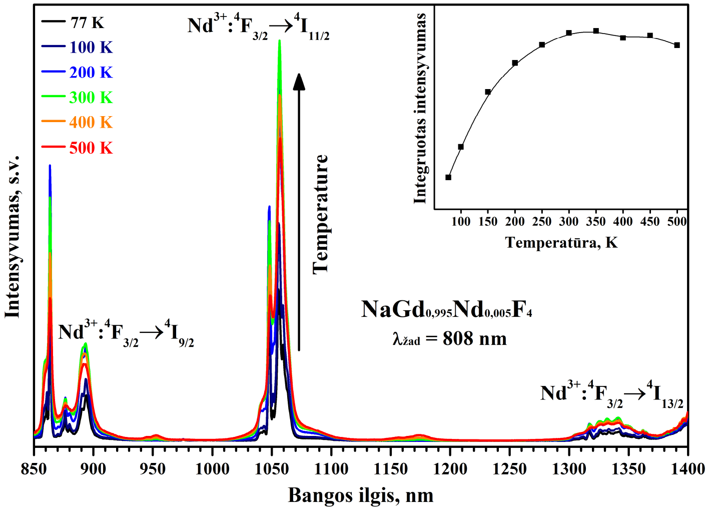

3.25 pav. NaGd$_{0,995}$Nd$_{0,005}$F$_4$ emisijos spektrai esant skirtingai temperatūrai ($\lambda_{žad}$ = 808 nm).

Liuminescencijos matavimai, esant skirtingai temperatūrai, taip pat atlikti ir junginiams NaGd$_{0,995-x}$Yb$_x$Nd$_{0,005}$F$_4$, kur Yb^{3+} $x = 0,01; 0,15; 0,2; 0,4$. Kaip ir 3.23 pav. matoma tendencija, taip ir šiuose, disertacijoje pateiktuose, spektruose matomas Yb^{3+} emisijos juostų intensyvumo didėjimas bei Nd^{3+} mažėjimas įterpiant didesnį kiekį iterbio jonų.

Liuminescencijos gyvavimo trukmės matavimai esant skirtingai temperatūrai (77 – 500 K) atliekami žadinant 808 nm lazerio impulsu NaGd$_{0,995}$Nd$_{0,005}$F$_4$ junginį ir registruojant emisiją 864 nm, bangos ilgyje. Iš eksperimentinių duomenų paskaičiuotos gyvavimo trukmės (1 formulė). Vidutinės gyvavimo trukmės junginiams su įterptais Yb^{3+} jonais paskaičiuotos naudojant (2) formulę ir pateikiamos 3.3 lentelėje. Matomos artimos gesimo trukmių vertės, kurios nežymiai padidėja esant 450 K temperatūrai. Manoma, jog aukštesnėje temperatūroje energija migruoja tarp

Nd^{3+} jonų didinant $^4I_{11/2}$ energijos lygmens užpildymo tikimybę. Tuo pačiu, $^4I_{11/2}$ užpildymas vyksta dėl $^4F_{3/2}$ energetinio lygmens emisijos ir gaunamos papildomos energijos iš relaksuojančio kaimyninio jono $^4F_{3/2}$ – $^4I_{9/2}$ lygmens.

3.3 lentelė. $NaGd_{0,995-x}Yb_xNd_{0,005}F_4$ junginių vidutinės gyvavimo trukmės (μs) ($\lambda_{\check{z}ad}$ = 808 nm, λ_{em} = 864 nm).

T, K	**$\bar{\tau}$, $^4F_{3/2}\rightarrow{}^4I_{9/2}$ (λ_{em} = 864 nm)**
77	371.75
100	374.72
150	380.40
200	385.53
250	395.83
300	401.31
350	411.18
400	419.64
450	425.14
500	367.09

Liuminescencijos gyvavimo trukmės matavimai esant skirtingai temperatūrai taip pat atlikti ir $NaGd_{0,995-x}Yb_xNd_{0,005}F_4$ junginiams, kai x = 0,1 ir 0,4. Iš disertacijoje pateiktų rezultatų, matoma, jog esant nedidelei Yb^{3+} jonų koncentracijai (x = 0,1), Nd^{3+} emisijos ($^4F_{3/2}\rightarrow{}^4I_{9/2}$) bei Yb^{3+} ($^2F_{5/2}\rightarrow{}^2F_{7/2}$) gyvavimo trukmės buvo artimos visame tiriamajame temperatūrų ruože. Tačiau Yb^{3+} koncentracijai esant x = 0,4, matomas $^4F_{3/2}\rightarrow{}^4I_{9/2}$ (Nd^{3+}) vidutinių gyvavimo trukmių sumažėjimas bei $^2F_{5/2}\rightarrow{}^2F_{7/2}$ (Yb^{3+}) padidėjimas (ties 350 K). Aukštesnės temperatūros sukeltas $^4I_{11/2}$ (Nd^{3+}) lygmens užpildymas vyksta per energijos migracijos tarp jonų bei energijos perdavos procesų. Šie procesai dalyvauja didinant Yb^{3+} emisijos intensyvumą, matomą iš padidėjusių energijos pernašos efektyvumo verčių (pateikiama disertacijoje).

Kadangi žinoma, jog Er^{3+} jonai turi termiškai susietus energijos lygmenis, buvo atlikti $NaGd_{0,475}Yb_{0,5}Er_{0,02}Nd_{0,005}F_4$ junginio liuminescencijos matavimai (3.26 pav.) esant skirtingai temperatūrai (77 – 500 K). Geresnei rezultatų interpretacijai, emisijos juostos normuojamos pagal 539 nm emisijos intensyvumą. 3.26 pav. matoma, jog mažas $^2H_{11/2}\rightarrow{}^4I_{15/2}$ energijos pernašos intensyvumas palaipsniui didėja nuo 200 K temperatūros. $^4S_{3/2}$ lygmuo yra užpildomas dėl relaksacijos procesų iš $^4F_{7/2}$ ar aukštesnių lygmenų, o $^2H_{11/2}$ užpildomas tik aukštesnėje temperatūroje.

Integruojant emisijos juostų intensyvumą galima paskaičiuoti atstumą (*ΔE*) tarp $^2H_{11/2}$ ir $^4S_{3/2}$ lygmenų (3 formulė). Gautos $NaGd_{0,475}Yb_{0,5}Er_{0,02}Nd_{0,005}F_4$ junginio *ΔE* vertės (699 ±16 cm^{-1}) atitinka literatūroje pateikiamas teorines vertes.

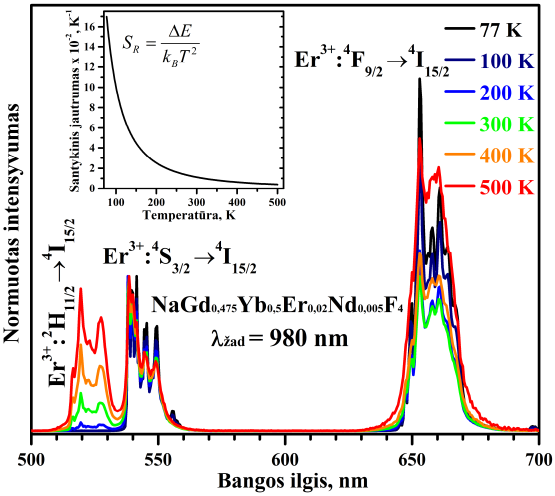

3.26 pav. $NaGd_{0,475}Yb_{0,5}Er_{0,02}Nd_{0,005}F_4$ emisijos spektrai esant skirtingai temperatūrai ($\lambda_{žad}$ = 980 nm).

Taip pat paskaičiuotas (4 formulė) šiluminio jautrumo parametras (S_r), kuris leidžia tarpusavyje palyginti skirtingus temperatūros jutiklius. $NaGd_{0,475}Yb_{0,5}Er_{0,02}Nd_{0,005}F_4$ paskaičiuota S_r vertė 1,11% K^{-1} 300 K temperatūroje parodo, jog šis junginys gali būti panaudojamas kaip temperatūros jutiklis.

IŠVADOS

1. Įterpinat skirtingų koncentracijų šarminių žemių metalų jonus (Li^+, K^+) į $Na_{1-x}Gd_{0,78}Yb_{0,2}Er_{0,02}F_4$ sistemą gauti vienfaziai heksagoninės kristalinės struktūros junginiai iki x = 0,4. Didesnių koncentracijų įterpimas lėmė kubinės $NaGdF_4$ ar GdF_3 junginių susidarymą.
2. Įterpiant Li^+ bei K^+ jonus į apkonvertuojančias optines savybes turinčius $Na_{1-x}Gd_{0,78}Yb_{0,2}Er_{0,02}F_4$ junginius keičiamas emisijos juostų (R/Ž) intensyvumo santykis. Didinant Li^+ jonų kiekį (x = 0,1 iki x = 0,7) R/Ž juostų santykis padidėjo. Tačiau didinant K^+ koncentraciją R/Ž juostų santykis sumažėjo nuo 1,7 iki 1,0. R/Ž juostų santykio didėjimas iki 1,6 buvo stebimas, kai įterptų K^+ jonų koncentracija x = 0,8.
3. Įterpiant iki x = 0,5 Mn^{2+} jonų į $NaY_{0,78-x}Yb_{0,2}Er_{0,02}F_4$ gauti vienfaziai kubinės kristalinės struktūros junginiai. Taip pat, įterpiant iki x = 0,5 Cr^{3+} jonų į $NaGd_{0,78-x}Yb_{0,2}Er_{0,02}F_4$ gauti vienfaziai heksagoninės kristalinės struktūros junginiai.
4. Pereinamųjų elementų įtaka optinėms savybėms buvo įvertinta ir stebimas R/Ž emisijos juostų pokytis. Įterpiant Mn^{2+} jonus, emisija yra paveikta atsiradusių papildomų energijos lygmenų, kurie dalyvauja nespindulinės energijos pernašos procesuose $NaY_{0,78-x}Yb_{0,2}Er_{0,02}F_4$ sistemoje. Esant x = 0,78 Mn^{2+} koncentracijai stebimas žaliosios emisijos juostos gesinimas, o $NaMn_{0,78}Yb_{0,2}Er_{0,02}F_4$ emisija yra raudonojoje regimojo spektro dalyje. Didinat Mn^{2+} ir Cr^{3+} jonų koncentraciją $NaGdF_4$ junginiuose stebima didėjanti, atitinkamai 6 ir 5 kartus, R/Ž emisijos juostų santykinė vertė.
5. Vienfaziai heksagoninės kristalinės fazės $NaGd_{0,995-x}Nd_{0,005}F_4$ junginiai gauti Yb^{3+} koncentracijai esant iki x = 0,5. Sėkmingas Yb^{3+} jonų įterpimas buvo įrodytas remiantis mažėjančiomis kristalinės gardelės parametrų vertėmis bei ICP matavimais.
6. $NaGd_{0,995-x}Yb_xNd_{0,005}F_4$ junginiuose stebimas Nd^{3+} jonų emisijos intensyvumo mažėjimas didinant Yb^{3+} koncentraciją žadinant 808 nm spinduliuote. Energijos pernašos $Nd^{3+} \rightarrow Yb^{3+}$ efektyvumas buvo įvertintas didinant Yb^{3+} jonų koncentraciją ir siekė 99 %, kai x = 0,6.
7. Neįprastas liuminescencinių savybių pokytis buvo pastebėtas $NaGd_{0,995}Nd_{0,005}F_4$ junginyje, matuojant emisiją 77 – 500 K temperatūros ruože. Padidėjusių integruotos emisijos verčių priežastis

gali būti dėl kaimyninių Nd^{3+} jonų temperatūros pokyčio sukelto nuolatinio tarpusavio energijos perdavimo.

8. Liuminescencijos gesimo kreivės $NaGd_{0,995-x}Yb_xNd_{0,005}F_4$ junginiuose, kur Yb^{3+} jonų koncentracija x = 0,4, buvo mažai paveiktos temperatūros pokyčio. Stebimos pailgėjusios Yb^{3+} emisijos gyvavimo trukmės, kai temperatūra yra didesnė nei 300 K. Taip pat, padidėjusios energijos pernašos vertės (~97 %) stebimos esant aukštesnei temperatūrai.
9. Fluorescensijos intensyvumo santykis bei atstumas tarp dviejų Er^{3+} termiškai susietų energetinių lygmenų (ΔE) buvo paskaičiuotas iš emisijos nuo temperatūros pokyčio matavimų. Nustatyta ΔE vertė $NaGd_{0,78}Yb_{0,2}Er_{0,02}F_4$ ir $NaGd_{0,475}Yb_{0,5}Er_{0,02}F_4$ junginiuose gerai sutampa su teorinėmis vertėmis ir atitinkamai yra 690 ± 6 cm^{-1} ir 699 ± 16 cm^{-1}.
10. Santykinio temperatūrinio jautrumo matavimai įrodė, jog ištirtos $NaGd_{0,78}Yb_{0,2}Er_{0,02}F_4$ ir $NaGd_{0,475}Yb_{0,5}Er_{0,02}F_4$ medžiagos gali būti sėkmingai naudojamos kaip temperatūriniai jutikliai, kadangi apskaičiuotos S_r vertės yra artimos 1 % K^{-1}.

CURRICULUM VITAE

Vardas, pavardė: Ieva Mikalauskaitė

Gimimo data: 1990-11-24

Išsilavinimas

2015-2019 m.	Vilniaus universitetas, gamtos mokslų srities, chemijos krypties doktorantūros studijos
2013-2015 m.	Vilniaus universitetas, chemijos magistro laipsnis
2009-2013 m.	Vilniaus universitetas, chemijos bakalauro laipsnis

Darbo patirtis

2015 m.-	Chemikė, „Eurofins Labtarna Lietuva, UAB“, Vilnius
2013-2017 m.	Vyresnioji specialistė, Neorganinės chemijos laboratorija, Chemijos ir geomokslų fakultetas, Vilniaus universitetas
2013 m. balandis-2013 m. rugpjūtis	Laborantė, Neorganinės chemijos laboratorija, Chemijos ir geomokslų fakultetas, Vilniaus universitetas

Projektai

2014 m. kovas-2016 m. lapkritis	Specialistė, Nacionalinis vėžio institutas, Mokslininkų grupių projektas Nr. MIP-030/2014 (LMT)

ACKNOWLEDGEMENTS

Not many people will come to this part of thesis, however, in my opinion, it is the most important one. Doctoral studies were the source of improvement of scientific knowledge and personal skills. However, the most treasured are the people who helped me during those years.

First of all, I would like to thank my parents who supported the idea to study this weird subject that I have come up with as my career choice. I would like to express my gratitude for prof. Aldona Beganskienė for the opportunity to pursue this path and for the creative freedom that was provided with continuous concern and a helping hand. This faculty was like a home for me for the last ten years. Meanwhile, I found my biggest supporter who understood the endless hours of experiments and the difficulties of managing a job and doctoral studies. Thank you, Martynas, for the unquestionable support and for always giving me a safe ride home with very few complaints.

A huge contribution on how not to let a pattern of failures to interfere with the mood was from Julija and Gintarė. You kept my morale higher during the time we spent together (not necessarily working). Thank you for the time spent revising and the valuable insights that were very helpful. The examples and support from Aleksandra, Olga, Skirmantė were inspiring and I have always felt your encouragement. I would like to express my gratitude to prof. Artūras Katelnikovas for the time and guidance in the field of luminescence. Finally, I would like to thank Valentina Plaušinaitienė for the support and warmth that I felt and discussions that went beyond scientific area.

LIST OF PUBLICATIONS

Publications Included in Thesis

Articles in Journals:

1. **I. Mikalauskaite**, G. Pleckaityte, M. Skapas, A. Zarkov, A. Katelnikovas, A. Beganskiene, "Emission spectra tuning of upconverting $NaGdF_4$:20% Yb, 2%Er nanoparticles by Cr^{3+} co-doping for optical temperature sensing". J Lumin, **213** (2019), 210-217. DOI: 10.1016/j.jlumin.2019.05.032.

2. **I. Mikalauskaite**, G. Pleckaityte, L. Sinusaite, V. Plausinaitiene, A. Katelnikovas, A. Beganskiene, "Temperature induced emission enhancement and investigation of Nd^{3+}→Yb^{3+} energy transfer efficiency in $NaGdF_4$:Nd^{3+}, Yb^{3+}, Er^{3+} upconverting nanoparticles". J Lumin, **223** (2020), 117237. DOI: 10.1016/j.jlumin.2020.117237.

Publications not Included in Thesis

Articles in Journals:

1. **I. Mikalauskaite,** E. Raudonyte-Svirbutaviciene, A. Linkeviciute, M. Urbonas, A. Katelnikovas, "Luminescence and luminescence quenching of $Sr_3Lu_2(Si_3O_9)_2$:Ce^{3+} phosphors", J Lumin, **184** (2017), 185-190. DOI: 10.1016/j.jlumin.2016.12.037.

ATTENDED CONFERENCES

Poster presentations:

1. **I. Mikalauskaitė,** A. Beganskienė, V. Karabanovas, G. Streckytė, R. Rotomskis, A.Kareiva, Crystal Phase and Size Dependence of Upconverting $NaYF_4$ Nanoparticles Obtained in Oleylamine, Chemistry and Chemical Technology, 2016, Vilnius, Lithuania.
2. **I. Mikalauskaitė,** G. Plečkaitytė, A. Beganskienė, V. Karabanovas, G. Streckytė, Thermal Decomposition Synthesis of $NaYF_4$:Yb^{3+}, Er^{3+}, Mn^{2+} with Shifted Yellow-Red Emission Output, 2nd International

conference “Current Trends in Cancer Theranostics”, 2016, Druskininkai, Lithuania.

3. **I. Mikalauskaitė,** G. Plečkaitytė, V. Karabanovas, R. Rotomskis, A. Kareiva, A. Beganskienė, Tuning $NaYF_4$: Yb^{3+}, Er^{3+} upconversion emission from green to yellow-red output colour by doping Mn^{2+} ions, 5th International Workshop on Advanced Materials Challenges for Health and Alternative Energy Solutions, 2016, Cologne, Germany.
4. G. Plečkaitytė, **I. Mikalauskaitė**, A. Katelnikovas, A. Beganskienė, Synthesis and investigation of dual excitation upconverting $NaGdF_4$ nanoparticles, 3rd Intertational conference “Current Trends in Cancer Theranostics”, 2017, Pakruojis, Lithuania.
5. **I. Mikalauskaitė**, G. Plečkaitytė, A. Katelnikovas, V. Karabanovas, R. Rotomskis, A. Beganskienė, Introducing Cr^{3+} ions into $NaGdF_4$: Yb^{3+}, Er^{3+} system, 3rd International conference “Current Trends in Cancer Theranostics”, 2017, Pakruojis, Lithuania.
6. **I. Mikalauskaitė**, G. Plečkaitytė, A. Beganskienė, Manipulating overall emission of $NaYF_4$: Yb^{3+}, Er^{3+} by introducing additional Mn^{2+} ions, „There Is No Future Without The Past“, The International Conference Dedicated to the 215th Birth Anniversary of Ignacy Domeyko, 2017, Vilnius, Lithuania.
7. **I. Mikalauskaitė**, G. Plečkaitytė, A. Katelnikovas, A. Beganskienė, Doping Cr^{3+} ions into $NaGdF_4$ as possible luminescence enhancer, “UPCON18: 2nd Conference and Spring School on Properties, Design and Applications of Upconversion Nanomaterials”, 2018, Valencia, Spain.
8. **I. Mikalauskaitė**, G. Plečkaitytė, A. Katelnikovas, A. Beganskienė, Outcome in structure and properties of luminescence when substituting Na^+ in $NaGdF_4$ with alkali ions, 4th International conference “Current Trends in Cancer Theranostics”, 2018, Trakai, Lithuania.
9. G. Plečkaitytė, **I. Mikalauskaitė**, A. Katelnikovas, A. Beganskienė Energy transfer in $NaGdF_4$:Nd^{3+}, Yb^{3+} hexagonal nanoparticles under 808 nm laser excitation, 4th Intertational conference “Current Trends in Cancer Theranostics”, 2018, Trakai, Lithuania.
10. **I. Mikalauskaitė**, G. Plečkaitytė, A. Katelnikovas, A. Beganskienė, Outcomes of Na^+ substitution with Li^+ or K^+ ions in $NaGdF_4$ upconverting nanoparticles, “E-MRS 2018 Fall Meeting“, 2018, Warsaw, Poland.

11. **I. Mikalauskaitė,** G. Plečkaitytė, K. Paulauskaitė, A. Beganskienė, Controling Upconversion Emission Outcome in Yb^{3+}/Er^{3+} Systems, “Chemistry and Chemical Technology“, 2019, Vilnius, Lithuania.
12. **I. Mikalauskaitė**, G. Plečkaitytė, A. Katelnikovas, A. Beganskienė, $Nd^{3+} \rightarrow Yb^{3+}$ energy transfer efficiency study in $NaGdF_4$ nanomaterials, “14th International conference on materials chemistry (MC14)“, 2019, Birmingham, United Kingdom.

1

Emission spectra tuning of upconverting $NaGdF_4$:20% Yb, 2% Er nanoparticles by Cr^{3+} co-doping for optical temperature sensing

I. Mikalauskaite, G. Pleckaityte, M. Skapas, A. Zarkov,
A. Katelnikovas, A. Beganskiene

Journal of Luminescence 213 (2019) 210–217

Contents lists available at ScienceDirect

Journal of Luminescence

journal homepage: www.elsevier.com/locate/jlumin

Emission spectra tuning of upconverting $NaGdF_4$:20% Yb, 2% Er nanoparticles by Cr^{3+} co-doping for optical temperature sensing

I. Mikalauskaite[a], G. Pleckaityte[a], M. Skapas[b], A. Zarkov[a], A. Katelnikovas[a,*], A. Beganskiene[a]

[a] Institute of Chemistry, Faculty of Chemistry and Geosciences, Vilnius University, Naugarduko 24, LT-03225 Vilnius, Lithuania
[b] Center for Physical Science and Technology, Saulėtekio Av. 3, LT-10259, Vilnius, Lithuania

A R T I C L E I N F O

Keywords:
Upconversion
Luminescence
Thermal quenching
$NaGdF_4$
Cr^{3+} co-doping

A B S T R A C T

Upconverting (UC) nanoparticles have gained much attention due to their unique properties of converting radiation with longer wavelength (usually infrared (IR)) to emission in the visible (VIS) range. In order to obtain efficiently emitting nanomaterials, proper amounts of rare-earth (RE) elements need to be doped into matrices with low phonon energies. $NaGd_{0.78\text{-}x}F_4$:$Yb_{0.2}$/$Er_{0.02}$/$Cr_x{}^{3+}$ nanoparticles were synthesized via thermal decomposition method. By varying concentration of Cr^{3+} a series of nanomaterials with composition of $NaGd_{0.78\text{-}x}F_4$:$Yb_{0.2}$/$Er_{0.02}$/$Cr_x{}^{3+}$ were synthesized and characterized. Addition of Cr^{3+} ions impacts UC emission due to possible energy migration and relaxation pathways in $Yb^{3+}-Er^{3+}-Cr^{3+}$ system. Effective energy difference was calculated from temperature dependent luminescence measurements of thermally coupled $^2H_{11/2}$ and $^4S_{3/2}$ levels. Values of calculated relative sensitivity (S_r = 1.12% K^{-1}) in $NaGdF_4$:Yb^{3+}/Er^{3+} compound were slightly higher comparing to $NaGd_{0.78\text{-}x}F_4$:$Yb_{0.2}$/$Er_{0.02}$/$Cr_x{}^{3+}$ samples; therefore, both systems could be considered for a possible application in luminescent temperature sensors.

1. Introduction

As upconverting (UC) nanoparticles have gained more attention throughout the years, a variety of different doping materials, having certain application purposes were taken into consideration. Unique electron configuration in Ln^{3+} ions provides at least one metastable level with a lifetime of 10^{-6}-10^{-2} s necessary for UC process to take place [1]. Furthermore, 4f orbitals of lanthanide ions are shielded with the filled outer 5s and 5p orbitals that result in sharp emission lines. When Ln^{3+} ions are located in a host lattice, parity-forbidden f-f electric dipole transitions become weakly allowed due to increased possibility to interact with opposite-parity configurations [2]. Thus, more asymmetric crystal field would increase optical transition probabilities improving efficiency of UC luminescence [3,4]. There are two main phases in $NaREF_4$ compounds family: $\alpha-NaREF_4$ (cubic) and β-$NaREF_4$ (hexagonal). The hexagonal phase possesses relatively low phonon energy (~350 cm^{-1}) [5] which, in fact, decrease possibility of non-radiative relaxation processes. Therefore, this matrix is frequently discussed as the most efficient matrix for utilizing UC emission.

Among the most commonly known Yb/Er, Yb/Tm, Yb/Ho doping pairs, other lanthanide ions (Eu^{3+} [6], Ce^{3+} [7], Tb^{3+} [8]) were additionally doped to generate upconverting luminescence in nanomaterials. Energy transfer upconversion (ETU) mechanism is suggested as one of the most efficient approaches [9–12] explaining upconversion luminescence in nanoparticles doped with lanthanide ions. Anti-Stokes emission and optical properties of nanoparticles are affected by relatively high surface-to-volume ratio [13], doping concentration and carefully selected donor-acceptor pairs [14]. In order to modulate outcome of UC emission core-shell structures [15–18] and incorporation of multiple Ln^{3+} ions [19,20] (more than two activators) were suggested. In recent years transition metal ions have also been considered as a type of dopant ions for UC nanomaterials. Transition metals provide complex upconverting system with intermediate energy levels for possible energy transfer routes [21]. Due to different ionic size of elements embedded into inorganic nanoparticles, spatial distance can be affected resulting in cross-relaxation and energy transfer processes [22]. Incorporation of Mn^{2+} ions into hexagonal $NaYF_4$:Yb/Er (18/2 mol%) matrix produces cubic phase nanoparticles when concentration of Mn^{2+} increases up to 30% [23]. Red-to-green intensity ratio was increased nearly 200 times achieving bright pure deep red emission which appears to be 15 times brighter than emission in Mn-free sample [23]. With addition of Mn^{2+} ions emission lifetimes of green (550 nm) and red (650 nm) bands decreased and increased, respectively. This suggests that single-red emission occurs as an outcome of presence of $^4T_1$ level as a possible non-radiative energy transfer channel [24]. Another approach of introducing Mn^{2+} ions into upconversion processes

---

[*] Corresponding author.
E-mail address: arturas.katelnikovas@chf.vu.lt (A. Katelnikovas).

https://doi.org/10.1016/j.jlumin.2019.05.032
Received 29 January 2019; Received in revised form 30 April 2019; Accepted 14 May 2019

is to employ Mn^{2+} as the main component of inorganic matrix. Various different host materials were synthesized ($KMnF_3$:Yb/Er, $KMnF_3$:Yb/Ho, $KMnF_3$:Yb/Tm [21], MnF_2:Yb/Er [25,26], $NaMnF_3$:Yb/Er [27]) followed by the same strategy of enhancing red emission for the possibility to use upconverting materials more efficiently, as aforementioned emission falls within the "optical window" of the living tissue [28].

Cr^{3+} energy levels overlap with the respective ones in Er^{3+} ions; therefore, a possibility of energy transfer between $Cr^{3+} - Er^{3+}$ might be considered. Recently, Z. Gerelkhuu et al. reported a $NaLu_{0.86-x}Gd_{0.12}F_4:Er_{0.02}{}^{3+}$ matrix where lutetium was partially substituted by Cr^{3+} ions (concentration of Cr^{3+} varied in the range $0 \le x \le 0.24$) [29]. They found out that Cr^{3+} ions take part in upconversion process as a sensitizer instead of the most commonly used Yb^{3+} ions. Optimal Cr^{3+} concentration for UC emission increase was found to be 18%, determined by the shorter distance between dopants. In hydrothermal synthesis approach [30] co-doping β-$NaYF_4:Yb^{3+}/Er^{3+}$ with various concentrations of Cr^{3+} ions has led to an increase in red and green emission for 7 and 16 times, respectively. It was assumed that stronger emission appears due to change in local surrounding symmetry of Er^{3+} resulting in enhanced intensity of upconversion luminescence [31]. Since luminescence and PL lifetime values of lanthanide based materials have a dependence on temperature [32–35], a possible application of UC nanomaterials for temperature sensing was proposed [36]. It was reported that sensitivity of UC nanoparticles is affected by crystal structure [34], size and Yb/Er concentration [37].

In this paper, $NaGd_{0.78-x}F_4:Yb_{0.2}/Er_{0.02}/Cr_x{}^{3+}$ (UC-Cr_x) nanoparticles with various concentrations of co-doped Cr^{3+} ions were obtained via thermal decomposition method and their properties were investigated. Crystal structure, particle size, upconversion luminescence, PL lifetime value dependence on Cr^{3+} concentration together with temperature dependent luminescence properties will be discussed in detail.

2. Experimental

$NaGd_{0.78-x}F_4:Yb_{0.2}/Er_{0.02}/Cr_x{}^{3+}$ nanoparticles were synthesized via modified thermal decomposition method [38,39]. Gd_2O_3 (Aldrich, 99.9%), Yb_2O_3 (Alfa Aesar, 99.9%) and Er_2O_3 (Alfa Aesar, 99.99%) were dissolved in diluted HCl (Eurochemicals, 37%) to obtain $RECl_3$. Solution of $CrCl_3 \cdot 6H_2O$ (Aldrich, ≥ 98.0%) in methanol was then added followed by the addition of 12 mL oleic acid (Alfa Aesar, 90%) and 30 mL of 1-octadecene (Alfa Aesar, 90%) and stirred for 1 h. This mixture was heated up to 120 °C under N_2 atmosphere and maintained until solution became clear. Then heating was cancelled and NaOH (Eurochemicals, 99%) together with NH_4F (Alfa Aesar, min 98.0%) dissolved in methanol were injected at room temperature. After stirring the solution for 0.5 h, temperature was increased to 120 °C in order to evaporate the methanol. Afterwards, temperature was increased to 300 °C and maintained for 1 h. Nanoparticles were precipitated with the addition of hexane:acetone (1:4) and centrifuged at 8000 rpm for 30 min. The washing was repeated twice, later re-dispersing nanoparticles in ethanol:acetone (1:1), followed by centrifugation and additional hexane:acetone (1:4) washing.

For identification of crystal structure powder XRD patterns of obtained specimens were recorded with Rigaku MiniFlex diffractometer from $10^\circ \le 2\theta \le 90^\circ$ using Ni-filtered Cu Kα radiation. Scanning speed and step width were 5°/min and 0.02°, respectively.

Elemental analysis of the synthesized samples was performed by inductively coupled plasma optical emission spectrometry (ICP-OES) with Agilent 5110 ICP-OES spectrometer. The samples were dissolved in nitric acid (HNO_3, Rotipuran® Supra 69%, Carl Roth) using microwave reaction system Anton Paar Multiwave 3000 equipped with XF100 rotor and PTFE liners. Calibration solutions were prepared by an appropriate dilution of the stock standard solutions (single-element ICP Standards 1000 mg/L, Carl Roth).

Transmission electron microscopy (TEM) images were taken on Tecnai G2 F20 X-TWIN (FEI, Netherlands, 2011) with Schottky type field emission electron source, high angle annular dark field (HAADF) detector using a single and double tilt specimen holders with 11 MPix ORIUS SC1000B (Gatan) CCD camera.

Upconversion luminescence spectra were recorded with Edinburgh Instruments FLS980 spectrometer with single-photon counting photomultiplier (Hamamatsu R928) using a 980 nm constant wavelength (CW) laser as an excitation source. Emission bandwidth and step size were set to 0.5 nm, integration time was 0.4 s. For upconversion luminescence measurements 8.8 mg of powder sample were dispersed in 2 mL toluene and measurements were carried out under continuous stirring.

Upconversion luminescence decay curves were recorded using a 980 nm pulsed laser as an excitation source. The frequency of laser was 100 Hz. Emission was monitored at 407, 539.5, and 653.5 nm wavelengths. The collected data were fitted using bi-exponential decay equation:

$$I(t) = A + B_1 e^{(-t/\tau_1)} + B_2 e^{(-t/\tau_2)} \tag{1}$$

Here $I(t)$ is intensity of luminescence at a given time t; A is background; B_1 and B_2 are constants; τ_1, and τ_2 are emission lifetime values.

For temperature dependent emission measurements cryostat MicrostatN was incorporated together with a flow system of liquid nitrogen as a cooling agent. Measurement temperature for emission spectra and decay curves were set initially to 77 K, followed by measurements in the 100–500 K range by 50 K interval. Temperature stabilization time and tolerance were set to 90 s and ± 5 K, respectively.

3. Results and discussion

Although many approaches of doping similar size ions instead of Y or Gd in Na(Y/Gd)F_4 have been published [40], the possibility of doping different size ions should also be taken into consideration. When smaller or larger ions are doped into crystal lattice, the distance between ions changes, ultimately changing fluorescence emission and energy transfer from Yb to Er [41]. Doping Cr^{3+} (r = 0.62 Å, CN = 6) ions instead of Gd^{3+} (r = 1.11 Å, CN = 9) [42,43] could either replace Gd^{3+} ions or at some level might also occupy interstitial positions [41,44]. The powder XRD patterns of synthesized $NaGd_{0.78-x}F_4:Yb_{0.2}/Er_{0.02}/Cr_x{}^{3+}$ nanoparticles are depicted in Fig. 1.

XRD patterns of $NaGd_{0.78-x}F_4:Yb_{0.2}/Er_{0.02}/Cr_x{}^{3+}$ powders with different Cr^{3+} concentrations (x = 0%, 5%, 15%, 20%, and 50%) clearly demonstrate that in each case a single hexagonal phase was synthesized. A slight shift of (201) peak at 40–45 2θ° towards larger 2θ angles is observed in Fig. 1b if the concentration of Cr^{3+} ions is increased. This is associated with reduction of unit cell parameters, since larger Gd^{3+} are replaced by smaller Cr^{3+} ions leading to diffraction peak shift to higher 2θ angles. No additional peaks of impurities were observed in XRD patterns regardless broad range of Cr^{3+} concentration.

In order to determine the actual concentration of ions existing in the synthesized compounds ICP-OES analysis was carried out. Elemental composition of $NaGdF_4$ nanoparticles doped with various concentrations of Cr^{3+} is represented in Table 1. Discrepancies from initial and actual concentration of Gd^{3+} and Cr^{3+} ions should be pointed out. The cause of mismatch of Gd^{3+} ions to a larger actual content measured with ICP and for Cr – vice versa, needs further investigation. Similar results were also observed by Wang et al. [29], however, no explanation for this phenomenon was given. At the moment it seems that part of the Cr^{3+} ions for some reason are just not incorporated into the crystal lattice and are lost during the washing process of nanoparticles.

To avoid any confusion, nanoparticles throughout this article were identified with the amount of Cr^{3+} which was expected. On the other hand, one should also keep in mind that the actual content differs.

The morphological features of the synthesized nanoparticles were evaluated by taking TEM images. The TEM images of specimens doped

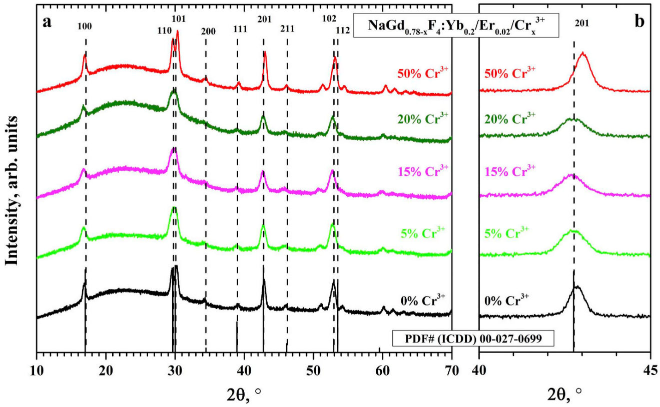

Fig. 1. XRD patterns of $NaGd_{0.78\text{-}x}F_4:Yb_{0.2}/Er_{0.02}/Cr_x^{3+}$ powders (x = 0, 5, 15, 20, 50%) and reference pattern of $NaGdF_4$ (PDF # (ICDD) 00-027-0699).

Table 1
Ratio of Gd, Yb, Er, Cr elements, measured with ICP-OES.

Expected ratio Gd:Yb:Er:Cr	Gd, %	Yb, %	Er, %	Cr, %
78:20:2:0	80.8	17.2	1.8	0
73:20:2:5	84.1	11.2	2.0	2.7
63:20:2:15	79.0	11.9	2.1	7.0
58:20:2:20	72.1	13.1	2.2	12.5
28:20:2:50	39.3	26.7	2.6	31.4

with 0%, 5%, 15%, 20%, and 50% Cr^{3+} are given in Fig. 2. Spherical shape nanoparticles are visible in all TEM images regardless the Cr^{3+} concentration. Besides, the particles also appear of relatively similar size, except for the sample with 50% Cr^{3+}, where very large particles are also visible. Moreover, atomic planes in larger magnification Fig. 2 B TEM image suggest high crystallinity of $NaGd_{0.78\text{-}x}F_4:Yb_{0.2}/Er_{0.02}$ sample. The TEM images were also used to evaluate particle size distribution of samples containing different amount of Cr^{3+} ions. The obtained results are summarized in Fig. S1.

Particle size distribution narrows down if Cr^{3+} concentration increases. However, a distribution with two distinct areas of frequency maxima is observed when concentration of Cr^{3+} increases to 50%. Moreover, the average particle size was also calculated from at least 200 particles. The calculated mean diameter of nanoparticles without Cr^{3+} ions was 11.4 ± 2.4 nm. Further doping of Cr^{3+} ions has led to a slight average particle size decrease (d = 9.0 ± 2.5 nm for 20% Cr^{3+}) followed by an increase and appearance of two distinct size distributions at 50% Cr^{3+}. The exact calculated nanoparticle diameters with standard deviations for all samples are summarized in Table S1. Fig. 2 F and histogram in Fig. S1 E reveals that powder doped with 50% Cr^{3+} ions contain small and large separate particles with average size of 10.0 and 16.9 nm, respectively. The formation of these different size particles seems to be Cr^{3+} concentration related, since up to 20% Cr^{3+} concentration the average nanoparticle size of $NaGd_{0.78\text{-}x}F_4:Yb_{0.2}/Er_{0.02}/Cr_x^{3+}$ materials is around 10 nm (within the margin of error). Furthermore, the XRD measurements (see Fig. 1) showed no additional phase formation, thus it can be clearly stated that nanoparticles of both sizes possess the same crystal structure.

Cr^{3+} concentration dependent UC emission spectra of $NaGd_{0.78\text{-}x}F_4:Yb_{0.2}/Er_{0.02}/Cr_x^{3+}$ compounds are presented in Fig. 3. A typical emission of Er^{3+} ions is observed in 350–750 nm region. Upconversion luminescence in this case occurs from absorption of 980 nm laser radiation by Yb^{3+} ions and subsequent energy transfer to intermediate energy levels of Er^{3+} ions, sequentially exciting energy levels resulting in radiative emission of Er^{3+}.

All the observed upconversion emission lines were attributed to

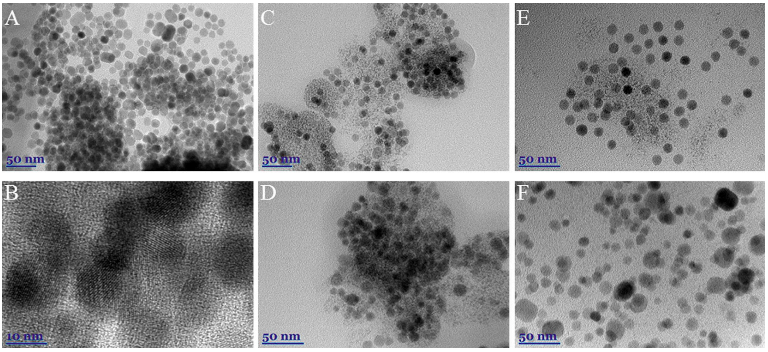

Fig. 2. Bright-field TEM images of $NaGd_{0.78\text{-}x}F_4:Yb_{0.2}/Er_{0.02}/Cr_x^{3+}$ nanoparticles: A and B – 0%, C – 5%, D – 15%, E – 20%, F – 50% Cr^{3+}.

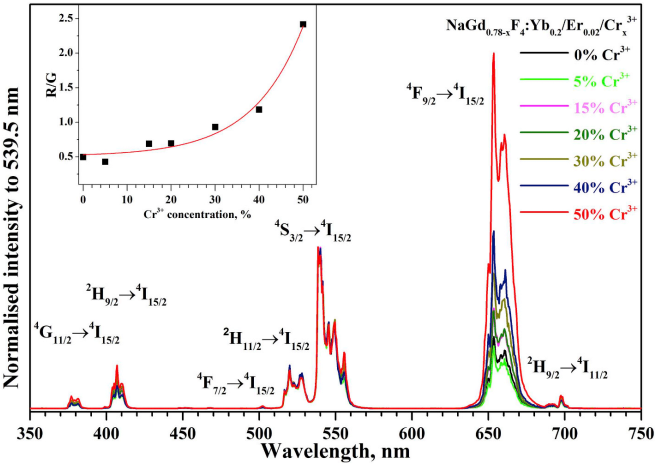

Fig. 3. UC luminescence spectra of $NaGd_{0.78\text{-}x}F_4$:$Yb_{0.2}$/$Er_{0.02}$/Cr_x^{3+} nanoparticles with different Cr^{3+}concentration. Inset: ratio of red (R) (635–680 nm) and green (G) (515–565 nm) emitting level integrated intensities. Line in inset graph was drawn to guide an eye.

Er^{3+} transitions: $^4G_{11/2} \rightarrow {}^4I_{15/2}$ (ca. 380 nm, violet region), $^2H_{9/2} \rightarrow {}^4I_{15/2}$ (ca. 405 nm, violet region), $^4F_{7/2} \rightarrow {}^4I_{15/2}$ (very weak, ca. 500 nm, cyan region), $^2H_{11/2} \rightarrow {}^4I_{15/2}$ (515 − 535 nm, green region), $^4S_{3/2} \rightarrow {}^4I_{15/2}$ (535 − 565 nm, green region), $^4F_{9/2} \rightarrow {}^4I_{15/2}$ (635 − 680 nm, red region), $^2H_{9/2} \rightarrow {}^4I_{11/2}$ (ca. 695 nm, red region). Emission in the visible region is observed due to similar energy level positioning between Yb^{3+} and Er^{3+} ions and occurrence of energy transfer from $^2F_{5/2}$ (Yb^{3+}) to various Er^{3+} energy levels followed by a population of emitting states [45]. The emission spectra shown in Fig. 3 were normalized for 539.5 nm intensity. This allows the better evaluation of the red to green (R/G) emission ratio change with increasing Cr^{3+} concentration. The ratio of integrated red $^4F_{9/2} \rightarrow {}^4I_{15/2}$ (635 − 680 nm) and green $^4S_{3/2}$;$^2H_{11/2} \rightarrow {}^4I_{15/2}$ (515 − 565 nm) emission lines (see inset of Fig. 3) has a slight tendency to increase with increasing Cr^{3+} concentration. Thus, one can manipulate the emission spectrum of the compounds in order to obtain the preferable colour output by simply varying Cr^{3+} doping concentration. Several approaches to explain such shift could be addressed. The excitation of Yb^{3+} $^2F_{7/2}$ level to $^2F_{5/2}$ can be followed by further energy transfer to Cr^{3+} [46]. Since no distinct emission of Cr^{3+} ions occur in our case, a possible energy transfer to Er^{3+} ions through Cr^{3+} [44,47] would be the cause of an intensity increase of red emission band with increasing Cr^{3+} concentration.

An UC luminescence scheme with the possible energy transfer mechanisms is represented in Fig. 4. Impact of Cr^{3+} ions on Er^{3+} emission was discussed in Na(Lu,Gd)F_4 system [44]. It was suggested that $^2T_2$ state could be populated by an energy transfer from $^2F_{7/2}$ (Yb^{3+}) followed by further relaxation to $^4T_2$. Enhancement of red emission occurs as a result of relaxation process between $^4T_2$ and $^4A_2$ states. Thus, the energy of $^4T_2 \rightarrow {}^4A_2$ transition is subsequently transferred to $^4F_{9/2}$ level of Er^{3+} ions.

Upconversion luminescence decay curves of UC-Cr_x (x = 0%, 5%, 15%, 20%, 30%, 40%, and 50%) were recorded under 980 nm excitation. Emission was monitored at 407, 539.5, and 653.5 nm wavelengths. The obtained PL decay curves (see Fig. S2) were fitted with a bi-exponential decay function (eq. (1)) and the obtained results are summarized in Table S2. The faster component τ_1 can be assigned to the Er^{3+} ions near the surface of nanoparticles whereas the slower component τ_2 is attributed to the Er^{3+} ions deeper inside the nanoparticle. Er^{3+} ions near the surface possess more disordered local environment and defects, thus the nonradiative relaxation of the excited state becomes more probable and the fluorescence lifetime decrease, i.e. becomes faster [48,49].

A decrease of PL lifetime values recorded for 407, 539.5, and 653.5 nm emission was observed when 5% of Cr^{3+} was added. However, further increasing dopant concentration to 15% resulted in slightly higher PL lifetime values. Nevertheless, the addition of higher concentration of Cr^{3+} ions (20%, 30%, 40% and 50%) has reduced the average PL lifetime values ($\bar{\tau}$) of green ($^4S_{3/2}$;$^2H_{11/2} \rightarrow {}^4I_{15/2}$) and blue ($^2H_{9/2} \rightarrow {}^4I_{15/2}$) transitions. Since the decrease of average lifetimes was observed with increasing Cr^{3+} concentration, a possible depletion pattern involving various non-radiative decay processes should be taken into consideration. Despite the fact that initial (Cr^{3+} free) nanoparticles had the highest $\bar{\tau}$, further doping of Cr^{3+} up to 15% showed an increase in blue and red emission lifetimes. From results in Table S2 a tendency of gradual average lifetime decrease of blue and green transitions for all analysed Cr^{3+} (20%, 30%, 40% and 50%) concentrations is observed. In the case of red emission transition an increasing average lifetime value could occur as a result of $^4T_2 \rightarrow {}^4A_2$ transition followed by a subsequent transfer to $^4F_{9/2}$ level of Er^{3+} ions.

Due to the thermally coupled green emission lines ($^4S_{3/2}$ and $^2H_{11/2}$ states), Er^{3+} ions are frequently used for applications involving temperature sensing [50,51]. Relative integrated emission intensities of $^2H_{11/2} \rightarrow {}^4I_{15/2}$ and $^4S_{3/2} \rightarrow {}^4I_{15/2}$ are proportional to the population of these energy levels following the Boltzmann distribution [52]:

$$FIR = \frac{I_{520}}{I_{540}} = Ce^{(-\Delta E/k_B T)} \tag{2}$$

where I_{520} and I_{540} are the fluorescence intensities of $^2H_{11/2} \rightarrow {}^4I_{15/2}$ and $^4S_{3/2} \rightarrow {}^4I_{15/2}$ transitions, respectively; C is a constant, ΔE – effective energy difference between these two thermally coupled energy levels, k_B – Boltzmann constant (8.617342×10^{-5} eV/K) [53], T – absolute temperature. Temperature dependent upconversion emission spectra of 15% Cr^{3+} doped sample recorded in the range of 77–500 K are shown in Fig. 5. At very low temperatures (i.e. 77 and 100 K) there is virtually no emission originating from the $^2H_{11/2} \rightarrow {}^4I_{15/2}$ transition. Very weak emission from this transition starts to appear only at 150 K and its relative intensity, if compared to the $^4S_{3/2} \rightarrow {}^4I_{15/2}$ transition, gradually increases with increasing temperature. These results clearly

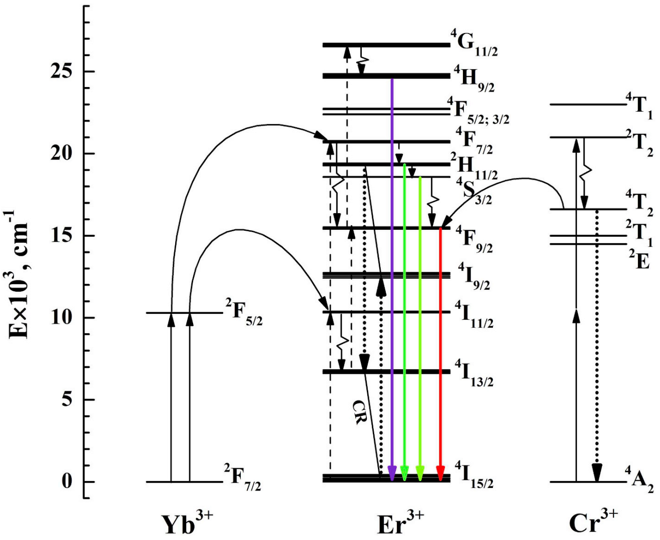

Fig. 4. Energy level diagram with possible transfer processes in $Yb^{3+} - Er^{3+} - Cr^{3+}$ system under 980 nm laser excitation. Solid violet, green and red lines represent UC emission occurring from energy transfer upconversion (ETU) processes.

show that relaxation from excited Er^{3+} $^4F_{7/2}$ and higher energy levels firstly occurs to $^4S_{3/2}$ level which later thermally populate the $^2H_{11/2}$ level. Similar results were also observed by A. Bayart et al. in $La_2Ti_2O_7$:Er^{3+} compound [54].

The normalized (to intensity at 539.5 nm) emission spectra were used to calculate FIR value employing equation (2) and the obtained Boltzmann fit is shown in inset of Fig. 5. Virtually perfect fit was obtained with $R^2 = 0.9995$. The emission intensity was integrated in wavelength ranges 507–534 nm for $^2H_{11/2} \rightarrow {}^4I_{15/2}$ transition and 534–560 nm for $^4S_{3/2} \rightarrow {}^4I_{15/2}$ transition. The calculated effective energy difference between $^2H_{11/2}$ and $^4S_{3/2}$ levels in Cr^{3+} – free and 15% Cr^{3+} doped sample was 690 ± 6 cm^{-1} and 576 ± 8 cm^{-1}, respectively.

In order to evaluate the possibility for UCNP's to be used for sensing application, absolute sensitivity (S_a) and relative sensitivity (S_r) of a certain system must be determined. S_r is described as the rate of FIR

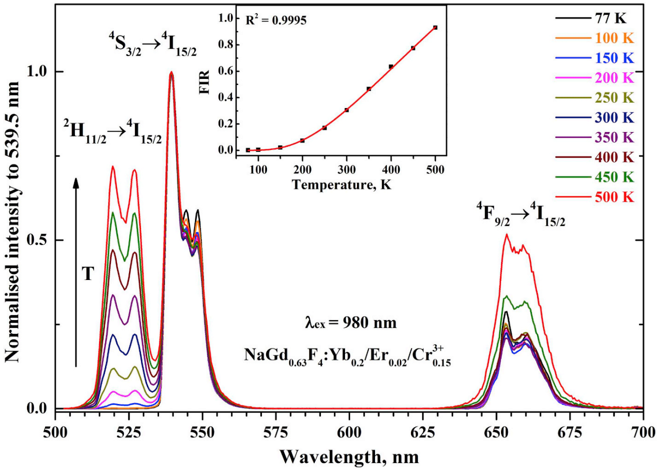

Fig. 5. Upconversion emission spectra (normalized to 539.5 nm) of $NaGd_{0.63}F_4$:$Yb_{0.2}$/$Er_{0.02}$/$Cr_{0.15}{}^{3+}$ recorded at various temperatures under 980 nm excitation. Inset shows FIR data fit by Boltzmann equation.

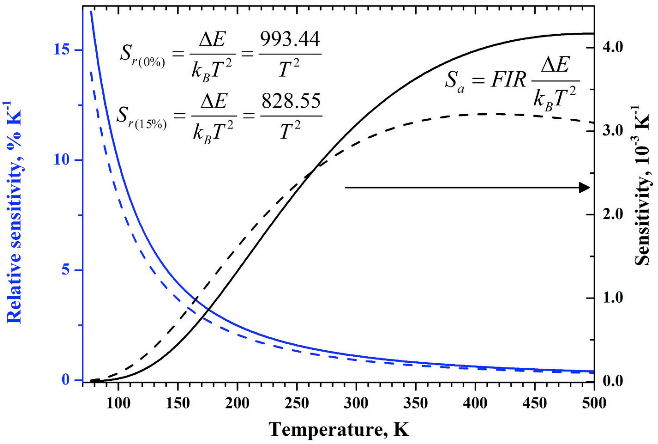

Fig. 6. Curves of relative (S_r) and absolute (S_a) sensitivities of $NaGd_{0.78}F_4$:$Yb_{0.2}$/$Er_{0.02}$ (solid line) and $NaGd_{0.63}F_4$:$Yb_{0.2}$/$Er_{0.02}$/$Cr_{0.15}^{3+}$ (dashed line).

change during certain variation of temperature. It indicates, that more responsive temperature change can be detected if the energy gap between two thermally coupled levels increases [51,52]. These parameters can be calculated from the following equations:

$$S_r = \frac{\Delta E}{k_B T^2} \tag{3}$$

$$S_a = FIR\frac{\Delta E}{k_B T^2} \tag{4}$$

S_r (eq. (3)) is commonly used in order to compare temperature sensing abilities of different host materials of various techniques and types of thermometers [55].

The obtained S_a and S_r curves for Cr^{3+} – free and 15% Cr^{3+} doped samples in the temperature range of 77–500 K are given in Fig. 6. The S_r and S_a values at the same temperature (298 K) were slightly higher for the Cr^{3+} – free sample (S_r = 1.12% K^{-1} and S_a = 3.05 $10^{-3} K^{-1}$) if compared to 15% Cr^{3+} doped sample (S_r = 0.93% K^{-1} and S_a = 2.84 $10^{-3} K^{-1}$). The comparison of the obtained S_r values with the ones reported by other scientists is summarized in Table 2. It is obvious, that these values are very similar, thus both Cr^{3+} – free and 15% Cr^{3+} doped samples could be applied as luminescent temperature sensors.

Upconversion decay curves of $NaGd_{0.63}F_4$:$Yb_{0.2}$/$Er_{0.02}$/$Cr_{0.15}^{3+}$ sample for 539 nm emission ($^4S_{3/2} \rightarrow {}^4I_{15/2}$ transition) were also measured in the temperature range of 77–500 K and are presented in Fig. S3.

The PL decay curves are virtually the same in the temperature range of 77–150 K. Later they become steeper with increasing temperature indicating that thermal quenching sets in above 150 K [56]. It is also interesting to note that the temperature dependent PL decay was single-exponential, contrary to bi-exponential decay of nanoparticles measured in solvent. The calculated PL lifetime values decreased from 251 μs at 77 K to 91 μs at 500 K. The exact calculated PL lifetime values are summarized in Table S3.

Table 2
Comparison of relative temperature sensitivity.

Matrix	T, K	S_r, % K^{-1}	Reference
$NaYF_4$:20% Yb, 2% Er	300	1.20	[57]
$NaYF_4$:Yb, Gd, Er, Nd	288	1.37	[58]
K_2GdF_5:18% Yb, 2% Er	307	1.1	[51]
$NaBiF_4$:Er/Yb	303	1.24	[59]
$NaGdF_4$: 20% Yb, 2% Er	298	1.12	this work
$NaGdF_4$: 20% Yb, 2% Er, 15% Cr	298	0.93	this work

4. Conclusions

In present study upconverting $NaGdF_4$ nanoparticles doped with Yb^{3+}, Er^{3+}, Cr^{3+} ions were synthesized by heating up the mixture of precursors in OA/ODE. Single phase nanoparticles were obtained by varying concentration of Cr^{3+} ions up to 50%. The increase of Cr^{3+} concentration in the synthesized compounds has affected their luminescence properties. The stronger red emission was observed if samples were doped with higher concentrations of Cr^{3+} ions. Temperature dependent upconversion luminescence was investigated for thermally coupled $^4S_{3/2}$ and $^2H_{11/2}$ Er^{3+} levels. The fluorescence intensity ratio (FIR) was investigated and ΔE was calculated to be 690 ± 6 cm^{-1} and 576 ± 8 cm^{-1} for Cr^{3+} – free and 15% Cr^{3+} doped sample, respectively. The relative sensitivity (S_r) of 1.12% K^{-1} was determined to be the highest in Cr^{3+} – free compound. However, introducing Cr^{3+} ions into the host lattice did not positively affect S_r values, which were slightly decreased if compared to Cr^{3+} – free sample. On the other hand, the S_r values were close to 1% K^{-1} and Cr^{3+} dopant could be considered as an emission band shifting ion with the possibility to use $NaGdF_4$:Yb^{3+}/Er^{3+}/Cr^{3+} compounds as a temperature sensors.

Author contributions

I.M. and G.P. prepared the samples and performed XRD and room temperature luminescence measurements. M.S. performed TEM analysis. A.Z. performed ICP measurements. I.M., G.P. and A.K. performed temperature dependent steady state and kinetic measurements. I.M., A.K. and A.B. initiated the research and wrote the manuscript. All authors discussed the results and reviewed the manuscript.

Acknowledgements

This research was funded by a grant (No. S-MIP-17-48) from the Research Council of Lithuania.

The authors are grateful to JSC “Interlux” for providing equipment for elemental analysis. V. Poderys is highly acknowledged for technical support and valuable consultations.

Appendix A. Supplementary data

Supplementary data to this article can be found online at https://doi.org/10.1016/j.jlumin.2019.05.032.

References

[1] J.F. Suyver, A. Aebischer, D. Biner, P. Gerner, J. Grimm, S. Heer, K.W. Kramer, C. Reinhard, H.U. Gudel, Novel materials doped with trivalent lanthanides and transition metal ions showing near-infrared to visible photon upconversion, Opt. Mater. 27 (2005) 1111–1130.

[2] S.Y. Han, R.R. Deng, X.J. Xie, X.G. Liu, Enhancing luminescence in lanthanide-doped upconversion nanoparticles, Angew. Chem. Int. Ed. 53 (2014) 11702–11715.

[3] A. Nadort, J.B. Zhao, E.M. Goldys, Lanthanide upconversion luminescence at the nanoscale: fundamentals and optical properties, Nanoscale 8 (2016) 13099–13130.

[4] A. Noculak, A. Podhorodecki, Size and shape effects in beta-NaGdF$_4$: Yb^{3+}, Er^{3+} nanocrystals, Nanotechnology 28 (2017) 175706.

[5] A. Ivaturi, S.K.W. MacDougall, R. Martin-Rodriguez, M. Quintanilla, J. Marques-Hueso, K.W. Kramer, A. Meijerink, B.S. Richards, Optimizing infrared to near infrared upconversion quantum yield of beta-NaYF$_4$:Er^{3+} in fluoropolymer matrix for photovoltaic devices, J. Appl. Phys. 114 (2013) 013505.

[6] C. Zhang, L. Yang, J. Zhao, B.H. Liu, M.Y. Han, Z.P. Zhang, White-Light emission from an integrated upconversion nanostructure: toward multicolor displays modulated by laser power, Angew. Chem. Int. Ed. 54 (2015) 11531–11535.

[7] R.R. Deng, F. Qin, R.F. Chen, W. Huang, M.H. Hong, X.G. Liu, Temporal full-colour tuning through non-steady-state upconversion, Nat. Nanotechnol. 10 (2015) 237–242.

[8] K. Prorok, A. Gnach, A. Bednarkiewicz, W. Strek, Energy up-conversion in Tb^{3+}/Yb^{3+} co-doped colloidal alpha-NaYF$_4$ nanocrystals, J. Lumin. 140 (2013) 103–109.

[9] H. Dong, L.D. Sun, C.H. Yan, Energy transfer in lanthanide upconversion studies for extended optical applications, Chem. Soc. Rev. 44 (2015) 1608–1634.

[10] X. Qin, J.H. Xu, Y.M. Wu, X.G. Liu, Energy-transfer editing in lanthanide-activated upconversion nanocrystals: a toolbox for emerging applications, ACS Cent. Sci. 5 (2019) 29–42.

[11] B. Zhou, L. Yan, L.L. Tao, N. Song, M. Wu, T. Wang, Q.Y. Zhang, Enabling photon upconversion and precise control of donor-acceptor interaction through interfacial energy transfer, Adv. Sci. 5 (2018) 1700667.

[12] J. Bergstrand, Q.Y. Liu, B.R. Huang, X.Y. Peng, C. Wurth, U. Resch-Genger, Q.Q. Zhan, J. Widengren, H. Agren, H.C. Liu, On the decay time of upconversion luminescence, Nanoscale 11 (2019) 4959–4969.

[13] J.B. Zhao, Z.D. Lu, Y.D. Yin, C. Mcrae, J.A. Piper, J.M. Dawes, D.Y. Jin, E.M. Goldys, Upconversion luminescence with tunable lifetime in NaYF$_4$:Yb,Er nanocrystals: role of nanocrystal size, Nanoscale 5 (2013) 944–952.

[14] L.P. Tu, X.M. Liu, F. Wu, H. Zhang, Excitation energy migration dynamics in upconversion nanomaterials, Chem. Soc. Rev. 44 (2015) 1331–1345.

[15] H.X. Mai, Y.W. Zhang, L.D. Sun, C.H. Yan, Highly efficient multicolor up-conversion emissions and their mechanisms of monodisperse NaYF$_4$:Yb, Er core and core/shell-structured nanocrystals, J. Phys. Chem. C 111 (2007) 13721–13729.

[16] L. Yan, B. Zhou, N. Song, X.L. Liu, J.S. Huang, T. Wang, L.L. Tao, Q.Y. Zhang, Self-sensitization induced upconversion of Er^{3+} in core-shell nanoparticles, Nanoscale 10 (2018) 17949–17957.

[17] D.G. Li, W.P. Qin, D. Zhao, T. Aidilibike, H. Chen, S.H. Liu, P. Zhang, L.L. Wang, Tunable green to red upconversion fluorescence of water-soluble hexagonal-phase core-shell CaF$_2$@NaYF$_4$ nanocrystals, Opt. Mater. Express 6 (2016) 270–278.

[18] F. Vetrone, R. Naccache, V. Mahalingam, C.G. Morgan, J.A. Capobianco, The active-core/active-shell approach: a strategy to enhance the upconversion luminescence in lanthanide-doped nanoparticles, Adv. Funct. Mater. 19 (2009) 2924–2929.

[19] G.Y. Chen, H.C. Liu, G. Somesfalean, H.J. Liang, Z.G. Zhang, Upconversion emission tuning from green to red in Yb^{3+}/Ho^{3+}-codoped NaYF$_4$ nanocrystals by tridoping with Ce^{3+} ions, Nanotechnology 20 (2009) 385704.

[20] S.J. Liu, Y.J. Li, C. Zhang, L. Yang, T.T. Zhao, R.L. Zhang, C.L. Jiang, Upconversion color tuning in Ce^{3+}-doped LiYF$_4$:Yb^{3+}/Ho^{3+}@LiYF$_4$ nanoparticles towards ratiometric fluorescence detection of chromium (III), J. Colloid Interface Sci. 493 (2017) 10–16.

[21] J. Wang, F. Wang, C. Wang, Z. Liu, X.G. Liu, Single-band upconversion emission in lanthanide-doped KMnF$_3$ nanocrystals, Angew. Chem. Int. Ed. 50 (2011) 10369–10372.

[22] H. Dong, L.D. Sun, C.H. Yan, Energy transfer in lanthanide upconversion studies for extended optical applications, Chem. Soc. Rev. 44 (2015) 1608–1634.

[23] G. Tian, Z.J. Gu, L.J. Zhou, W.Y. Yin, X.X. Liu, L. Yan, S. Jin, W.L. Ren, G.M. Xing, S.J. Li, Y.L. Zhao, Mn^{2+} dopant-controlled synthesis of NaYF$_4$:Yb/Er upconversion nanoparticles for in vivo imaging and drug delivery, Adv. Mater. 24 (2012) 1226–1231.

[24] Z.Y. Huang, H.P. Gao, Y.L. Mao, Understanding the effect of Mn^{2+} on Yb^{3+}/Er^{3+} upconversion and obtaining a maximum upconversion fluorescence enhancement in inert-core/active-shell/inert-shell structures, RSC Adv. 6 (2016) 83321–83327.

[25] M.Y. Xie, X.N. Peng, X.F. Fu, J.J. Zhang, G.L. Lia, X.F. Yu, Synthesis of Yb^{3+}/Er^{3+} co-doped MnF$_2$ nanocrystals with bright red up-converted fluorescence, Scripta Mater. 60 (2009) 190–193.

[26] Z.H. Bai, H. Lin, J. Johnson, S.C.R. Gui, K. Imakita, R. Montazami, M. Fujii, N. Hashemi, The single-band red upconversion luminescence from morphology and size controllable Er^{3+}/Yb^{3+} doped MnF$_2$ nanostructures, J. Mater. Chem. C 2 (2014) 1736–1741.

[27] Y. Zhang, J.D. Lin, V. Vijayaragavan, K.K. Bhakoo, T.T.Y. Tan, Tuning sub-10 nm single-phase NaMnF$_3$ nanocrystals as ultrasensitive hosts for pure intense fluorescence and excellent T$_{-1}$ magnetic resonance imaging, Chem. Commun. 48 (2012) 10322–10324.

[28] J. Merian, J. Gravier, F. Navarro, I. Texier, Fluorescent nanoprobes dedicated to in vivo imaging: from preclinical validations to clinical translation, Molecules 17 (2012) 5564–5591.

[29] Z. Gerelkhuu, B.T. Huy, J.W. Chung, T.L. Phan, E. Conte, Y.I. Lee, Influence of Cr^{3+} on upconversion luminescent and magnetic properties of NaLu$_{0.86-x}$Gd$_{0.12}$F$_4$:Cr$_x^{(3+)}$/Er$_{0.02}^{(3+)}$ ($0 < x < 0.24$) material, J. Lumin. 187 (2017) 40–45.

[30] C.Y. Wang, X.H. Cheng, Influence of Cr^{3+} ions doping on growth and upconversion luminescence properties of beta-NaYF$_4$:Yb^{3+}/Er^{3+} microcrystals, J. Alloy. Comp. 649 (2015) 196–203.

[31] Q.M. Huang, J.C. Yu, E. Ma, K.M. Lin, Synthesis and characterization of highly efficient near-infrared upconversion Sc^{3+}/Er^{3+}/Yb^{3+} tridoped NaYF$_4$, J. Phys. Chem. C 114 (2010) 4719–4724.

[32] L.N. Sun, J.B. Yu, H.S. Peng, J.Z. Zhang, L.Y. Shi, O.S. Wolfbeis, Temperature-sensitive luminescent nanoparticles and films based on a terbium (III) complex probe, J. Phys. Chem. C 114 (2010) 12642–12648.

[33] J.B. Yu, L.N. Sun, H.S. Peng, M.I.J. Stich, Luminescent terbium and europium probes for lifetime based sensing of temperature between 0 and 70°C, J. Mater. Chem. 20 (2010) 6975–6981.

[34] X.Q. Ge, L.N. Sun, S. Dang, J.L. Liu, Y.X. Xu, Z.W. Wei, L.Y. Shi, H.J. Zhang, Mesoporous upconversion nanoparticles modified with a Tb(III) complex to display both green upconversion and downconversion luminescence for in vitro bioimaging and sensing of temperature, Microchim. Acta 182 (2015) 1653–1660.

[35] A. Sedlmeier, D.E. Achatz, L.H. Fischer, H.H. Gorris, O.S. Wolfbeis, Photon upconverting nanoparticles for luminescent sensing of temperature, Nanoscale 4 (2012) 7090–7096.

[36] Q. Qiang, Y. Wang, Enhanced optical temperature sensing and upconversion emissions based on the Mn^{2+} codoped NaGdF$_4$:Yb^{3+},Ho^{3+} nanophosphor, New J. Chem. 43 (2019) 5011–5019.

[37] L. Marciniak, K. Prorok, A. Bednarkiewicz, Size dependent sensitivity of Yb^{3+}, Er^{3+} up-converting luminescent nano-thermometers, J. Mater. Chem. C 5 (2017) 7890–7897.

[38] F. Wang, R.R. Deng, X.G. Liu, Preparation of core-shell NaGdF$_4$ nanoparticles doped with luminescent lanthanide ions to be used as upconversion-based probes, Nat. Protoc. 9 (2014) 1634–1644.

[39] F. Chen, W.B. Bu, S.J. Zhang, X.H. Liu, J.N. Liu, H.Y. Xing, Q.F. Xiao, L.P. Zhou, W.J. Peng, L.Z. Wang, J.L. Shi, Positive and negative lattice shielding effects Co-existing in Gd (III) ion doped bifunctional upconversion nanoprobes, Adv. Funct. Mater. 21 (2011) 4285–4294.

[40] H.X. Mai, Y.W. Zhang, R. Si, Z.G. Yan, L.D. Sun, L.P. You, C.H. Yan, High-quality sodium rare-earth fluoride nanocrystals: controlled synthesis and optical properties, J. Am. Chem. Soc. 128 (2006) 6426–6436.

[41] Q.Q. Dou, Y. Zhang, Tuning of the structure and emission spectra of upconversion nanocrystals by alkali ion doping, Langmuir 27 (2011) 13236–13241.

[42] R.D. Shannon, Revised effective ionic radii and systematic studies of interatomic distances in halides and chalcogenides, Acta Crystallogr. A32 (1976) 751–767.

[43] A. Herrmann, M. Tylkowski, C. Bocker, C. Russel, Cubic and hexagonal NaGdF$_4$ crystals precipitated from an aluminosilicate glass: preparation and luminescence properties, Chem. Mater. 25 (2013) 2878–2884.

[44] B.T. Huy, Z. Gerelkhuu, J.W. Chung, V.D. Dao, G. Ajithkumar, Y.I. Lee, Enhanced light harvesting with chromium in NaLu$_{0.70-x}$Gd$_{0.10}$F$_4$: Yb$_{0.18}$Er$_{0.02}$Cr$_x$ ($0 < x < 0.25$) upconversion system, Mater. Sci. Eng. B-Adv. 223 (2017) 91–97.

[45] M.Y. Hossan, A. Hor, Q. Luu, S.J. Smith, P.S. May, M.T. Berry, Explaining the nanoscale effect in the upconversion dynamics of beta-NaYF$_4$:Yb^{3+}, Er^{3+} core and core-shell nanocrystals, J. Phys. Chem. C 121 (2017) 16592–16606.

[46] S. Heer, K. Petermann, H.U. Gudel, Upconversion excitation of Cr^{3+} emission in YAlO$_3$ codoped with Cr^{3+} and Yb^{3+}, J. Lumin. 102 (2003) 144–150.

[47] S. Ye, E.H. Song, E. Ma, S.J. Zhang, J. Wang, X.Y. Chen, Q.Y. Zhang, J.R. Qiu, Broadband Cr^{3+}-sensitized upconversion luminescence in La$_3$Ga$_5$GeO$_{14}$: Cr^{3+}, Yb^{3+}, Er^{3+}, Opt. Mater. Express 4 (2014) 638–648.

[48] G.Y. Chen, T.Y. Ohulchanskyy, W.C. Law, H. Agren, P.N. Prasad, Monodisperse NaYbF$_4$: Tm^{3+}/NaGdF$_4$ core/shell nanocrystals with near-infrared to near-infrared upconversion photoluminescence and magnetic resonance properties, Nanoscale 3 (2011) 2003–2008.

[49] W. Yu, W. Xu, H.W. Song, S. Zhang, Temperature-dependent upconversion luminescence and dynamics of NaYF$_4$:Yb^{3+}/Er^{3+} nanocrystals: influence of particle size and crystalline phase, Dalton Trans. 43 (2014) 6139–6147.

[50] K. Nigoghossian, S. Ouellet, J. Plain, Y. Messaddeq, D. Boudreau, S.J.L. Ribeiro, Upconversion nanoparticle-decorated gold nanoshells for near-infrared induced heating and thermometry, J. Mater. Chem. B 5 (2017) 7109–7117.

[51] F.F. Chi, F.F. Hu, X.T. Wei, Y.H. Chen, M. Yin, Synthesis and thermometric properties of Yb^{3+}-Er^{3+} co-doped K$_2$GdF$_5$ up-conversion phosphors, J. Rare Earth 35 (2017) 436–440.

[52] S.A. Wade, S.F. Collins, G.W. Baxter, Fluorescence intensity ratio technique for optical fiber point temperature sensing, J. Appl. Phys. 94 (2003) 4743–4756.

[53] CRC Handbook of Chemistry and Physics, 90th ed. (CD-ROM Version 2010); CRC Press/Taylor and Francis: Boca Raton, FL, in.

[54] A. Bayart, F. Szczepanski, J.F. Blach, J. Rousseau, A. Katelnikovas, S. Saitzek, Upconversion luminescence properties and thermal quenching mechanisms in the layered perovskite La$_{1.9}$Er$_{0.1}$Ti$_2$O$_7$ towards an application as optical temperature sensor, J. Alloy. Comp. 744 (2018) 516–527.

[55] D. Manzani, J.F.D. Petruci, K. Nigoghossian, A.A. Cardoso, S.J.L. Ribeiro, A portable luminescent thermometer based on green up-conversion emission of Er^{3+}/Yb^{3+} co-doped tellurite glass, Sci. Rep. 7 (2017) 41596.

[56] I. Hyppanen, N. Perala, R. Arppe, M. Schaferling, T. Soukka, Environmental and excitation power effects on the ratiometric upconversion luminescence based temperature sensing using nanocrystalline $NaYF_4:Yb^{3+},Er^{3+}$, ChemPhysChem 18 (2017) 692–701.

[57] S.S. Zhou, K.M. Deng, X.T. Wei, G.C. Jiang, C.K. Duan, Y.H. Chen, M. Yin, Upconversion luminescence of $NaYF_4$: Yb^{3+}, Er^{3+} for temperature sensing, Optic Commun. 291 (2013) 138–142.

[58] D.T. Klier, M.U. Kumke, Upconversion $NaYF_4$:Yb:Er nanoparticles co-doped with Gd^{3+} and Nd^{3+} for thermometry on the nanoscale, RSC Adv. 5 (2015) 67149–67156.

[59] P. Du, L.H. Luo, X.Y. Huang, J.S. Yu, Ultrafast synthesis of bifunctional Er^{3+}/Yb^{3+}-codoped $NaBiF_4$ upconverting nanoparticles for nanothermometer and optical heater, J. Colloid Interface Sci. 514 (2018) 172–181.

2

Temperature induced emission enhancement and investigation of Nd^{3+}→Yb^{3+} energy transfer efficiency in $NaGdF_4$:Nd^{3+}, Yb^{3+}, Er^{3+} upconverting nanoparticles

I. Mikalauskaite, G. Pleckaityte, L. Sinusaite, V. Plausinaitiene,
A. Katelnikovas, A. Beganskiene

Journal of Luminescence 223 (2020) 117237

Contents lists available at ScienceDirect

Journal of Luminescence

journal homepage: http://www.elsevier.com/locate/jlumin

Temperature induced emission enhancement and investigation of $Nd^{3+}\rightarrow Yb^{3+}$ energy transfer efficiency in $NaGdF_4:Nd^{3+}$, Yb^{3+}, Er^{3+} upconverting nanoparticles

I. Mikalauskaite, G. Pleckaityte, L. Sinusaite, V. Plausinaitiene, A. Katelnikovas*, A. Beganskiene

Institute of Chemistry, Vilnius University, Naugarduko 24, LT-03225, Vilnius, Lithuania

ARTICLE INFO

Keywords:
Downconversion
Upconversion
Temperature induced luminescence
$NaGdF_4$
Nd^{3+} co-doping

ABSTRACT

Inorganic upconverting nanoparticles that can be excited with 808 nm laser radiation are gaining much attention recently. Living tissues, as well as water do not heat up as intensively when embedded upconverting nanoparticles are excited under such wavelength if compared to commonly used 980 nm laser radiation for excitation. To this end, a series of $NaGd_{0.995-x}Yb_xNd_{0.005}F_4$ nanoparticles were synthesized in order to investigate energy transfer efficiency between Nd^{3+} and Yb^{3+} dopants under 808 nm laser excitation to better suit biological applications. The impact of Yb^{3+} concentration increase on crystal phase formation as well as downconversion (DC) properties was investigated. Temperature dependent luminescence measurements in NIR region revealed that no thermal quenching of Nd^{3+}–Yb^{3+} pair in $NaGdF_4$ system was observed in the entire 77–500 K temperature range. Finally, Er^{3+} ions were introduced in the investigated system in order to obtain multiple excitation and visualisation tool with performance in both VIS and NIR regions. The effective energy difference (ΔE) was also calculated from the thermally coupled levels (TCLs) of Er^{3+}. The promising results and observations of synthesized compounds will be discussed, as $NaGd_{0.475}Yb_{0.5}Er_{0.02}Nd_{0.005}F_4$ has a potential to be used as a luminescent temperature sensor.

1. Introduction

Upconverting (UC) nanoparticles (NPs) have been considered as a beneficial luminescent tool in tissue and cell imaging fields. Despite the promising future perspectives, the performance improvement of these nanomaterials is still necessary in order to meet the requirements for practical application. The major challenges that limit the successful application of such nanomaterials in biomedical field are overheating of biological tissues when 980 nm laser is used for excitation, and low luminescence efficiency of upconversion process [1]. The conventional bio-imaging techniques utilize fluorescent dyes or quantum dots. In this sense, the upconverting NPs have lots of advantages, because the near infrared (NIR) radiation used to excite these NPs, can penetrate deeper into the tissue (several centimetres [1]) if compared to short wavelength radiation used to excite fluorescent dyes or quantum dots. Moreover, UC NPs provide narrower emission bands (lines) and weaker autofluorescence [2,3]. Recently, a 915 nm excitation wavelength was proposed for $NaYbF_4$ system yielding lower temperature rise of biological tissue sample over the prolonged irradiation [4]. Another way of shifting excitation to even shorter wavelengths is adding Nd^{3+} ions into the inorganic matrices. Neodymium ions are frequently considered as an alternative sensitizer in UC systems since they possess larger absorption cross-section [5] than Yb^{3+} ions, and several absorption bands in the NIR region where absorption of water is relatively weak. Thus, a deep tissue imaging using NIR emission of Nd^{3+} ions is also considered as an advantageous approach, which eliminates the negative impact of the biological components from the outcoming signal [6,7]. To avoid any overheating and suppression of signal due to the interaction with biological tissue, an emission in the second near infrared (NIR-II) biological window has been proposed as a subject for investigation. There are several lanthanide ions (i.e., Tm^{3+}, Nd^{3+}, Yb^{3+}, Pr^{3+}, Er^{3+}, and Ho^{3+}) possessing emission bands in the NIR-II region. These bands can be employed in bio-imaging through downconversion (DC) approach [8–10]. The advantage of Nd^{3+} doping is the shift of excitation wavelength to ca. 808 nm, what significantly reduces the overheating effect. Besides, an additional combination of DC and UC emission in single

---

* Corresponding author.
E-mail address: arturas.katelnikovas@chf.vu.lt (A. Katelnikovas).

https://doi.org/10.1016/j.jlumin.2020.117237
Received 15 November 2019; Received in revised form 19 March 2020; Accepted 21 March 2020
Available online 28 March 2020

nanoparticle system might also be realized [11]. Nd^{3+} ions can be used in combination with any other lanthanide pair showing UC emission (for instance, $Yb^{3+}-Er^{3+}$, $Yb^{3+}-Ho^{3+}$, $Yb^{3+}-Tm^{3+}$). The choice of UC lanthanide pair depends on intended application and desired emission colour output under a single excitation wavelength [12]. Nd^{3+} ions become like a bridge when used with the previously mentioned UC lanthanide pairs; therefore, it is very important to find the optimal concentration of Nd^{3+} ions yielding the highest energy transfer efficiency to Yb^{3+} ions.

Moreover, Nd^{3+} ions are also considered as one of the main elements in a field of nanothermometry [13]. Since thermal sensing and nanothermometry became frequently discussed throughout the years [14], an additional lanthanide luminescence application possibilities ought to be explored. In fact, temperature is one of the most important factors affecting lanthanide luminescence intensity because of their unique energy level distribution [15]. Energy levels, that are used for temperature sensing are usually spaced near each other and follows a Boltzmann distribution of populating these levels under influence of temperature [16]. Thermally coupled energy levels (TCL) are reported as a basis for exploiting Yb^{3+}/Er^{3+} in the field of nanothermometry [1]. Furthermore, besides $^2H_{11/2}$ and $^4S_{3/2}$ energy levels of Er^{3+} ions [17], Tm^{3+} [18], Ho^{3+} [19] and Nd^{3+} [20] are also considered to be used for thermal sensing applications due to corresponding TCLs [21]. It is important to have a TCL with an energy difference between 200 and 2000 cm^{-1}, since it affects the efficiency of sensitivity [17]. Nd^{3+} doped phosphors have been designed as an optical thermometer materials and investigated upon excitation of higher energy photons (green) or 980 nm with additional energy transfer from Yb^{3+} ions to Nd^{3+} [22,23]. Recently, a temperature induced luminescence intensity enhancement via thermal population of Nd^{3+} ladder-like energy levels [24] was also reported.

In order to obtain a multiple visualisation tool that could be used in both visible (VIS) and NIR regions, a combination of $Nb^{3+}-Yb^{3+}-Er^{3+}$ dopant ions in one matrix was investigated. In our study, a series of $NaGdF_4$:0.5% Nd^{3+}, x% Yb^{3+} samples with varying Yb^{3+} (where $0\% \leq x \leq 99.5\%$) concentration was prepared by thermal decomposition synthesis method. The co-doped Yb^{3+} ions affected the crystal lattice parameters and luminescence properties. Since doping concentration of sensitizer and activator ions plays a crucial role in UC emission intensity [5], an energy transfer efficiency measurements between $Nd^{3+}-Yb^{3+}$ pair has drawn our attention. The temperature dependent luminescence spectra were also recorded and interesting behaviour of Nd^{3+} luminescence properties in 77–500 K temperature range was observed. A series of 0.5% Nd^{3+}, x% Yb^{3+}, 2% Er^{3+} doped $NaGdF_4$ nanoparticles was also prepared, in order to find the optimal Yb^{3+} concentration yielding the most efficient luminescence suitable for both, UC and DC visualisation, and thermal sensing.

2. Experimental

$NaGd_{0.995-x}Yb_xNd_{0.005}F_4$ nanoparticles were synthesized via thermal decomposition method. Gd_2O_3 (Aldrich, 99.9%), Nd_2O_3 (Alfa Aesar, 99.99%) and Yb_2O_3 (Alfa Aesar, 99.9%) were dissolved in a mixture of 5 mL trifluoroacetic acid (Carl Roth, 99.9%) and 5 mL distilled water. This mixture was heated for few hours with a constant stirring until it became clear. After drying the products under vacuum, sodium trifluoroacetate (Alfa Aesar, 98.0%) was added followed with the addition of 7.5 mL oleic acid and 7.5 mL 1-octadecene (Alfa Aesar, 90.0%). The mixture was stirred under N_2 flow at 150 °C (Solution A). 12.5 mL of oleic acid and 1-octadecene were added to 250 mL three neck round bottomed flask which was heated to 330 °C under N_2 flow. After trifluoroacetates were fully dissolved, the Solution A was slowly injected to 330 °C and maintained with constant stirring for 1 h. The mixture was cooled down to room temperature and nanoparticles were precipitated with the addition of hexane:acetone (1:4) and centrifuged at 7000 rpm for 30 min. The washing was repeated twice and the powder was dried at room temperature. The same synthesis procedure was applied to obtain $NaGd_{0.975-x}Yb_xEr_{0.02}Nd_{0.005}F_4$ nanoparticles.

Powder XRD patterns of obtained compounds were recorded with Rigaku MiniFlex diffractometer within the range $10° \leq 2\theta \leq 90°$ using Ni-filtered Cu Kα radiation. Scanning speed and step width were 5°/min and 0.02°, respectively.

For determination of lattice parameters, powder XRD patterns of obtained compounds were recorded with Bruker D8 Advance using Cu Kα radiation at $10° \leq 2\theta \leq 90°$ (integration time and step width were 0.3 s and 0.001°, respectively) with Bragg-Brentano focusing geometry and LynxEYE detector. Lattice parameters were evaluated with TOPAS program using Le Bail's method.

Synthesized samples were analysed by inductively coupled plasma optical emission spectrometry (ICP-OES) with PerkinElmer Optima 7000 DV. Dissolving of samples was implemented by using microwave reaction system Anton Paar Multiwave 3000 (XF100 rotor and PTFE liners) adding nitric acid (HNO_3, Rotipuran® Supra 69%, Carl Roth). Calibration solutions were prepared from single-element ICP Standards (1000 mg/L, Carl Roth).

Transmission electron microscopy (TEM) images were obtained with Tecnai G2 F20 X-TWIN (FEI) with high angle annular dark field (HAADAF) detector using single and double tilt holders with 11 MPix ORIUS SC1000B (Gatan) CCD camera. Schottky type field emission electron source was used.

Downconversion and upconversion luminescence spectra were obtained by measuring samples with Edinburgh Instruments FLS980 spectrometer equipped with Hamamatsu R928P photomultiplier and double grating Czerny-Turner emission monochromator. Constant wavelength lasers (808 nm (for DC) or 980 nm (for UC)) were used for excitation. Both, step size and emission bandwidth were set to 0.5 nm, and integration time was 0.4 s. For measurements powder samples (8.8 mg) were dispersed in 2 mL toluene for DC and UC luminescence measurements, which were carried out under continuous stirring.

When measuring DC decay curves, pulsed 808 nm laser with frequency of 100 Hz and 50 Hz was used for excitation, while emission was monitored at 864 and 976 nm, respectively. When recording UC decay curves a pulsed 980 nm laser with frequency of 100 Hz was used for excitation, whereas the emission was monitored at 407, 539.5, and 653.5 nm. The collected data were fitted using the following equation:

$$I(t) = A + B_1 e^{(-t/\tau_1)} + B_2 e^{(-t/\tau_2)} \tag{1}$$

Here $I(t)$ is intensity of luminescence at a certain time t; A, B_1, B_2 corresponds to background and pre-exponentials constants, respectively; τ_1, τ_2 are emission lifetime values.

Temperature dependent luminescence measurements were performed employing a cryostat MicrostatN from Oxford Instruments. Samples were cooled with liquid nitrogen. Initial measurement temperature was set to 77 K; later temperature increase was set in the 100–500 K range with the continuous increase at 50 K interval. 90 s and ±5 K were set as temperature stabilization time and temperature tolerance interval, respectively.

3. Results and discussion

In order to investigate the impact of co-doping of Yb^{3+} ions into $NaGd_{0.995}Nd_{0.005}F_4$, a series of synthesis were carried out. Analysis of XRD measurements reveal that incorporating small amounts of Yb^{3+} instead of Gd^{3+} results in formation of pure hexagonal phase (Fig. 1, PDF#(ICDD) 00-027-0699) $NaGdF_4$. Additional peaks of cubic phase were found when concentration of Yb^{3+} increased up to 60% (Fig. 1). According to the literature [25], lanthanides with larger ionic radii favour hexagonal phase formation, which occurs due to lowered energy barrier for $\alpha \rightarrow \beta$ phase transition [26]. Thus, by gradual elimination of Gd^{3+} ions, a more probable $\beta \rightarrow \alpha$ phase transition took place resulting in hexagonal and cubic phase mixture. Successful Yb^{3+} incorporation is

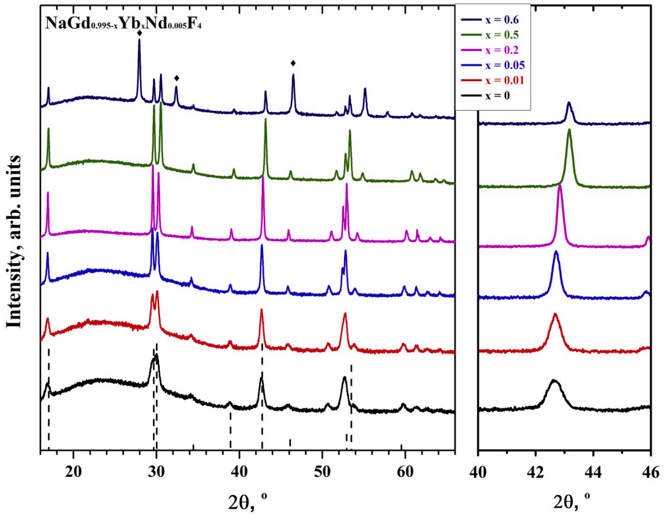

Fig. 1. Powder XRD patterns of $NaGd_{0.995\text{-}x}Yb_xNd_{0.005}F_4$ powders (x = 0, 1, 5, 20, 50, 60%) and reference pattern (dashed line) of $NaGdF_4$ (PDF#(ICDD) 00-027-0699). Cubic phase peaks are marked with ◆.

confirmed by the shift of XRD peaks towards higher 2θ angles (Fig. 1). Since larger Gd^{3+} ions (r = 1.107 Å for CN = 9) are replaced by smaller Yb^{3+} ions (r = 1.042 Å for CN = 9) [27] the reduction of unit cell parameters is evident from shift of 42–44 $2\theta°$ (201) peak. The evolution of unit cell parameters upon Yb^{3+} concentration increase is depicted in Fig. 2 (the exact obtained values are tabulated in Table S1). It is evident that both hexagonal phase unit cell parameters (a and c) of the nanoparticles have a tendency to decrease in size; thus, confirming a shrinkage in unit cell volume.

ICP-OES analysis was carried out in order to determine the actual concentration of ions in $NaGd_{0.995\text{-}x}Yb_xNd_{0.005}F_4$ compounds. The determined elemental composition of the samples is represented in Table S2. The deviation from initial concentration of Yb^{3+}, Er^{3+}, Nd^{3+}, Gd^{3+} ions used during synthesis is very small, thus it is concluded that the intended compounds were successfully synthesized.

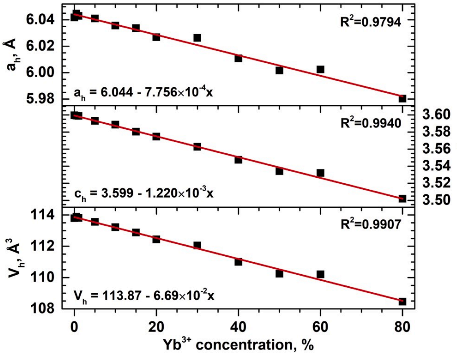

Fig. 2. Unit cell parameters of $NaGd_{0.995}Nd_{0.005}F_4{:}Yb^{3+}$ nanoparticles obtained from Le Bail fit.

The morphology of $NaGd_{0.995\text{-}x}Yb_xNd_{0.005}F_4$ were evaluated from TEM images. TEM images of samples doped with 1%, 60% and 99.5% Yb^{3+} ions are represented in Fig. 3. The calculated average nanoparticle size for these compounds is 22.2, 48.1, and 57.2 nm, respectively. High crystallinity of $NaGd_{0.985}Yb_{0.01}Nd_{0.005}F_4$ nanoparticles is evidenced by atomic planes in larger magnification of Fig. 3a image. According to XRD data, samples with 60% and 99.5% Yb^{3+} consist of two distinct crystalline phases (α and β); however, no difference in the shape of particles shown in Fig. 3b and c was observed.

Emission spectra of $NaGd_{0.995\text{-}x}Yb_xNd_{0.005}F_4$ series were recorded under 808 nm excitation and are presented in Fig. 4. These spectra were normalized to 976 nm for better interpretation of the results. There are several sets of emission lines and one broad emission band in the recorded spectra. The emission lines were attributed to Nd^{3+} transitions $^4F_{3/2} \rightarrow {}^4I_{9/2}$ (ca. 870 nm) and $^4F_{3/2} \rightarrow {}^4I_{11/2}$ (ca. 1060 nm), whereas the broad emission band was assigned to $^2F_{5/2} \rightarrow {}^2F_{7/2}$ transition (ca. 976 nm) of Yb^{3+} ions. When concentration of Yb^{3+} is low, $Nd^{3+} \rightarrow Yb^{3+}$ energy transfer is indistinguishable. However, as the amount of Yb^{3+} increases, the intensity of emission peaks originating from $^4F_{3/2} \rightarrow {}^4I_{9/2}$ and $^4F_{3/2} \rightarrow {}^4I_{11/2}$ transitions of Nd^{3+} ions decrease gradually. This, in fact, is expected, since with the increasing Yb^{3+} concentration, the Yb^{3+} ions statistically get closer to Nd^{3+} ions and facilitate the $Nd^{3+} \rightarrow Yb^{3+}$ energy transfer; hence, the Nd^{3+} emission decreases [28].

A possible energy transfer pathway was proposed by several groups [29–31] and are represented in Fig. 5. Nd^{3+} ions have one order of magnitude larger absorption cross-section at 808 nm than most commonly used ions (Yb^{3+}) in typical upconverting systems [5]. Thus, Nd^{3+} is considered as a promising candidate to be used in both DC and UC approaches. Since energy is pumped through "bridging" ions (Nd^{3+}) it is very important to investigate the efficiency of such energy transfer to Yb^{3+} in $NaGdF_4$ matrix.

For this reason, decay curves (Fig. 6) of $NaGd_{0.995\text{-}x}Yb_xNd_{0.005}F_4$ were recorded using 808 nm laser excitation. DC luminescence decay curves were monitored at 864 and 976 nm (Fig. 6a and b). The average lifetime values were calculated by fitting the experimental results with bi-exponential function (eq. (1)) and are presented in Table 1.

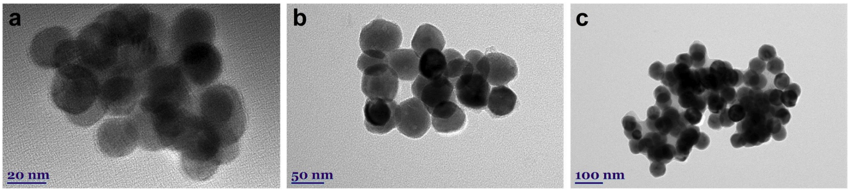

Fig. 3. Bright-field TEM images of $NaGd_{0.995\text{-}x}Yb_xNd_{0.005}F_4$ nanoparticles: a – 1%, b – 60%, c – 99.5% Yb^{3+}.

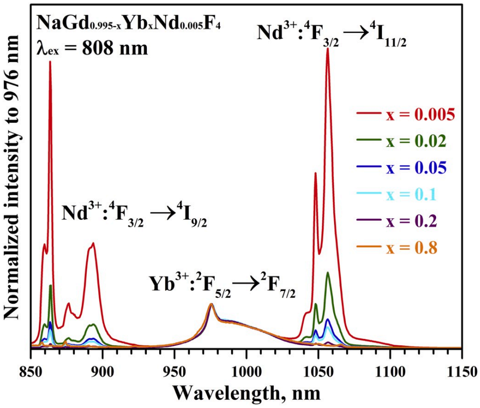

Fig. 4. Emission spectra of $NaGd_{0.995\text{-}x}Yb_xNd_{0.005}F_4$ nanoparticles under 808 nm laser excitation.

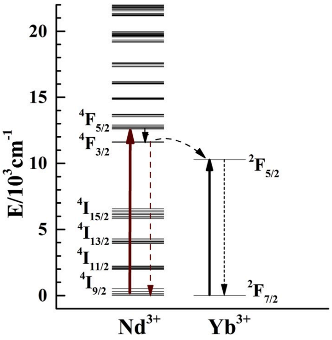

Fig. 5. $Nd^{3+}\rightarrow Yb^{3+}$ energy transfer diagram under 808 nm laser excitation.

Decay curves given is Fig. 6 become steeper with increasing Yb^{3+} concentration regardless the monitored emission wavelength. This indicates that the average luminescence lifetime values of both Nd^{3+} ($^4F_{3/2} \rightarrow {}^4I_{9/2}$, Fig. 6a) and Yb^{3+} ($^2F_{5/2} \rightarrow {}^2F_{7/2}$, Fig. 6b) ions are decreasing when concentration of Yb^{3+} is increasing. The luminescence lifetime values of Nd^{3+} ions decrease from 320 μs (for 0% Yb^{3+}) to 8 μs (for 50% Yb^{3+}) because the probability of energy transfer to Yb^{3+} ions increases considerably. A significant drop in Yb^{3+} ($^2F_{5/2} \rightarrow {}^2F_{7/2}$) luminescence lifetime values could be a result of energy migration among adjacent Yb^{3+} ions followed by energy back transfer to Nd^{3+} ions or other impurities in a crystal lattice [32]. The luminescence lifetime value calculation was followed by the evaluation of energy transfer efficiency (η_{tr}) (eq. (2) [33]) in $Nd^{3+}\rightarrow Yb^{3+}$ system (see Table 1).

$$\eta_{tr} = 1 - \frac{\tau_{Nd-Yb}}{\tau_{Nd}} \tag{2}$$

Here, $\tau_{Nd\text{-}Yb}$ and τ_{Nd} are average luminescence lifetime values of Nd^{3+} $^4F_{3/2} \rightarrow {}^4I_{9/2}$ transition for samples with presence and absence of Yb^{3+} ions, respectively.

The results presented in Table 1 indicate that $Nd^{3+}\rightarrow Yb^{3+}$ energy transfer efficiency of 97.4% is achieved when concentration of Yb^{3+} reaches 50%. This value is higher or very close to those reported for other fluoride and oxide matrices as shown in Table 2. Authors have approached this investigation by additionally varying amount of Nd^{3+} [32,34,35]; however, our scope was intentionally limited to constant Nd^{3+} concentration. Further addition of ytterbium ions led to a slight increase in $Nd^{3+}\rightarrow Yb^{3+}$ energy transfer efficiency value. However, when concentration of Yb^{3+} is above 50% the synthesized compounds contain both cubic and hexagonal crystal phase. Thus, the pathways of energy transfer processes become more complex when additional crystalline phase occurs in a single sample.

Moreover, the temperature dependent emission under 808 nm laser excitation was investigated in $NaGd_{0.995\text{-}x}Yb_xNd_{0.005}F_4$ (x = 0, 0.1, 0.15, 0.2, 0.4) matrix. Firstly, the temperature dependent Nd^{3+} emission for $NaGd_{0.995}Nd_{0.005}F_4$ sample was recorded in the range of 77–500 K (see Fig. 7). The temperature dependent integrated emission values are plotted in the inset of Fig. 7. It is interesting to note, that the integrated emission values increased in the 77–350 K temperature range followed by slight decrease of intensity in the 400–500 K range. Similar results were also reported by Wawrzynczyk et al. the thermal population of higher excited state energy levels was assigned as the cause of this phenomenon [36].

The temperature dependent luminescence decay curves for Nd^{3+} $^4F_{3/2} \rightarrow {}^4I_{9/2}$ transition in $NaGd_{0.995}Nd_{0.005}F_4$ are given in Fig. 8. The given curves are overlapping; thus, this indicates that the PL lifetime values are very close and almost do not change in the given temperature range. It is, however, evident that the decay curve recorded at 400 K is the least steep and it is concluded that the luminescence lifetime value at this temperature is the highest. These results go hand in hand with temperature dependent emission spectra given in Fig. 7 where the strongest Nd^{3+} emission was observed at 350 K. A mechanism involving neighbouring Nd^{3+} ions with temperature induced energy circling, which later results in an increased emission has already been discussed in the literature [37]. Temperature induced energy transfer between Nd^{3+} ions is suggested to occur as a result of increased population of the $^4I_{11/2}$ state. By increasing its population proportionally to the temperature increase, an emission from $^4F_{3/2}$ level takes place together with a cross relaxation process involving $^4F_{3/2}$ – $^4I_{9/2}$ energy levels of two separate ions, thus doubling the population of $^4I_{11/2}$ [37].

Furthermore, when Yb^{3+} concentration was increased, at first (1% Yb^{3+}) no distinct effect on the temperature dependent luminescence was

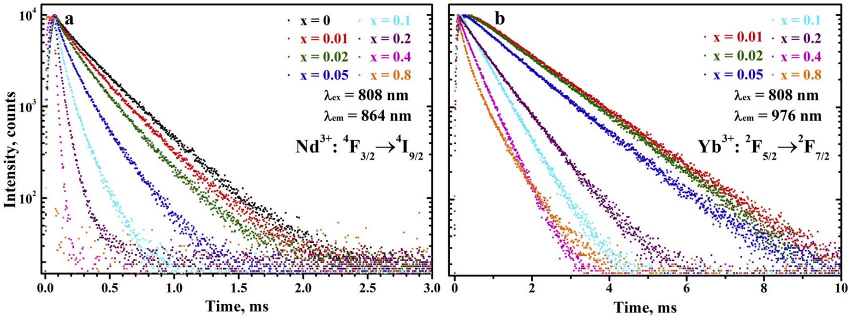

Fig. 6. Decay curves of $\mathrm{NaGd_{0.995\text{-}x}Yb_xNd_{0.005}F_4}$ samples (λ_{ex} = 808 nm) for Nd^{3+} emission (a) and Yb^{3+} emission (b).

Table 1
Calculated lifetime values (λ_{ex} = 808 nm) and Nd^{3+}→Yb^{3+} energy transfer efficiencies for $\mathrm{NaGd_{0.995\text{-}x}Yb_xNd_{0.005}F_4}$ samples.

Yb^{3+}, %	$\bar{\tau}$ (λ_{em} = 864 nm), μs	$\bar{\tau}$ (λ_{em} = 976 nm), μs	Nd^{3+}→Yb^{3+} energy transfer efficiency, %
0	320		
0.5	320	1530	0
1	294	1453	8.1
2	258	1455	19.1
5	195	1258	38.9
10	117	591	63.3
15	85	441	73.3
20	74	798	76.8
40	27	458	91.5
50	8	441	97.4
60	3	567	99.1
80	1	551	99.7
99.5	1	117	99.6

Table 2
Comparison of Nd^{3+}→Yb^{3+} energy transfer efficiency values in different matrices.

Matrix	Nd^{3+}→Yb^{3+} energy transfer efficiency (max), %	Ref.
$NaYF_4$:0.5%Nd^{3+}, 10%Yb^{3+}	92.0	[32]
$NaGdF_4$:10%Nd^{3+}, 4%Yb^{3+}	98.7	[34]
$CaIn_2O_4$:1%Nd^{3+}, 30%Yb^{3+}, 1.5%Er^{3+}	92.3	[35]
$NaGdF_4$:0.5%Nd^{3+}, 50%Yb^{3+}	97.4	This work

observed (Fig. S2a) except of the appearance of $^2F_{5/2}$ → $^2F_{7/2}$ emission band of Yb^{3+} ions at ca. 975 nm. Further increase of Yb^{3+} concentration was followed by an expected tendency of more evident growth of Yb^{3+} emission, while the intensity of all Nd^{3+} emission lines decreased. This is a direct evidence that part of radiation absorbed by Nd^{3+} ions is transferred to adjacent Yb^{3+} ions. Eventually, the Nd^{3+} emission vanishes when Yb^{3+} concentration in samples exceeds 40%. However, there is a Nd^{3+} emission increase at relatively low temperatures, followed by a decrease from 200 K for all investigated Yb^{3+} concentrations (1% Yb^{3+}, 15% Yb^{3+}, 20% Yb^{3+}, and 40% Yb^{3+} as depicted in figS2Figs. S2a, S2b, S2c, and S2d, respectively). These observations were followed by temperature dependent decay measurements (Fig. S3, figS4Fig. S4) where transitions of both Nd^{3+} ($^4F_{3/2}$ → $^4I_{9/2}$) and Yb^{3+} ($^2F_{5/2}$ → $^2F_{7/2}$) ions were monitored. At low Yb^{3+} concentration (1%) PL decay curves of Nd^{3+} ($^4F_{3/2}$ → $^4I_{9/2}$) ions are virtually the same having an average lifetime value about 340–360 μs (Table S3). More interesting effects appear when Yb^{3+} concentration reaches 40%. PL decay curves of Yb^{3+} ($^2F_{5/2}$ → $^2F_{7/2}$) transition appear to be more affected by the temperature, while Nd^{3+} ($^4F_{3/2}$ → $^4I_{9/2}$) curves become steeper as the temperature increases. Moreover, this behaviour suggests that thermal population and energy circling in Nd^{3+} contributes to Yb^{3+} emission at elevated temperatures as it can be seen from the increasing energy transfer efficiency values calculated for 1% and 40% Yb^{3+} doped samples (see Table S3). The temperature induced luminescence quenching appears only at elevated temperatures (500 K) as the energy transfer efficiency begins to decrease.

As a result of this interesting temperature dependent luminescence behaviour in Nd–Yb system, further co-doping with Er^{3+} ions was performed with the purpose to obtain a visualisation tool that gives a performance under double excitation (808 and 980 nm) covering a broad range of emission (VIS–NIR). To investigate an impact of triple doping into $NaGdF_4$ matrix without adding additional shell, a series of samples with different Yb^{3+} concentrations was synthesized while Nd^{3+} and Er^{3+} concentrations were fixed at 0.5% and 2%, respectively.

Fig. 9 represents powder XRD patterns of $\mathrm{NaGd_{0.975\text{-}x}Yb_xEr_{0.2}Nd_{0.005}F_4}$ with different Yb^{3+} concentration. XRD data of $\mathrm{NaGd_{0.78}Yb_{0.2}Er_{0.02}F_4}$ powder is also included for comparison. In all cases, a single hexagonal phase is formed as it was observed in previously described samples without Er^{3+} ions (see Fig. 1). The diffraction peak at 2θ 42–44 (201) shifts towards higher 2θ values indicating that incorporation of Yb^{3+} ions into the host matrix was successful. These results were confirmed by ICP-OES analysis. The obtained concentrations of rare earth ions are given in Table S4. The theoretical and experimental values are in good agreement with negligible deviations. Thus, the addition of Er^{3+} had no impact on the formation of $\mathrm{NaGd_{0.975\text{-}x}Yb_xEr_{0.02}Nd_{0.005}F_4}$ nanoparticles.

Since the compounds were designed to be used as a tool for VIS and NIR visualisation, luminescence properties at both excitation (808 and 980 nm) wavelengths were investigated. Firstly, the spectra obtained under 808 nm laser excitation were analysed (see Fig. 10) attributing energy transitions of Er^{3+} ions (in VIS region) and Nd^{3+}, Yb^{3+} ions (in NIR region). Several sets of emission lines occurring in the visible part of the spectra were assigned to Er^{3+} transitions, namely, $^4G_{11/2}$ → $^4I_{15/2}$ at ca. 380 nm, $^2H_{9/2}$ → $^4I_{15/2}$ at ca. 407 nm, $^2H_{11/2}$ → $^4I_{15/2}$ at ca. 520 nm, $^4S_{3/2}$ → $^4I_{15/2}$ at ca. 545 nm, and $^4F_{9/2}$ → $^4I_{15/2}$ at ca. 655 nm. For better interpretation of the results, emission spectra were normalized to intensity at 653 nm. In fact, a gradual increase of Yb^{3+} concentration could be considered as the cause of decrease in relative green emission intensity. With the addition of Yb^{3+} ions a change in green/red emission ratio occurs from an increased number of supplementary relaxation pathways at the expense of suppressed green emission [38]. Moreover, emission peaks originating from electronic transitions of Nd^{3+} and Yb^{3+} ions under 808 nm excitation were also observed in NIR range

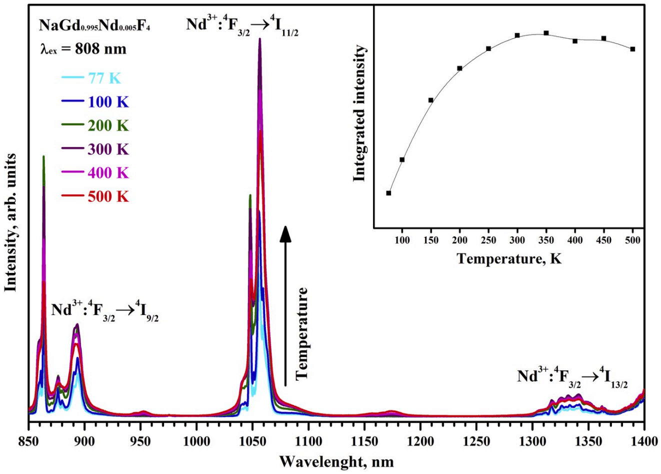

Fig. 7. Emission spectra of $NaGd_{0.995}Nd_{0.005}F_4$ nanoparticles recorded at various temperatures under 808 nm laser excitation. Inset shows integrated emission intensity at certain temperature (the line was drawn to guide an eye).

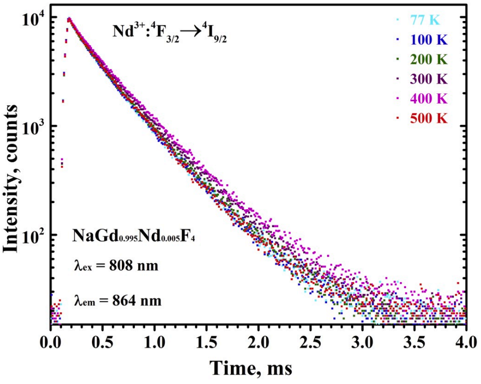

Fig. 8. Decay curves of $NaGd_{0.995}Nd_{0.005}F_4$ nanoparticles recorded at various temperatures (λ_{ex} = 808 nm).

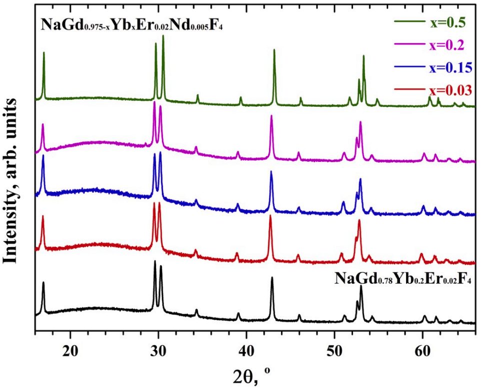

Fig. 9. Powder XRD patterns of $NaGd_{0.975\text{-}x}Yb_xEr_{0.02}Nd_{0.005}F_4$ (x = 0.03, 0.15, 0.2, 0.5) and $NaGd_{0.78}Yb_{0.2}Er_{0.02}F_4$ powders.

(850–1100 nm). In this case, the spectra were normalized to intensity at 976 nm. Fig. 10, clearly shows that emission intensity of Nd^{3+} transitions ($^4F_{3/2} \rightarrow {}^4I_{9/2}$ at ca. 860 nm and $^4F_{3/2} \rightarrow {}^4I_{11/2}$ at ca. 1064 nm) is gradually decreasing with the addition of Yb^{3+}. These results are consistent with $NaGd_{0.995\text{-}x}Yb_xNd_{0.005}F_4$ samples where Yb^{3+} addition alters pathways of energy transfer in Nd−Yb system. A comparison of emission in NIR region under 808 nm excitation between $NaGd_{0.475}Yb_{0.5}Er_{0.02}Nd_{0.005}F_4$ and $NaGd_{0.495}Yb_{0.5}Nd_{0.005}F_4$ samples (Fig. S5) confirmed additional energy transfer pathway due to addition of Er^{3+} ions by the decreased intensity of Yb^{3+} ($^2F_{5/2} \rightarrow {}^2F_{7/2}$) emission band.

The previously mentioned results were supported with the PL decay measurements involving emission transitions monitored at 539 nm ($^4S_{3/2} \rightarrow {}^4I_{15/2}$ transition) and 653 nm ($^4F_{9/2} \rightarrow {}^4I_{15/2}$ transition) for Er^{3+} ions under 808 nm wavelength laser excitation (see Fig. S6). The calculated PL lifetime values are tabulated in Table S5. The PL lifetime values of $^4S_{3/2} \rightarrow {}^4I_{15/2}$ transition decreased gradually with increasing Yb^{3+} concentration, i.e., from ca. 389 μs for 3% Yb^{3+} to ca. 110 μs for 50% Yb^{3+} doped sample. However, different behaviour of PL lifetime values was observed for $^4F_{9/2} \rightarrow {}^4I_{15/2}$ transition of Er^{3+} ions. Here, PL lifetime values were ca. 550 μs for 3% Yb^{3+} doped sample and remained virtually constant (ca. 385 μs) for Yb^{3+} concentration in the range of 15%–50% (see Table S5). Moreover, the PL decay curves for Nd^{3+} ($^4F_{3/2} \rightarrow {}^4I_{9/2}$ transition, figS7Fig. S7a) and Yb^{3+} ($^2F_{5/2} \rightarrow {}^2F_{7/2}$ transition, figS7Fig. S7b) in $NaGd_{0.975}Yb_xEr_{0.02}Nd_{0.005}F_4$ samples under 808 nm wavelength laser excitation were also recorded as a function of Yb^{3+} concentration. The PL lifetime values of Nd^{3+} ions decrease considerably with increasing Yb^{3+} concentration (from ca. 208 μs for 3% doped sample to ca. 57 μs for 50% doped sample), indicating the increase of $Nd^{3+} \rightarrow Yb^{3+}$ energy transfer efficiency as was also observed in samples without Er^{3+} ions. Similar behaviour of Yb^{3+} PL decay curves was also

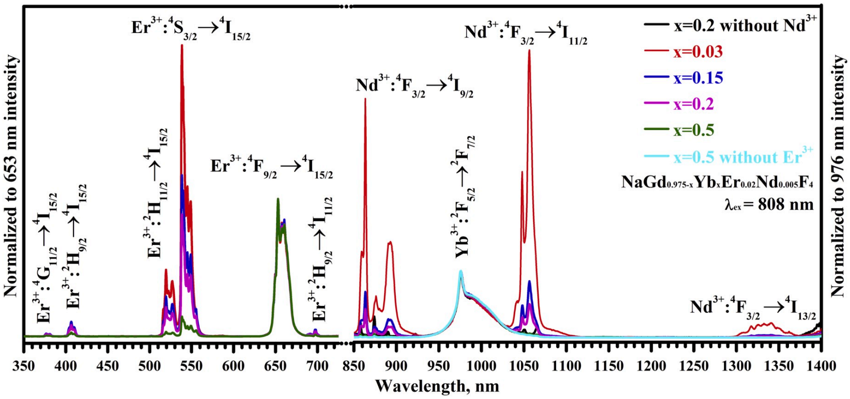

Fig. 10. Emission spectra of $NaGd_{0.975-x}Yb_xEr_{0.02}Nd_{0.005}F_4$ nanoparticles with different Yb^{3+} concentration (x = 0.03, 0.15, 0.2, 0.5) under 808 nm laser excitation.

observed. Here PL lifetime values of Yb^{3+} emission decreased from ca. 635 µs to ca. 180 µs for 3% and 50% Yb^{3+} doped samples, respectively. The decrease of Yb^{3+} PL lifetime values can be associated with an increased amount of Yb^{3+} ions located at the surface of nanoparticle. This results in increased number of non-radiative relaxations due to a higher possibility of surface defects quenching the emission of $^2F_{5/2} \rightarrow {}^2F_{7/2}$ transition [39].

Moreover, $NaGd_{0.975-x}Yb_xEr_{0.02}Nd_{0.005}F_4$ samples (x = 0.03, 0.15, 0.2, 0.5) were also investigated under 980 nm excitation. Emission bands corresponding to Er^{3+} electronic transitions in VIS range were attributed (see Fig. 11). Position and wavelength of emission bands were in good agreement with the results from excitation with 808 nm laser (as shown in Fig. 10). In fact, the same tendency of emission intensity decrease in the green region in comparison to the red emission band was observed with the increase of Yb^{3+} concentration. From the data represented in Table S5, it can be concluded that the average PL lifetime values of $^4S_{3/2} \rightarrow {}^4I_{15/2}$ (539 nm) and $^4F_{9/2} \rightarrow {}^4I_{15/2}$ (653 nm) transitions under both excitation wavelengths (808 and 980 nm) were virtually the same. The results, obtained by investigating DC and UC emission of $NaGd_{0.975-x}Yb_xEr_{0.02}Nd_{0.005}F_4$ samples, have shown that the VIS emission of Er^{3+} ions tends to shift to the red spectral region due to additional interaction with Yb^{3+} ions. The increase of intensity in the red spectral region could be very beneficial if these luminescent materials are considered for application in photodynamic therapy [40].

Er^{3+} ions have two TCLs ($^4S_{3/2}$ and $^2H_{11/2}$) in the green spectral region. These TCLs are frequently proposed for luminescent temperature sensor application [41,42]. In order to investigate a possibility to use $NaGd_{0.975-x}Yb_xEr_{0.02}Nd_{0.005}F_4$ for temperature sensing, temperature dependent luminescence measurements were carried out. UC luminescence spectra of $NaGd_{0.475}Yb_{0.5}Er_{0.02}Nd_{0.005}F_4$ sample, recorded in temperature range of 77–500 K, are given in Fig. 12. The emission from $^2H_{11/2} \rightarrow {}^4I_{15/2}$ transition does not occur at low temperatures and can only be observed if the sample temperature rises above 150 K. Moreover, comparing relative $^2H_{11/2} \rightarrow {}^4I_{15/2}$ intensity to $^4S_{3/2} \rightarrow {}^4I_{15/2}$ shows a gradual increase of emission centred at 520 nm with the increase of

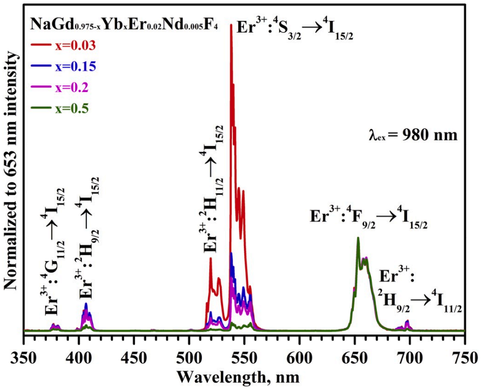

Fig. 11. Emission spectra of $NaGd_{0.975-x}Yb_xEr_{0.02}Nd_{0.005}F_4$ nanoparticles with different Yb^{3+} concentration (x = 0.03, 0.15, 0.2, 0.5) under 980 nm laser excitation.

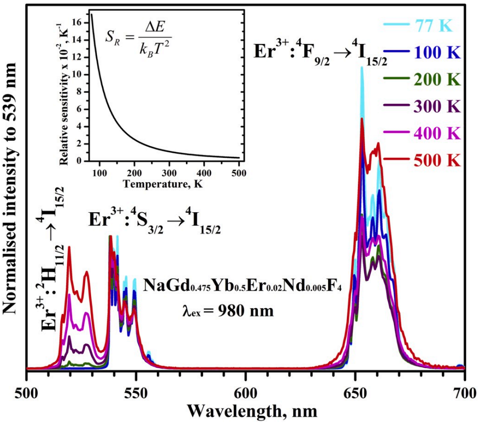

Fig. 12. Emission spectra (normalized to 539 nm) of $NaGd_{0.475}Yb_{0.5}Er_{0.02}Nd_{0.005}F_4$ nanoparticles recorded at various temperatures under 980 nm excitation. Inset shows relative temperature sensitivity (S_r) values in 77–500 K temperature range.

temperature. The absence of emission from $^2H_{11/2} \rightarrow {}^4I_{15/2}$ transition at low temperatures shows that the $^2H_{11/2}$ level can be only thermally populated from lower lying $^4S_{3/2}$ level. From these results the FIR value was calculated employing eq. (3) [43]:

$$FIR = \frac{I_{520}}{I_{520}} = Ce^{\left(-\Delta E / k_g T\right)} \tag{3}$$

Here I_{520} and I_{540} are the integrated intensities of $^2H_{11/2} \rightarrow {}^4I_{15/2}$ and $^4S_{3/2} \rightarrow {}^4I_{15/2}$ emission transitions, respectively. C is a constant, ΔE – effective energy difference between these TCLs, k_B – Boltzmann constant (8.617342×10^{-5} eV/K) [44], T – absolute temperature. An effective energy distance between $^2H_{11/2}$ and $^4S_{3/2}$ was calculated (699 ± 16 cm^{-1}) with nearly perfect Boltzmann fit ($R^2 = 0.9988$). The obtained value is close to the discussed theoretical value of 700–800 cm^{-1} [45]. Besides, for compounds where TCLs are present, an additional evaluation of relative sensitivity (S_r) can be carried out following this equation [46]:

$$S_r = \frac{\Delta E}{k_B T^2} \tag{4}$$

As it can be seen from eq. (4), S_r indicates that with the increase of energy gap between two TCLs, the material becomes more sensitive to a temperature change. The obtained S_r value (Fig. 11 inset) for $NaGd_{0.475}Yb_{0.5}Er_{0.02}Nd_{0.005}F_4$ at 300 K was 1.11% K^{-1} which indicates that the compound could successfully be proposed for the application as a temperature sensor [30,45].

4. Conclusions

In the current study, inorganic $NaGdF_4$ nanoparticles doped with Nd^{3+} and Yb^{3+} ions were analysed. A single hexagonal phase compounds were formed until Yb^{3+} concentration reached 50%. The increase of Yb^{3+} concentration resulted in decrease of hexagonal lattice parameters. The additional cubic phase formation was also observed if Yb^{3+} concentration exceeded 50%. DC emission and PL decay measurements confirmed a successful $Nd^{3+} \rightarrow Yb^{3+}$ energy transfer under 808 nm laser excitation. The highest energy transfer efficiency value for single phase compound was obtained when Yb^{3+} concentration reached 50%. Temperature dependent emission spectra of $NaGd_{0.995}Nd_{0.005}F_4$ revealed the emission intensity increase up to 350 K showing almost inert behaviour of 864 nm emission from temperature dependent decay curves. Abnormal temperature induced emission with 1%, 15%, 20% and 40% Yb^{3+} was also observed under influence of elevated temperature. An additional doping with 2% Er^{3+} ions was also performed in a series of synthesized compounds. Dual excitation (808 and 980 nm) measurements for analysing DC and UC materials revealed a suppressed green emission band ($^4S_{3/2};{}^2H_{11/2} \rightarrow {}^4I_{15/2}$) due to Yb^{3+} concentration increase. Moreover, an effective energy distance (ΔE) of thermally coupled levels (TCL) of Er^{3+} was calculated ($\Delta E = 699 \pm 16\ cm^{-1}$) from fluorescence intensity ratio (FIR) and was in good agreement with the theoretical value. The relative sensitivity (S_r) of $NaGd_{0.475}Yb_{0.5}Er_{0.02}Nd_{0.005}F_4$ value (1.11% K^{-1}) suggests these materials have a broad area of application not only in DC and UC visualisation, but also as temperature sensors.

CRediT authorship contribution statement

I. Mikalauskaite: Methodology, Investigation, Writing - original draft, Visualization. **G. Pleckaityte:** Investigation, Visualization. **L. Sinusaite:** Investigation. **V. Plausinaitiene:** Investigation, Formal analysis. **A. Katelnikovas:** Conceptualization, Resources, Writing - review & editing, Supervision, Funding acquisition. **A. Beganskiene:** Conceptualization, Writing - review & editing, Funding acquisition.

Acknowledgements

This project has received funding from the Research Council of Lithuania (LMTLT), agreement No (S-MIP-17-48) and No (S-LU-18-13).

Appendix A. Supplementary data

Supplementary data to this article can be found online at https://doi.org/10.1016/j.jlumin.2020.117237.

References

[1] B. del Rosal, D. Jaque, Upconversion nanoparticles for in vivo applications: limitations and future perspectives, Methods Appl. Fluoresc. 7 (2019), 022001.

[2] C. Ash, M. Dubec, K. Donne, T. Bashford, Effect of wavelength and beam width on penetration in light-tissue interaction using computational methods, Laser Med. Sci. 32 (2017) 1909–1918.

[3] S.H. Nam, Y.M. Bae, Y.I. Park, J.H. Kim, H.M. Kim, J.S. Choi, K.T. Lee, T. Hyeon, Y. D. Suh, Long-term real-time tracking of lanthanide ion doped upconverting nanoparticles in living cells, Angew. Chem. Int. Ed. 50 (2011) 6093–6097.

[4] Q.Q. Zhan, J. Qian, H.J. Liang, G. Somesfalean, D. Wang, S.L. He, Z.G. Zhang, S. Andersson-Engels, Using 915 nm laser excited Tm3+/Er3+/Ho3+-doped NaYbF4 upconversion nanoparticles for in vitro and deeper in vivo bioimaging without overheating irradiation, ACS Nano 5 (2011) 3744–3757.

[5] L.P. Tu, X.M. Liu, F. Wu, H. Zhang, Excitation energy migration dynamics in upconversion nanomaterials, Chem. Soc. Rev. 44 (2015) 1331–1345.

[6] X. Wu, G.Y. Chen, J. Shen, Z.J. Li, Y.W. Zhang, G. Han, Upconversion nanoparticles: a versatile solution to multiscale biological imaging, Bioconjugate Chem. 26 (2015) 166–175.

[7] Z. Wang, P. Zhang, Q.H. Yuan, X. Xu, P.P. Lei, X.L. Liu, Y. Su, L.L. Dong, J. Feng, H. J. Zhang, Nd3+-sensitized NaLuF4 luminescent nanoparticles for multimodal imaging and temperature sensing under 808 nm excitation, Nanoscale 7 (2015) 17861–17870.

[8] U. Resch-Genger, H.H. Gorris, Perspectives and challenges of photon-upconversion nanoparticles - Part I: routes to brighter particles and quantitative spectroscopic studies, Anal. Bioanal. Chem. 409 (2017) 5855–5874.

[9] E. Hemmer, P. Acosta-Mora, J. Mendez-Ramos, S. Fischer, Optical nanoprobes for biomedical applications: shining a light on upconverting and near-infrared emitting nanoparticles for imaging, thermal sensing, and photodynamic therapy, J. Mater. Chem. B 5 (2017) 4365–4392.

[10] E. Hemmer, H. Takeshita, T. Yamano, T. Fujiki, Y. Kohl, K. Low, N. Venkatachalam, H. Hyodo, H. Kishimoto, K. Soga, In vitro and in vivo investigations of upconversion and NIR emitting Gd2O3:Er3+,Yb3+ nanostructures for biomedical applications, J. Mater. Sci. Mater. Med. 23 (2012) 2399–2412.

[11] X.M. Li, R. Wang, F. Zhang, L. Zhou, D.K. Shen, C. Yao, D.Y. Zhao, Nd3+ sensitized up/down converting dual-mode nanomaterials for efficient in-vitro and in-vivo bioimaging excited at 800 nm, Sci. Rep. 3 (2013) 3536.

[12] F. He, L.L. Feng, P.P. Yang, B. Liu, S.L. Gai, G.X. Yang, Y.L. Dai, J. Lin, Enhanced up/down-conversion luminescence and heat: simultaneously achieving in one single core-shell structure for multimodal imaging guided therapy, Biomaterials 105 (2016) 77–88.

[13] W. Xu, Q.T. Song, L.J. Zheng, Z.G. Zhang, W.W. Cao, Optical temperature sensing based on the near-infrared emissions from Nd3+/Yb3+ codoped CaWO4, Opt. Lett. 39 (2014) 4635–4638.

[14] I.E. Kolesnikov, A.A. Kalinichev, M.A. Kurochkin, E.V. Golyeva, E.Y. Kolesnikov, A. V. Kurochkin, E. Lahderanta, M.D. Mikhailov, YVO4: Nd3+ nanophosphors as NIR-to-NIR thermal sensors in wide temperature range, Sci. Rep. 7 (2017) 18002.

[15] D. Jaque, F. Vetrone, Luminescence nanothermometry, Nanoscale 4 (2012) 4301–4326.

[16] Y. Cheng, Y. Gao, H. Lin, F. Huang, Y.S. Wang, Strategy design for ratiometric luminescence thermometry: circumventing the limitation of thermally coupled levels, J. Mater. Chem. C 6 (2018) 7462–7478.

[17] K. Pavani, J.S. Kumar, K. Srikanth, M.J. Soares, E. Pereira, A.J. Neves, M.P. F. Graca, Highly efficient upconversion of Er3+ in Yb3+ codoped non-cytotoxic strontium lanthanum aluminate phosphor for low temperature sensors, Sci. Rep. 7 (2017) 17646.

[18] B.S. Cao, J.L. Wu, Z.Q. Feng, B. Dong, Investigation of near-infrared-to-ultraviolet upconversion luminescence of Tm3+ doped NaYF4 phosphors by Yb3+ codoping, Mater. Chem. Phys. 142 (2013) 333–338.

[19] W. Xu, H. Zhao, Y.X. Li, L.J. Zheng, Z.G. Zhang, W.W. Cao, Optical temperature sensing through the upconversion luminescence from Ho3+/Yb3+ codoped CaWO4, Sensor. Actuator. B Chem. 188 (2013) 1096–1100.

[20] P. Huang, W. Zheng, D.T. Tu, X.Y. Shang, M.R. Zhang, R.F. Li, J. Xu, Y. Liu, X. Y. Chen, Unraveling the electronic structures of neodymium in LiLuF4 nanocrystals for ratiometric temperature sensing, Adv. Sci. 6 (2019) 1802282.

[21] K.Z. Zheng, Z.Y. Liu, C.J. Lv, W.P. Qin, Temperature sensor based on the UV upconversion luminescence of Gd3+ in Yb3+-Tm3+-Gd3+ codoped NaLuF4 microcrystals, J. Mater. Chem. C 1 (2013) 5502–5507.

[22] X.F. Wang, Q. Liu, Y.Y. Bu, C.S. Liu, T. Liu, X.H. Yan, Optical temperature sensing of rare-earth ion doped phosphors, RSC Adv. 5 (2015) 86219–86236.

[23] C. Mi, J.J. Zhou, F. Wang, D.Y. Jin, Thermally enhanced NIR-NIR anti-Stokes emission in rare earth doped nanocrystals, Nanoscale 11 (2019) 12547–12552.

[24] G.J. Gao, D. Busko, S. Kauffmann-Weiss, A. Turshatov, I.A. Howard, B.S. Richards, Wide-range non-contact fluorescence intensity ratio thermometer based on Yb3+/Nd3+ co-doped La2O3 microcrystals operating from 290 to 1230 K, J. Mater. Chem. C 6 (2018) 4163–4170.

[25] F. Wang, Y. Han, C.S. Lim, Y.H. Lu, J. Wang, J. Xu, H.Y. Chen, C. Zhang, M. H. Hong, X.G. Liu, Simultaneous phase and size control of upconversion nanocrystals through lanthanide doping, Nature 463 (2010) 1061–1065.

[26] J.A. Damasco, G.Y. Chen, W. Shao, H. Agren, H.Y. Huang, W.T. Song, J.F. Lovell, P. N. Prasad, Size-tunable and monodisperse Tm3+/Gd3+-doped hexagonal NaYbF4 nanoparticles with engineered efficient near infrared-to-near infrared upconversion for in vivo imaging, ACS Appl. Mater. Interfaces 6 (2014) 13884–13893.

[27] R.D. Shannon, Revised effective ionic radii and systematic studies of interatomic distances in halides and chalcogenides, Acta Crystallogr. A A32 (1976) 751–767.

[28] L.J. Tian, Z. Xu, S.L. Zhao, Y. Cui, Z.Q. Liang, J.J. Zhang, X.R. Xu, The upconversion luminescence of Er3+/Yb3+/Nd3+ triply-doped beta-NaYF4 nanocrystals under 808-nm excitation, Materials 7 (2014) 7289–7303.

[29] J. Shen, G.Y. Chen, A.M. Vu, W. Fan, O.S. Bilsel, C.C. Chang, G. Han, Engineering the upconversion nanoparticle excitation wavelength: cascade sensitization of tri-doped upconversion colloidal nanoparticles at 800 nm, Adv Opt Mater 1 (2013) 644–650.

[30] D.T. Klier, M.U. Kumke, Upconversion NaYF4:Yb:Er nanoparticles co-doped with Gd3+ and Nd3+ for thermometry on the nanoscale, RSC Adv. 5 (2015) 67149–67156.

[31] L.J. Tian, Z. Xu, S.L. Zhao, Y. Cui, Z.Q. Liang, J.J. Zhang, X.R. Xu, The upconversion luminescence of Er3+/Yb3+/Nd3+ triply-doped β-NaYF4 nanocrystals under 808-nm excitation, Materials 7 (2014) 7289–7303.

[32] X.B. Dong, F.T. You, H.S. Peng, S.H. Huang, Ultraviolet to near-infrared energy transfer in NaYF4:Nd3+,Yb3+ crystals, J. Rare Earths 34 (2016) 863–867.

[33] A. Lupei, V. Lupei, A. Ikesue, C. Gheorghe, S. Hau, Nd→Yb energy transfer in (Nd, Yb):Y2O3 transparent ceramics, Opt. Mater. 32 (2010) 1333–1336.

[34] F.J. Pedraza, C. Rightsell, G.A. Kumar, J. Giuliani, C. Monton, D.K. Sardar, Emission enhancement through Nd3+-Yb3+ energy transfer in multifunctional NaGdF4 nanocrystals, Appl. Phys. Lett. 110 (2017) 223107.

[35] X. Liu, T. Li, X.Q. Zhao, H. Suo, Z.Y. Zhang, P.J. Zhao, S. Gao, M. Niu, 808 nm-triggered optical thermometry based on up-conversion luminescence of Nd3+/Yb3+/Er3+ doped MIn2O4 (M = Ca, Sr and Ba) phosphors, Dalton Trans. 47 (2018) 6713–6721.

[36] D. Wawrzynczyk, A. Bednarkiewicz, M. Nyk, W. Strek, M. Samoc, Neodymium (III) doped fluoride nanoparticles as non-contact optical temperature sensors, Nanoscale 4 (2012) 6959–6961.

[37] L. Marciniak, A. Bednarkiewicz, K. Elzbieciak, NIR-NIR photon avalanche based luminescent thermometry with Nd3+ doped nanoparticles, J. Mater. Chem. C 6 (2018) 7568–7575.

[38] A. Podhorodecki, B. Krajnik, L.W. Golacki, U. Kostiv, G. Pawlik, M. Kaczmarek, D. Horak, Percolation limited emission intensity from upconverting NaYF4:Yb3+, Er3+ nanocrystals - a single nanocrystal optical study, Nanoscale 10 (2018) 21186–21196.

[39] M.Y. Hossan, A. Hor, Q. Luu, S.J. Smith, P.S. May, M.T. Berry, Explaining the nanoscale effect in the upconversion dynamics of β-NaYF4:Yb3+, Er3+ core and core-shell nanocrystals, J. Phys. Chem. C 121 (2017) 16592–16606.

[40] G. Tian, W.L. Ren, L. Yan, S. Jian, Z.J. Gu, L.J. Zhou, S. Jin, W.Y. Yin, S.J. Li, Y. L. Zhao, Red-Emitting upconverting nanoparticles for photodynamic therapy in cancer cells under near-infrared excitation, Small 9 (2013) 1929–1938.

[41] F.F. Chi, F.F. Hu, X.T. Wei, Y.H. Chen, M. Yin, Synthesis and thermometric properties of Yb3+-Er3+ co-doped K2GdF5 up-conversion phosphors, J. Rare Earths 35 (2017) 436–440.

[42] K. Nigoghossian, S. Ouellet, J. Plain, Y. Messaddeq, D. Boudreau, S.J.L. Ribeiro, Upconversion nanoparticle-decorated gold nanoshells for near-infrared induced heating and thermometry, J. Mater. Chem. B 5 (2017) 7109–7117.

[43] S.A. Wade, S.F. Collins, G.W. Baxter, Fluorescence intensity ratio technique for optical fiber point temperature sensing, J. Appl. Phys. 94 (2003) 4743–4756.

[44] CRC Handbook of Chemistry and Physics, 90th ed. (CD-ROM Version 2010); CRC Press/Taylor and Francis: Boca Raton, FL, in.

[45] S.S. Zhou, K.M. Deng, X.T. Wei, G.C. Jiang, C.K. Duan, Y.H. Chen, M. Yin, Upconversion luminescence of NaYF4: Yb3+, Er3+ for temperature sensing, Optic Commun. 291 (2013) 138–142.

[46] D. Manzani, J.F.D. Petruci, K. Nigoghossian, A.A. Cardoso, S.J.L. Ribeiro, A portable luminescent thermometer based on green up-conversion emission of Er3+/Yb3+ co-doped tellurite glass, Sci. Rep. 7 (2017) 41596.

Vilnius University Press
9 Saulėtekio Ave., Building III, LT-10222 Vilnius
Email: info@leidykla.vu.lt,
www.leidykla.vu.lt
Print run copies 20